Publication 4 (P4)

S. Marrone, A. Colagrossi, J. Calderon-Sanchez and **J. Martinez-Carrascal** (2021). A numerical study on the dissipation mechanisms in sloshing flows induced by violent and high frequency accelerations. Part II: comparison against experimental data. Physical Review Fluids, 6 114802, 2021. DOI: https://doi.org/10.1103/PhysRevFluids.6.114802. 6 citations. JCR(2021): 2.895, Physics, Fluids and Plasmas (Q2).

A numerical study on the dissipation mechanisms in sloshing flows induced by violent and high frequency accelerations. Part II: comparison against experimental data.

S. Marrone and A. Colagrossi*

CNR-INM, INstitute of Marine Engineering,

Via di Vallerano 139,

00128 Rome, Italy.

J. Calderon-Sanchez and J. Martinez-Carrascal

School of Naval Engineering,

Universidad Politécnica de Madrid,

Avda. de la Memoria 4 28040 Madrid Spain

(Dated: October 21, 2022)

Abstract

In Paper I of this series [Marrone, Colagrossi, Gonzalez,"A numerical study on the dissipation mechanisms in sloshing flows induced by violent and high frequency accelerations. Part I: Theoretical formulation and numerical investigation"], a theoretical formulation and the numerical model were developed in order to obtain a complete perspective of the energy balance of a violently accelerated flow confined inside a rectangular tank. The tank-fluid system was periodically excited with a predetermined law of motion and the force between the wall and the fluid and the global energy balance were computed. In this second part, the experimental validation of the previous formulation is presented. In order to make a comparison with a previous experimental campaign, where the tank moves along a single degree of freedom mechanical guide, two numerical problems have been studied: in the first, the decaying movement of the tank is prescribed according to the experimental measurements, and in the second the tank is coupled to a mass-spring-damper equation, and the sloshing force produced by the confined fluid acts as an external force. Both problems have been studied for two different fluids, water and oil, which implies a difference of two orders of magnitude in terms of Reynolds number. A complete description of the energy balance inside the fluid tank is performed and the complexity of the fluid dynamic behaviour that takes place inside the tank is explained. The results are compared to the experimental measurements in terms of fluid-wall interaction and energy dissipation.

* andrea.colagrossi@cnr.it

I. INTRODUCTION

A theoretical and numerical scheme to compute the dynamics of a confined liquid that moves inside the tank with high accelerations and strong wall impacts, referred to hereinafter as "sloshing flow" or "shaken flow", has been developed in Paper I of the present work.

In this part we will consider the particular fluid-structure interaction problem where the external excitations that generate the fluid movement come from the damped oscillations of a structure. This situation mimics what happens in reality with external wind gusts and air turbulence in fuel sloshing in aircraft wings. In our numerical and experimental model, the fluid is initially confined in a closed tank and accelerated to typical values of 10g in the vertical direction. The initial amplitude is comparable to the tank height and frequencies approximate the Froude scaling law. Previous experiments [15] have demonstrated that the fluid action plays an important damping role on the structure.

First, in order to understand the complexity of the flow involved in the problem and test the fluid Smoothed Particle Hydrodynamics (SPH) solver performance, the system will be uncoupled, and the tank movement will be externally prescribed according to previous experimental records. Second, the fully coupled system is solved where a sloshing forced mass-spring-damper system is coupled with an SPH code that computes the fluid action. The results obtained in this coupled case are compared to their previous equivalent experiments [15]. Similarly to the procedure followed in [5, 6] the extra damping added by the fluid's presence is computed numerically and compared to the experimental results.

Following the terminology explained in the introduction of Paper I, in decaying excitation flows an impulsive heave motion of the tank produces a violent slamming against the top and bottom tank walls. This initial stage of these violent flows, referred to as "shaken flow", is essentially driven by inertial forces which are much larger than the gravitational ones.

These kinds of sloshing flows can be studied either experimentally or computationally using different techniques. Regarding the experimental studies the first references can be found during the mid-1960s [1, 8, 10]. These experiments normally study horizontally moving tanks, or rotating tanks but only a few recently published studies focus on violent vertical tank movements [7, 14]). In a recent experimental campaign [18] a partially filled tank was attached to the end of an elastic beam trying to reproduce the scaled situation found in aircraft wing tanks. The beam was deformed and released, and the tank containing the fluid

would move with a decaying, heave, oscillatory motion characterized by a peak acceleration near 10g. This behaviour has been also reproduced in the experimental campaign developed in the CEHINAV [15] and in the University of Bristol [11] based on a series of single degree of freedom vertical sloshing experiments. In this work, a Froude scaled experiment has been devised measuring the sloshing force acting on the tank when the accelerations are similar to the ones found in a real wing, confirming that the fluid presence notably increases the damping of the system. Ongoing projects, such as the EU-SLOWD [13] are planning ambitious experimental campaigns in the future that include a full scale aircraft wing structure with corresponding fuel tanks. This structure will be excited to the most critical conditions where sloshing effects are likely to be relevant.

Regarding the numerical approach, in agreement with the first part of this work, a SPH method has been used. The important improvements of the classical SPH method explained in Part I are now applied to different decaying cases. As was discussed, these new ideas are very important when violent free surface flows with strong wall impacts are computed using the SPH methodology, showing its reliability in problems involving free-surface breakage, which occurs frequently during violent sloshing. Alternatively, different techniques can be used in order to solve the fully coupled problem involving fluid and structural motions. For example, in [12] the potential flow theory is used, whilst [19] and [17] use a a mass-spring system.

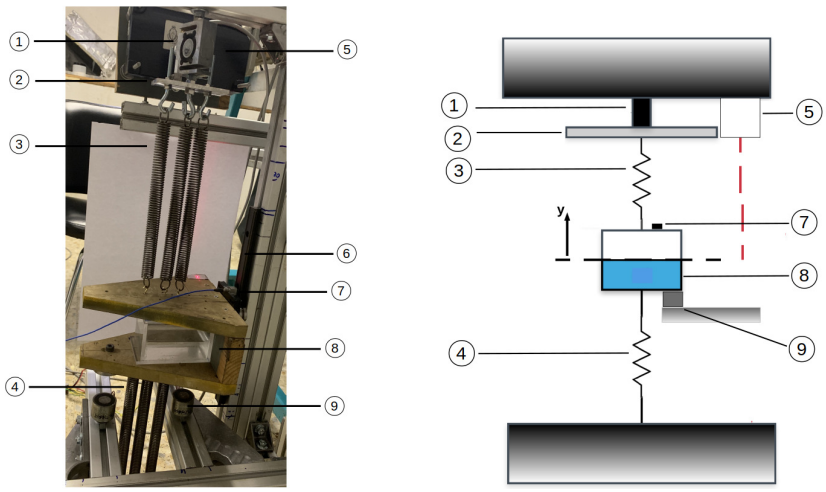
As in the first part of this work, this paper is not limited to obtaining accurate simulations of these violent sloshing flows; it also tries to study the energy dissipation mechanisms that occur in these kinds of violent and confined flows which, eventually, are of interest in aeronautics applications.

This work is organized as follows: Section 2 describes the experimental setup used for the validation of the numerical results. Section 3 briefly recalls the adopted mathematical model which is described in detail in the first part of the paper (Part I). The results of the numerical simulations for both forced motion and fully coupled tests are presented in Section 4. Finally, the main findings are summarized in the conclusions section.

II. EXPERIMENTAL MODEL FOR THE VALIDATION

In [15], the experiment by [18] was simplified into a Single Degree of Freedom (SDOF) vertically moving tank and represents a more damped version of the experiment conducted by [11] in 2021. Taking into account the dimensional analysis of the problem at hand and applying the Π theorem to a reference variable [3], for example the damping ratio added by the fluid to the system, one can find a dimensional relation between this variable and several non-dimensional groups, such as the Reynolds number, Froude number, density ratio, etc. In sloshing problems, a Froude scaling is usually performed [3] where $Fr = \sqrt{\omega_0^2 H/Ng}$ is defined based on the maximum acceleration of the problem which is N times the gravity. In the Froude number definition, ω_0 represents the characteristic angular frequency of the problem, H represents the height of the tank, Ng is the maximum acceleration of the problem, being $N \approx 10$ in this study. Next, a geometrical scaling parameter is considered $\lambda = H_{SDOF}/H_W$ defined as the ratio between the heights of the SDOF tank and the wing tank. For the SDOF sloshing tests, a 1:5 scale was selected ($\lambda = 0.2$) which results in a tank geometry of 10×6×6 cm. The scaled tank is filled up to 50 % of its volume which results in a water mass of $m_l = 0.18$ kg and it oscillates at a characteristic frequency of $f_0 = 6.51$ Hz.

A photograph of the experimental setup at the Model Basin Research group sloshing laboratory of the UPM and a simplified outline are shown in figure 1. The experimental rig is an SDOF system composed of a mechanical guide that allows the single degree of freedom constraint. This guide is attached to a C-shaped wooden structure that holds the tank with a structural mass of $m_s = 2.403$ kg. Similarly, the C-shaped wooden structure is attached to a set of 6 springs, each one having an individual spring constant of $k = 718.05$ N/m, 3 on the upper side and 3 on the bottom side. The lower springs are mechanically embedded into the floor, and on the opposite side the upper set of springs is attached to a metallic plate that acts as a joint between them and the embedded load cell. This setup also includes an accelerometer attached to the C-shaped wooden structure, a laser sensor aimed at the wooden block and two solenoids acting as a release mechanism. The structure is deflected to an initial amplitude and it is fixed by the magnetic force of the solenoids. When the electrical current is turned on, the structure is released triggering the beginning of the experiment. The acceleration and position of the tank as well as load cell measurements are recorded allowing the calculation of the sloshing force acting on the system. A more



(a) Experimental setup (b) Outline of the setup

FIG. 1: Experimental setup and outline. (1) Load cell, (2) Metallic plate with mass $m_p = 0.06$ kg, (3) Upper set of springs with stiffness constant $k_1 = 2154.17$ N/m, (4) Lower set of springs with stiffness constant $k_2 = 2154.17$ N/m, (5) Laser sensor, (6) Mechanical guide, (7) Accelerometer, (8) Methacrylate tank and C-shaped wooden structure with mass $m_s = 2.403$ kg, (9) Pair of solenoids acting as release mechanism.



FIG. 2: Experimental snapshots of the SDOF vertical sloshing water experiments carried out in [15] for 10 g and 50 % filling level.

detailed description of the experimental setup and vertical sloshing force derivation can be found in [15].

In figure 2 it can be seen that the flow is divided into four main stages. First, right after the release at $t = 0.108$ s the meniscus present in the hydrostatic state travels horizontally forming a ripple at the free surface that triggers a vertical Rayleigh-Taylor instability. The instability travels in the upward direction and causes the first fluid to wall impact

at $t = 0.130$ s. After that, the free surface is fragmented and the flow can be considered as highly turbulent, characterized by many fluid-fluid and fluid-wall impacts. Finally, when the tank motion is attenuated, at around $t = 2.45$ s the last fluid-wall impact happens and a standing wave regime develops until the system reaches the rest condition.

From this experimental study, the vertical sloshing force, tank acceleration and position are obtained. Each experimental test was repeated three times, finding very small variability among repetitions. These results are used in Section IV to validate the numerical outcomes.

III. BRIEF RECALL OF THE ADOPTED MODEL

In this section, the main hypotheses underlying the numerical model and the equations of the system's energy balance are briefly recalled. For a complete derivation and discussion of the hypotheses and the equations described below, the reader is referred to the first part of the paper (Part I).

The governing equations adopted are the Navier-Stokes equations (NSE) for a single-phase weakly-compressible fluid. Because of the high Reynolds number related to the experiments described in the previous section, in the numerical scheme a sub-grid model for the turbulent viscosity is needed. To this end the δ-LES-SPH model described [2] is considered, where a Large Eddy Simulation (LES) modeling is rewritten in a Lagrangian formalism and introduced in the SPH system of equations.

The main simplifications adopted in the numerical model to reproduce the experiment are:

- a two-dimensional framework;
- the air phase is neglected (only the liquid phase is modelled);
- thermal conductivity and surface tension effects are neglected;
- weakly-compressible regime is always attained using a sufficiently large artificial speed of sound .

Furthermore, in simulations involving water, the adopted spatial resolution is not sufficient to resolve the Wall Boundary Layer (WBL) regions and, for this reason, the free-slip conditions are used. Conversely, for simulations involving oil, due to the lower Reynolds

number it is possible to resolve the WBL regions, and therefore, for these simulations the no-slip conditions are used. In Appendix A a study of the relevance of WBL modelling is addressed.

Due to its easier implementation in Part I of the paper the implementation of the Non-inertial Frame of Reference (Ni-FoR) is preferred with respect to the Inertial Frame of Reference (I-FoR). This is also because it avoids numerical errors related to the tank motion. This choice is made in the present work as well. Besides the technical numerical aspects, the energy balance written in both of the frames of reference will be useful for the analysis of the data and the comparison against the experimental measurements.

Recalling the derivation in Part I, the δ-LES-SPH energy balance can be written as:

$$\dot{\mathcal{E}}_M \,+\, \dot{\mathcal{E}}_C \,=\, \mathcal{P}_V \,+\, \mathcal{P}_V^{turb} \,+\, \mathcal{P}_{\mathcal{N}} \,+\, \mathcal{P}_{ext}\,, \qquad \mathcal{P}_{\mathcal{N}} \,:=\, \mathcal{P}_\delta \,+\, \mathcal{P}(\delta \boldsymbol{u}) \tag{1}$$

where $\dot{\mathcal{E}}_M$ is the time derivative of the mechanical energy of the particle system, $\dot{\mathcal{E}}_C$ is the time derivative of the elastic potential energy associated to fluid compressibility, $\mathcal{P}_{ext}$ is the external power due to the tank motion. The terms $\mathcal{P}_V$, $\mathcal{P}_V^{turb}$, and $\mathcal{P}_{\mathcal{N}}$, are power terms related only to energy dissipation: $\mathcal{P}_V$ and $\mathcal{P}_V^{turb}$ correspond respectively to fluid viscous stresses and modelled turbulent viscous stresses, and $\mathcal{P}_{\mathcal{N}}$ is related to numerical diffusive terms. The energy dissipated in the numerical scheme, $\mathcal{E}_{diss}$, is therefore directly evaluated as:

$$\mathcal{E}_{diss} \,=\, \int_{t_0}^{t} \left(\mathcal{P}_V \,+\, \mathcal{P}_V^{turb} \,+\, \mathcal{P}_{\mathcal{N}}\right)\, dt\ . \tag{2}$$

IV. RESULTS: SLOSHING IN FORCED DECAY HEAVE MOTION

In this section the experiment described in Section II is addressed. The problem is studied following two steps of increasing complexity.

- Test N.1: the acceleration time history recorded in the experiments in [15] is applied to the tank. In this case it is possible to also compare the forces obtained in the numerical simulation with those recorded in the experiment.
- Test N.2: the complete coupled Fluid Structure Interaction (FSI) problem is considered. In this case one can directly compare the observed numerical tank displacements to the experimental ones, also avoiding the uncertainties related to the computation of the experimental work done by the tank.

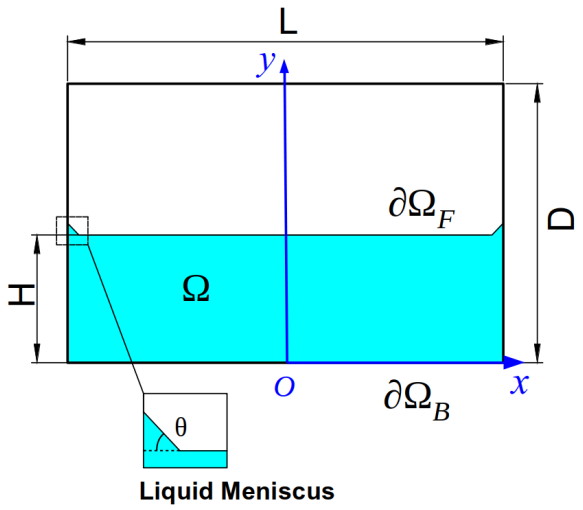


FIG. 3: Sketch of the problem geometry and initial conditions (see Part I for more details).

For all the test cases the numerical setup is the same as the one described in Part I. Specifically, the tank height is D=0.06 m, the width is L=0.1 m and the tank filling level is 50%, that is, the water depth is H=0.03 m. The liquid used is characterised by density $\rho = 1000$ kg/m^3 and corresponding viscosity in order to match the desired Re for each fluid.

In the experiment, when the fluid is at rest, a meniscus is formed close to the vertical walls because of the surface tension. This is numerically replicated in the initial conditions by adding, close to the vertical boundaries, a small fluid triangle of the same angle and height as in the experiment (figure 3), respectively $\theta = 45°$and $l = 1.5$ mm. As it is also reported in Part I, surface tension effects are negligible in terms of damping added to the system. This has already been studied by [9]. The speed of sound adopted in all the simulations of the present section is the same as in Part I, $c_0 = 40$ m/s.

A. Test N. 1: Sloshing in forced motion: experimental damped motion law

In this section the law of motion resulting from the experiment in [15] is imposed on the tank. Distinct from the test case in the first part of the paper (Part I), here the law of motion presents an exponential decay due to the energy that is quickly dissipated by the liquid, and to a lesser extent, by the springs and the supporting rails. In addition to the study of the energy dissipation under decaying motion, this test case allows for a comparison of the obtained forces (and related work) acting on the tank with those recorded in the experiment.

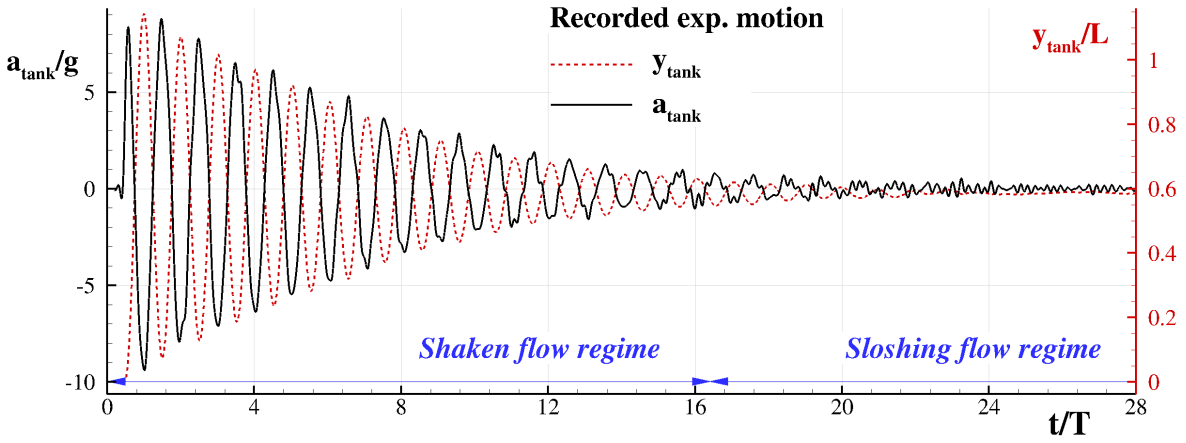


FIG. 4: Tank motion recorded in the experiment of [15] plotted in terms of elevation (dashed line) and acceleration of the tank (solid line).

The maximum amplitude of the oscillation motion, taken from recordings in the experiment, is $2A/L = 1.14$. The frequency of motion is defined as $f_0 = \sqrt{k/m}/(2\pi) = 6.51$ Hz where k is the total spring stiffness and m the sum of the masses of the tank, the liquid and the springs. The period $T = 1/f_0 = 0.154$ s will be used as a characteristic time scale. We can define the characteristic velocity to be $U_{max} = 2\pi A/T = 2.33$ m/s. The corresponding Reynolds number depends on the fluid tested. The reference case used in this work corresponds to water, with Re$= \rho UL/\mu = 233,000$, with dynamic viscosity $\mu = 0.001$ Pa $\cdot$ s. Throughout the session the dissipated energy, $\mathcal{E}_{diss}$, is made non-dimensional by the potential energy $\Delta\mathcal{E} = \rho\, LHg2A = 3.355$ J, unless otherwise specified, corresponding to a power in one cycle equal to $\Delta\mathcal{P} = \Delta\mathcal{E}/T = 21.84$ W. In figure 4 the recorded motion of the tank is plotted in terms of elevation and acceleration of the tank. In the same figure the portion of the time evolution for which the flow is in the "shaken flow" regime is highlighted. We define here the "sloshing" regime as starting when $a_{tank}/g \leq 1$, a_{tank} being the tank acceleration.

In figure 5 the energy decay obtained by the SPH simulation is reported along with the tank displacement. In this case the adopted resolution is $N = H/\Delta x = 400$. The same stepped shape of the simulations in Part I can be recognised in the first 5 periods of oscillation. However, in the present case the rate of dissipated energy decreases in time and becomes very small when the flow is in the sloshing regime. In the same figure, the analytical solution by the 1D model described in Part I (Section VII C) is also reported. It represents a

lower boundary of the system energy and in this case where only the δ-LES-SPH results are discussed, it is far too dissipative with respect to the numerical simulation. Note that, when the "shaken" flow regime ends, the 1D model does not predict any dissipated energy any more. This is due to the hypotheses underlying this simplified model: energy is dissipated only through impacts against either the ceiling or the bottom of the tank.

In the same figure 5, some relevant instants of the flow are labelled. Labels a) to d) are reported in figure 6, in terms of free-surface configuration and contour of the turbulent viscosity ratio μ_T/μ. The initial flow evolution is analogous to the periodic case but for the time of the first impact: in the present case the impact occurs at t/T=1.26 whereas in the previous case it happened at t/T=0.64. This is due to the lower acceleration acting in this case which causes a delayed detachment of the flow. Apart from that, the flow evolves in the same way: in a) the Rayleigh-Taylor instability is triggered; in b) the fluid impacts against the tank ceiling with production of small jets on the sides and high velocity gradients in the center where the two main jets collide; then, the fluid starts a series of cyclical impacts against the bottom of the tank as in c) and d), in which two impacts at the tank bottom are shown: the fluid is mostly fragmented in multiple jets and the energy is mainly dissipated in free-surface re-connections and the consequent generation of vorticity.

The values observed for the ratio μ_T/μ in plots b), c) and d) are order $\mathcal{O}(1)$. Following the analysis presented in Part I, this represents an indication that the inertial turbulent scale is resolved. However, as shown below in the analysis of the energy components, a further increase of the resolution would be needed even if at $N = 400$ the result is close to its convergent limit.

In figure 7, the flow evolution at the time instants related to labels e) and f) of figure 5 is shown in terms of vorticity contours. These two time instants are representative of the transition from the "shaken" flow regime to the "sloshing flow" regime: in plot e) the flow is still highly fragmented with production of vorticity distributed on a wide range of length scales; in f) the vorticity intensity is strongly reduced and no roof impacts occur anymore: the fluid appears compact with very small local breakings and a large gravity wave travels on the liquid surface. This is the typical behaviour of moderate sloshing flows.

In the left plot of figure 8 the different energy components are reported. The amount of energy dissipated through resolved viscous stresses is 8.6%, which is similar to the result obtained for the periodic case presented in Part I. At the same time, the term related

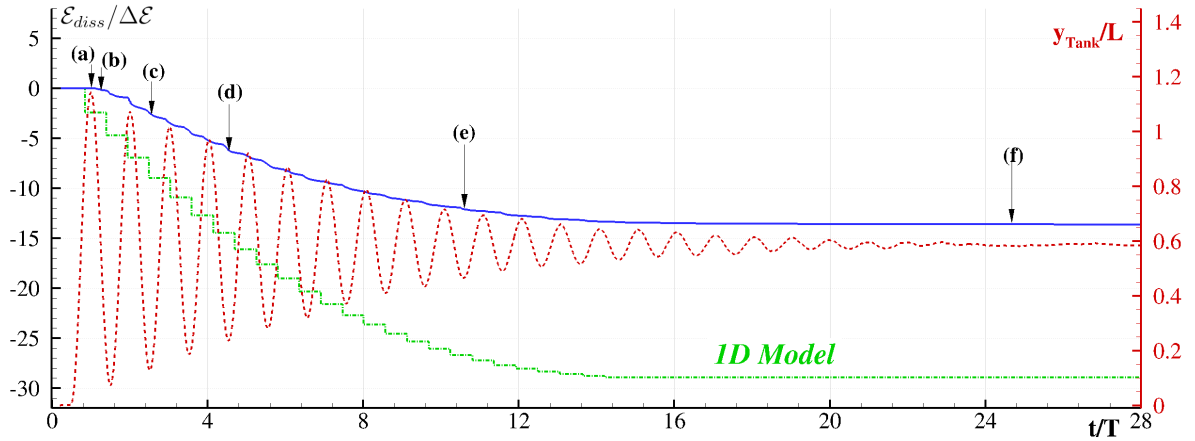


FIG. 5: Time history of the energy decay obtained by the SPH simulation at $N = 400$ and by the 1D analytical model as described in Part I (solid lines). The dashed line represents the tank elevation. Labels (a) to (f) correspond to the same time instants of figure 6 and 7.

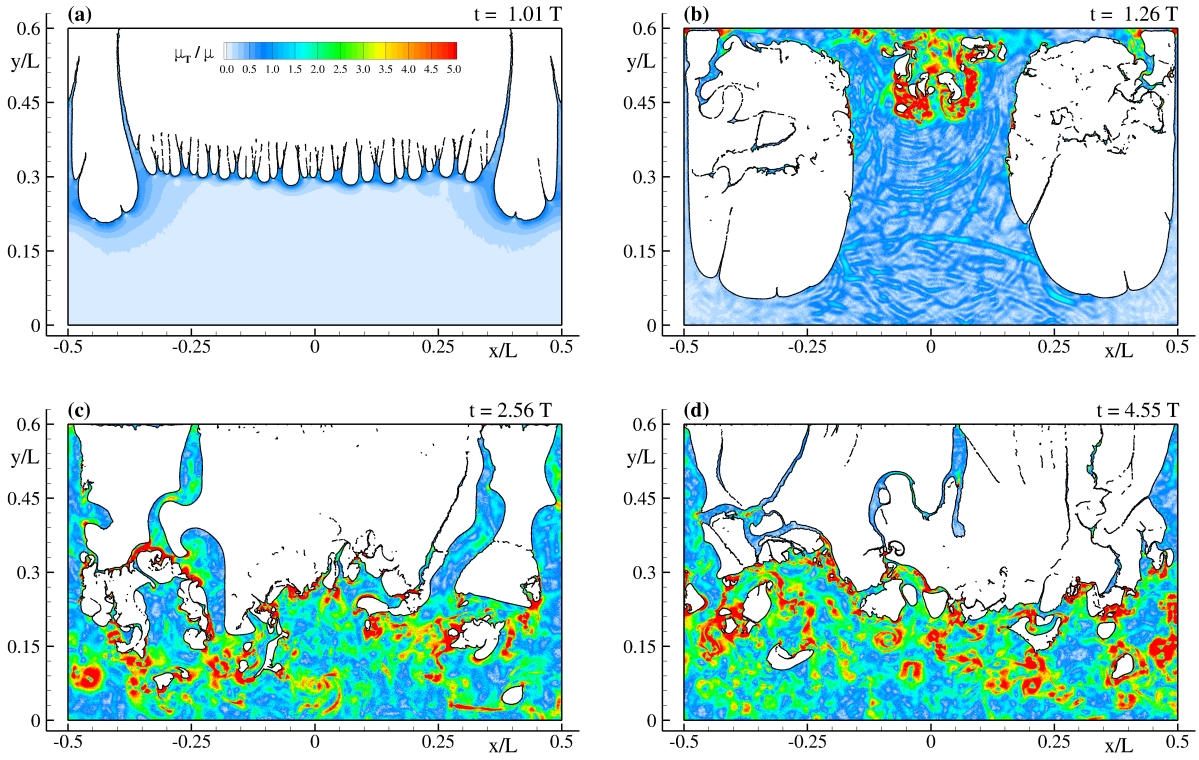


FIG. 6: Four representative instants of the flow evolution obtained by the SPH simulation at $N = 400$ for the Re=233,000 case. Contours refer to turbulent viscosity ratio μ_T/μ.

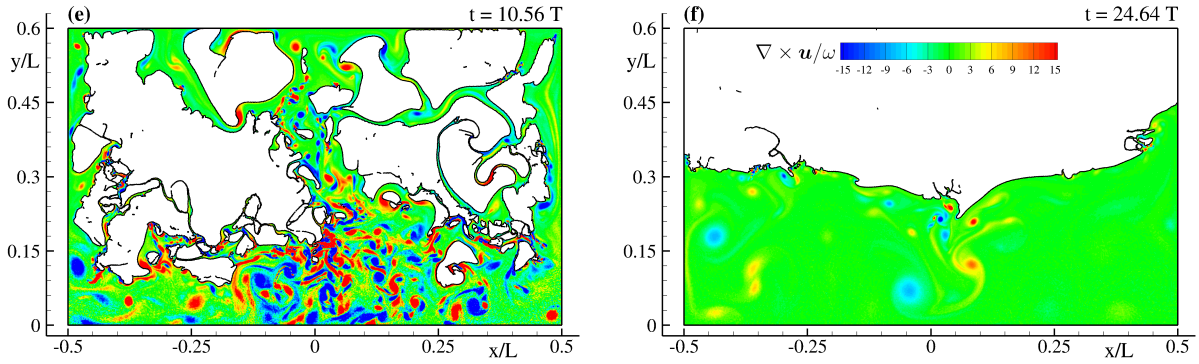


FIG. 7: SPH simulation at $N = 400$ for the Re=233,000 case: vorticity contour at $t/T = 10.56$ (left plot) and $t/T = 24.64$ (right plot).

to numerical energy dissipation, $\mathcal{E}_{\mathcal{N}}$, is decreased to 24.2% of the total dissipated energy. As already mentioned in Part I, $\mathcal{E}_{\mathcal{N}}$ is mainly related to energy diffusion in impacts, and therefore, in this problem and for the resolutions adopted it plays a non-negligible role. In order to investigate the numerical convergence for this problem, the same procedure described in section VII F of Part I has been applied: four spatial resolutions have been considered, namely $N = H/\Delta x$=50,100,200 and 400; and for each discretization 10 repetitions of the same simulation have been performed applying a noise of $0.01\Delta r$ on the initial lattice. The result of this study is summarized in the right plot of the figure 8. Each curve represents the ensemble average of the 10 repetitions of the same simulation and the error bars indicate the standard deviation.

Conversely to the periodic test case, the numerical solution exhibits a more marked convergence in terms of average curves. The convergence is on the order of about 1.5. Note that in the periodic case the Re is about twice the present case and that decay motion implies a decreasing turbulent motion in time. Regarding the standard deviation, this does not monotonically decrease with the increasing resolution. A possible reason is related to the limited time history of the simulation. In fact, in the short time range the variability becomes prominent, the flow not being driven by a long-term periodic forcing.

In order to better investigate the role of viscous effects, the same simulation has been conducted by drastically reducing the simulation Reynolds number. To this end, the considered liquid has been changed to oil, which has kinematic viscosity of $5 \cdot 10^{-5}$ m^2/s corresponding to Re=4,660 (oil density $\rho = 900$ kg/m^3, dynamic viscosity $\mu = 4.5 \cdot 10^{-2}$

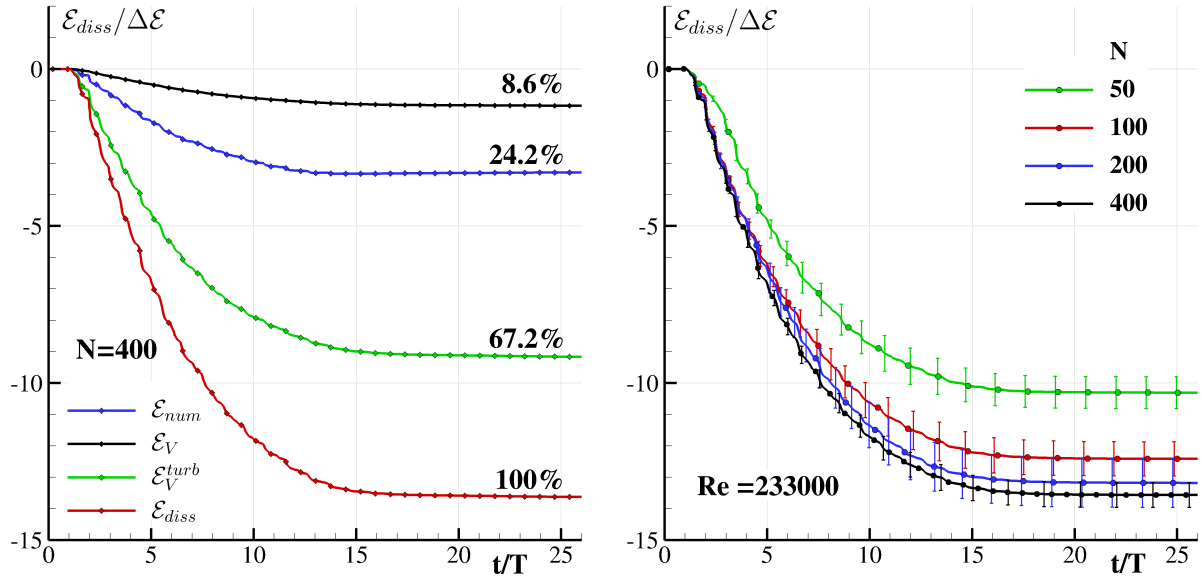


FIG. 8: Left: time history of the energy components defined in Section III: resolved viscous dissipation $\mathcal{E}_V$, modelled turbulent viscous dissipation $\mathcal{E}_V^{turb}$, numerical diffusion $\mathcal{E}_\mathcal{N}$, total energy dissipation $\mathcal{E}_{diss}$ for the case $N = 400$ and Re=233,000. Right: ensemble average of of the energy dissipation $\mathcal{E}_{diss}$ time history for resolutions $N = 50$, $N = 100$, $N = 200$ and $N = 400$; error bars refer to the computed standard deviation.

Pa· s). In this case the energy terms are made non-dimensional through the potential energy $\Delta\mathcal{E} = \rho\, LHg2A = 3.020$ J. The spatial resolution is again $N = 400$. As mentioned in Section III, for this simulation no-slip wall boundary conditions are used due to the relevance of boundary layers for this test case. Indeed, using the Blasius theory as in Part I, the thickness δ_{BL} of the wall boundary layer for this case is estimated to be $H/\delta_{BL} = \mathcal{O}(10^2)$ which can be adequately resolved with the adopted spatial discretization.

In figure 9 the flow evolution for the same time instants as in figure 5 is reported. Due to the greater viscosity, the liquid does not truly impact against the roof in the first cycle of the tank motion: only two thin jets go to the ceiling at $t = 1.18T$, but the bulk of the flow has not got enough kinetic energy to reach it when the tank acceleration inverts its motion (top-right plot of figure 9). Notwithstanding, the small jets are energetic enough to disrupt the compact shape of the fluid when they fall back down, generating large vortical structures. In the bottom plots of figure 9 the contour plots of the ratio μ_T/μ are shown for two bottom impacts corresponding to labels c) and d) of figure 5. In this case the highest

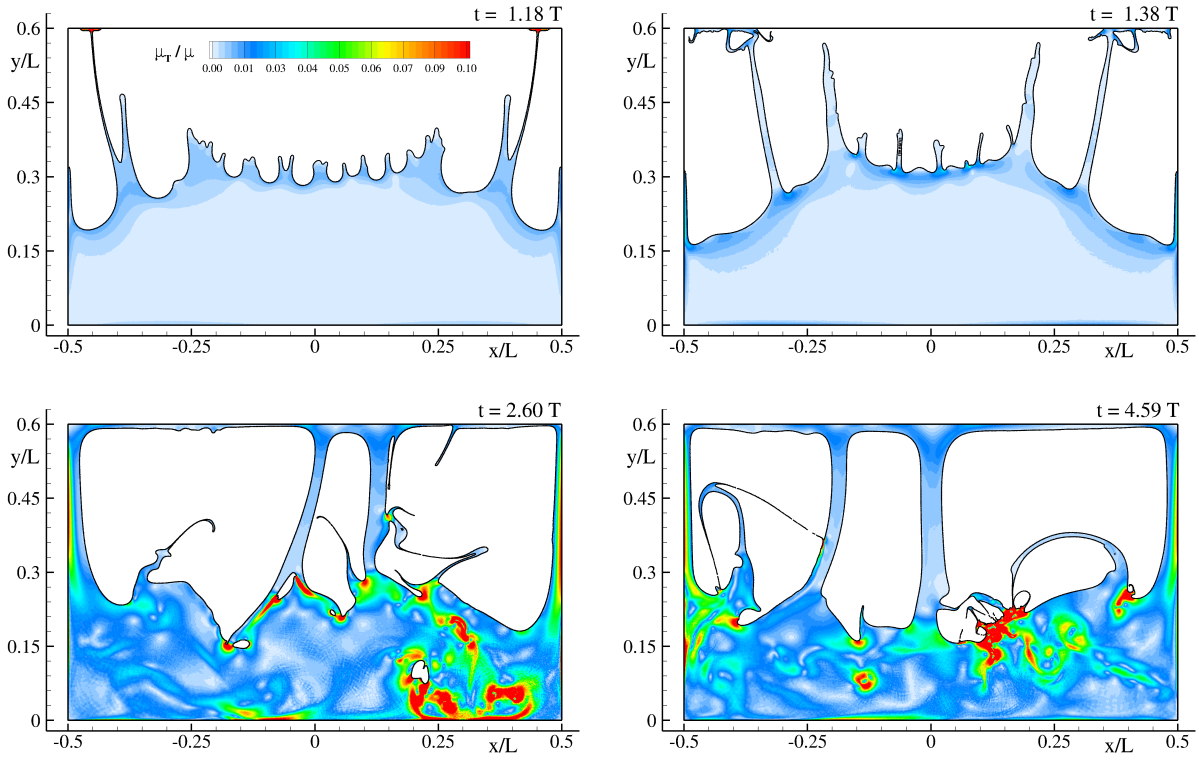


FIG. 9: Four representative instants of the flow evolution obtained by the SPH simulation at $N = 400$ for the Re=4,660 case. Contours refer to turbulent viscosity ratio μ_T/μ.

values attain $\mu_T/\mu = 0.1$, showing that the solution is now close to a DNS.

At this viscosity level, the main eddies are much larger with respect to the water case, as shown in figure 10: vortical structures are few and cover a narrow range of length scales. Also, the vorticity generated at the boundaries represents a large portion of the total vorticity. The wall boundary layer is discretized with about 10 particles for this spatial resolution, confirming the appropriateness of the above estimation. In the right plot of figure 10 the vorticity field is reported for the same instant as label f) of figure 7. Most of the flow's mechanical energy has been dissipated, and as a consequence the free surface is smooth and no vortices are generated anymore.

In the left plot of figure 11 the dissipative energy components are reported. The most prominent energy component in this case is represented by the resolved viscous term $\mathcal{P}_\mathcal{V}$, which at the end of the simulation amounts to 74% of the total dissipation. The numerical dissipation $\mathcal{E}_\mathcal{N}$ is almost halved with respect to the case with water whereas the modelled turbulent viscous energy dissipation is dramatically reduced. This reflects the fact that at

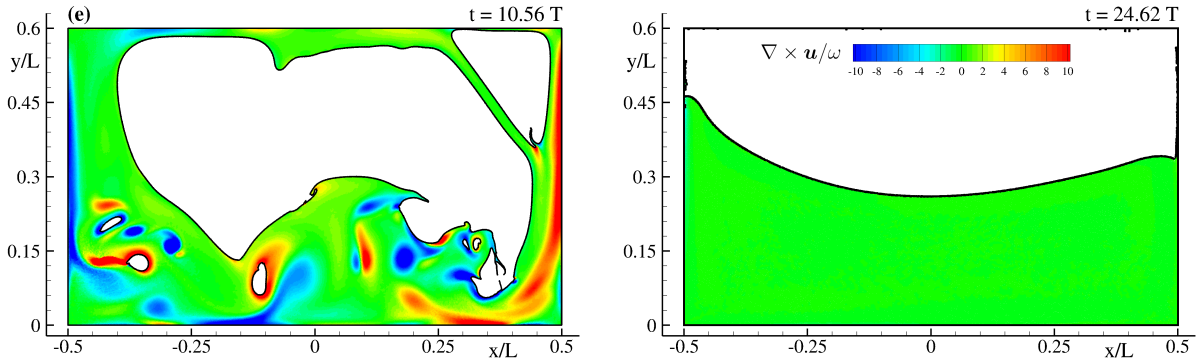


FIG. 10: SPH simulation at $N = 400$ for the Re=4,660 case: vorticity contour at the same time instants of figure 7.

this Re a large portion of the viscous dissipation is resolved and the remaining amount of residual energy is dissipated during impacts by means of the power terms $\mathcal{P}_{\mathcal{N}}$ and $\mathcal{P}_V^{turb}$.

Also for this test case the convergence study (right plot of figure 11) has been performed in terms of ensemble average of the energy time history. Differently from the water test case, only three spatial resolutions have been considered, namely $N = 50, 100$ and 200; and 10 repetitions of the simulations have been performed. In this case it is clear that the average solution does not depend significantly on the spatial resolution. This fact suggests that the adopted LES filter lies well below the inertial range for all the adopted discretizations [16], and therefore, even for the coarsest resolution the obtained solution is an acceptable representation of the large eddies developed in the flow. Further, the standard deviation is largely reduced, which is an expected behaviour for this lower regime of Reynolds number, contributing to decreasing the uncertainty of the obtained solution.

It is worth noting that in the oil test case the total amount of non-dimensional dissipated energy is lower with respect to the water one. This result is, indeed, consistent with the findings in [4] where similar results were found experimentally. In particular, it was explained that water sloshing flows dissipate energy mostly through energetic impacts and breaking wave phenomena. Therefore, in liquids characterised by higher viscosity as in the oil case, the breaking events are less intense, and therefore less dissipative. On the top of that, oil is 0.9 times less dense than water, which further enlarges the dimensional energy dissipation difference between both fluids. Clearly, for these kinds of problems, in [9] it is emphasized that density variations have substantial effects on energy dissipation with respect to viscosity,

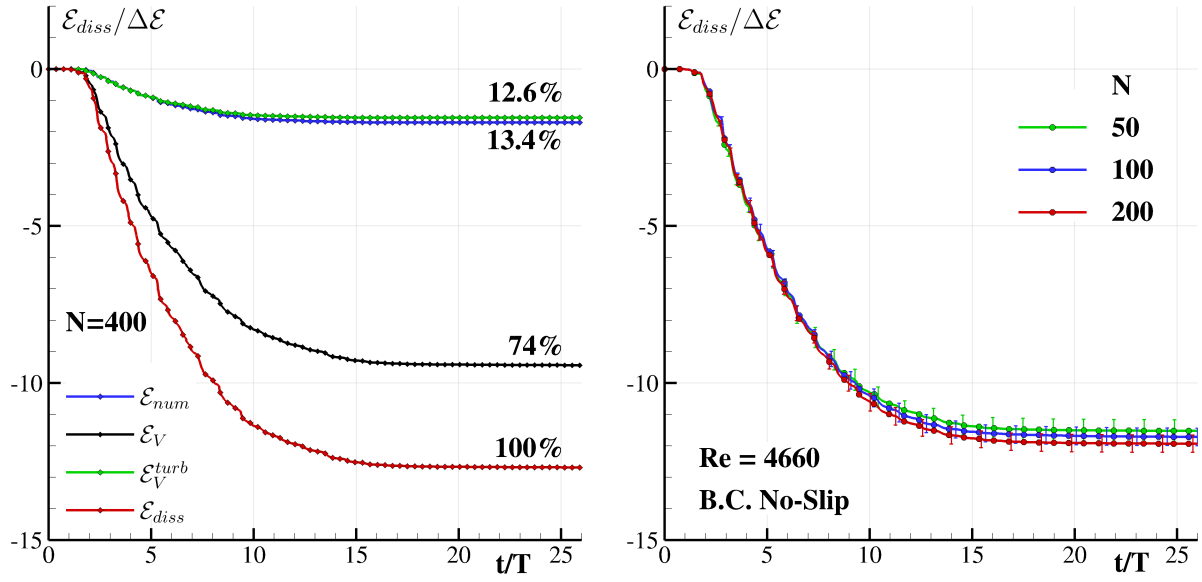


FIG. 11: Left: time history of the energy components defined in section III: resolved viscous dissipation $\mathcal{E}_V$, modelled turbulent viscous dissipation $\mathcal{E}_V^{turb}$, numerical diffusion $\mathcal{E}_\mathcal{N}$, total energy dissipation $\mathcal{E}_{diss}$ for the case $N = 400$ and Re=4,660. Right: ensemble average of of the energy dissipation $\mathcal{E}_{diss}$ time history for resolutions $N = 50$, $N = 100$, $N = 200$; error bars refer to the computed standard deviation.

especially when Re $> 10^4$.

As far as the CPU costs are concerned, ten cluster nodes equipped with dual 12-core Intel Xeon (Haswell) E5-2680v3 processors at 2.5 GHz, were used for 15 days to perform the 90 simulations. The only ten simulations with N=400, performed for the water case, required 8.4 days using the ten cluster nodes (*i.e.* 240 cores). The above CPU costs are practically the same of those requested to perform the simulations discussed in the Part I. The whole 122 simulations executed for the present research investigation (Part I and Part II) required an overall amount of one month of calculation on 10 cluster nodes.

Validation against the experimental vertical forces

The vertical forces obtained in the numerical simulations are here compared to those measured in the experiment for the water case, as a validation of the numerical outcome. In figure 12 the vertical forces obtained for resolutions $N = 50, 100$ and 200 are reported

in terms of average ensemble over the 10 repetitions performed for each spatial resolution. Remarkably, only small discrepancies are observed between the different resolutions. This is to be ascribed to the inertial forces which account for a large part of the total force. To better appreciate this, in the same figure the non-dimensional F_y^{stat} component (see Part I for a definition) is reported. At the beginning of the simulation, when the Rayleigh-Taylor instability has not developed yet, the computed forces are trivially equal to the inertial ones. After t/T=1 the flow detaches from the bottom and the hydrodynamic forces come into play. However, their role remains limited with respect to inertia, apart from the first oscillations where the violent impacts cause a sharp peak of the vertical force.

In figure 13 the computed force at $N = 400$ is compared to the experimental observation. Note that experimental data are filtered through a $4th$ order Butterworth filter with a cutoff frequency of $f_{cut} = 7.7 f_0 = 50$ Hz (see [15]) In the top plot of figure 13 the numerical vertical force F_y is compared to the experimental measurement. The numerical outcome is, generally, in good agreement with the experiment, especially if one considers the different approximations inherent in the adopted numerical model. In the initial stage of the simulation, around $t/T = 1$, a large discrepancy is observed. At this stage, in the numerical simulation the flow has not impacted yet against the roof (see figure label (a) of 6). Therefore, this could be due to a non-perfect action of the release mechanism in the experiment, or to differences in the initial flow deformation.

In bottom plot of figure 13 only the hydrodynamic component of the vertical force is compared, namely F_y^{dyn} (see Part I equation 21 for a definition). This comparison is more challenging than the previous one, as a large part of the total force is represented by F_y^{stat}. In this sense, it is also more appropriate to compare only the F_y^{dyn} component since the F_y^{stat} component in fact is not a part of the solution, but rather an input of the problem. The agreement between the experiment and the numerical solution is less clean in this case, due to the complex flow evolution in the tank which results in a large number of local minor force peaks. Furthermore, as highlighted in [15] before the first liquid impact the measure of the hydrodynamic component of the vertical force, F_y^{dyn}, is affected by an incorrect overestimation related to the accelerometer measurements and caused by the release mechanism. For this reason this part of the experimental hydrodynamic force is not taken into account when evaluating the external work $\mathcal{W}_{ext}^{dyn}$.

In top plot of figure 14 the numerical force F_y^{dyn} is plotted together with the tank velocity.

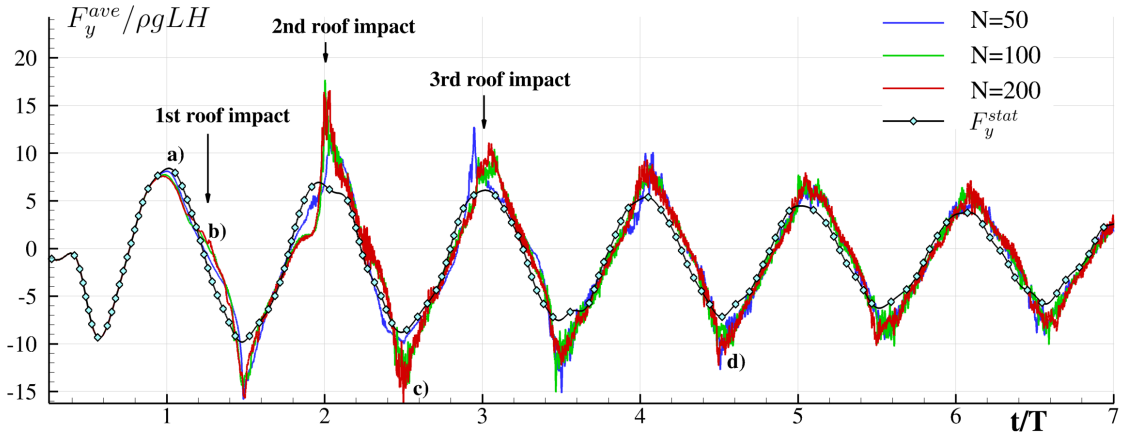


FIG. 12: Ensemble average of the total vertical force for resolutions $N = 50$, $N = 100$, $N = 200$ for Re=233,000. The F_y^{stat} force component is also reported.

In the same plot the first three roof impacts are indicated. The force peak occurring at the first roof impact has the opposite sign to that of the tank velocity. Therefore, a large amount of work done by the solid walls on the fluid is expected during this stage. Conversely, for the second and third peaks a phase shift has occurred and both the force and the velocity have the same sign. The same happens for the subsequent force peaks as well. The corresponding power, $\mathcal{P}_{ext}^{dyn}$, computed as (see Part I):

$$\mathcal{P}_{ext}^{dyn} = v_{tank}\, \boldsymbol{j} \cdot \boldsymbol{F}_y^{dyn} \tag{3}$$

is plotted in bottom plot of figure 14. It turns out that, apart from the first roof impacts where a large negative peak is observed (the tank is doing work on the fluid), the roof impacts correspond to positive peaks of $\mathcal{P}_{ext}^{dyn}$ which, conversely, means that the fluid is doing work on the tank. This may appear in contradiction with what shown in Part I: the most intense stages of the flow where energy is dissipated are roof and floor impacts. In fact, to get the full picture of the energy balance, the complete equation has to be considered:

$$-\mathcal{P}_{ext}^{dyn} + \dot{\mathcal{E}}_M^{dyn} + \dot{\mathcal{E}}_C = \mathcal{P}_{diss} \leq 0\,. \tag{4}$$

In figure 15 the terms $-\mathcal{P}_{ext}^{dyn}$,$-\dot{\mathcal{E}}_M^{dyn}$ and $\mathcal{P}_V$ are plotted (the term $\dot{\mathcal{E}}_C$ being negligible, and thus not relevant to the present discussion). It can be seen that the power related to the energy dissipation $\mathcal{P}_V$ is always negative, as expected. To this end, the term $-\dot{\mathcal{E}}_M^{dyn}$ related to the time derivative of the mechanical energy plays an important role. Indeed, especially

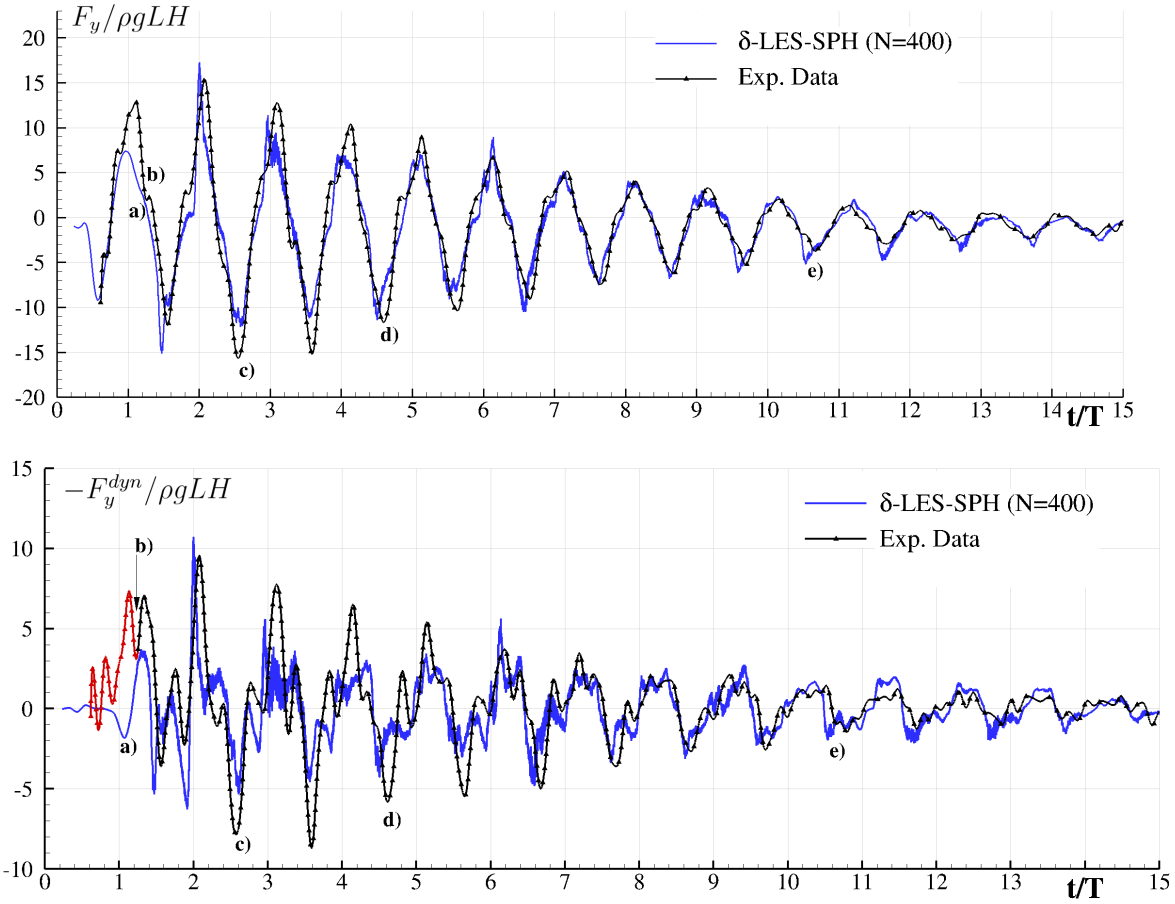


FIG. 13: Force comparison between the experimental data and the SPH simulation at N=400 and Re=233,000: total force (top) and F_y^{dyn} component (bottom). On the bottom plot the initial part of the experimental F_y^{dyn} is colored in red where incorrect overestimation of the force is linked to the release mechanism.

during impacts, this term overshoots the $-\mathcal{P}_{ext}^{dyn}$ term thus always resulting in negative values of the viscous dissipation $\mathcal{P}_{diss}$. Therefore, even if in some impact events a relevant amount of work is done by fluid on the tank, large variations of $\mathcal{E}_M^{dyn}$ guarantee that the energy of the system is always dissipated in those stages as well.

In figure 16 the time histories of the system energy components $\mathcal{E}_M^{dyn}$, -$\mathcal{W}_{ext}^{dyn}$ and $\mathcal{E}_{diss}$ are reported for N=400. These quantities have been obtained by integrating in time the power time histories of figure 15. Remarkably, the mechanical energy $\mathcal{E}_M^{dyn}$ remains limited in time, even though its time derivative can be locally quite high as seen in figure 15. Consequently, the terms -$\mathcal{W}_{ext}^{dyn}$ and $\mathcal{E}_{diss}$ are quite close each other until the end of the simulation when $\mathcal{E}_M^{dyn}$

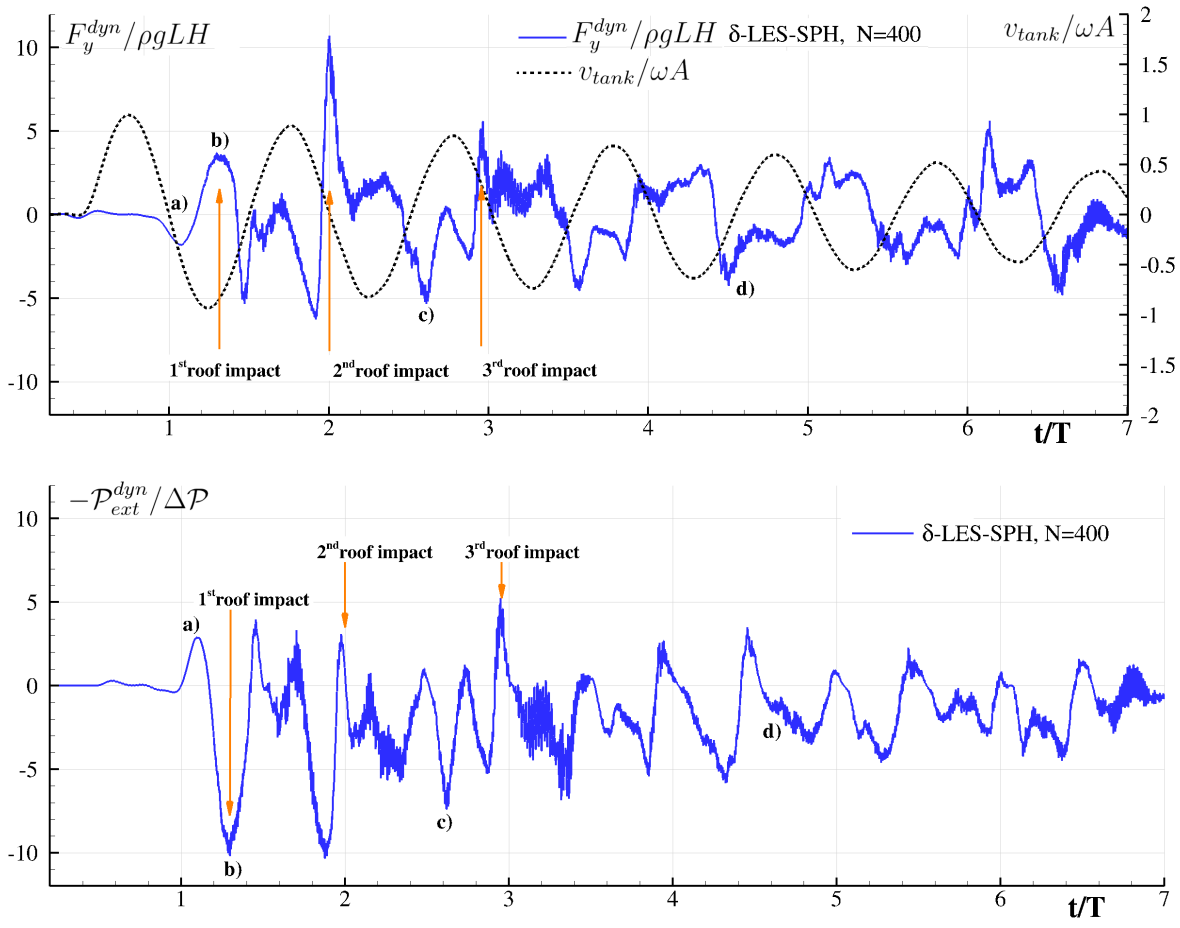


FIG. 14: SPH simulation at N=400 and Re=233,000. Top plot: total force against the tank velocity; bottom plot: time history of the power $-\mathcal{P}_{ext}^{dyn}$ (see definition in the text).

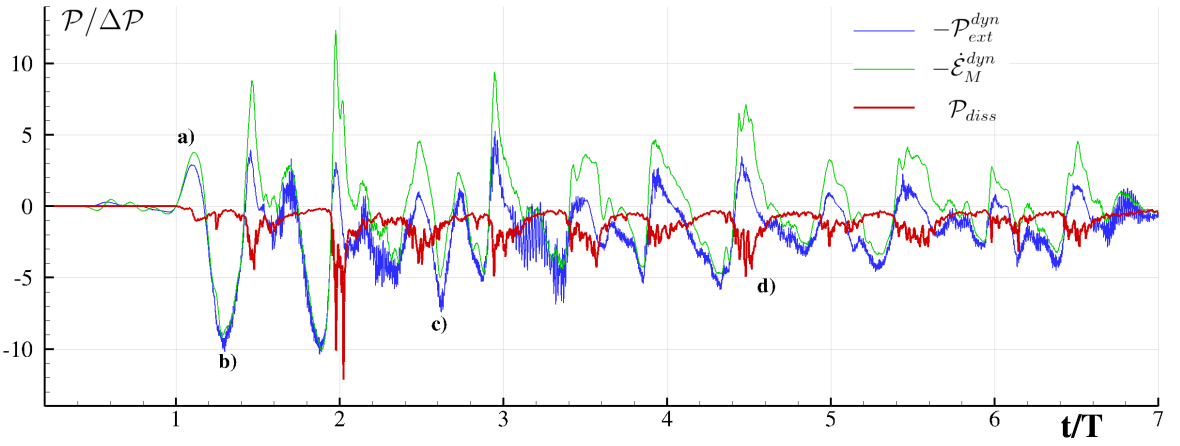


FIG. 15: SPH simulation at N=400 and Re=233,000. Time history of the powers $-\mathcal{P}_{ext}^{dyn}$, $-\dot{\mathcal{E}}_M^{dyn}$ and $\mathcal{P}_V$ (see definitions in the text)

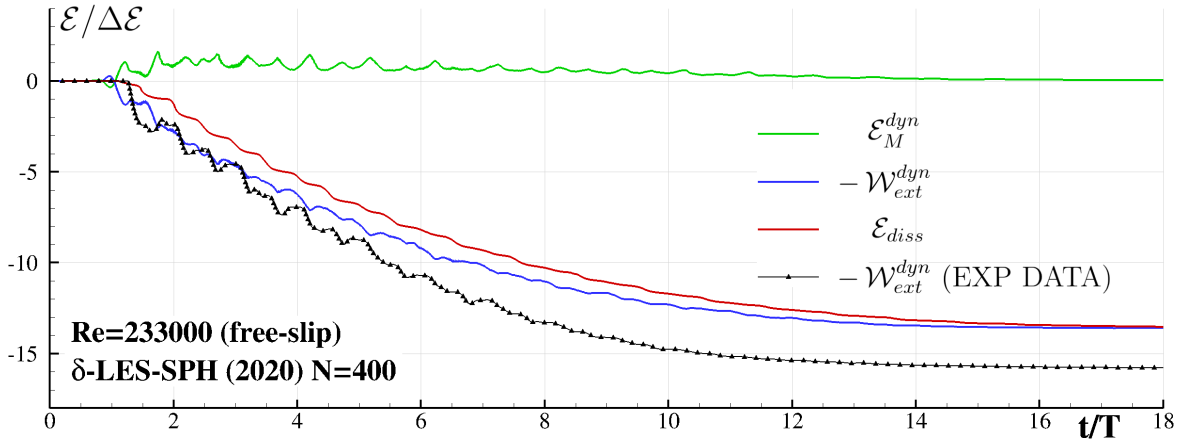


FIG. 16: SPH simulation at N=400 and Re=233,000. Time history of the mechanical energy $\mathcal{E}_M^{dyn}$, the dissipated energy $\mathcal{E}_{diss}$, the external work $\mathcal{W}_{ext}^{dyn}$. The solid line with Δ symbols represents $\mathcal{W}_{ext}^{dyn}$ as computed through the experimental data.

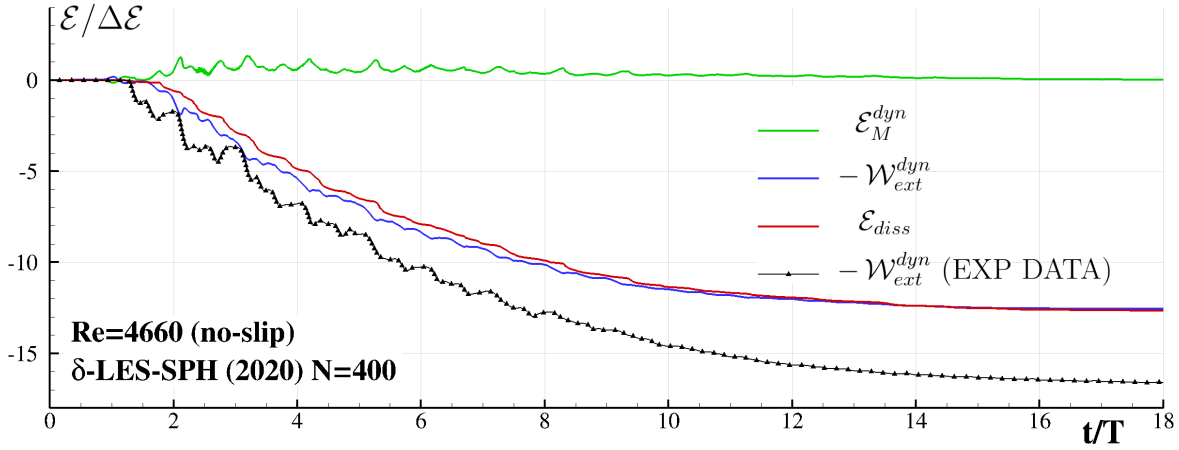


FIG. 17: SPH simulation at N=400 and Re=4,660. Time history of the mechanical energy $\mathcal{E}_M^{dyn}$, the dissipated energy $\mathcal{E}_{diss}$, the external work $\mathcal{W}_{ext}^{dyn}$. The solid line with Δ symbols represents $\mathcal{W}_{ext}^{dyn}$ as computed through the experimental data.

becomes null and they coincide. This allows comparison of the dissipated energy evaluated in the numerical simulation with the experimental measurement. Indeed, even if in the experiment it is not possible to measure the quantity $\mathcal{E}_M^{dyn}$, it is possible to estimate $\mathcal{W}_{ext}^{dyn}$ and compare its final value to the numerical counterpart. In figure 16 the experimental $\mathcal{W}_{ext}^{dyn}$ has been depicted. Apart from an initial discrepancy between $t/T = 1$ and $t/T = 2$, due to the observed differences in the force acting at the initial stage of the experiment, the

numerical and experimental curves slightly diverge. The final difference is about 14% of the total dissipated energy.

In figure 17 the same comparison of figure 16 is replicated for the oil simulation at Re=4,660. In this case the experimental and numerical curves related to $\mathcal{W}_{ext}^{dyn}$ are very close each other, up to about $t/T = 5$. Then they start to diverge, and at the end of the simulation the relative error is about 24%. For this case the 3D effects are likely to be more important than for the water test case: wall boundary layers develop also on the front and the rear walls which are not modelled in the present 2D simulation. This aspect will be further investigated in future work where 3D simulations will be performed.

Throughout this session the tank motion has been imposed, and it is important to underline that the experimental measure of $\mathcal{W}_{ext}^{dyn}$ presents various difficulties since even smaller errors on the force and the tank velocity measurements may induce large errors in the evaluation of the external work. To avoid the above drawbacks for the validation of the SPH outputs against the experimental data, in the next section the full FSI problem is studied. Therefore, the tank motion becomes an unknown variable of the problem. Thus, the behaviour of the repeatability of simulations is analysed to assess possible differences with respect to the cases with imposed motion.

B. Test N.2: Sloshing in coupled motion: comparison with the experimental results

Finally, in this section a set of simulations are carried out this time considering the influence of the liquid on the overall motion of the structure, hence analyzing the coupled system for which the tank motion becomes an unknown. Results will again be compared with experiments to report influence of the coupling on the previous results. The considered system is a 1-DoF system, in the same fashion as is done in the experiments, having the form:

$$F_{\text{slosh}} - B_{0d} \cdot \text{sign}\left(\frac{dy}{dt}\right) - B_{1d} \cdot \frac{dy}{dt} - K \cdot y = m_s \frac{d^2y}{dt^2} \tag{5}$$

where forces coming from different sources that act on the tank are: F_{slosh} is the contribution from the internal fluid action, $K \cdot y$ corresponds to the restoring force that comes from

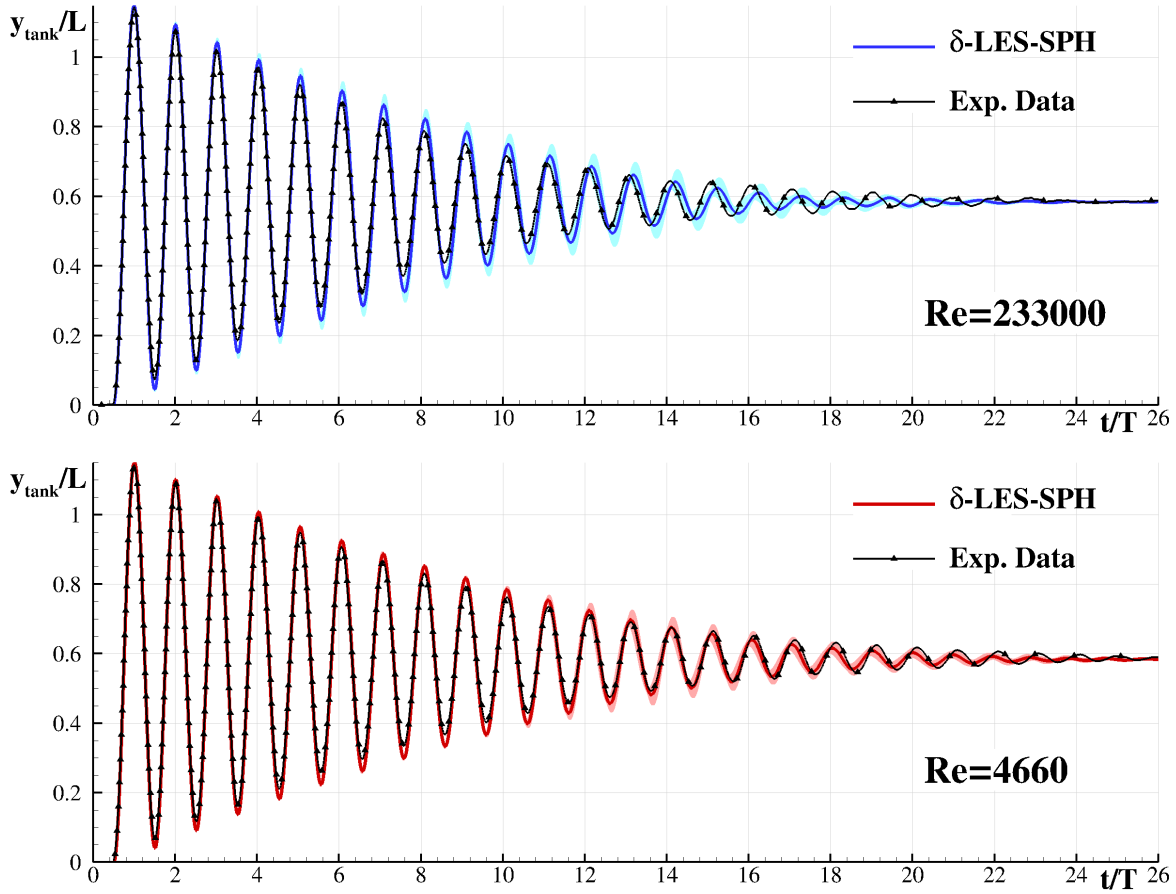


FIG. 18: Evolution of the vertical position of the tank over time obtained from the FSI-SPH simulation at N=200. Top figure corresponds to Re=233,000 for water and bottom figure to Re=4,660 for oil. The experimental signal obtained from the accelerometer is plotted for comparison. Variability of the numerical outcome, represented in terms of standard deviation, is plotted in lighter color(light blue on the top plot and pink on the bottom one).

the springs in this particular configuration (see figure 1) and $B_{0d} \cdot \text{sign}\left(\frac{dy}{dt}\right) - B_{1d} \cdot \frac{dy}{dt}$ is composed by two terms modelling a Coulomb friction and a viscous friction term respectively. Both B_{0d} and B_{1d} are coefficients that can be determined experimentally with a dry test, and do not vary independently with the fluid that is being tested. Hence, determining these coefficients allows numerical testing of a wide range of fluids and configurations. For this particular set-up, values for each of these coefficients are $m_s = 2.403$ kg, $K = 4321.62$ N/m, $B_{0d} = 0.38$ N and $B_{1d} = 1.73$ kg/s.

Figure 18 presents the evolution of the tank vertical position for both cases tested in this work. The top figure shows the water test (Re = 233,000) whilst bottom figure illustrates the oil test (Re = 4,660). In both figures, the tank position obtained from the coupled simulations, in which the forces are computed by SPH, is compared to the ones measured in the experiments. As it can be seen, the agreement between experimental and numerical curves is very good. The numerical curves depicted (blue on the top and red on the bottom) correspond to the ensemble average computed from a set of 10 repetitions in the same fashion as is done in section IV A of the present paper, and in Part I, where variations on the order of 1% are applied to the initial particle positions. Accordingly, variability between the simulations is represented in terms of standard deviation, which is shown in this figure in a lighter color (light blue on the top plot and pink on the bottom one). It is worth noting that the standard deviation increases towards the end of the simulation; this is a consequence of a slight phase shift occurring between the different realizations rather than an actual variation of the motion amplitude. However, from the results in figure 18 it can be observed that the repeatability is high in terms of tank motion when the full coupled system is taken into account. Moreover, results obtained are consistent with previous ones, confirming that variability reduces for the oil case in comparison to the higher Re water case.

The resolution adopted for both test case series is $N = 200$. As discussed in the previous section, this is considered sufficient to obtain results close to convergence. The good agreement shown here between the experimental data and the numerical outcome confirms this estimation. Moreover, two other aspects already discussed in the previous section are confirmed here: i) the 2D SPH simulation predicts a lower dissipation with respect to the experimental case; ii) in the water test case the energy is dissipated more rapidly with respect to the oil case, confirming that in latter case the energy dissipation mechanism is less effective.

V. CONCLUSIONS

The SPH formulation developed in the first part of this paper series for this particular study of violent confined flows has been extended in this second part to forced decay heave motions, confirming that the formulation presented provides a good estimation of the energy

dissipation and of the impact forces for the two different fluids that have been tested in this work. An important difference that can be appreciated with these kinds of time decay laws of motion is that the shaken and sloshing regimes are clearly identified in terms of free surface fragmentation and vorticity fields.

Despite the simplified physical model of the problem that is utilized, including a 2D computational domain, single-phase fluid, lack of surface tension forces or the weakly-compressible fluid assumption, the formulation is able to obtain accurate results, not only with prescribed movement coming from the records registered from the experiments, but also if the tank is coupled to a mass-spring-damper model.

Two different regimes corresponding to two different fluids (water and oil) have been tested. For the water case, Re $\approx O(10^5)$, the maximum numerical resolution adoptes, $N = 400$, exhibits turbulent/ fluid viscosity ratios μ_{turb}/μ of order $\mathcal{O}(1)$ indicating that the inertial turbulent scale is sufficiently resolved while the viscous scale is approximated by the sub-scale model. Conversely, for the oil case, Re $\approx O(10^3)$, the ratio decreases to $\mu_{turb}/\mu = 0.1$, which is close to a DNS description. This is also confirmed because the dependency on the spatial resolution is less significant.

The energy dissipation corresponding to both fluids behaves as expected, and for the largest Reynolds number more than 67% of the total dissipation corresponds to modeled turbulent dissipation and less than 9% is resolved viscous dissipation, while in the oil case these trends invert and 74% corresponds to resolved viscous dissipation and less than 13% to modeled turbulent dissipation. Also, the total dissipated energy measured is larger in the water case than in the oil case, due mainly to the greater amount of energy dissipated during impacts and wave breaking effects that are present in the water test. This result confirms predictions that have been already presented in previous experimental campaigns.

When numerical predictions are compared to experiments, good agreement is obtained in terms of global forces. However, discrepancies are found if the hydrodynamic component of this force, represented by F_{dyn}, is extracted and compared to the experimental version. Complex flow evolution within the tank results in a large number of minor peaks that make the comparison less clean than for the global component.

Also, an interesting conclusion can be drafted from the role of the derivative of the mechanical energy, which keeps a balance with the amount of work done by the fluid on the tank, in order to guarantee the negative sign of the energy dissipation during the complete

simulation.

The time histories of the work done by the system are compared to the experimental estimations, showing a larger discrepancy for the oil case than for the water case, probably due to 3D viscous effects on the walls that are not modelled in this set of 2D cases.

Finally, a fully coupled FSI-SPH simulation is carried out for the same cases. In this case, the tank motion is in principle unknown and has to be computed from the information coming from a mass-spring-damper system and the forces computed by SPH. Results confirm the trends observed for the imposed motion analysis, showing however that the predicted tank motions are less affected by repeatability issues with respect to the forced motion cases and that tank motions time histories are quite close to the ones obtained experimentally. As a final remark, the adopted spatial resolution, which in Part I was shown not to be fine enough to fully resolve all the viscous scales, is indeed sufficient to allow an accurate prediction of the tank motion decay.

ACKNOWLEDGEMENTS

The work was supported by the SLOWD project which received funding from the European Union's Horizon 2020 research and innovation programme under grant agreement No 815044. All the authors would like to thank Mr. Ciaran Stone for his valuable assistance during the preparation of this manuscript.

Appendix A: Role of the boundary layer regions on the energy dissipation process

In this section the relevance of the wall boundary layer (WBL) modelling is investigated. As described in section VII of the first part of the paper (Part I), for the considered sloshing case involving water the adopted particle discretization is not fine enough to resolve the WBL. Indeed, for this case the WBL thickness ends up at least one order of magnitude smaller than the finest particle size adopted. In order to further analyse the relevance of WBL, we performed a comparison of the simulation with no-slip and free-slip boundary conditions, being aware of the fact that, in the former case the boundary layers will be overestimated by at least a factor of 10 (in fact it is even larger due to the smoothing action of the SPH kernel). Notwithstanding, the study will give significant indications about the

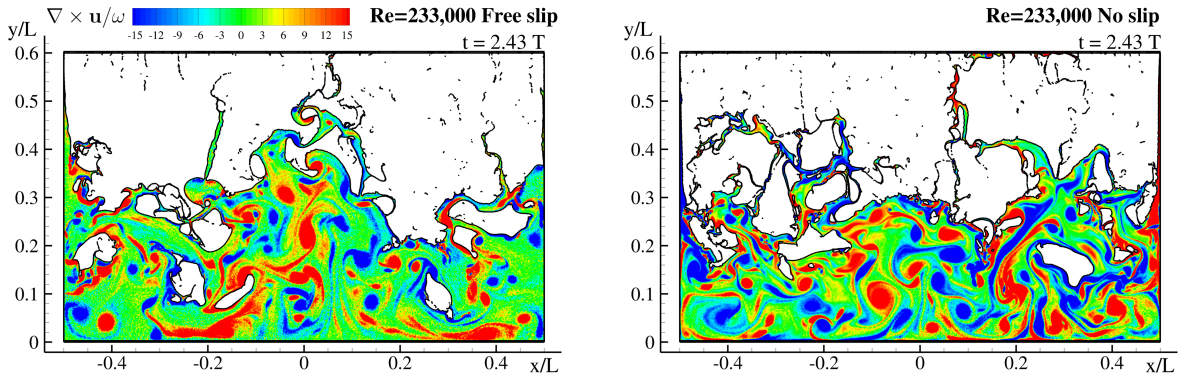


FIG. 19: Vorticity fields of the simulations with free-slip (left plot) and no-slip (right plot) conditions at time $t/T = 2.43$, N=200.

WBL relevance in a conservative sense: if the simulations turn out to be little affected by the presence of an overestimated WBL, one can reasonably expect that the same holds for a WBL ten-times smaller.

In figure 19 the vorticity fields of the simulations with free-slip (left plot) and no-slip (right plot) conditions are reported for time instant $t/T = 2.43$. Regardless, both the vorticity levels and the flow configurations are similar: in the no-slip case the number of vortex structures is larger and the vorticity content is higher. This is mainly due to the vortex sheets generated at the boundaries which detach and roll up, interacting with the pre-existing vortices and eventually moving in the bulk of the flow. Conversely, in the free-slip case the eddies collide against the walls elongating and stretching, but without further production of vortex structures. In the left plot of figure 20 the effect on the energy dissipation of the different boundary conditions is reported. For both free-slip and no-slip cases 10 simulations have been run for the spatial resolution $N = 200$. In the plot the ensemble averages are shown along with the corresponding standard deviation. The two curves are very close: up to about $t/T = 5$, then they slightly diverge, the difference on the final value being about 4% of the total dissipation. This discrepancy is within the standard error obtained for both cases, and is therefore acceptable for the inherent approximations of the simulation. This reasoning applies *a fortiori* if one considers the fact that the boundary layers in the simulation are overestimated by a factor of 10. We note that for this Re number the no-slip case is more dissipative than the free-slip and this fact is likely due to the higher vorticity produced in the field. Furthermore, the no-slip simulation is characterized by a

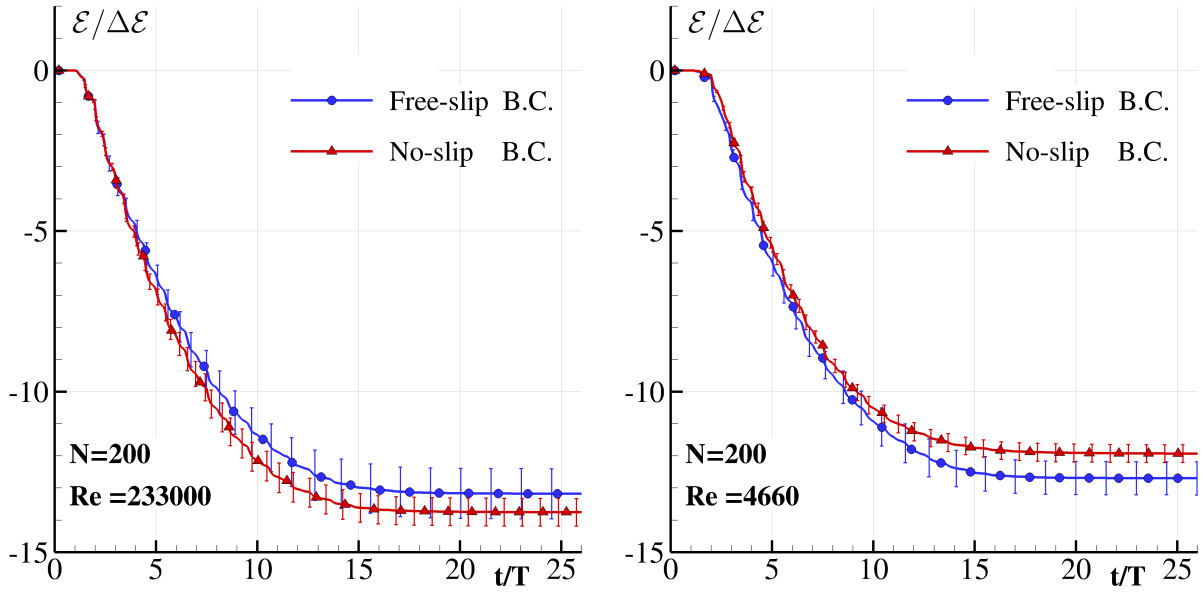


FIG. 20: Time history of the ensemble average of the energy dissipation $\mathcal{E}_{diss}$ for resolutions $N = 200$ using free-slip and no-slip conditions on the solid boundaries. Error bars refer to the computed standard deviation. Left: Re=233,000 for water case. Right: Re=4,660 for oil case.

smaller standard deviation which can be attributed to a stabilising effect of the boundary layers, especially in the initial stages of the flow.

In the right plot of figure 20 the same study has been conducted for the oil case at Re=4,660. In this case the discrepancy is slightly larger (about 6% of the total dissipation), but interestingly, both curves are inverted with respect to the water case, *i.e.*, the free-slip case results the more dissipative condition. This effect is related to the fact that, at this Re, the large boundary layers tend to slow down the flow remarkably, resulting in less energetic impacts, and thus in lower dissipation. This mechanism follows the general behaviour, already observed in [6], for which a higher viscosity leads to lower levels of dissipated energy. We note that also in this case, a smaller standard deviation is observed for the no-slip case with respect to the free-slip one.

---

[1] H Norman Abramson, W Chu, and Luis R Garza. Liquid sloshing in spherical tanks. *AIAA Journal*, 1(2):384–389, 1963.

[2] M Antuono, S Marrone, A Di Mascio, and A Colagrossi. Smoothed particle hydrodynamics method from a large eddy simulation perspective. generalization to a quasi-lagrangian model. *Physics of Fluids*, 33(1):015102, 2021.

[3] R. L. Bass et al. Modeling criteria for scaled lng sloshing experiments. *Transactions of the ASME Journal of Fluids Engineering*, 107, June 1985.

[4] B. Bouscasse, A. Colagrossi, A. Souto-Iglesias, and J. L. Cercos-Pita. Mechanical energy dissipation induced by sloshing and wave breaking in a fully coupled angular motion system. II. Experimental investigation. *Physics of Fluids (1994-present)*, 26(3):–, 2014.

[5] Benjamin Bouscasse, Andrea Colagrossi, Antonio Souto-Iglesias, and JL Cercos-Pita. Mechanical energy dissipation induced by sloshing and wave breaking in a fully coupled angular motion system. i. theoretical formulation and numerical investigation. *Physics of Fluids*, 26(3):033103, 2014.

[6] Benjamin Bouscasse, Andrea Colagrossi, Antonio Souto-Iglesias, and JL Cercos-Pita. Mechanical energy dissipation induced by sloshing and wave breaking in a fully coupled angular motion system. ii. experimental investigation. *Physics of Fluids*, 26(3):033104, 2014.

[7] H Bredmose, M Brocchini, DH Peregrine, and Laurent Thais. Experimental investigation and numerical modelling of steep forced water waves. *Journal of Fluid Mechanics*, 490:217, 2003.

[8] Bernard Budiansky. Sloshing of liquids in circular canals and spherical tanks. *Journal of the Aerospace Sciences*, 27(3):161–173, 1960.

[9] J. Calderon-Sanchez, J. Martinez-Carrascal, L. González, and Colagrossi A. A global analysis of a coupled violent vertical sloshing problem using an 3 sph methodology. *Engineering Applications of Computational Fluid Mechanics*, 2021.

[10] Wen-Hwa Chu. Fuel sloshing in a spherical tank filled to an arbitrary depth. *AIAA Journal*, 2(11):1972–1979, 1964.

[11] L. Constantin, J. de Courcy, B. Titurus, T.C.S. Rendall, and J.E. Cooper. Analysis of damping from vertical sloshing in a SDOF system. *Mechanical Systems and Signal Processing*, 152:107452, 2021.

[12] J.B. Frandsen. Numerical predictions of tuned liquid tank structural systems. *Journal of Fluids and Structures*, 20(3):309–329, 2005.

[13] F Gambioli, A Chamos, S Jones, P Guthrie, J Webb, J Levenhagen, P Behruzi, F Mastroddi, A Malan, S Longshaw, et al. Sloshing wing dynamics–project overview. *Proceedings of 8th*

Transport Research Arena TRA 2020, April 27-30, 2020, Helsinki, Finland, 2020.

[14] Francesco Gambioli and A Malan. Fuel loads in large civil airplanes. In *International Forum on Aeroelasticity and Structural Dynamics IFASD 2017*, 2017.

[15] J. Martinez-Carrascal and L. M. Gonzalez-Gutierrez. Experimental study of the liquid damping effects on a sdof vertical sloshing tank. *Journal of fluids and structures*, 100, 2021.

[16] Stephen B Pope. Ten questions concerning the large-eddy simulation of turbulent flows. *New journal of Physics*, 6(1):35, 2004.

[17] M.J. Tait. Modelling and preliminary design of a structure-TLD system. *Engineering Structures*, 30(10):2644–2655, 2008.

[18] Branislav Titurus, Jonathan E Cooper, Francesco Saltari, Franco Mastroddi, and Francesco Gambioli. Analysis of a sloshing beam experiment. In *International Forum on Aeroelasticity and Structural Dynamics. Savannah, Georgia, USA, paper*, volume 139, 2019.

[19] Jin-Kyu Yu, Toshihiro Wakahara, and Dorothy A Reed. A non-linear numerical model of the tuned liquid damper. *Earthquake Engineering and structural dynamics*, 28(6):671–686, 1999.

Publication 5 (P5)

Jon Martinez-Carrascal, L M. González-Gutiérrez and Javier Calderon-Sanchez (2022). Experimental and numerical characterization of violent sloshing flows. A single degree of freedom approach to the problem. SN Applied Sciences, 12 (15), 7897, 2022. DOI: https://doi.org/10.3390/app12157897. 0 citations. JCR(2021): not available, Multidisciplinary Sciences (Q2).

MDPI

Article

Experimental and numerical characterization of violent sloshing flows using a single degree of freedom approach.

Jon Martinez-Carrascal [1,‡] https://orcid.org/0000-0003-1110-6700, L M. González-Gutiérrez[1,‡] https://orcid.org/0000-0002-1629-0001 and Javier Calderon-Sanchez [1,‡] https://orcid.org/0000-0003-0636-8853

[1] Canal de Ensayos Hidrodinámicos de la ETSI Navales (CEHINAV). Universidad Politécnica de Madrid (UPM), Madrid, Spain
* Correspondence: leo.gonzalez@upm.es
‡ These authors contributed equally to this work.

Abstract: In this work, the most fundamental aspects of an aeronautical sloshing problem have been studied using an alternative and simplified model. This model consists of a single degree of freedom version of the original problem which keeps the essence of the fluid structure interaction and also the most relevant physical aspects of the industrial case. Two independent methodologies have been used: first an experimental rig has been designed to measure and visualize different magnitudes of the problem and also a smoothed particle hydrodynamics formulation has been adapted to obtain a local representation of the flow interaction. Two very different fluids in terms of viscosity have been tested, and the differences in terms of the characteristics of the sloshing regimes, free surface fragmentation and relative kinetic energy have been described and compared. Apart from the comparison of the results obtained by both methodologies in terms of tank acceleration, sloshing forces and free surface evolution, a deep study of the sloshing force has been performed. This study focuses on a deeper understanding of the different aspects that constitute the sloshing force, such as: its synchronization with the tank movement, the relation to the movement of the liquid's center of mass and the physical projection of the force on the pressure and viscous parts. Additionally a reconstruction of the sloshing force as a sum of the pressure signal recorded by a finite number of pressure sensors has been also performed.

Keywords: vertical sloshing; smoothed particle hydrodynamics; sloshing forces; violent flows; pressure fields; pressure sensors; center of mass, fluid impacts

Citation: Martinez-Carrascal, J.; González-Gutiérrez, L.M.; Calderon-Sanchez, J. Title. *Appl. Sci.* **2022**, *1*, 0. https://doi.org/

Received:
Accepted:
Published:

Publisher's Note: MDPI stays neutral with regard to jurisdictional claims in published maps and institutional affiliations.

Copyright: © 2022 by the authors. Submitted to *Appl. Sci.* for possible open access publication under the terms and conditions of the Creative Commons Attribution (CC BY) license (https://creativecommons.org/licenses/by/4.0/).

1. Introduction

Atmospheric turbulence or gusts produce significant deformations when they encounter highly flexible structures such as aircraft wings. These deformations can reach 20% of the wing span in some severe cases. The fuel tanks, which are placed inside the wings, carry a weight of fuel comparable to the oscillating structural components. The current engineering practices for wing design do not include the dynamical effects that the fuel produces within the tanks which could affect the aircraft design loads. The major experimental tests to identify and verify the dynamic characteristics of the aircraft structure (Ground Vibration and Flight Flutter tests) are limited to small amplitudes and barely excite significant sloshing modes.

In this context, the EU-SLOWD research project [1,2] aims to study how much fuel sloshing affects the structural damping of the wing oscillations. One of the main ideas of the SLOWD project is to present a comparable set of experimental and numerical campaigns based on scaled and simplified experiments, that could predict some quantitative results up to a full-scale wing experiment where the amplitudes are large enough to produce relevant sloshing effects. During this project a large amount of experimental and numerical studies have been produced.

Despite violent sloshing is a highly nonlinear phenomenon some early theoretical approaches to the problem are found in this field, see for example the classical references [3–5]. In terms of experimental results, the first studies based on a partially filled tank attached to an oscillating cantilever beam which demonstrated that the extra damping that appears is due to the sloshing motion, see[6,7]. This extra damping was measured in terms of decrements on the tip beam acceleration. In this experiment a baffled water tank is mounted on a 2.35 m cantilever which is broadly representative of a wing and its fuel tanks. The cantilever is forced into a deflected shape and suddenly released, such that the free beam decaying oscillations are recorded by several accelerometers while the forces between the beam and the tank are measured by load cells. Based on these promising results, and taking into account that the damping of the tank acceleration and the vertical sloshing force that interacts between the liquid and the tank are the two most relevant outcomes from the experiment, a similar Froude multi-scale campaign was carried out at the Model Basin Research Group Sloshing Laboratory of the UPM in Madrid, Spain, see [8]. In this work, an experimental methodology is developed to quantify the kinematics and the sloshing forces on a vertical Single Degree Of Freedom (SDOF) tank excited with real wing accelerations. These experiments confirmed again that the fluid sloshing increases the global damping of the system notably, finding that the slosh-induced damping force includes an inertial term and a dissipative term. An important conclusion obtained was that the time shift between the force impacts and the tank maximum displacement is a very relevant magnitude in fluid-induced energy dissipation. Another experimental campaign based on a release test of a vertically vibrating structure, again confirmed the additional damping created by the sloshing motion, see [9]. These experiments show that the damping depends on the amount of fluid in the tank and the initial maximum acceleration. In this experiment, where the tank is not guided vertically and the structural damping is reduced, three distinct response regimes corresponding to different motions of the fluid are observable during the transient decay, the starting one being the most important in the overall energy dissipation. Other experimental campaigns where the tank is moved periodically with different amplitudes and frequencies and the sloshing force and the tank kinematics are measured are performed in [10–12].

The other methodology used to study violent sloshing flows is the computational one, where different numerical techniques can be applied. Recent relevant studies based on different mesh-based techniques, such as the finite volumes proposed in [13], or the particle finite element method (p-FEM) [14] are examples of the different strategies used to tackle different sloshing problems. However, in this work, the Lagrangian meshless method Smoothed Particle Hydrodynamics (SPH) has been used instead to discretize the liquid phase of the problem, assuming that the gas phase plays a negligible role. The SPH method has been widely extended to different applications in the past decades, such as free surface flows [15]. The SPH technique already has an important background solving complex computational engineering problems [16,17], which includes fluid-structure interaction problems [18] and violent sloshing problems in the presence of complex geometries [19]. Recently, a thorough validation on sloshing flows occurring in tanks of different shapes has been carried out by Green [20]. A very focused application of a reformulated and adapted version of Weakly-Compressible SPH to this violent problem is performed by [21,22]. In this two-part paper a tank-fluid system is first periodically excited with a prescribed law of motion and the nonlinear features are observed. The force between the wall and the fluid and the global energy balance are both computed. Then, a validation against experimental results using a fluid-structure interaction formulation is carried out in the second part of this work. After this work, SPH can be considered an efficient and accurate methodology when compared to mesh-based methods to simulate free surface flows, and particularly violent sloshing flows.

A very detailed study on the initial stages of this sloshing problem where the Rayleigh-Taylor instability alters the free surface is performed in [23]. Normally the Rayleigh-Taylor instability (RTI) appears when the density gradient due to the presence of different fluids

and gravity are opposed. This situation is present at the initial stages of our problem, when the two different fluids are confined and the tank is accelerated upwards. In our case, the light fluid overlies a heavier fluid by the action of gravity, but the RTI is developed when a larger acceleration than gravity is applied to both fluids in the direction opposite to the force of gravity. As explained before, the density gradient is opposed to the difference between the inertial force and gravity. In order to understand what is causing the initial free surface deformation, the Rayleigh-Taylor instability can be studied comparing the results from the SPH simulations and other results obtained when the Navier-Stokes equations are perturbed and linearized, see [23]. Very few SPH approaches [24,25] contain a detailed quantitative comparison to other classical numerical formulations where well-established results such as the growth rate of the linear parts of the RTI are monitored.

This paper shows a dual approach, experimental and numerical, to the study of the violent vertical sloshing flows described above in the context of aeronautics applications. This paper will be focused on the comparison of both methodologies in terms of the most primitive results obtained from both approaches. Consequently, the visualization and kinematics of the flow evolution will be compared, and the physical insights of the sloshing force will be deeply studied. The present article is organized as follows: in Section 2 the process followed to transform the aeronautical problem into a simpler problem is laid out, and is later studied deeply from both an experimental and numerical point of view. In Section 3 both the numerical and the experimental methodologies are explained. In Section 4, the results obtained when both the methodologies are applied and compared, are presented. Finally, the conclusions are summarized and discussed in Section 5.

2. Modeling of the problem

In this section the general approach to model this complex problem will be explained, where a good number of simplifications are assumed to transform the real aeronautical problem into a simple experimental rig and its corresponding numerical version, both containing the most relevant physics from the original case.

When all the complexity of the industrial case is tried to be described, a problem where an immiscible multiphase fluid confined inside a deformable moving tank is considered. The tank moves with a trajectory given by the deformations of the aircraft wing, which gives rise to a great number of vibration modes and therefore to complex movement. Both fluids, liquid and gas, are viscous with surface tension between them and initial formation of menisci caused by the walls. The movements of both fluids inside the tank are characterized by high Reynolds numbers and therefore turbulence and non-linear effects are relevant. The numerical simulations must model those turbulent scales that normally the computational mesh does not resolve. Gravity and inertial forces due to acceleration are also present and especially relevant in this problem. It should also be remarked that a fluid-structure interaction case is faced, where in addition to the possible deformations of the container, there is a two-way interaction between the fluid and the tank through the pressure fields and viscous stresses produced, which makes the dynamics of the tank and those of the fluid clearly coupled.

Given such a number of complexities, if a simple model that contains the physical phenomena that are taking place has to be manufactured, some simplifications need to be assumed:

- The tank is manufactured in such a way that very small deformations appear and then it can be considered as a rigid solid.
- Even though the tank moves with complex 6 degrees of freedom (DoF) kinematics inside the wing, the movement in the vertical direction is much larger than in any other, and as a consequence, the tank movement will be simplified to a vertical 1-DoF movement with no rotations.
- Despite the fluid has a 3-D movement inside the tank giving a 3-D pressure field, 3-D computations are very costly in terms of computational time and the 2-D results

are accurate enough to obtain good performance, see [26], the computational fluid dynamics will be performed using a 2-D domain.

Assuming all these simplifications, the fuel tank inside the aircraft wing will be simplified to a experimental rig that consists of a vertically guided tank that is partially filled with liquid and air. An initially deformed spring system generates a decaying oscillating movement in the tank and the confined fluid. A more detailed description of the system is performed in the next Section 3.1.

3. Methodology description

The two different approaches, experimental and numerical, give a double perspective that allows a very complete and rigorous analysis of this complex problem. On one hand, the double approach implies comparison of some of the magnitudes that can be obtained independently by both methodologies, but also brings the possibility of testing whether some of the simplifications assumed in the computational framework are justified. On the other hand, both perspectives are complementary as the experimental measures are basically global magnitudes, while the computational approach is able to compute local pressure and velocity values.

3.1. Experimental approach

In this section, the vertical sloshing experimental setup, which is an improved version of the one used in [8], will be briefly described. The sloshing rig is a 1 degree of freedom system composed of a mechanical guide that allows only vertical motion. This guide is attached to a C-shaped wooden structure that holds the tank. This C-shaped wooden structure is attached to a set of 6 springs (3 on the upper side and 3 on the lower side) each of them having an individual spring constant of $k_i = 708.3$ N/m. The lower springs are mechanically embedded to the floor and on the opposite side, the upper set of springs is attached to a metallic plate that acts as a joint between them and the embedded load cell. A photograph of the 1/5 scale experimental setup at the Model Basin Research group sloshing laboratory of the UPM and a simplified outline are both shown in figure 1.

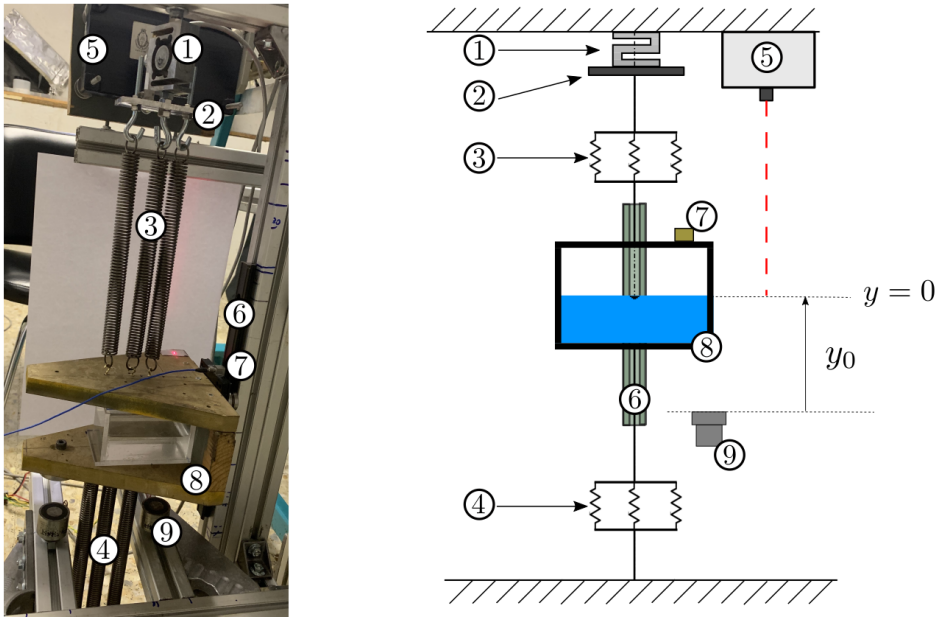


Figure 1. Snapshot of the experimental setup for the $\lambda = 1/5$ scale (left) and outline (right). (1) Load cell, (2) Metallic plate with mass $m_p = 0.06$ kg, (3) Upper set of springs with stiffness constant $k_1 = 2125$ N/m, (4) Lower set of springs with stiffness constant $k_2 = 2125$ N/m, (5) Laser sensor, (6) Mechanical guide, (7) Accelerometer, (8) Methacrylate tank and C-shaped wooden structure, (9) Pair of solenoids acting as release mechanism.

The tank dimensions of a scaled experiment with a scale parameter $\lambda = H/H_W$ are: H for the height and depth, L for the length and h represents the liquid height. The length H_W represents the tank height of the aircraft fuel tank. The system is displaced by an initial amplitude y_0 until it is fixed by the action of the pair of solenoids located at the bottom of the setup at $y = -y_0$. The permanent solenoids produce a magnetic force until the electrical current is turned on, triggering the release of the structure and the beginning of the oscillatory movement. In figure 2, the experimental snapshots of a 50% fill level $f = 0.5$ water test for $\lambda = 1/5$ and $y_0/H = 1$ are presented. The timeline of the snapshots has been referenced to the wing scale according to the Froude scaling laws ($t/\sqrt{(\lambda)}$).

Once the system is released and accelerated upwards, the initial flat free surface is rippled, see for example figures **a)** and **b)** in figure 2. Several effects cause the initial free surface deformation, the main cause is the meniscus deformation generated at the boundaries but also in those cases where the tank ceiling contains droplets of liquid attached: these droplets can cause a relevant perturbation when falling down from the upper wall and impacting the free surface. These perturbations in the free surface grow as Rayleigh-Taylor instabilities **c)** and **d)**. The instabilities grow and form liquid jets that impact the upper wall of the tank **e)** producing the first sloshing force peak. The linear growth of these instabilities has been deeply studied in [23] where the initial stages of an SPH computation are compared to the linear stability analysis of the Navier-Stokes equations in terms of growth rate and mode shape.

For the rest of the test a violent and turbulent regime is developed where the free surface is fragmented, small bubbles form, splashing occurs and liquid to liquid and liquid to wall impacts are seen **f)**. When the sloshing force is lower than the liquid weight the violence of the sloshing decreases **g)**, bigger bubbles form and fewer impacts occur. The liquid starts to return to its initial state with moderate liquid impacts to the lateral walls and it starts to develop a standing wave-like regime **h)**. It finally restores its initial state displaying a rotary motion that is attenuated over time **i)**. This general description will be particularized for the two liquids studied in this paper in Section 4.

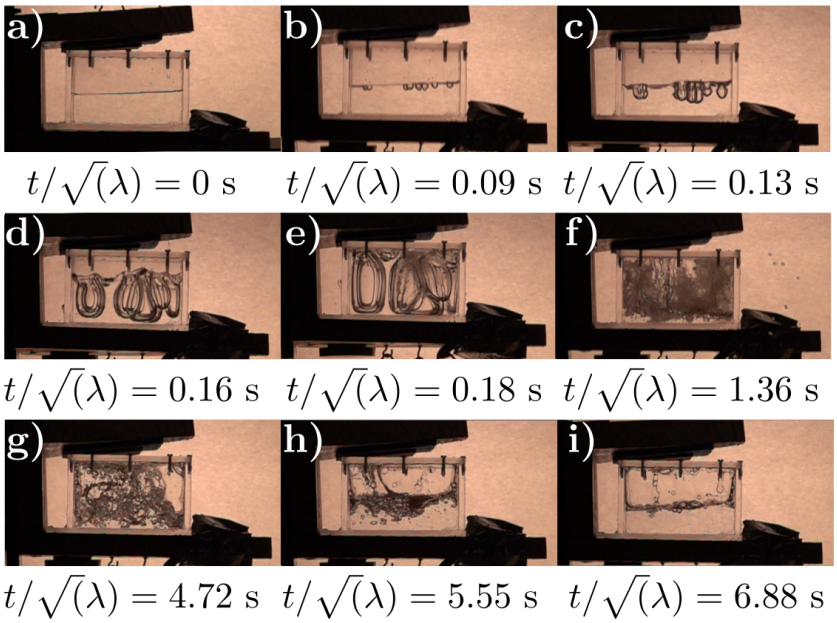


Figure 2. Experimental snapshots of the reference case for $\lambda = 1/5$. **a)** Initial state. **b)** Ripple formation in the free surface. **c)** Rayleigh-Taylor instabilities formation. **d)** Rayleigh-Taylor instabilities growth. **e)** First liquid to wall impact. **f)** Violent and turbulent regime. **g)** Ending of the turbulent and violent regime when F_{slosh} is lower than the liquid weight. **h)** Last lateral impacts and standing wave regime. **i)** Restoration of the initial state with rotary motion.

In this experimental setup there are 3 magnitudes that are being measured: acceleration, position and force. The characteristics of the measuring devices can be found in [8]. The measured signals are all filtered using a 4^{th} order Butterworth filter with a cutoff frequency of 20 Hz. The uncertainty analysis of the measurements has been performed in [27].

Once the acceleration, position and force measurements are post-processed, the following magnitudes are derived: the damping ratio, vertical sloshing force and the phase-shift between liquid action and tank motion. These magnitudes are defined in the subsequent subsections.

3.1.1. Damping ratio, ζ

Following the procedure explained in [28], the Hilbert transform of the acceleration signal is calculated in order to obtain the envelope function of the decay. By denoting the acceleration signal as a, the equation reads as:

$$\tilde{a}(t) = \mathscr{H}(a) = \frac{1}{\pi} \int_{-\infty}^{\infty} \frac{a(\tau)}{t-\tau} \quad d\tau \tag{1}$$

Where $\tilde{a}(t)$ is an imaginary signal that is shifted 90° in the complex plane from the real signal $a(t)$. Defining a function $A(t) = a(t) + i\tilde{a}(t)$ which is the sum of the real and imaginary parts and considering that the envelope function is the absolute value of this sum:

$$env(t) = |A|(t) = \sqrt{a^2(t) + \tilde{a}^2(t)} \tag{2}$$

Then, by assuming a linear decay of the signal, the envelope function is equal to:

$$env(t) = a_0 e^{-\zeta \omega_0 t} \tag{3}$$

Where a_0 represents the initial acceleration, ω_0 is 2π times the natural frequency of the experiment and ζ is the damping ratio. The natural frequency ω_0 is computed using the mean period, which is obtained as the mean over the number of cycles within the acceleration range $[a_0, 0.1a_0]$. To calculate the damping ratio ζ, a linear fitting is performed to the logarithm of the envelope signal in the same acceleration range. An example of this procedure is shown in figure 3 for the scale $\lambda = 1/5$ reference test (water and glycerine tests at 50 % and 39 % fill level respectively, $a_0 = 10$g). The damping ratio ζ is calculated as the slope of the linear fitting divided by ω_0.

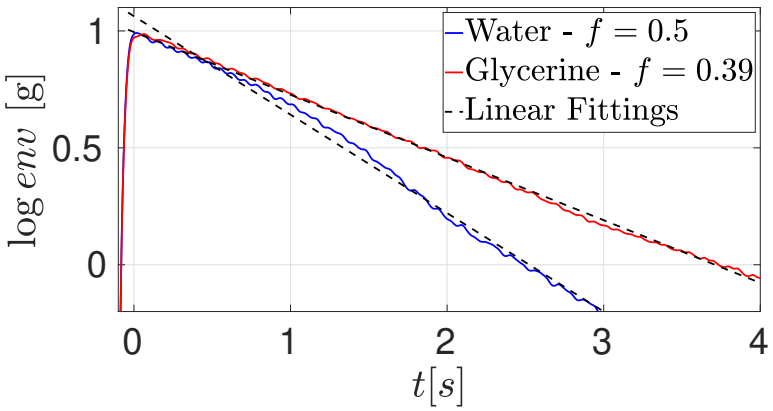


Figure 3. Logarithm of the envelope function and performed linear fitting for water and glycerine tests at $f = 0.5$ and $f = 0.39$ respectively, $y_0/H = 1$ and $\lambda = 1/5$.

3.1.2. Sloshing force, F_{slosh}

The vertical sloshing force acting on the SDOF system is experimentally calculated following the procedure shown in [8] for a similar setup. Denoting the load-cell measurement as T_{LC}, the vertical sloshing force is:

$$F_{slosh} = 2T_{LC} + m_s a, \tag{4}$$

where the solid moving mass m_s accounts for the masses of the C-shaped wooden structure, tank, mechanical bearing system and attachments. An in depth explanation of the derivation of equation (4) can be found in [8]. Using the liquid mass m_l and its initial acceleration due to the tank movement $\omega_0^2 y_0$ as characteristic values, the vertical sloshing forces presented in this paper are non-dimensionalized with $F_0 = m_l \omega_0^2 y_0$.

3.1.3. Phase-shift, ϕ

The phase-shift ϕ is defined as the angle related to the time-shift between the vertical sloshing force peaks F_{slosh} and tank position peaks y. The first 3 time-shifts Δt_i are shown in figure 4 for a water test at 50 % fill level and $a_0 = 10$g.

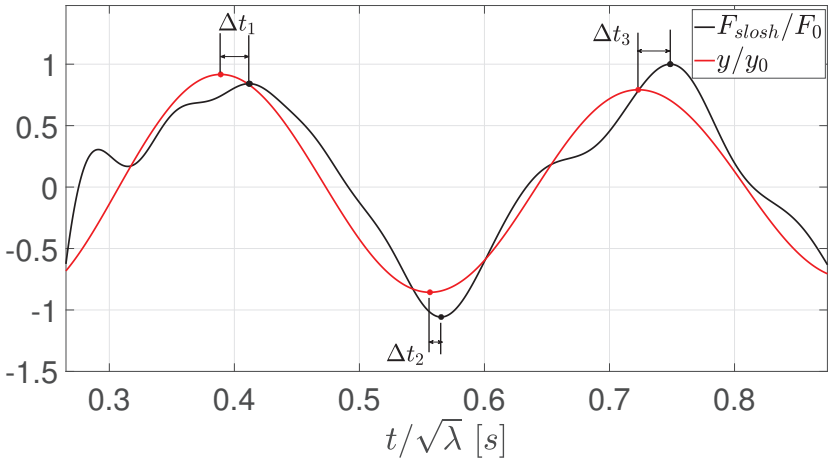


Figure 4. Normalized vertical sloshing force and tank position for a water test at 50 % fill level and $a_0 = 10$g. The first 3 time-shifts have been indicated as Δt_1, Δt_2 and Δt_3.

For each time-shift, a phase-shift between the sloshing force is defined and the tank motion as $\phi_i = \Delta t_i \omega_0$ and the averaged phase-shift for one experiment is the mean over the first 10 phase-shifts.

Keeping the experimental rig constant, this means using the same linear guide, springs, measuring devices, and rest of mechanical auxiliary parts; the parameter space that this problem involves is still large. The dimensional analysis of this problem has already been performed in several papers, see [8,27,29]. The remaining degrees of freedom of the experiment can be listed as:

- Sloshing liquid. Changing the liquid that partially fills the tank implies changing the density, viscosity and the surface tension of the dominant fluid.
- Initial amplitude y_0. This change implies a different initial acceleration and inertial forces.
- Fill level. This change implies varying the liquid mass inside the tank and consequently the mass ratio $r = m_l/m_s$ between the liquid and the solid moving masses.
- The global tank dimensions can also be scaled, see [27].

The variation of these degrees of freedom, which imply the variation of the dominant non-dimensional numbers of the problem in the context of our experimental rig, has been thoroughly studied experimentally in [27] and computationally in [26] where it has been found that the maximum damping is obtained for a 50 % filling level and the

sloshing induced damping ratio increases with the liquid density. Additionally, it has been concluded that the damping ratio increases with the initial amplitude up until a threshold amplitude $y_0/H \approx 0.4$ after which it starts to decrease. No relevant influence on the damping ratio has been reported due to surface tension variation. The damping ratio is unaffected by liquid dynamic viscosity changes if the flow is at high Reynolds numbers.

3.2. Numerical approach

SPH formulation for free-surface flows can be based on a weakly-compressible formulation, in which fluid pressure and density are linked through a barotropic law. Under this assumption, Navier-Stokes equations can be written as:

$$\begin{cases} \dfrac{D\rho}{Dt} = -\rho\, \nabla \cdot \boldsymbol{u} \\ \dfrac{D\boldsymbol{u}}{Dt} = \boldsymbol{g} + \dfrac{\nabla \cdot \mathbb{T}}{\rho} + \boldsymbol{a}_{st} \\ \boldsymbol{u} = \dfrac{D\boldsymbol{r}}{Dt}, \qquad p = p(\rho) \end{cases} \tag{5}$$

where $\dfrac{D}{Dt}$ is the material derivative, ρ is the fluid density, p the pressure, $\boldsymbol{u}$ the fluid velocity, that is defined from the fluid particles position, $\boldsymbol{r}$, $\boldsymbol{g}$ a generic external volumetric force field F and $\boldsymbol{a}_{st}$ is a surface tension force field. $\mathbb{T}$ indicates the stress tensor, that for a Newtonian fluid such as the ones used in the applications of this work, is defined as:

$$\mathbb{T} = (-p + \eta\, \mathrm{tr}\mathbb{D})\mathbb{I} + 2\mu\mathbb{D}\,, \tag{6}$$

with $\mathbb{D}$ being the rate of strain tensor, i.e. $\mathbb{D} = \left(\nabla\boldsymbol{u} + \nabla\boldsymbol{u}^T\right)/2$; $\mathbb{I}$ the identity matrix and μ and η the fluid viscosity coefficients respectively.

Relationship between pressure and density in (5) is established by means of a linear stiff equation of state (EOS). This allows to adjust compressibility so that the speed of sound (c_s) can be artificially lowered [30]. In a weakly-compressible context, the condition to be satisfied corresponds to Mach number Ma < 0.1. In this work, this condition is met if $cs > 10 \cdot U$, being U the maximum speed in the system, that is taken as the maximum speed of the tank.

Hence, set of Equations in (5) become in SPH:

$$\begin{cases} \dfrac{D\rho_i}{Dt} = -\rho_i \displaystyle\sum_j \boldsymbol{u}_{ji} \cdot \nabla_i W_{ij} V_j + h\, c_s\, \delta \sum_j \boldsymbol{\psi}_{ji} \cdot \nabla_i W_{ij} V_j \\ \dfrac{D\boldsymbol{u}_i}{Dt} = -\dfrac{1}{\rho_i} \displaystyle\sum_j (p_i + p_j) \nabla_i W_{ij} V_j + \boldsymbol{g}_i + \dfrac{\mu K}{\rho_i} \sum_j \pi_{ij} \nabla_i W_{ij} V_j + \boldsymbol{a}_{st_i} \\ \dfrac{D\boldsymbol{r}_i}{Dt} = \boldsymbol{u}_i \qquad p = p_0 + c_s^2(\rho_i - \rho_0) \end{cases} \tag{7}$$

where $\boldsymbol{u}_{ji} := (\boldsymbol{u}_j - \boldsymbol{u}_i)$ and V_j represents the volume of the neighbor particles j, defined as $V_j = m_j/\rho_j$. In the present work, the kernel function, defined $W_{ij} = W(\boldsymbol{r}_j - \boldsymbol{r}_i, h)$ is a Wendland C2 kernel with $h/dr = 2$ is used, where h corresponds to the smoothing length and dr to the particle distance.

The dissipation effects due to viscosity are modeled through π_{ij}, as is the standard in the literature (see e.g. [31]). This function is defined as:

$$\pi_{ij} := \frac{\boldsymbol{u}_{ji} \cdot \boldsymbol{r}_{ji}}{\| \boldsymbol{r}_{ji} \|^2}\,, \qquad \boldsymbol{r}_{ji} := (\boldsymbol{r}_j - \boldsymbol{r}_i) \tag{8}$$

An extra numerical term is added to the continuity equation in order to avoid spurious high-frequency pressure oscillations. The model used in this work corresponds to the one developed by [30], which is known as δ-SPH. The function $\boldsymbol{\psi}_{ji}$ from this term is defined as:

$$\boldsymbol{\psi}_{ji} := 2\left[(\rho_j - \rho_i) - \frac{1}{2}\left(\langle\nabla\rho\rangle_j^L + \langle\nabla\rho\rangle_i^L\right)\cdot\boldsymbol{r}_{ji}\right]\frac{\boldsymbol{r}_{ji}}{\|\boldsymbol{r}_{ji}\|^2} \tag{9}$$

where $\langle\nabla\rho\rangle_i^L$ represents the renormalized density gradient, as defined by [32]. The value for δ is set always to 0.1.

Boundaries are modeled according to the numerical boundary integrals approach, as described by [33]. They are discretized by elements that are defined by geometrical properties, such as their area, normal and tangent. Connectivity between nodes is avoided, allowing a faster and more efficient computation, even though a truncation error is assumed. Lately, some features have been added , and the Shepard factor is now computed geometrically through a semi-analytical approach, improving stability and robustness of the simulations [34].

Generally, no-slip boundary conditions should be used for the tank walls. However, when the Reynolds number is around 10^5 and greater, the wall boundary layer is thinner than the resolutions tested in the present work. Then, free slip boundary conditions are used on the tank walls instead, even though the expected difference is small, as it has been already discussed by [22].

Time integration is performed by means of a predictor-corrector scheme. Due to the violence of the impacts expected during the simulation, the Courant-Friedrichs-Lewy (CFL) condition is set to 0.1. Several time step constraints are imposed in order to consider all the phenomena involved, taking the minimum of them at every time step:

$$\begin{aligned} \Delta t &\leq \mathrm{CFL}\frac{h^2}{v} & \Delta t &\leq \mathrm{CFL}\min_i\left(\frac{h}{c_s + h\max_j \pi_{ij}}\right) \\ \Delta t &\leq \mathrm{CFL}\min_i\left(\frac{h}{\|\boldsymbol{u}_i\|}\right) & \Delta t &\leq \mathrm{CFL}\min_i\sqrt{\frac{h}{\left\|\frac{D\boldsymbol{u}_i}{Dt}\right\|}} \end{aligned} \tag{10}$$

Simulations have been carried out with the open-source SPH software AQUAgpusph developed by CEHINAV-UPM. As a reference, see e.g. [26,33–36] for applications done with this software. For further information, and to download the official release of the code, it can be accessed at http://canal.etsin.upm.es/aquagpusph/.

3.2.1. Additional model corrections: particle shifting and free-surface tracking

The problems covered in this work involve large pressure gradients that can lead to large areas with negative gauge pressures. Under this circumstances, it is possible that numerical cavitation appears. This is a phenomena known in SPH as tensile instability, and is still a great challenge for the method.

There are several sources in the literature that deal explicitly with tensile instability (see e.g. [37,38]). Normally, the solution consists on adding a correction term to the momentum equation. Recently, there are several works that follow a different approach, based on the application of the particle shifting technique (PST) introduced by [39]. Then, in this work a shifting algorithm with a tensile instability correction term will be used, in the same fashion as it was proposed by [40]. As it will be shown, this will be enough to avoid numerical cavitation in the simulations. A similar approach to the problem has been followed by [26] with satisfactory results.

The PST will also improve the accuracy of the scheme, as it will keep the particle distribution regular. However, the system in (7) needs to be rewritten in an Arbitrary Lagrangian Eulerian (ALE) framework. This implies new terms linked to the particle shifting velocity to be included in the governing equations, as discussed by [40,41].

Hence, the particle shifting velocity is defined according to [40] as:

$$\delta\tilde{\boldsymbol{u}}_i = -U_{ref}\, 2\,h \sum_j \left[1 + 0.2\left(\frac{W_{ij}}{W(dr)}\right)^4\right] \nabla_i W_{ij} V_j\,. \tag{11}$$

The shifting velocity points towards the areas where particle distribution is irregular, and its intensity is modulated by the constant $U_{ref}\,(2\,h)$, which is problem dependent. In this work, $U_{ref} = Ma \cdot c_s$. Normally, shifting velocity remains low enough, but an upper limit is established in the present work, being $0.25\,U_{ref}\,\delta\tilde{\boldsymbol{u}}_i / \parallel \delta\tilde{\boldsymbol{u}}_i \parallel$. Finally, shifting velocity is added to the particle velocity, and integrated in time to obtain the corrected position of the particles, such that:

$$\frac{D\tilde{\boldsymbol{r}}_i}{Dt} = \tilde{\boldsymbol{u}}_i + \delta\tilde{\boldsymbol{u}}_i, \tag{12}$$

In flows involving a free surface, an additional control is needed for the PST. In this case, a similar approach to the one carried out by [38] is established:

$$\delta\boldsymbol{u}_i = \begin{cases} 0 & \text{if } \lambda_i < 0.55 \text{ and } i \in \mathcal{F} \\ \kappa_i(\boldsymbol{I} - \boldsymbol{n}_i \otimes \boldsymbol{n}_i)\delta\boldsymbol{u}_i^* & \text{if } \lambda_i \geq 0.55, \boldsymbol{n}_i \cdot \delta\boldsymbol{u}_i^* \geq 0 \text{ and } i \in \mathcal{F} \\ \delta\boldsymbol{u}_i^* & \text{if } \lambda_i \geq 0.55, \boldsymbol{n}_i \cdot \delta\boldsymbol{u}_i^* < 0 \text{ and } i \in \mathcal{F} \\ \delta\boldsymbol{u}_i^* & \text{if } i \notin \mathcal{F} \end{cases} \tag{13}$$

where $\mathcal{F}$ is the region close to the free surface (defined at a distance h, and a scalar coefficient κ_i is defined such that:

$$\kappa_i = \begin{cases} 0 & \text{if } \max_j \left[\arccos\left(\boldsymbol{n}_i \cdot \boldsymbol{n}_j\right)\right] \geq 15^\circ \\ 1 & \text{otherwise} \end{cases} \tag{14}$$

Free surface tracking algorithm to detect free surface particles is implemented in accordance to the work developed by [40,42] Those works use thresholds to define different regions depending on how close a particle is from the free surface, based on the minimum eigenvalue (λ_i) of the renormalization matrix, that is defined as:

$$\boldsymbol{L}_i := \left[\sum_j \boldsymbol{r}_{ji} \otimes \nabla_i W_{ij} V_j\right]^{-1}. \tag{15}$$

In a second step, free surface particles can be fully identified, and normal vector found according to the following expression:

$$\boldsymbol{n}_i = \frac{\langle\nabla\lambda\rangle_i}{\|\langle\nabla\lambda\rangle_i\|} \quad \text{with} \quad \langle\nabla\lambda\rangle_i = -\sum_j (\lambda_j - \lambda_i)\,\boldsymbol{L}_i \nabla_i W_{ij} V_j \tag{16}$$

As it is also discussed by [40], the presence of solid walls have an influence in the computation of the free surface particles and their associated normal value. In order to have a proper definition of these, eigenvalues a the boundary need to be taken into account in Equation (16). However, this is not the case when computing shifting velocities from Equation (13), in which the extension at the boundaries is not considered. Taking into account these details, tips and jets are correctly identified and the simulations remain stable.

3.2.2. Surface tension model

A general surface tension field $\boldsymbol{a}_{st}$ is added to the momentum equation in Eq. (7) to deal with effects at the interface. These are specially notorious at initial stages of the tests performed in the present work and become crucial to obtain a satisfactory results in terms of impacts and lag between fluid and tank motions.

This force has been included in SPH. It is based on the term proposed by [43], and reads:

$$\boldsymbol{a}_{st_i} = -\frac{\sigma}{\rho_i}\sum_j (\boldsymbol{n}_j - \boldsymbol{n}_i)\cdot\nabla W_{ij} V_j \boldsymbol{n}_i \tag{17}$$

where σ is the surface tension coefficient.

3.2.3. Sloshing force and fluid structure interaction

In order to control tank's vertical motion, a second order equation is derived from the application of Newton's second law to the solid mass m_s. It is assumed that the forces that are applied to the tank come from three different components, in the same fashion as it has been proposed by [8]: the spring forces $-Ky$, the vertical component of the sloshing force coming from the internal fluid action F_{slosh} and the vertical component of the damping force $F_D = B_{0d}\cdot sign(dy/dt) - B_{1d}\cdot dy/dt$. The last component is assumed to include all sources of energy dissipation in the system that are not due to fluid slosh. In the present work, these are a Coulomb friction and a viscous friction term respectively. The resulting equation reads:

$$F_{slosh} - B_{0d}\cdot sign\left(\frac{dy}{dt}\right) - B_{1d}\cdot\frac{dy}{dt} - K\cdot y = m_s\frac{d^2y}{dt^2}\,, \tag{18}$$

where $B_{0d} = 0.38$ N represents the Coulomb damping coefficient and $B_{1d} = 1.73$ kg/s is the viscous damping coefficientFinally, the vertical sloshing force F_{slosh} is given, for a Newtonian fluid, by

$$F_{slosh} = -\int_{S_{tank}} p\,\mathbf{n}\,dS + 2\,\mu\int_{S_{tank}} \mathbb{D}\,\mathbf{n}\,dS \tag{19}$$

The first term in Equation (19) represents the contribution of the pressure forces, and the second term the one from the viscous forces. S_{tank} corresponds to the tank's internal walls and the normal $\mathbf{n}$ is defined such that is pointing outwards. These forces can be computed in SPH, according to the boundary integrals approach, on the boundary elements. The resulting expressions are:

$$\begin{aligned} F^p_{slosh} &= -\sum_i\sum_{j\in BE}(p_j + p_i)\,\mathbf{n}_j\,W_{ij}\,V_i\,S_j\,, \\ F^V_{slosh} &= \mu\sum_i\sum_{j\in BE}\left[\pi_{ij}\,\mathbf{n}_j + \frac{(\boldsymbol{I} - \boldsymbol{n}_j\otimes\boldsymbol{n}_j)\,\boldsymbol{u}_{ji}}{|\boldsymbol{r}_{ij}\cdot\boldsymbol{n}_j|}\right]W_{ij}\,V_i\,S_j\,. \end{aligned} \tag{20}$$

The second term of the viscous force F^V_{slosh} is taken into account if no slip boundary conditions are enforced. A similar procedure to compute the forces can be found in [44].

Then, forces obtained according to expressions in Equation (20) can be applied to Equation (18) to obtain the vertical motion of the tank.

A 4^{th} order Runge-Kutta integrator (RK4) is used to obtain accelerations, velocities and positions at each time step. The resulting fields are then appied to the boundary elements in which the tank walls are discretized. This exchange of information is done at every time step. SPH integration algorithm implies much smaller time steps than the ones needed by the RK4 algorithm used for tank motion evolution, and this way it receives updated information every loop, assuring the stability of the coupled system.

4. Results and discussion

As explained at the beginning of the paper, this work is focused on the physical aspects of the problem, which implies a deep insight into the flow characterization, tank and fluid kinematics (initial jet velocities, final standing wave...) and the sloshing force interchanged between the fluid and the tank.

Liquid	$\rho[kg/m^3]$	$\mu[Pa \cdot s]$	$Re = \rho\omega_0 y_0 H/\mu$	$\sigma[mN/m]$
Water	998	$8.9{\cdot}10^{-4}$	$1.6{\cdot}10^5$	72.7
Glycerine	1262	1.49	130	64

Table 1. Physical properties and characteristic Reynolds number of the two fluids, water and glycerine, used in the experiments.

The sloshing force is measured experimentally according to Expression (4) and computed numerically according to Expression (20). Both forces have been accurately compared as part of the code validation in [22,26]. The advantage of the computational methodology is among others that the pressure and viscous contributions can be obtained separately. To understand the contributions of these two sloshing force sources, two cases corresponding to two different fluids, water and glycerine, have been studied with the same initial acceleration $a_0 = 10g$, same scale $\lambda = 1/5$ and same mass ratio $r = 7.4\%$. As these two fluids have different densities, the initial filling level is different for these two cases, ($f = 50\%$ for water) and ($f = 39\%$ for glycerine), in order to keep the mass ratio constant. These two fluids, water and glycerine, have the properties shown in Table 1. As Table 1 shows, the flows studied have very different Reynolds numbers, which implies a laminar regime in the case of glycerine, and a fully turbulent flow for the water. This difference in terms of Reynolds numbers is mainly caused by the large difference in terms of viscosity, and consequently significant differences in the flow behaviour and force decomposition between the pressure and viscous parts are observed.

4.1. Comparison of the flow evolution: experimental visualization versus numerical computation.

In this subsection the different stages of the flow from both points of view, numerical and experimental, are compared in order to observe the common characteristics. First the case of water will be described, and then that of the glycerine in order to remark on the clear differences between both cases. Previous to this work, in [26] the fact that the extra damping added by the fluid depends on the Reynolds number only when it is below a critical Reynolds value Re_c was observed. Denoting the characteristic Reynolds number for the water and glycerine cases as Re_0 and Re_g respectively, this critical Reynolds number is approximately an order of magnitude lower than the case of water $Re_c \sim Re_0/10$. Consequently, the Reynolds numbers of the water and the glycerine are placed at two different sloshing regimes $Re_g \ll Re_c < Re_0$

4.1.1. Water case $Re_0 \sim O(10^5)$.

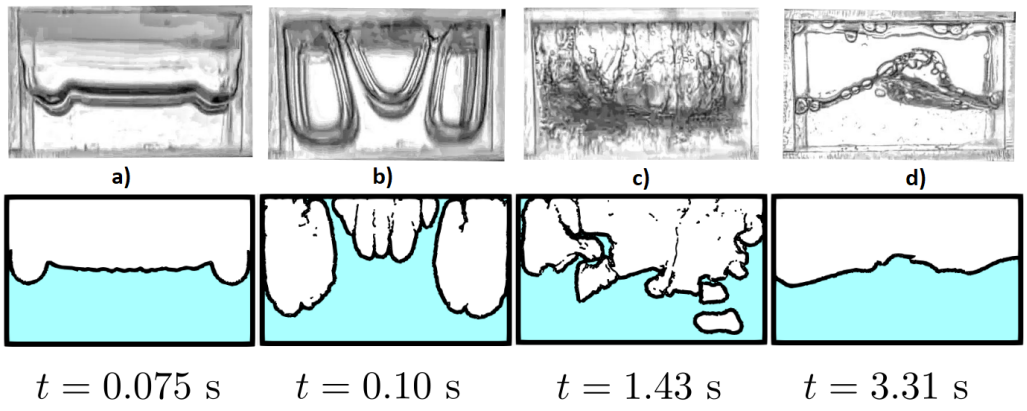


Figure 5. Experimental snapshots (top) of a vertical sloshing experiment with water at a 50% filling level and 10g of maximum acceleration. Numerical counterparts (bottom) simulated the δ-SPH method.

For the water, three different stages in the flow evolution can be distinguished. Denoting as t_1 and t_2 the instants when the first and the second stage finish and t_{fi} and t_{li} as the instants where the first and last ceiling impacts are observed.

- As displayed in figure 5, during the first instants a ripple generated from the free surface deformation due to the initial meniscus travels horizontally through the free surface from the lateral walls towards the tank center, see a snapshot of this traveling wave in figure 5.a) ($t = 0.075s$). This initial stage can be interpreted as a classical evolution of a Rayleigh-Taylor instability. This initial stage finishes with the first fluid-wall impact, see figure 5.b)($t_1 \equiv t_{fi} \sim 0.1s$). In this instant a four jet symmetrical image is observed, where two central jets impact at the tank ceiling while the other two after traveling up the lateral walls impact at the lateral-top corners.

- A chaotic and turbulent regime dominates during the longest part of the experiment. At this stage the liquid and the gas are chaotically mixed up, making the two fluids difficult to distinguish. The free surface is very fragmented and air bubbles of different sizes merge and collapse. This second stage finishes at time $t_2 \sim 2.84$. A typical snapshot of this regime can be seen in figure 5.c)($t = 1.43s$).

- The last stage shows up after $t_2 = 2.84s$, where a mostly compact fluid is observed. The flow transitions to a standing-wave like behaviour that displays some similarities to the rotary sloshing phenomenon observed in [45,46], with very small vertical sloshing force variations. The last ceiling impact at time $t_{li} \sim 3.56s$ is part of this stage. A typical snapshot of this regime can be observed in figure 5.d)($t = 3.31s$)

It can be observed that the 2D computational simulation is able to reproduce the free surface behaviour when corresponding snapshots are compared, see figure 5. Details such as the double traveling wave that initiates the free surface deformation, the four jets impacting structure and the final standing-wave are well captured by the numerical model.

4.1.2. Glycerine case $Re_g \sim O(10^2)$.

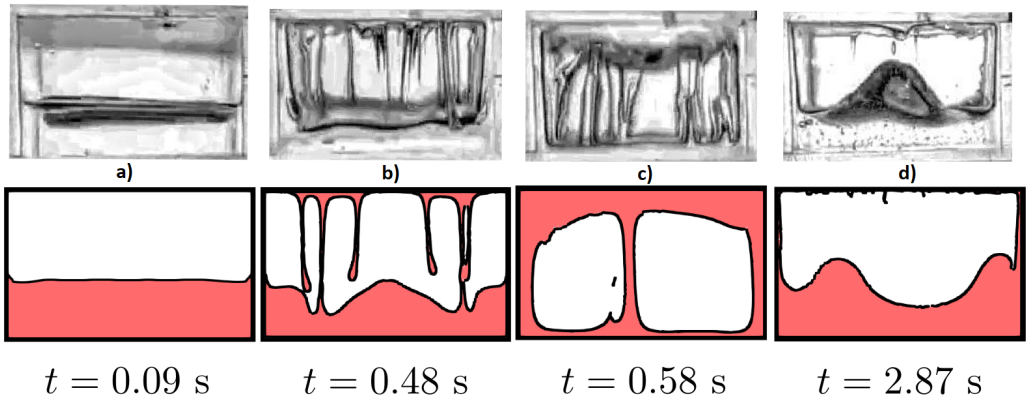


Figure 6. Experimental snapshots (top) of a vertical sloshing experiment with glycerine at a 39% filling level and 10g of maximum acceleration. Numerical counterparts (bottom) simulated the δ-SPH method.

For the glycerine case, the Reynolds number is three orders of magnitude lower, but it can also be distinguished three different stages in the flow evolution, where the same time notation will be used.

- As displayed in figure 6, during the first instants no free surface deformation is observed with the exception of the lateral wall meniscus, see a snapshot in figure 6.a) ($t = 0.09s$). As demonstrated in [47], the increment of viscosity decreases the growth

rate of the Rayleigh-Taylor instability. It could be assumed that this initial stage finishes with the first fluid-wall impact ($t_1 \equiv t_{fi} = 0.41s$), which happens at the third tank cycle (first in the case of water). It is worth commenting that three dimensional effects are more present at this first stage in the case of glycerine compared to water, and this can be interpreted by the more dominant role of the viscous stress tensor in this flow.

- The second regime of the glycerine is less chaotic and turbulent when compared to the water regime, in this case jets and traveling boundary layers are clearly observable and fewer droplets and bubbles appear in the flow. As expected, the higher viscosity makes the liquid more compact and less fragmented. This stage takes approximately the same amount of time compared to the water and also dominates during the longest part of the experiment. As already measured in [21] comparing water and oil, the damping capacity of a fluid is related to the number of violent impacts, and high viscosity plays an opposite role for this behaviour. As a consequence the more viscous the liquid, the less damping generated. The last ceiling impact is observed at time $t_{li} \sim 2.46s \ll 3.56$ which corresponds to the case of water.

- After a similar duration to the water $t_2 = 2.58s$, the flow transitions to a standing-wave like behaviour. This stage takes less time to relax towards a final flat free surface, with very small vertical sloshing force variations. A typical snapshot of this stage can be observed in figure 6.d)($t = 2.87s$). It could also be observed that in contrast to the water case the final low amplitude oscillations of the glycerine case have no impact in the free surface and the glycerine remains as a block at the bottom of the tank.

The videos corresponding to the cases of water and glycerine can be downloaded from http://canal.etsin.upm.es/files/SLOWD/videos

An interesting comparison between these two cases can be made in terms of the relative kinetic energy, and this time dependant number is defined as:

$$\varepsilon_k = \sum_i \frac{1}{2} m_i (v_i - v_t)^2 \tag{21}$$

where v_i and m_i are the absolute velocity and mass of a fluid particle respectively and v_t is the tank velocity. When the evolution of this relative kinetic energy is plotted for both fluids, see figure 7, it is observed that they both start with a similar energy value but the energy growth for the water is completely different from the glycerine, especially during the first half second of the experiment. The relative energy has been normalized by the initial elastic potential energy introduced in the system $\varepsilon_0 = \frac{1}{2} K y_0^2$ where K is the spring constant of the experimental setup. Despite the fact that both flows produce impulsive impacts with the upper and lower tank walls, the higher fragmentation of the water produces larger levels of relative kinetic energy. This high energy stage takes approximately the same time for both fluids $t_2 - t_1 \sim 2s$, after which the impacts are clearly smoothed. In this second stage during the interval $2 - 3$ seconds, the water free surface continues to be clearly fragmented, while the glycerine seems to be more compact with a more smoothed free surface. After 3 seconds, the water still impacts the ceiling and wave breaking is observed for the water while no top impacts are observed and only a combination of standing waves are detected for the glycerine. An interesting difference appears during the last part of the experiment. In the case of the water the tank movement is more damped and the oscillations are lowered sooner, but a remaining standing wave can be observed for a long time as the viscosity action takes a long time to dissipate its energy. In the case of the glycerine, the tank oscillates a longer time, but the liquid remains a flat block during the whole final part as the viscosity dissipates the standing wave quickly.

Liquid	ζ [%]	t($a = 0.1 \cdot a_0$) (s)
Water	2.5	2.29
Glycerine	1.7	3.19

Table 2. Damping ratio and characteristic decaying time for the water and glycerine cases .

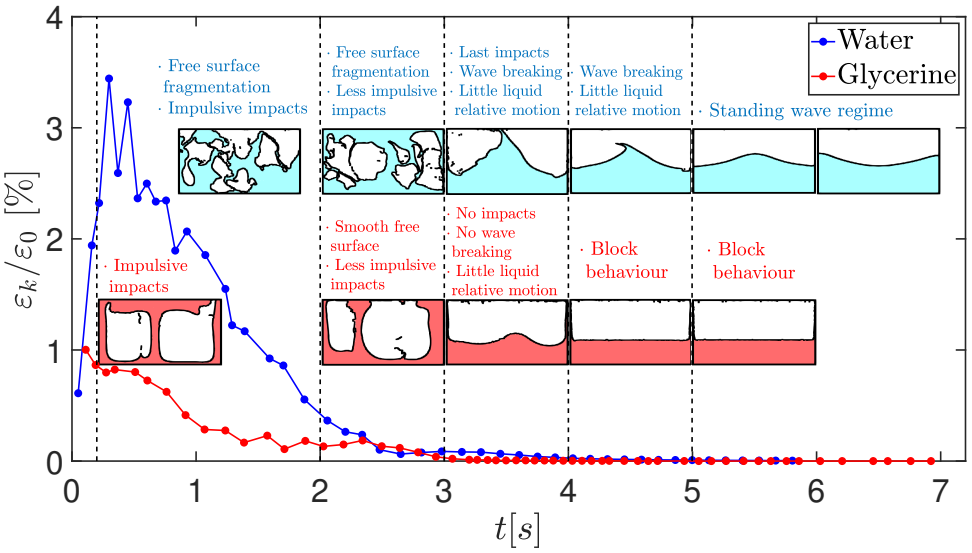


Figure 7. Normalized amplitude of the relative kinetic energy of the liquid. Comparison between water and glycerine.

In figure 8 the tank accelerations of both cases are shown for the same mass ratio and natural frequency. First of all, it can be observed that the matching between the experimental and computational results is very accurate. This validation was already performed in [26] with an older version of the AQUAgpusph code.

In table 2 the damping ratio ζ defined in section 3.1.1 and the time necessary to decrease the tank acceleration to 10% of its initial value $t(a = 0.1 \cdot a_0)$ are quantified for the water and glycerine. It is confirmed again that the damping of the water is larger than the glycerine.

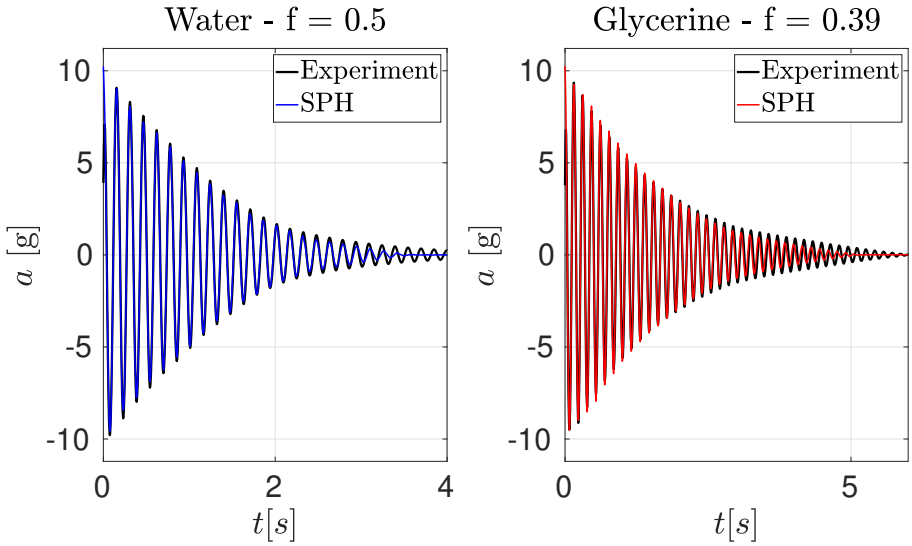


Figure 8. Comparison between δ-SPH simulations and experimental data of the acceleration of the tank over time for water and glycerine decay tests at 10g of maximum acceleration.

In figure 9 the vertical sloshing force is plotted for both fluids non-dimensionalized with $F_0 = m_l \omega_0^2 y_0$ where m_l is the liquid mass, ω_0 is the characteristic angular velocity and y_0 the initial displacement of the tank. Despite a similar plot being shown in previous publications[26], this new and improved version of the AQUAgpusph code has been able to produce more accurate results than the previous ones. The agreement between the experimental and computational is accurate in both cases. It is interesting to confirm some physical findings that appear in this plot. First, the initial impacts of both cases are quite similar $\sim 20N$ as the mass ratio, and the fluid densities are similar as well. Second, the time required for the water to produce impacts lower that 10% of the initial impact is 2.29 seconds while the glycerine needs 3.19 seconds to decrease the vertical impacts.

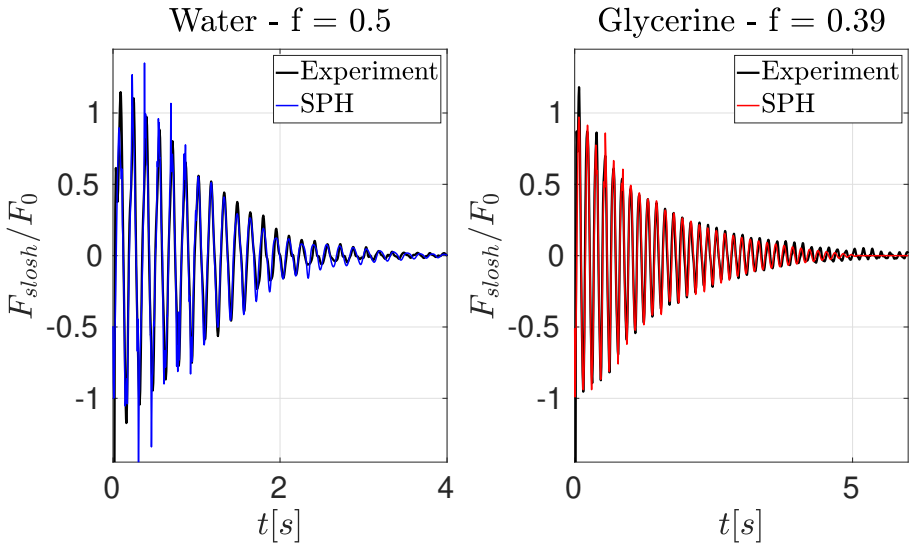


Figure 9. Comparison between δ-SPH simulations and experimental data of the nondimensional vertical sloshing force over time for water and glycerine decay tests at 10g of maximum acceleration.

4.2. Flow kinematics

As explained in section 4.1, three stages can be distinguished for both fluids. The fluid kinematics corresponding to the first and last parts will be studied in detail in this section for the case of water. Due to the complexity of the middle part, that part will be studied with other methodologies such as Dynamic Mode Decomposition, see [48–50], in future works. It was also observed that for the glycerine three dimensional effects are dominant and consequently the comparison to the 2D computational approximation is not so clear and will require a future 3D computation.

4.2.1. First stage

As explained in section 4.1, this first stage starts with the relative flow movement inside the tank and finishes with the first ceiling impact. In the case of water the initial free surface deformation can be studied in terms of impelling jets, which are created symmetrically to the middle vertical plane. In figure 10 the free surface obtained by the SPH computation and the one obtained by image processing from experimental snapshots are compared at different time steps before the ceiling impact. The free surface position from the experimental snapshots is extracted by taking into account the decrease in luminosity close to the free surface. The gradient of the luminosity of the snapshot is computed and the points with the most negative gradient values are extracted. Complex dynamic phenomena are present in the flow such as: traveling wave formation, free surface deformation, central jet formation and the boundary layer evolution on the lateral walls. These are all well captured qualitatively. Although the 2D computational flow shows a very realistic representation of the experimental one, it was observed that the computational region allows the formation of more ripples on the free surface than the real flow is able to diffuse.

Although this code has been validated in a typical free surface evolution problem such as the Rayleigh-Taylor one [23] including surface tension and viscosity, the results obtained here show that when higher velocities and accelerations are present in the free surface the viscosity and surface tension models should be able to damp these short wavelength instabilities.

The authors would like to underline that in the comparison of the free surface evolution in figure 10 a 2D simulation is being compared with a 3D flow therefore, some differences in terms of flow morphology should be expected. Furthermore, since the tank is moving and the camera is at a fixed position the angle of view varies with time and the free surface represented in the experimental snapshots presents some perspective which is not present in 2D simulations.

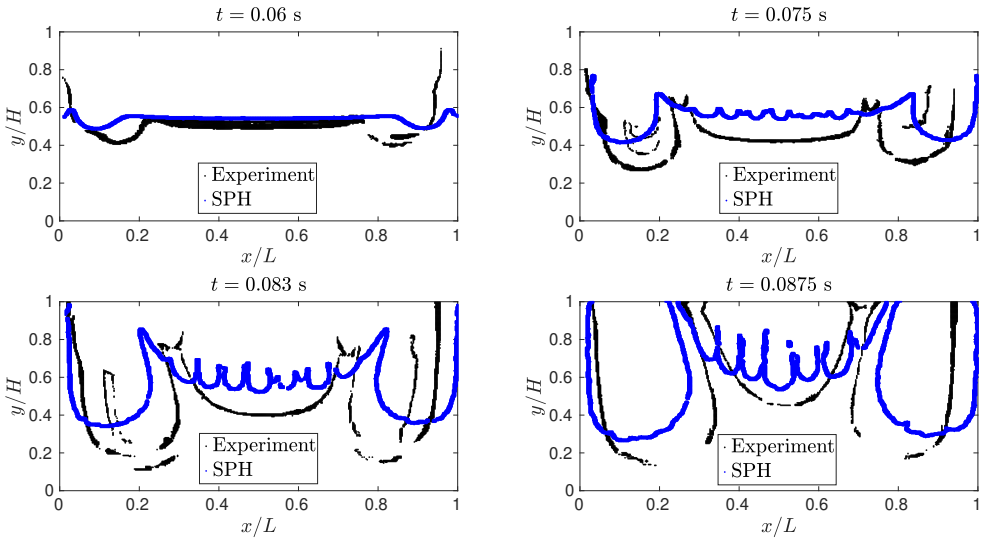


Figure 10. Comparison between the free surface position obtained by the SPH computation and the image processing obtained from experimental snapshots.

The symmetric dominant central jets that appear in the free surface have been monitored in terms of relative velocity magnitude for both methodologies, and the quantitative results have been compared in figure 11 where the modulus of the velocity has been non-dimensionalized with $v_0 = \omega_0 y_0$. During tank deceleration a linear growth is observed in the relative jet velocity, and this tendency is well captured by the computations. It is particularly interesting to see that before the final impact, during the whole jet acceleration process the tank is decelerating. The dispersion of the experimental results when compared to the computational ones is due to the image processing technique where jet velocity is approximated graphically.

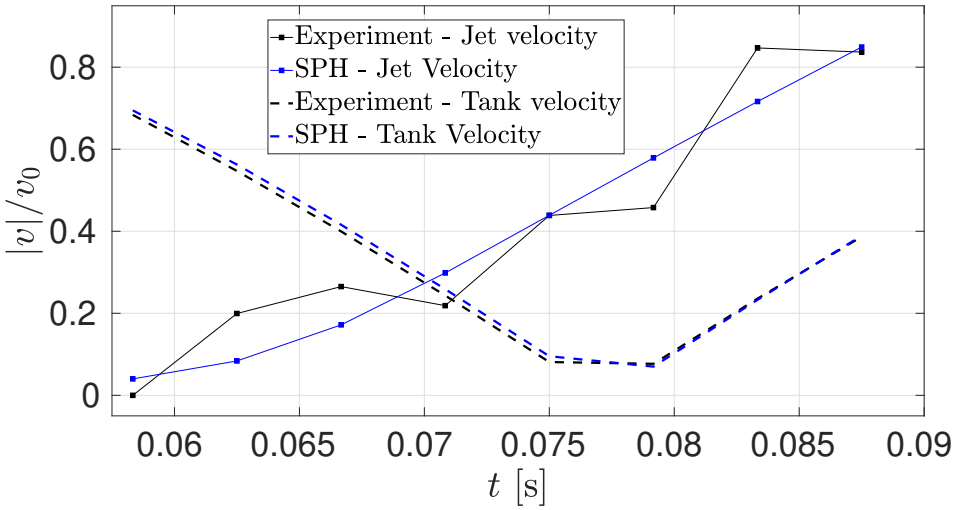


Figure 11. Non-dimensional velocity magnitude of the central jets measured from the SPH computation and the experimental snapshots. The decreasing tank velocity is also plot to have a reference for the jet evolution.

4.2.2. Last stage: standing wave

As explained in section 4.1 the last stage of this kind of flow when no violent impacts take place tends towards a typical viscous standing wave in the cases of the water and the glycerine. Two typical snapshots of the standing wave delayed half period for the water can be seen in figure 12. The 2D periodic fluid problem can be modeled as a damped mass-spring system[51], where the mass is equal to the liquid mass, the spring constant is equal to the liquid mass times the square of the characteristic sloshing frequency $\omega = \sqrt{gk \tanh kh_l}$, where k is the wave number associated with the distance between the vertical lateral walls and h_l is the liquid height, which is 3 cm for water. As in our case the problem is confined between the lateral walls and the analytical solution can be only considered an approximation. In this simplified mechanical model the damping coefficient $\beta = \beta(k, Re)$ depends on the wave number k and the Reynolds number $Re = \rho\sqrt{gh_l}/\mu$, see [52] for details about the analytical solution. This analytical analogy can only considered for the case of the water as the glycerine does not satisfy one of the main hypotheses of the analytical solution which is $Re \gg 1$.

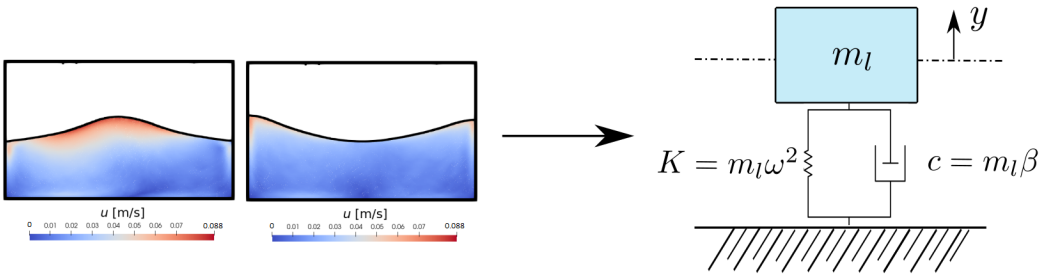


Figure 12. Left: Snapshots of the velocity contour for two instant separated half period. Right: Mechanical analogy of the standing wave.

In figure 13 the kinetic energy of the standing wave has been represented using the damped mass-spring model described above and also for the fluid kinetic energy given by expression (21). It can be observed that the amplitude of the oscillation is more attenuated for the SPH solution, and this difference can be explained by the presence of surface tension and no-slip boundary conditions on the lateral walls in the SPH simulation. The effect

of the lateral walls when viscosity is present was studied in [23], in this work the growth rate variation of the Rayleigh-Taylor instability was quantified by comparison between the confined and the periodic case with the same tank geometry. A lower growth rate value for two different geometries was observed in the confined case when compared to the periodic case for the dominant linear mode. The frequency given by the analytical model matches the SPH solution very well until the flow velocity is extremely low.

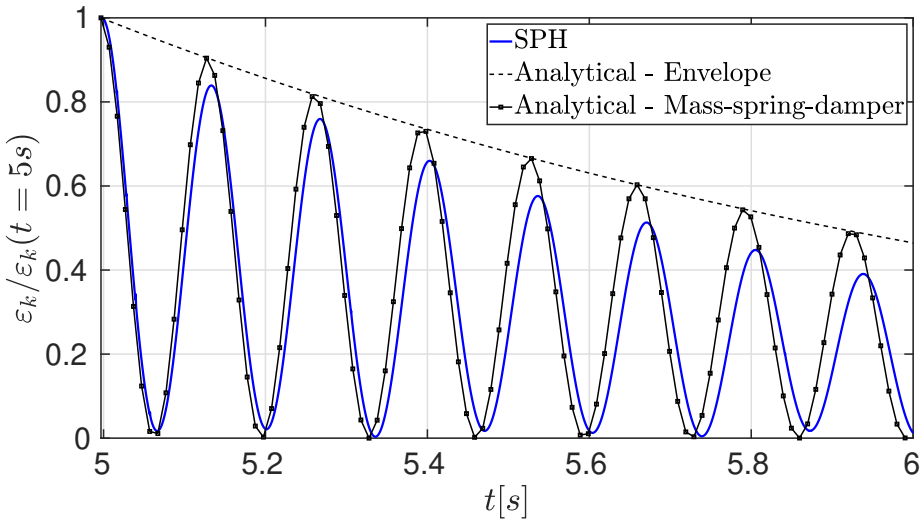


Figure 13. Comparison of the evolution of the relative liquid kinetic energy and the analytical periodic approximation and its envelope.

4.3. Sloshing force decomposition

According to [8] the sloshing force, either measured in the experiments using expression (4) or computed using the pressure and velocity fields by equations (19)-(20) can be divided into three components: the inertial part which is related to the inertia of the tank motion, and would be present even in the case where there is no relative movement of the liquid in the tank, for example if $f = 1$; a dissipative contribution that is related to the relative movement of the liquid inside the tank and is responsible for the damping increase of the mechanical system and a high frequency contribution of the harmonics with higher frequencies than the natural one. This last contribution is filtered out by using a 4th Butterworth filter around the natural frequency of the system.

$$F_{slosh} = \underbrace{m_l a_t}_{\text{Inertial}} + \underbrace{\Delta F_{slosh}}_{\text{Dissipative}} + \underbrace{F_{\mathcal{H}.\mathcal{F}}}_{\text{High frequency}} \tag{22}$$

The part of the force that causes the extra damping in the tank oscillation is clearly the dissipative one, this force ΔF_{slosh} can be modeled as an amplitude multiplied by a shifted cosine function with the natural frequency ω_0. Expanding the cosine, two terms are generated which can be related with the typical force decomposition in velocity and acceleration projections [53].

$$\begin{aligned} \Delta F_{slosh} &= F\cos(\omega_0 t - \phi) = \\ F\cos(\omega_0 t)\cos(\phi) &+ F\sin(\omega_0 t)\sin(\phi) = \\ -\beta m_l \omega_0^2 Y\cos(\omega_0 t) &+ \gamma\omega_0 Y\sin(\omega_0 t) = \\ \underbrace{\beta m_l a_t}_{\text{Sloshing effective mass}} &+ \underbrace{\gamma v_t}_{\text{Sloshing induced dissipation}} \end{aligned} \tag{23}$$

where the β and γ coefficients can be related with the amplitude F and the shift angle ϕ by the equations:

$$\beta = \frac{F}{-m_l\omega_0^2 Y}\cos(\phi) \quad , \quad \gamma = \frac{F}{\omega_0 Y}\sin(\phi) \quad \text{with} \quad Y = y_0 e^{-\zeta\omega_0 t} \tag{24}$$

The filtered version of the total sloshing force, where the high frequency component is removed, can be expressed using both formulations as:

$$\widehat{F}_{slosh} = F_{slosh} - F_{\mathcal{H}.\mathcal{F}} = (1+\beta)m_l a_t + \gamma v_t = m_l a_t + F\cos(\omega_0 t + \phi) \tag{25}$$

Another way of understanding the vertical sloshing force is by relating it to the motion of the Center of Mass (CM) of the liquid. Dividing $\widehat{F}_{slosh}$ by $-m_l\omega_0^2$, the following equation is obtained:

$$y_{CM} = \frac{\widehat{F}_{slosh}}{-m_l\omega_0^2} = \frac{m_l a_t}{-m_l\omega_0^2} + \frac{\Delta F_{slosh}}{-m_l\omega_0^2} = \underbrace{y_t}_{\text{Tank position}} + \underbrace{y_{rel}}_{\text{Relative motion to the tank}} \tag{26}$$

Equation (26) identifies the inertial component of the vertical sloshing force with the tank motion and the dissipative component with the relative motion of the liquid with respect to the tank. In figure 14 the non-dimensional relative position of the liquid center of mass y_{rel} is compared to the term $-\Delta F_{slosh}/m_l\omega_0^2$ for both water and glycerine test cases. In this figure, the relative position has been non-dimensionalized with half the liquid height $h_l/2$ which is the initial and final position of the liquid CM relative to the tank. It is worth noting that in figure 14 the amplitude of the signals have been extracted from the time domain SPH computation in order to perform the comparison. The overall amplitude of the relative motion of the liquid center of mass matches the amplitude of the dissipative vertical sloshing force as equation (26) indicates. Therefore, in order to understand the dissipation of the vertical sloshing problem it is only necessary to track the relative motion of the liquid center of mass with respect to the tank. This suggests the possibility of using simpler equivalent mechanical models such as the bouncing ball model described in [54].

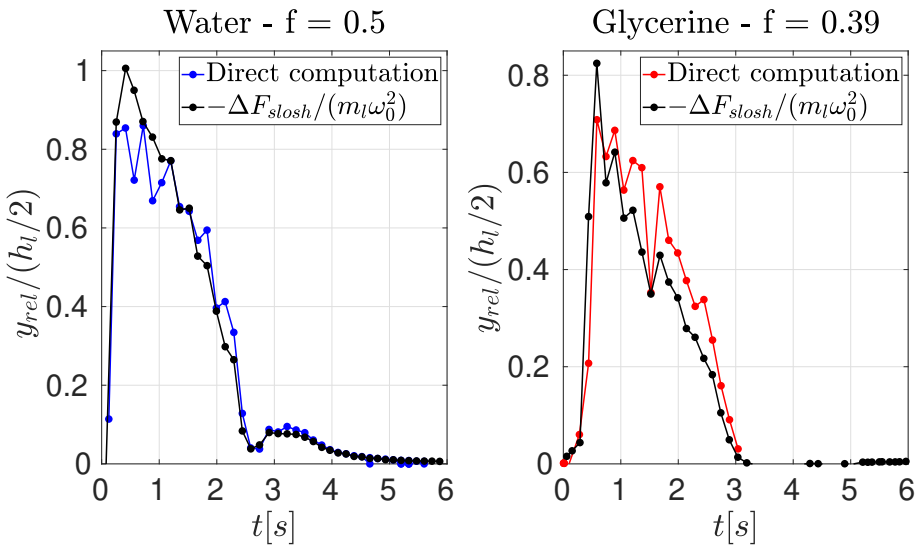


Figure 14. Nondimensional amplitude of the relative motion of the liquid center of gravity with respect to the tank over time for water $f = 0.5$ (left) and glycerine $f = 0.39$ (right). Comparation between SPH calculation and the expression given by equation 26, $-\Delta F_{slosh}/(m_l\omega_0^2)$.

In figure 15 the filtered sloshing force has been plotted with the direct computation of expression (20) and also with both versions of expression (25) for the water and glycerine.

As can be observed the agreement between the SPH computation and the derived versions either considering the γ and β parameters or the force maxima F and the shift angle ϕ are both close. This means that the apparently complex sloshing force that comes from a violent and turbulent flow described in section 4.1 can be reconstructed using a simple analytical expression based on a cosine function. This fact confirms the possibility of using reduced order models (ROMs) for this kind of problem as has been demonstrated in [53].

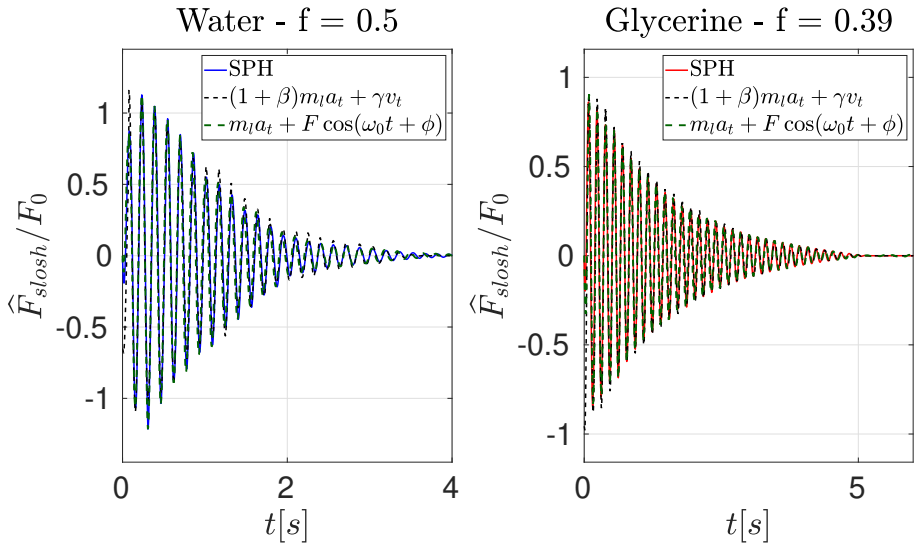


Figure 15. Filtered nondimensional sloshing force computed directly from the SPH formulation and also using the alternative force reconstruction given by the equation 25.

In order to understand the difference in terms of Reynolds numbers and the impact on the sloshing force, the pressure and viscous contributions to the sloshing force have been separated according to expression (19) for the water and glycerine. It can be observed that the global sloshing force being similar for both fluids according to figure 15, the viscous contribution is much smaller in the case of water when both fluids are compared, see figure 16. This is an expected result and confirms the negligible role of the viscous forces when the Reynolds number is high enough $Re \sim 10^5$ as in the case of water. The pressure forces are on the same order of magnitude for both fluids, being smaller in the case of glycerine. It is also interesting to mention that the viscous forces for the glycerine start having a significant role after $t > 0.52$ seconds of simulation. This can be accounted for by the fact that the violent relative movement of the glycerine inside the tank starts after three cycles of the tank and not since the beginning, the first impact being at $t = 0.41s$, see section 4.1.2. The period of time between $t = 0.41s$ and $t = 0.52s$ is the time required for the velocity gradients to grow on the wall boundary layers that flow over the surfaces.

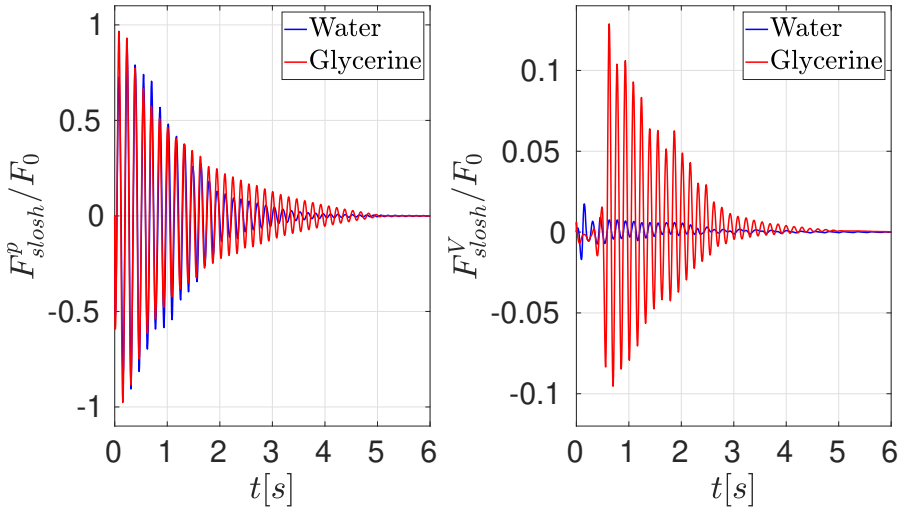


Figure 16. Nondimensional sloshing force components separated into their pressure and viscous contributions, for both the water and the glycerine cases.

The energy dissipated by the different physical components of the sloshing force can also be studied, where F^p_{slosh} and F^V_{slosh} denote the pressure and viscous parts respectively, and also considering the dissipated energy given by the structural damping force $F_D = B_{0d} sign(v_t) + B_{1d} v_t$. These energies are computed using the expression (27) and then normalized by ε_0.

$$\varepsilon_{diss} = \int F \quad dy \tag{27}$$

In equation (27) F could be any of the three forces mentioned in the previous paragraph. It was observed that the sum of the structural and the pressure forces are above 90%. The energy dissipated by the viscous part of the sloshing force is below 4% in all cases, nevertheless the glycerine viscous dissipation is notably larger compared to water. The total dissipated energy quantified by these three forces sums to 97.4% for the water and to 96.7% for the glycerine, see figure 17. The rest of the dissipation comes from the additional numerical terms that are introduced into the model for stability, such as the δ-SPH. Another interesting fact is that in these kinds of experiments, the structural energy dissipated is comparable to the energy dissipated by the fluid in the case of water 55%(structural) versus 42.4%(fluid), but is significantly larger 71%(structural) versus 25.7%(fluid) for the glycerine.

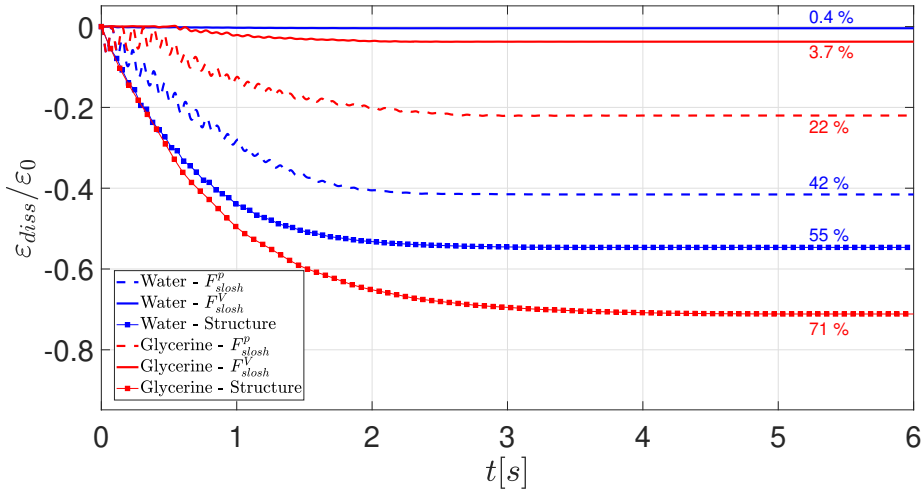


Figure 17. Normalized dissipated energy by the pressure and viscous components of the sloshing force and the structural damping force coming from the linear guide.

4.4. Pressure measurements

In this subsection the possibility of reconstructing the pressure contribution of the sloshing force F^p_{slosh} as a sum of a discrete number of pressure sensors multiplied by their corresponding areas is explored. This computation is important to test the accuracy of the pressure fields computed by the SPH formulation, which will be compared in future work with the measurements given by the experimental pressure sensors, see [55] as an example of these sensors used in sloshing experiments. This fact reveals that the sloshing force is in first approximation caused by a succession of impact pressures. In figure 18 a scheme is shown where thirty four pressure sensors are used, seventeen on the top wall p^u_i and seventeen on the bottom wall p^b_i. The pressure signal is computed by a smoothed interpolation using the particles which are within a smoothing length distance h from the sensor position.

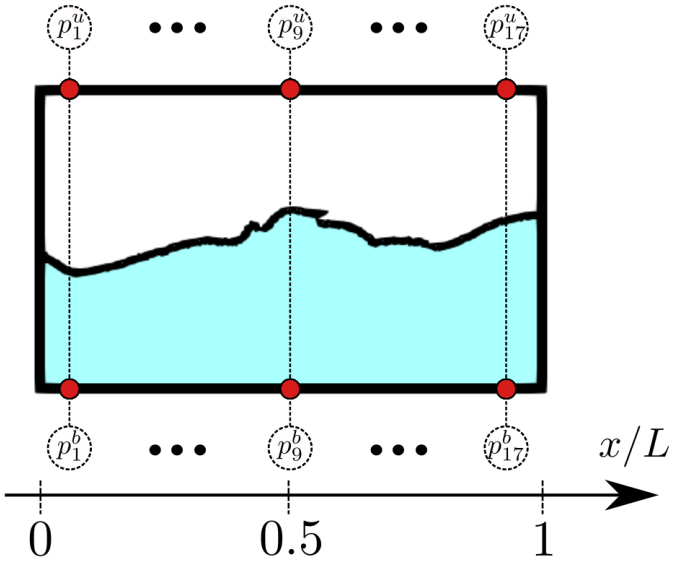


Figure 18. Outline of the pressure sensor distribution when 34 sensors are used.

In figure 19 the top and bottom pressure signals obtained from the middle sensor 9 are plotted as a function of time for both the water and glycerine. The pressure signals presented in this section have been filtered around the natural frequency of the experiment

using a 4th order Butterworth filter. The pressure values have been normalized with the hydrostatic pressure value at the tank bottom $\rho g h_l$ where h_l represents the liquid height. In both glycerine and water cases, the bottom pressures are larger than the upper values largely due to the weight contribution. It was also observed that at the end of the simulation, the sensor value tends towards zero in the upper case and towards the final hydrostatic value for the bottom case. Focusing on the glycerine, it was observed that the upper signal starts close to the first impact $t_{fi} \sim 0.41s$ and finishes quickly, approximately 2 seconds later. This is because the glycerine impacts with the upper wall finishing at $t_{li} \sim 2.46s$. The rest of the upper signal is nearly zero as the glycerine behaves similarly to a standing wave confined at the bottom of the tank, something clearly shown by the bottom signal. Additionally, figure 20 displays the map of the nondimensional pressure maxima extracted from the 34 pressure signals over time and the normalized x/L coordinate. In this figure, it can be observed that the impacts against the upper wall are mostly localized to the middle region of the tank $x/L \in (0.4, 0.6)$ presenting maximum nondimensional pressures of 8.66 and 6.84 for water and glycerine respectively. The pressure impacts against the upper wall for the glycerine are less intense and frequent when compared to the water, which could be related to the fact that the glycerine test case presents less liquid induced dissipation as indicated in table 2. When looking at the pressure maps for the bottom wall presented in figure 20, higher pressure maxima than the ones registered for the upper wall with a maximum pressure of 10.63 and 9.9 for water and glycerine respectively, are observed. The pressure impacts against the bottom wall are larger than the ones registered for the upper wall due to the influence of the liquid's weight. The decay rate of the pressure maxima appears to be higher for the glycerine case indicating that the pressure impacts and the violent regime of the flow last for shorter times. This observation is backed up by figure 7.

The force reconstruction based on the sensors is given by the expression:

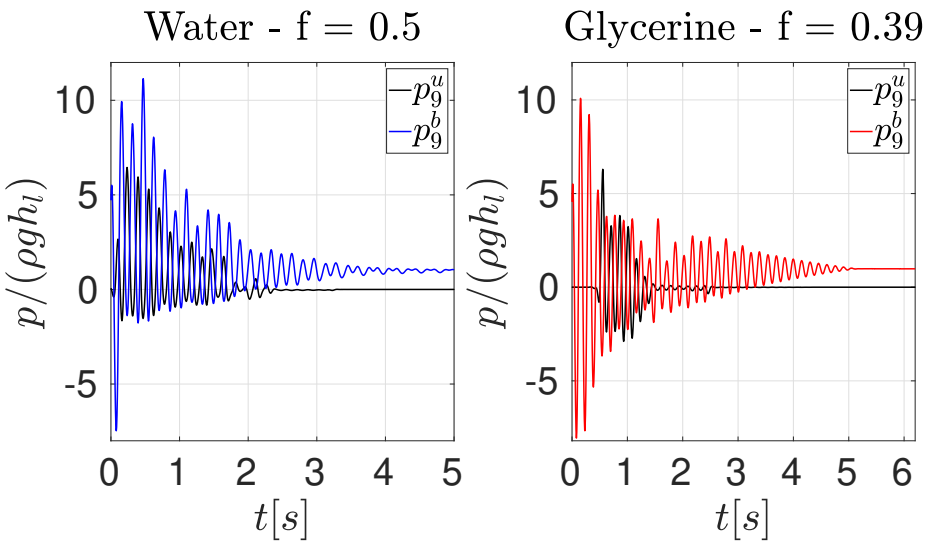


Figure 19. Normalized pressure signals at the top and bottom middle sensors (sensors p_9^b and p_9^u) for the water and glycerine cases.

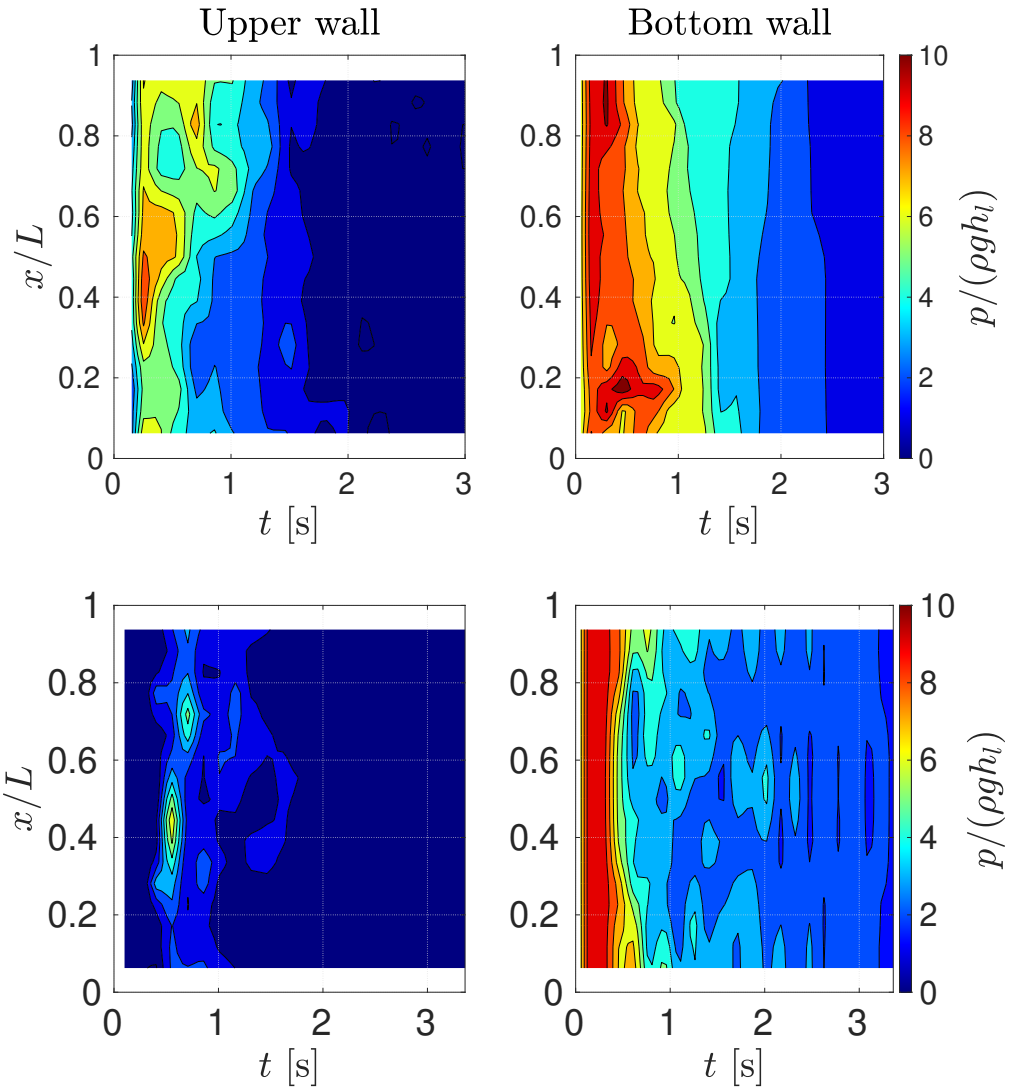


Figure 20. Nondimensional pressure maxima as a function of time and x coordinate for the upper (left) and bottom wall (right) in the water case at $f = 0.5$ (top) and glycerine case at $f = 0.39$ (bottom). The contour plot has been interpolated using 17 pressure signals for each wall.

$$F_{slosh}^{sensors}(n) = \sum_{i}^{n} F_{slosh}^{sensors,i} = \sum_{i}^{n} (p_i^b - p_i^u) A_i = \sum_{i}^{n} (p_i^b - p_i^u) \frac{Lb}{n} \tag{28}$$

where $A_i = \frac{Lb}{n}$ is the area associated to each sensor, b is the tank dimension in the transverse direction and n the number of sensors. The force $F_{slosh}^{sensors}$ computed from the pressure signals multiplied by the corresponding associated wall areas of all sensors are added, see equation (28), and the result is compared to the pressure component of the sloshing force F_{slosh}^{p} computed by the SPH formulation, see equation (20). These two signals are both plotted in figure 21 for the water and glycerine fluids, the agreement between both signals being very good for both cases. It should be clarified that the liquid weight has been removed from both signals and consequently all forces tend to zero at the end of the computation. The differences are caused by numerical error due to the limited number of sensors.

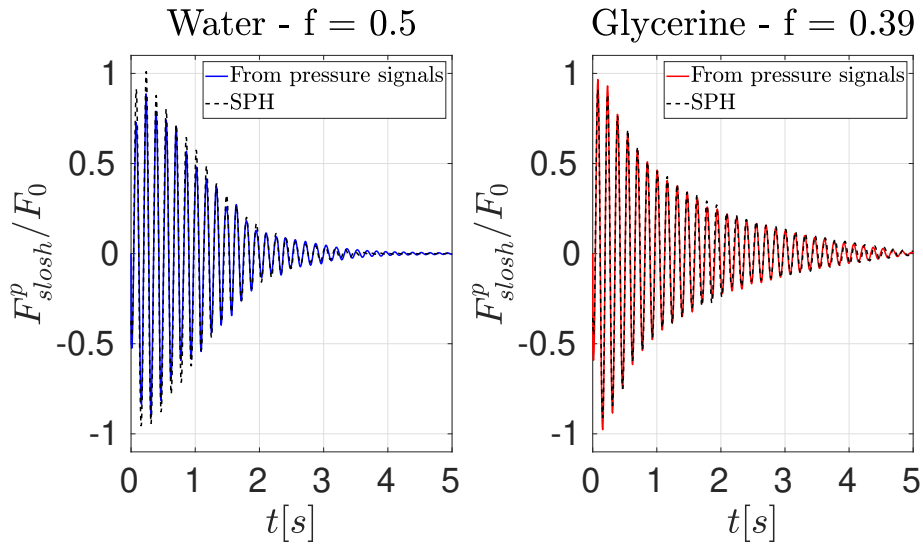


Figure 21. Comparison between the pressure contribution to the SPH sloshing force and the sum of the local force measured by the sensors.

To quantify the effect on the $F^{sensors}_{slosh}$ when the number of sensors is varied, the root mean square error $RMSE$ between the pressure sloshing force computed by expression (28) and the SPH pressure component is defined as:

$$RMSE(n) = \sqrt{\frac{\sum_{j=1}^{N}\left(F^{sensors}_{slosh,j}(n) - F^{p}_{slosh,j}\right)^2}{N}} \tag{29}$$

where N is the number of time steps recorded. Figure 22 shows the evolution of the relative difference between the $RMSE$ values using n sensors with respect to the case where only two sensors are used. It can be observed that the water tends towards a constant value $\sim -39\%$ meaning that when using more than 30 sensors the level of approximation is reasonable. In the case of the glycerine, the convergence is not so evident, and even when using 34 sensors the force still has some small variations.

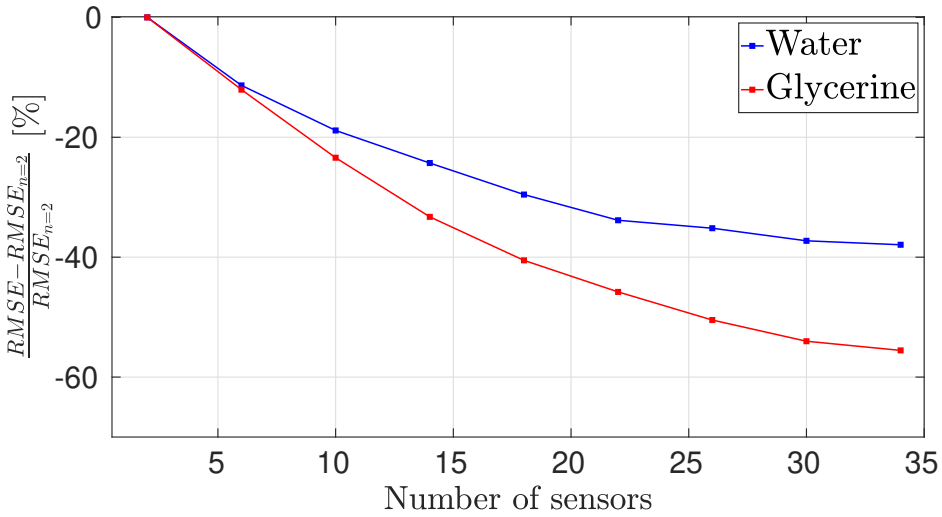


Figure 22. Relative variation of the root mean square of the sloshing force reconstruction error when the number of pressure sensors is varied.

5. Conclusions

In this work, an experimental methodology and a computational methodology are presented in order to study a simplified version of the sloshing phenomenon that takes place inside aircraft fuel tanks. The single degree of freedom numerical model based on a fluid-structure interaction coupling contains the most relevant non linear phenomena in terms of fluid-wall impacts and free surface breaking that dominate the most real-world versions of this problem.

In order to test the influence of the viscosity on this kind of flow, two fluids have been tested which are very different in terms of viscosity, but similar in terms of density. A clear conclusion is that there is a critical Reynolds number $Re_c \sim O(10^4)$ where, depending on whether the flow is below or above this critical number, important differences in terms of the characteristics of the sloshing regimes, free surface fragmentation and relative kinetic energy distribution are observed. It was also concluded that the less viscous fluid is able to obtain a larger damping in terms of tank movement, something that might challenge our intuition.

The comparison between the experiments and numerical simulation has been performed both on the tank kinematics and on the fluid magnitudes. In regard to the fluid study, some integral fluid magnitudes have been compared, including the sloshing force, liquid center of mass position and liquid kinetic energy; but also local measurements such as free surface location and the jet velocities were examined. There are three well separated stages during the flow evolution for both fluids studied, the first and the last being less chaotic and particularly appropriate for numerical validations. The 2D numerical model is able to compute either the evolution of the impelling jets at the initial stage or the kinetic energy of the remaining standing wave in the last part the flow evolution. An important conclusion is that despite some differences appearing when local values such as free surface position or jet velocities are compared, the numerical model approximates the results very well in terms of global magnitudes such as tank acceleration, sloshing force and liquid center of mass.

A direct conclusion coming from the application of the momentum conservation to these apparently complex flows is that there is a direct relation between the vertical component of the sloshing force and the vertical position of the liquid center of mass. Showing in this work that this relation is satisfied by both fluids.

Other important conclusions of this article are based on the study of the intrinsic properties of the sloshing force. First is that a simplified version of the the sloshing force can be modeled as a shifted cosine function with decaying amplitude. The projection of the force on the tank velocity and acceleration confirms that one of the key magnitudes of the sloshing phenomenon is the shift angle between the force and the tank position maxima. Second, the sloshing force can be interpreted as a sum of the inertial force and a second part that depends on the relative movement of the liquid inside the tank. As a result, the dissipative part of the sloshing force has been related to the product of the liquid mass times the center of mass of the liquid. Third, the viscous and pressure components of the sloshing force and the derived dissipated energy have been compared for both liquids and the relevance of the viscous part is not negligible when high viscosity fluids such as glycerine are used. Finally the pressure fields computed with the SPH methodology on the horizontal walls of the tank have been discretized using several pressure sensors on each wall. It was proven that with the pressure field recorded, a minimum number of sensors are necessary to obtain an accurate sloshing force reconstruction, this number varying depending on the fluid contained within. The conclusions presented in this double perspective study are especially useful for the design of a reduced order model for the sloshing force, where the behaviour of this complex dynamical system can be approximated by simpler differential equations with lower computational demand.

Author Contributions: Conceptualization, J. Martínez-Carrascal and L. González; methodology, J.Martínez-Carrascal and L. González; software, J.Cálderón-Sanchez; validation, J.Cálderón-Sanchez;

investigation,J. Martínez-Carrascal, J.Cálderón-Sánchez and L. González; resources, J. Martínez-Carrascal, J.Cálderón-Sánchez and L. González; data curation, J.Martínez-Carrascal; writing—original draft preparation, J. Martínez-Carrascal, J.Cálderón-Sánchez and L. González; visualization, X.X.; supervision, L. González; project administration, L. González; funding acquisition, L. González. All authors have read and agreed to the published version of the manuscript.", please turn to the CRediT taxonomy for the term explanation. Authorship must be limited to those who have contributed substantially to the work reported.

Funding: This research was funded by the SLOWD project, which has received funding from the European Union's Horizon 2020 research and innovation programme under grant agreement No. 815044.

Acknowledgments: In this section you can acknowledge any support given which is not covered by the author contribution or funding sections. This may include administrative and technical support, or donations in kind (e.g., materials used for experiments).

Conflicts of Interest: The authors declare no conflict of interest.

References

1. The European Commission. *SLOWD*; 2019.
2. Gambioli, F.; Chamos, A.; Jones, S.; Guthrie, P.; Webb, J.; Levenhagen, J.; Behruzi, P.; Mastroddi, F.; Malan, A.; Longshaw, S.; et al. Sloshing Wing Dynamics–Project Overview. *Proceedings of 8th Transport Research Arena TRA 2020, April 27-30, 2020, Helsinki, Finland* **2020**.
3. Lamb, H. *Hydrodynamics*; Cambridge University Press, 1932.
4. Faltinsen, O.M.; Timokha, A.N. *Sloshing*; Cambridge University Press, 2009.
5. Ibrahim, R.A. *Liquid Sloshing Dynamics : Theory And Applications*; Cambridge University Press, 2005.
6. Gambioli, F.; Usach, R.A.; Kirby, J.; Wilson, T.; Behruzi, P. Experimental evaluation of fuel sloshing effects on wing dynamics. *International Forum on Aeroelasticity and Structural Dynamics* **2019**.
7. Titurus, B.; Cooper, J.E.; Saltari, F.; Mastroddi, F.; Gambioli, F. Analysis of a Sloshing Beam Experiment. In Proceedings of the International Forum on Aeroelasticity and Structural Dynamics. Savannah, Georgia, USA, paper, 2019, Vol. 139.
8. Martinez-Carrascal, J.; Gonzalez-Gutierrez, L.M. Experimental study of the liquid damping effects on a SDOF vertical sloshing tank. *Journal of Fluids and Structures* **2021**, *100*, 103172. doi:https://doi.org/10.1016/j.jfluidstructs.2020.103172.
9. Constantin, L.; De Courcy, J.; Titurus, B.; Rendall, T.C.; Cooper, J.E. Analysis of damping from vertical sloshing in a SDOF system. *Mechanical Systems and Signal Processing* **2021**, *152*, 107452. doi:https://doi.org/10.1016/j.ymssp.2020.107452.
10. Constantin, L.; De Courcy, J.; Titurus, B.; Rendall, T.C.; Cooper, J.E. Sloshing induced damping across Froude numbers in a harmonically vertically excited system. *Journal of Sound and Vibration* **2021**, *510*, 116302.
11. Saltari, F.; Pizzoli, M.; Coppotelli, G.; Gambioli, F.; Cooper, J.E.; Mastroddi, F. Experimental characterisation of sloshing tank dissipative behaviour in vertical harmonic excitation. *Journal of Fluids and Structures* **2022**, *109*, 103478.
12. Coppotelli, G.; Franceschini, G. Experimental Investigation on the damping mechanism in sloshing structures. In Proceedings of the AIAA Scitech 2021 Forum, 2021, p. 1388.
13. F.Gambioli.; Malan, A. Fuel Loads in Large Civil Airplanes. In Proceedings of the International Forum Aeroelasticity and Sructural Dynamics IFASD, 2017, pp. 161–174.
14. Gimenez, J.M.; González, L.M. An extended validation of the last generation of particle finite element method for free surface flows. *J. Comput. Phys.* **2015**, *284*, 186–205. doi:https://doi.org/10.1016/j.jcp.2014.12.025.
15. Monaghan, J.J. Simulating free surface flows with SPH. *J. Comput. Phys.* **1994**, *110*, 399–406. doi:https://doi.org/10.1006/jcph.1994.1034.
16. Delorme, L.; Colagrossi, A.; Souto-Iglesias, A.; Zamora-Rodríguez, R.; Botía-Vera, E. A set of canonical problems in sloshing, Part I: Pressure field in forced roll-comparison between experimental results and SPH. *Ocean Engineering* **2009**, *36*, 168–178. doi:https://doi.org/10.1016/j.oceaneng.2008.09.014.
17. Gotoh, H.; Khayyer, A.; Ikari, H.; Arikawa, T.; Shimosako, K. On enhancement of Incompressible SPH method for simulation of violent sloshing flows. *Applied Ocean Research* **2014**, *46*, 104–115. doi:https://doi.org/10.1016/j.apor.2014.02.005.
18. Stasch, J.; Avci, B.; Wriggers, P. Numerical simulation of fluid-structure interaction problems by a coupled SPH-FEM approach. *PAMM* **2016**, *16*, 491–492. doi:https://doi.org/10.1002/pamm.201610234.
19. Sun, L.; Fujino, Y. A semi-analytical model for tuned liquid damper (TLD) with wave breaking. *J. Fluids and Structures* **1994**, *8*, 471–488. doi:https://doi.org/10.1006/jfls.1994.1023.
20. Green, M.D.; Peiró, J. Long duration SPH simulations of sloshing in tanks with a low fill ratio and high stretching. *Computers & Fluids* **2018**, *174*, 179–199. doi:https://doi.org/10.1016/j.compfluid.2018.07.006.
21. Marrone, S.; Colagrossi, A.; Gambioli, F.; González-Gutiérrez, L. Numerical study on the dissipation mechanisms in sloshing flows induced by violent and high-frequency accelerations. I. Theoretical formulation and numerical investigation. *Phys. Rev. Fluids* **2021**, *6*, 114801. doi:10.1103/PhysRevFluids.6.114801.

22. Marrone, S.; Colagrossi, A.; Calderon-Sanchez, J.; Martinez-Carrascal, J. Numerical study on the dissipation mechanisms in sloshing flows induced by violent and high-frequency accelerations. II. Comparison against experimental data. *Phys. Rev. Fluids* **2021**, *6*, 114802. doi:10.1103/PhysRevFluids.6.114802.
23. Martinez-Carrascal, J.; Calderon-Sanchez, J.; González-Gutiérrez, L.M.; de Andrea González, A. Extended computation of the viscous Rayleigh-Taylor instability in a horizontally confined flow. *Phys. Rev. E* **2021**, *103*, 053114. doi:10.1103/PhysRevE.103.053114.
24. Shadloo, M.; Zainali, A.; Yildiz, M. Simulation of single mode Rayleigh–Taylor instability by SPH method. *Computational Mechanics* **2013**, *51*, 699–715. doi:https://doi.org/10.1007/s00466-012-0746-2.
25. Rahmat, A.; Tofighi, N.; Shadloo, M.; Yildiz, M. Numerical simulation of wall bounded and electrically excited Rayleigh–Taylor instability using incompressible smoothed particle hydrodynamics. *Colloids and Surfaces A: Physicochem. Eng. Aspects* **2014**, *460*, 60–70. doi:https://doi.org/10.1016/j.colsurfa.2014.02.044.
26. Calderon-Sanchez, J.; Martinez-Carrascal J., Gonzalez-Gutierrez, L.M.; A., C. A global analysis of a coupled violent vertical sloshing problem using an SPH methodology. *Engineering Applications of Computational Fluid Mechanics* **2021**, *15*, 865–888. doi:https://doi.org/10.1080/19942060.2021.1921849.
27. Martinez-Carrascal, J.; Gonzalez-Gutierrez, L.M. On the experimental scaling and power dissipation of violent sloshing flows. *Journal of Fluids and Structures* **2022**, *under revision*.
28. Cooper, J.E.; Emmet, P.R.; R., W.J. Envelope function - A tool for analyzing flutter data. *International Forum on Aeroelasticity and Structural Dynamics* **2017**.
29. Wright, M.D.; Gambioli, F.; Malan, A.G. CFD based non-dimensional characterization of energy dissipation due to verticle slosh. *Applied Sciences* **2021**, *11*, 10401. doi:https://doi.org/10.3390/app112110401.
30. Antuono, M.; Colagrossi, A.; Marrone, S.; Molteni, D. Free-surface flows solved by means of SPH schemes with numerical diffusive terms. *Computer Physics Communications* **2010**, *181*, 532–549. doi:https://doi.org/10.1016/j.cpc.2009.11.002.
31. Marrone, S.; Antuono, M.; Colagrossi, A.; Colicchio, G.; Le Touzé, D.; Graziani, G. δ-SPH model for simulating violent impact flows. *Computer Methods in Applied Mechanics and Engineering* **2011**, *200*, 1526–1542. doi:https://doi.org/10.1016/j.cma.2010.12.016.
32. Randles, P.; Libersky, L. Smoothed Particle Hydrodynamics: some recent improvements and applications. *Computer methods in applied mechanics and engineering* **1996**, *39*, 375–408. doi:https://doi.org/10.1016/S0045-7825(96)01090-0.
33. Cercos-Pita, J.L. AQUAgpusph, a new free 3D SPH solver accelerated with OpenCL. *Computer Physics Communications* **2015**, *192*, 295–312. doi:https://doi.org/10.1016/j.cpc.2015.01.026.
34. Calderon-Sanchez, J.; Cercos-Pita, J.; Duque, D. A geometric formulation of the Shepard renormalization factor. *Computers & Fluids* **2019**, *183*, 16 – 27. doi:https://doi.org/10.1016/j.compfluid.2019.02.020.
35. Serván-Camas, B.; Cercós-Pita, J.; Colom-Cobb, J.; García-Espinosa, J.; Souto-Iglesias, A. Time domain simulation of coupled sloshing–seakeeping problems by SPH–FEM coupling. *Ocean Engineering* **2016**, *123*, 383–396. doi:https://doi.org/10.1016/j.oceaneng.2016.0
36. Bulian, G.; Cercos-Pita, J.L. Co-simulation of ship motions and sloshing in tanks. *Ocean Engineering* **2018**, *152*, 353–376. doi:https://doi.org/10.1016/j.oceaneng.2018.01.028.
37. Monaghan, J.J. SPH without a tensile instability. *Journal of computational physics* **2000**, *159*, 290–311. doi:https://doi.org/10.1006/jcph.2000.64
38. Sun, P.; Colagrossi, A.; Marrone, S.; Antuono, M.; Zhang, A. Multi-resolution Delta-plus-SPH with tensile instability control: Towards high Reynolds number flows. *Computer Physics Communications* **2018**, *224*, 63–80. doi:https://doi.org/10.1016/j.cpc.2017.11.016.
39. Lind, S.J.; Xu, R.; Stansby, P.K.; Rogers, B.D. Incompressible smoothed particle hydrodynamics for free-surface flows: A generalised diffusion-based algorithm for stability and validations for impulsive flows and propagating waves. *Journal of Computational Physics* **2012**, *231*, 1499–1523. doi:https://doi.org/10.1016/j.jcp.2011.10.027.
40. Sun, P.; Colagrossi, A.; Marrone, S.; Antuono, M.; Zhang, A.M. A consistent approach to particle shifting in the δ-Plus-SPH model. *Computer Methods in Applied Mechanics and Engineering* **2019**, *348*, 912–934. doi:https://doi.org/10.1016/j.cma.2019.01.045.
41. Antuono, M.; Sun, P.; Marrone, S.; Colagrossi, A. The δ-ALE-SPH model: An arbitrary Lagrangian-Eulerian framework for the δ-SPH model with particle shifting technique. *Computers & Fluids* **2021**, *216*, 104806. doi:https://doi.org/10.1016/j.compfluid.2020.104806.
42. Marrone, S.; Colagrossi, A.; Le Touzé, D.; Graziani, G. Fast free-surface detection and level-set function definition in SPH solvers. *Journal of Computational Physics* **2010**, *229*, 3652–3663. doi:https://doi.org/10.1016/j.jcp.2010.01.019.
43. Morris, J.P. Simulating surface tension with smoothed particle hydrodynamics. *International journal for numerical methods in fluids* **2000**, *33*, 333–353. doi:https://doi.org/10.1002/1097-0363(20000615)33:3<333::AID-FLD11>3.0.CO;2-7.
44. Chiron, L.; De Leffe, M.; Oger, G.; Le Touzé, D. Fast and accurate SPH modelling of 3-D complex wall boundaries in viscous and non viscous flows. *Computer Physics Communications* **2019**, *234*, 93–111. doi:https://doi.org/10.1016/j.cpc.2018.08.001.
45. Hernandez-Hernandez, D.; Larkin, T.; Chouw, N.; Banide, Y. Experimental findings of the suppression of rotary sloshing on the dynamic response of a liquid storage tank. *Journal of Fluids and Structures* **2020**, *96*, 103007. doi:https://doi.org/10.1016/j.jfluidstructs.2020.1030
46. Iguchi, D.; Ueda, Y.; Ohmi, T.; Iguchi, M. Self-Induced Rotary Sloshing Caused by an Upward Off-Centered Jet in a Cylindrical Container. *Materials Transactions - MATER TRANS* **2008**, *49*, 1874–1879. doi:10.2320/matertrans.MRA2008038.
47. González-Gutiérrez, L.M.; de Andrea González, A. Numerical computation of the Rayleigh-Taylor instability for a viscous fluid with regularized interface properties. *Phys. Rev. E* **2019**, *100*, 013101. doi:10.1103/PhysRevE.100.013101.
48. Le Clainche, S.; Izbassarov, D.; Rosti, M.; Brandt, L.; Tammisola, O. Coherent structures in the turbulent channel flow of an elastoviscoplastic fluid. *Journal of Fluid Mechanics* **2020**, *888*, A5. doi:10.1017/jfm.2020.31.
49. Le Clainche, S.; Vega, J.M.; Soria, J. Higher order dynamic mode decomposition of noisy experimental data: The flow structure of a zero-net-mass-flux jet. *Experimental Thermal and Fluid Science* **2017**, *88*, 336–353. doi:https://doi.org/10.1016/j.expthermflusci.2017.06.011.

50. Pagliaroli, T.; Gambioli, F.; Saltari, F.; Cooper, J. Proper orthogonal decomposition, dynamic mode decomposition, wavelet and cross wavelet analysis of a sloshing flow. *Journal of Fluids and Structures* **2022**, *112*, 103603. doi:https://doi.org/10.1016/j.jfluidstructs.2022.10
51. Abramson, H. *The dynamic behaviour of liquids in moving containers*; NASA SP-106, 1966.
52. Colagrossi, A.; Souto-Iglesias, A.; Antuono, M.; Marrone, S. Smoothed-particle-hydrodynamics modeling of dissipation mechanisms in gravity waves. *Phys. Rev. E* **2013**, *87*, 023302. doi:10.1103/PhysRevE.87.023302.
53. Saltari, F.; Pizzoli, M.; Gambioli, F.; Jetzschmann, C.; Mastroddi, F. Sloshing reduced-order model based on neural networks for aeroelastic analyses. *Aerospace Science and Technology* **2022**, p. 107708. doi:https://doi.org/10.1016/j.ast.2022.107708.
54. Pizzoli, M.; Saltari, F.; Mastroddi, F.; Martinez-Carrascal, J.; González-Gutiérrez, L.M. Nonlinear reduced-order model for vertical sloshing by employing neural networks. *Nonlinear Dynamics* **2022**, *107*, 1469–1478. doi:https://doi.org/10.1007/s11071-021-06668-w.
55. Lobovský, L.; Botia-Vera, E.; Castellana, F.; Mas-Soler, J.; Souto-Iglesias, A. Experimental investigation of dynamic pressure loads during dam break. *Journal of Fluids and Structures* **2014**, *48*, 407–434. doi:https://doi.org/10.1016/j.jfluidstructs.2014.03.009.

Publication 6 (P6)

Javier Calderon-Sanchez, **Jon Martinez-Carrascal** and Leo M. González (2022). Computational scaling of SPH simulations for violent sloshing problems in aircraft fuel tanks. Acta Mechanica Sinica, 39 722051, 2023. DOI: https://doi.org/10.1007/s10409-022-22051-x. 0 citations. JCR(2021): 2.910, Engineering, Mechanical (Q2) and Mechanics (Q2).

Computational scaling of SPH simulations for violent sloshing problems in aircraft fuel tanks

Calderon-Sanchez Javier[1*], Martinez-Carrascal Jon[1] and González Leo Miguel[1]

[1*]CEHINAV Model Basin, ETSI Navales, Universidad Politécnica de Madrid, Avda Memoria n4, Madrid, 28040, Madrid, Spain.

*Corresponding author(s). E-mail(s): javier.calderon@upm.es;

Abstract

The wings of large civilian aircraft are designed to withstand a variety of loads whose causes range from atmospheric gusts to turbulence to landing impacts. Aircraft wings are essential structures that demand further research. One of the primary methods used for improving wing design is analysis of the damping effects that sloshing induces on the dynamics of flexible wing-like structures carrying liquids. This will be attained through the development of experimental set-ups that will help in building up numerical models that are used to reproduce the physics involved. Hence, the aim of this work is to analyze the effect of sloshing in reducing the design loads on aircraft structures using the numerical method Smoothed Particle Hydrodynamics (SPH) as the main numerical tool. One of the key considerations in this research is the demand for scaled experiments, making it a necessary step in assessing whether computational tools are able to approximate the registered measurements for different scales accurately. To this end, a numerical model of a vertically oscillating tank built as a fully coupled fluid-structure interaction problem is developed. The structure is modelled through a mass-spring-damper system, and for the inner fluid the $\boldsymbol{\delta}$-SPH methodology is used. In particular, two open questions are studied: the first one is to what extent gravity has an influence on the damping and energy dissipation phenomena when the initial acceleration of the tank is ten times the standard gravity value. The second seeks to confirm that the SPH equations correctly reproduce the scaling laws when the problem parameters are scaled according to the dimensional analysis.

Keywords: SPH, sloshing, gravity, computational scaling

1 Introduction

Challenges in the aerospace industry, and especially those linked to the increase in passenger aircraft size in the near future, demand further research of associated systems that might influence aircraft behaviour during operation. In particular, there is an interest in optimizing the wings of such means of transportation, which are designed to withstand the loads generated from different sources such as atmospheric gusts, turbulence or landing impacts. This goal is hoped to be achieved through the investigation of the damping effect of sloshing on the dynamics of such wings in which the fuel is normally stored, through optimization of their inner configuration and analysis of liquid filling level.

Controlled sloshing has been proved to be effective in dampening movements of analogous structures, and different examples can be found in different industries such as civil engineering, where Tuned Liquid Dampers (TLDs) are designed to mitigate skyscraper's motions when earthquakes occur (Bulian et al, 2009; Tait, 2008) or in the naval industry, where anti roll tanks have been widely employed to mitigate the rolling motion of ships (Souto-Iglesias et al, 2004, 2006). These ideas have recently been studied within the aerospace industry for propellant rocket tanks, as has been noted in Arndt and Dreyer (2008) or in preliminary studies on sloshing on aircraft fuel tanks (Gambioli, 2009).

The main objective of the present work is to extend the knowledge on damping effects due to sloshing on aircraft wing tanks when they undergo initial tank accelerations of the order of $a_0 \approx 10\,g$, i.e. one order of magnitude larger than gravity on Earth, by analysing the influence of the gravity term in the Navier-Stokes equations.

In a general fluid mechanics context the Froude number represents the ratio between the gravitational forces and the inertial forces. This number appears naturally when the Navier-Stokes equations are expressed in non-dimensional form. In violent sloshing problems, we can usually generalize the definitions of Froude number as being inertial Froude number ($Fr_a = \frac{U}{\sqrt{a_0\,H}}$) and gravity Froude number ($Fr_g = \frac{U}{\sqrt{g\,H}}$) (Tyvand and Miloh, 2012). According to these definitions, U and H represent the characteristic velocity and length of the problem respectively. In this context, H will be considered to be the tank height and U the maximum tank velocity.

When the wing is deformed and accelerated by, for example, an external atmospheric gust, a violent sloshing phenomenon starts inside the fuel tanks. Under these circumstances, Fr_a is much larger than Fr_g, up until the moment when the liquid action is of the order of the liquid weight, i.e. $Fr_a \approx Fr_g$. At that moment, the sloshing dynamics changes, and damping trends show a different regime, as reported by Constantin et al (2020). Since a parametric study of gravity is to be performed in the present work, these changes are expected in the acceleration envelopes of the numerical experiments.

Additionally, we aim to confirm that the scale laws work properly when the geometry is increased in size for the SPH formulation that is used to reproduce

sloshing. Previous SPH approaches of a similar problem have been carried out in Bouscasse et al (2014a,b), where a dynamical system consisting of a periodically oscillating tank filled with different fluids is studied. A non-linear model for motion was used, and the authors focused on the understanding of energy dissipation mechanisms. Similarly, in this work the SPH tool will be complemented by a set of numerical models that reproduce tank motion. The way the tank moves is affected at the same time by the SPH computed sloshing loads. The SPH code used has been previously validated with experimental tests carried out for this problem by Calderon-Sanchez et al (2021). These tests consist of a tank filled partially with water and linked to a structure by a set of springs that allows purely vertical oscillation. The tank is displaced from its equilibrium position, fixed by the action of solenoids. When it is released, the accelerations at different points are recorded. Also the liquid motion is visually recorded with high speed cameras in order to understand the liquid sloshing happening inside the tank.

SPH method has been chosen as the numerical tool to solve this problem. This method has shown reliability previously when used in the context of sloshing problems, where highly fragmented, non linear breaking flow is expected. In SPH, that is a fully Lagrangian method, free surface can be tracked automatically, conversely to alternative Eulerian methods, where free surface definition is a complex matter that might derive into numerical diffusion. Additionally, SPH has demonstrated good capabilities when dealing with impact problems, as it has been reported from several references, such as Souto-Iglesias et al (2006); Marrone et al (2011); Liu et al (2018); Sun et al (2019).

In this work the particular SPH numerical model that has been used to solve the fully coupled fluid-structure interaction problem is presented. In particular, a WC-SPH single phase model is used, where fluid phase is solved by means of the δ-SPH model Marrone et al (2011) and boundary integrals methodology, as implemented by Calderon-Sanchez et al (2019) is used to deal with solid boundaries. The motion is modeled through a forced damped mass spring system and the corresponding differential equation is solved numerically. The emphasis is made on the evaluation of gravity influence and the understanding of the scaling laws.

The paper is structured as follows: first, the outline of the problem is described, second a preliminary perspective of the overall dimensional analysis is presented. Third, the δ-SPH model and the numerical models used for the tank are introduced. Fourth, the results for the two questions previously raised regarding the influence of gravity and the scaling laws are presented. Finally, conclusions are drawn and directions for future work are established.

2 Problem description

As explained in the introduction of the paper, these tanks are placed inside the aircraft wings where the tank movement is mainly caused by the first oscillation mode of the wing. The accelerations corresponding to this mode are dominated

by the vertical direction, approximately $\sim 10g$, which is clearly larger than the other accelerations that the tank could encounter. Consequently, a single degree of freedom model is an accepted approach, and it has lately been very used, as it is reported by Marrone et al (2021b,a); Martinez-Carrascal and Gonzalez-Gutierrez (2021); Constantin et al (2020); Calderon-Sanchez et al (2021).

As a result, the problem can be simplified to a partially filled vertically oscillating tank attached to a spring-damper element. To start the sloshing phenomenon, the springs are deformed and the tank is separated from its equilibrium position and then is released. The tank then oscillates during a few seconds and finally reaches the initial equilibrium position again. For this problem, we define H as the height of the tank, d is the width, L represents the length and h_f is the liquid height or filling level. The corresponding and necessary liquid properties are density ρ and viscosity μ. We denote the surface tension with σ, and θ is the initial contact angle. Figure 1 **a)** shows a schematic of the experimental setup that can be used as a reference for the problem studied in the numerical context. The corresponding physical quantities are illustrated in 1 **b)**. Regarding the structural components, we note m_s, c and K as the structural mass, stiffness and damping coefficients respectively. If m_l is the liquid mass inside of the tank and m the total mass of the system then $m = m_s + m_l$. The one degree of freedom system is deflected with an initial displacement y_0 and then starts oscillating when the release mechanism is activated.

The evolution of the flow was recorded in the experiments conducted in Martinez-Carrascal and Gonzalez-Gutierrez (2021) and it is displayed in Figure 2. It can be seen that the liquid, initially at rest, is accelerated upwards and the flat free surface starts to deform at a time $t = 0.068$ s. The meniscus travels in the horizontal direction and forms Rayleigh-Taylor instabilities that grow and develop into two jets that impact the upper wall of the tank ($t = 0.09$ s). After the first impact, the free surface is fragmented and a violent and turbulent regime develops with bubble formation and many liquid to liquid and liquid to tank impacts. Finally, for the last low amplitude cycles of the tank motion, the free surface definition is recovered and a standing wave-like regime forms with fewer and less intense liquid impacts.

3 Dimensional analysis

Applying the Buckingham Π theorem to the power dissipated by the liquid action, one can stablish dimensional relationships between the variation of the sloshing induced damping ratio $\Delta\xi$ and the most relevant non-dimensional numbers, as explained in Wright et al (2021). The damping ratio is calculated following the procedure shown in Cooper et al (2017) as the slope of the logarithm of the tank acceleration envelope. To perform the dimensional analysis,

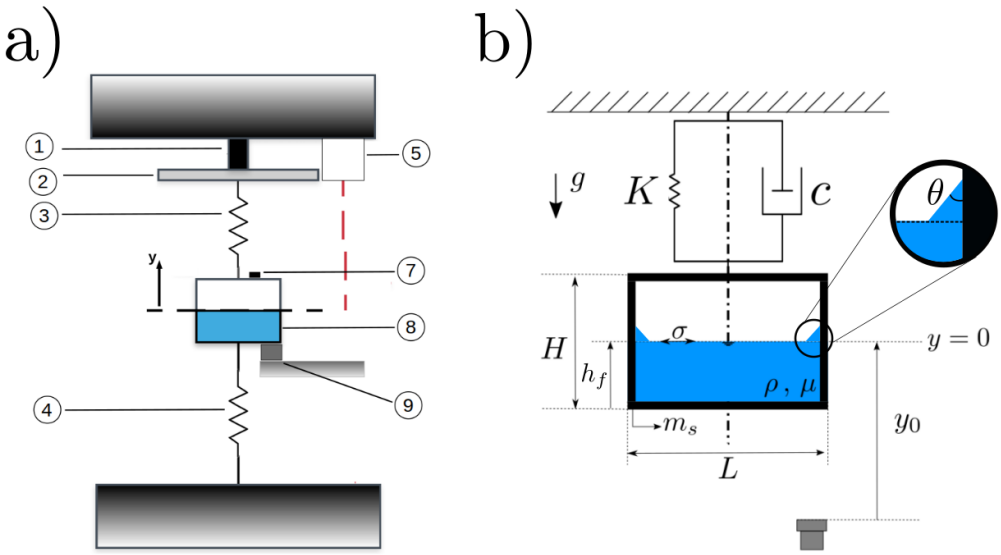


Fig. 1 **a)** Scheme of the experimental setup tested in Martinez-Carrascal and Gonzalez-Gutierrez (2021). (1) Load cell, (2) Metallic plate (3) Upper set of springs, (4) Lower set of springs, (5) Laser sensor, (6) Mechanical guide, (7) Accelerometer, (8) Methacrylate tank and C-shaped wooden structure, (9) Pair of solenoids acting as release mechanism. **b)** Dimensional parameters of the vertical sloshing problem.

we use H, $m_l = \rho H^3$ and $1/\omega = \sqrt{m/K}$ as length, mass and time dimensional units respectively, and we can express the variation of the damping as a function of the following non-dimensional numbers:

$$\Delta\xi = \mathcal{F}\left(Re, f, Fr_g, \frac{L}{H}, \frac{y_0}{H}, r, We, \theta\right) \tag{1}$$

where Re is the Reynolds number, $f = h_f/H$ is the filling level, taking as reference velocity $U = \omega H$ we have that $Fr_g = \sqrt{\frac{\omega^2 H}{g}}$ is the Froude number defined in terms of gravity, L/H is the tank aspect ratio, y_0/H is the non-dimensional initial displacement, $r = m_l/m_s$ is the mass ratio, $We = \frac{\rho\omega^2 H^3}{\sigma}$ is the Weber number and θ the contact angle.

To define a perfect geometrical scaling between the two scales we denote them with the sub-index P(prototype) and M(model) respectively, such that $H_P/H_M = L_P/L_M = y_{0P}/y_{0M} = 1/\lambda$, where $\lambda < 1$ is the scale factor. As an example, when the model is four times smaller than the prototype, the corresponding notation will be $1:4$, which is equivalent to a scaling factor $\lambda = 1/4$. From this relation, the relevant experimental parameters can be scaled. For the scaling process, we assume that both elongation y_0/H and Froude number Fr_g remain constant. The relevant quantities are related at different scales according to the following expressions:

$$\frac{t_M}{t_P} = \sqrt{\lambda} \tag{2}$$

$$\frac{\mu_P}{\mu_M} = \lambda^{3/2} \tag{3}$$

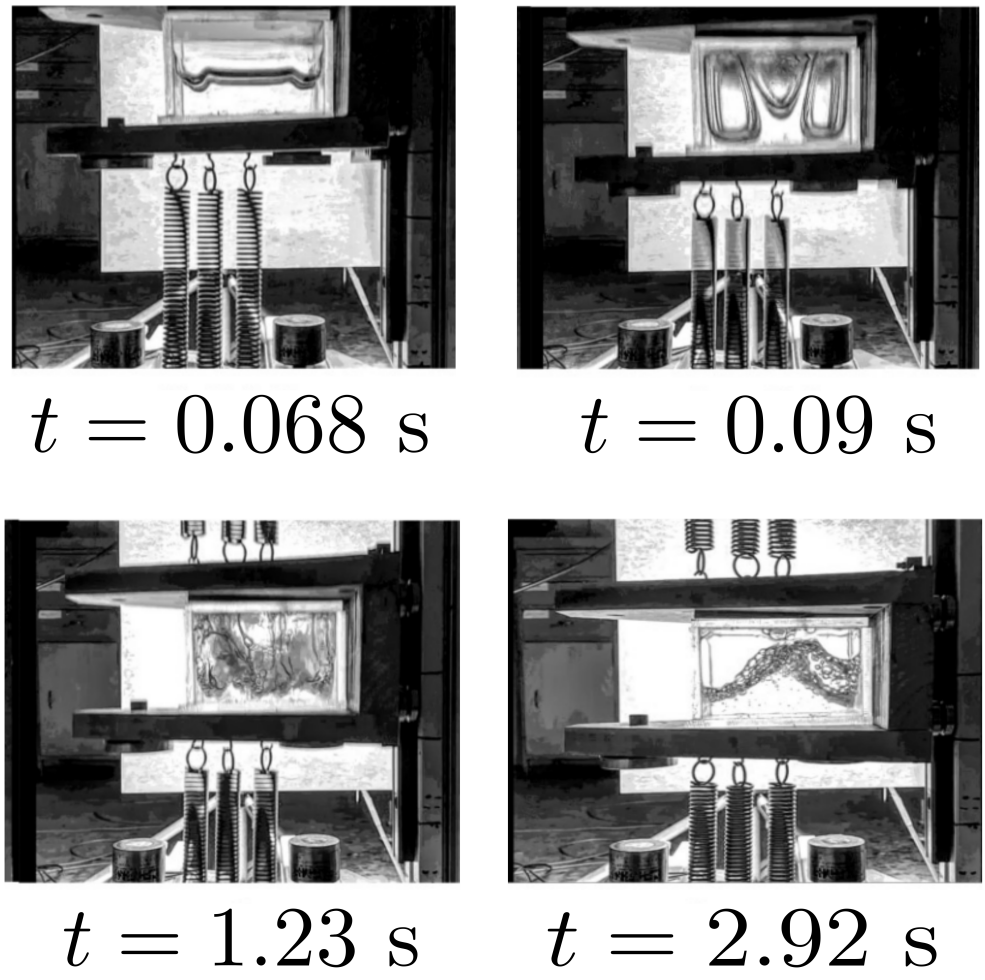


Fig. 2 Evolution of the vertical sloshing experimental test presented in Martinez-Carrascal and Gonzalez-Gutierrez (2021), at four characteristic time instants, for a water test with a 50% filling level and 10g of maximum acceleration.

$$\frac{m_P}{m_M} = \lambda^3 \tag{4}$$

$$\frac{K_P}{K_M} = \lambda^2 \tag{5}$$

$$\frac{c_P}{c_M} = \lambda^{5/2} \tag{6}$$

Additionally, expressions for the relevant scaling laws for the resulting variables – force (F), work (W) and power ($\dot{W}$) – are respectively given by:

$$\frac{F_M}{F_P} = \lambda^3, \qquad \frac{W_M}{W_P} = \lambda^4, \qquad \frac{\dot{W}_M}{\dot{W}_P} = \lambda^{\frac{5}{2}} \tag{7}$$

In Calderon-Sanchez et al (2021) a complete non-dimensional analysis of the problem in terms of extra damping added by the fluid has been performed, and the dependency on the most relevant non-dimensional numbers has been

monitored. As viscous dissipation is involved, one of the non-dimensional numbers studied is the Reynolds number. It was observed that only when the Reynolds number is below a critical threshold Re_c, the extra damping barely changes. This critical Reynolds number Re_c is at least two orders of magnitude lower than the turbulent ones considered in our study. As the scales tested are changed in the same order of magnitude, little extra-damping variations are expected due to scale changes. For the water case studied in this paper, very small scales would be required in order to be close to that critical Reynolds number.

4 Numerical model

4.1 SPH model

The Navier-Stokes equations for a weakly-compressible and barotropic fluid can be written in Lagrangian form as:

$$\begin{cases} \dfrac{D\rho}{Dt} = -\rho\nabla\cdot\boldsymbol{u}, \quad p = f(\rho) \\ \dfrac{D\boldsymbol{u}}{Dt} = \dfrac{1}{\rho}\nabla p + \dfrac{1}{\rho}\nabla\cdot\mathbb{V} + \boldsymbol{g} + \Omega_{ST}\,, \quad \dfrac{D\boldsymbol{r}}{Dt} = \boldsymbol{u}\,, \end{cases} \tag{8}$$

where $\dfrac{D}{Dt}$ represents the Lagrangian derivative, p is the pressure field, $\boldsymbol{g}$ is a generic external volumetric force field, Ω_{ST} a surface force field and $\mathbb{V}$ the viscous stress-tensor. The flow velocity, $\boldsymbol{u}$, is defined as the material derivative of a fluid particle position, $\boldsymbol{r}$.

Based on the weakly-compressible assumption, pressure is determined as a function of density fluctuations through an Equation of State (EOS). In particular, in this work a simple linearised EOS is chosen, such that:

$$p = c_0^2\left(\rho - \rho_0\right)\,. \tag{9}$$

Viscous stress-tensor, for a Newtonian fluid, can be rewritten in the form:

$$\mathbb{V} = \lambda\, tr(\mathbb{D})\,\mathbb{I} + 2\mu\mathbb{D}\,, \tag{10}$$

where $\mathbb{D}$ is the strain rate tensor, $\mathbb{D} = (\nabla\boldsymbol{u} + \nabla\boldsymbol{u}^T)/2$, $\mathbb{I}$ the Identity tensor and λ and μ the bulk and dynamic viscosity coefficients respectively.

In this work, the δ-SPH model proposed by Antuono et al (2012) is used. The system of equations in (8) become a discrete set of particles in SPH:

$$\begin{aligned}
\frac{D\rho_i}{Dt} &= -\rho_i \sum_j (\boldsymbol{u}_j - \boldsymbol{u}_i)\cdot\nabla W_{ij} V_j \quad + hc_s\delta \sum_j \mathcal{D}_{ij}\cdot\nabla W_{ij} V_j \,, \\
\frac{D\boldsymbol{u}_i}{Dt} &= \boldsymbol{g} - \frac{1}{\rho_i}\sum_j (p_i + p_j)\,\nabla W_{ij} V_j + \frac{\mu K}{\rho_i}\sum_j \Pi_{ij}\nabla_i W_{ij} V_j + \Omega_{ST} \\
\frac{d\boldsymbol{r}_i}{dt} &= \boldsymbol{u}_i + \delta\boldsymbol{u}_i \,, \qquad\qquad p = p_0 + c_s^2(\rho_i - \rho_0)
\end{aligned} \tag{11}$$

where j represents a general neighbor particle and V_j accounts for the volume of the neighbor particles j, defined for a fluid particle as $V_j = m_j/\rho_j$. $W_{ij} = W(\boldsymbol{r}_j - \boldsymbol{r}_i, h)$ is the kernel function at constant smoothing length h. Therefore, $\nabla_i W_{ij}$ represents the derivative of the kernel function with respect to the $i-th$ particle. In the present work, a Wendland C2 kernel with $h/dr = 2$ is used, dr being the particle distance.

Besides, $\mathcal{D}_{ij}$ and Π_{ij} are the diffusive terms added to the continuity equation in the standard δ-SPH model Antuono et al (2012) and the viscous part of the momentum equation respectively. They can be expressed as:

$$\begin{aligned}
\mathcal{D}_{ij} &= 2\left[(\rho_j - \rho_i) - \frac{1}{2}\left(\langle\nabla\rho\rangle^L_{j*} + \langle\nabla\rho\rangle^L_i\right)\cdot\boldsymbol{r}_{ji}\right]\frac{\boldsymbol{r}_{ji}}{\|\boldsymbol{r}_{ji}^2\|} \\
\Pi_{ij} &= \frac{(\boldsymbol{u}_j - \boldsymbol{u}_i)\cdot\boldsymbol{r}_{ji}}{\boldsymbol{r}_{ji}^2}\,, \quad \boldsymbol{r}_{ji} = \boldsymbol{r}_j - \boldsymbol{r}_i
\end{aligned} \tag{12}$$

where $\langle\nabla\rho\rangle^L_i$ represents the renormalized density gradient, as defined in Randles and Libersky (1996) and $j*$ refers only to fluid neighbor particles.

For fully turbulent regimes an alternative formulation derived from the present one, known as δ-LES-SPH, that is based on an LES subgrid model presented by Di Mascio et al (2017) can be adopted for the present problem, see Marrone et al (2021b,a). An analysis of the influence of viscosity for the present problem is carried out in Calderon-Sanchez et al (2021).

Finally, several corrections are performed on the model. Undesirable numerical cavitation occurring in areas where large negative pressure gradients may arise due to inertial forces. This is known in the SPH literature as tensile instability. The accelerations linked to it are considerably greater than $g_0 = 9.81 m/s^2$. In order to avoid it, particle shifting ($\delta\boldsymbol{u}_i$) is applied. In this work, the formulation presented by Sun et al (2019) is followed.

As in this work only one phase is considered, it is necessary to add a free-surface tracking algorithm to the model in order to avoid shifting velocities normal to the free surface. All the details regarding the shifting technique and the free-surface tracking algorithm can be found in Calderon-Sanchez et al (2021).

A general surface tension field Ω_{ST} is added to the momentum equation in Eq. (11) to deal with interface surface forces, which have shown to be relevant for this problem, especially at initial stages when a Rayleigh-Taylor instability is triggered. A similar force term to the one derived by Morris (2000) is implemented here, and it reads:

$$\Omega_{ST} = -\frac{\sigma}{\rho_i} \sum_j (\boldsymbol{n}_j - \boldsymbol{n}_i) \cdot \nabla W_{ij} V_j \, \boldsymbol{n}_i \tag{13}$$

where $\boldsymbol{n}_k$ is the normal at the free surface for a general particle k, computed as:

$$\boldsymbol{n}_i = \frac{\langle \nabla \lambda \rangle_i}{\| \langle \nabla \lambda \rangle_i \|} \quad \text{with} \quad \langle \nabla \lambda \rangle_i = -\sum_j (\lambda_j - \lambda_i) \, \boldsymbol{L}_i \nabla_i W_{ij} V_j \tag{14}$$

with λ being the minimum eigenvalue of the renormalization matrix defined by:

$$\boldsymbol{L}_i := \left[\sum_j \boldsymbol{r}_{ji} \otimes \nabla_i W_{ij} V_j \right]^{-1} . \tag{15}$$

For solid boundaries, the numerical boundary integrals approach, as described by Cercos-Pita (2015) is followed. In the boundary integrals formulation, the differential operators from (8) are defined in the presence of a boundary as:

$$\langle \nabla f \rangle_i = \frac{1}{\gamma_i} \left(\sum_{j*} f_{j*} \cdot \nabla W_{ij} V_{j*} + \sum_{\bar{j}} f_{\bar{j}} \cdot \boldsymbol{n}_{\bar{j}} W_{ij} s_{\bar{j}} \right) , \tag{16}$$

where f_i is a generic field function, $\boldsymbol{n}_j$ the normal of the surface, pointing outwards, s_j the area of the surface element and γ_i the Shepard renormalization factor, that in this case is computed geometrically through a semi-analytical approach as described in Calderon-Sanchez et al (2019). Note that broadly speaking, in the presence of a boundary, the computation of the renormalized gradient is sub-divided to account for the contribution of the neighbouring fluid particles, j^*, and neighbouring boundary particles, $\bar{j}$.

Subsequently, in the present work this is the general expression used to compute all the gradients, unless otherwise stated. The approach described in the present work is similar to the one presented recently by Michel et al (2022); Vergnaud et al (2022).

4.2 Tank model

The equation that describes the tank motion can be written as:

$$F_{slosh} - B_0 \operatorname{sgn}\left(\frac{dy}{dt}\right) - B_1 \frac{dy}{dt} - Ky = m_s \frac{d^2 y}{dt^2} , \tag{17}$$

where y is the vertical tank displacement and t the time. m_s is the tank mass, B_0 and B_1 account for the internal damping of the rig, K is the spring stiffness and F_{slosh} the sloshing force.

The equation in (17) is solved using a 4th-order Runge-Kutta algorithm.

The work W_{slosh} done by the sloshing force F_{slosh}, is computed with the following integral:

$$W_{slosh} = \int_{y_0}^{0} F_{slosh}\, dy \tag{18}$$

4.3 Coupling

In order to obtain displacements, velocities and accelerations in the tank, the force that is exerted by fluid motion F_{slosh} is needed. This force is actually the fluid force acting on the tank and being transmitted to the tank. The forces are obtained from the SPH solver according to $F_{slosh} = F^p_{slosh} + F^V_{slosh}$, where:

$$\begin{cases} F^p_{slosh} := \displaystyle\int_{\partial\Omega} -p\,\boldsymbol{n}\,dS\,, \\ F^V_{slosh} := \displaystyle\int_{\partial\Omega} 2\,\mu\,\mathbb{D}\cdot\boldsymbol{n}\,dS\,, \end{cases} \tag{19}$$

with $\boldsymbol{F}_{slosh}$ being the total force applied on the boundaries $\partial\Omega$ and $\boldsymbol{F}^p_{slosh}$, $\boldsymbol{F}^V_{slosh}$ the corresponding pressure and viscous components.

According to the boundary integrals formulation, these forces can be expressed in the SPH model as:

$$\begin{aligned} F^p_{slosh} &= -\sum_i \sum_{\bar{j}} (p_j + p_i)\ \mathbf{n}_j\, W_{ij}\, V_i\, S_j\,, \\ F^V_{slosh} &= \mu \sum_i \sum_{\bar{j}} \left[\Pi_{ij}\mathbf{n}_j + \frac{(\boldsymbol{I} - \boldsymbol{n}_j \otimes \boldsymbol{n}_j)\,\boldsymbol{u}_{ji}}{|\boldsymbol{r}_{ij}\cdot\boldsymbol{n}_j|} \right] W_{ij} V_i S_j\,. \end{aligned} \tag{20}$$

where the second term of the viscous force F^V_{slosh} is taken into account if no-slip boundary conditions are enforced. A similar procedure to compute the forces is followed by Chiron et al (2019).

4.4 Validation

Figure 3 shows the flow evolution of a δ-SPH simulation of the vertical sloshing problem. The selected snapshots represent the same time instants displayed in Figure 2 and overall there is a very good match of the flow kinematics when compared to the experimental snapshots. The match of the simulation with the experimental snapshots is best at the beginning and end of the simulation when the flow is not fragmented. After the first impact ($t = 0.09$ s), 3D and multiphase effects are involved and the flow kinematics are not captured with

great level of detail. However, the motion of the center of mass of the liquid is well matched by the SPH simulation. The numerical simulations obtained with our code have been previously validated with experiments and these comparisons have been reported in previous papers such as Marrone et al (2021a) and Calderon-Sanchez et al (2021). In those articles the numerical convergence of the method is studied and a complete validation against experimental measurements is performed for different fluids (water, acetone, oil and glycerine) in terms of sloshing force, tank kinematics and energy dissipation. An example of this validation procedure will be shown in Figures 6 and 7 in terms of tank acceleration and decay envelope where we see a reasonable match between the SPH simulation and experimental data.

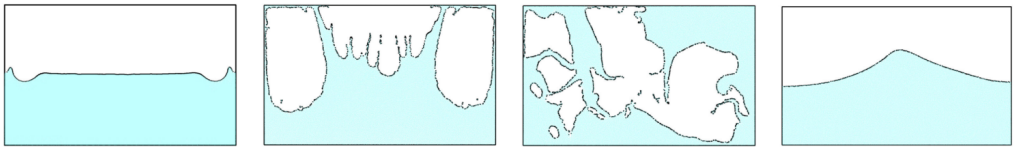


Fig. 3 Flow evolution of a water, 50% filling level and 10g maximum acceleration FSI $\delta-$SPH simulation of the vertical sloshing problem. The snapshots represent the simulated counterparts of the experimental snapshots presented in Figure 2.

5 Results

In this section, the results for two numerical campaigns are presented. First, the effect of gravity on the overall damping is assessed. Then, simulations are carried out at different scales following the dimensional analysis presented in section 4. Even though filling height h_f, represented in the analysis through non-dimensional number f can be varied, in this work it is kept constant and therefore all results presented refer to a filling level $f = 0.5$.

Compact support and speed of sound are chosen the same for both the gravity and the scale studies, such that $h/dr = 2$ and $c_s = 30$ m/s. Resolution is established in terms of the vertical number of particles as $h_f/dr = 100$. Initially, a meniscus is added to the liquid free surface near the wall. The influence of the meniscus in this problem has already been assessed by Calderon-Sanchez et al (2021). For this work, the meniscus length is set at $l = 2.5 \cdot 10^{-3}$ m and $\theta = 45°$. All the tests carried out in this work assume that the fluid tested is water at standard conditions. Then, $\rho = 998$ kg/m^3, $\mu = 8.9 \cdot 10^{-4}$ Pa $\cdot$ s and $\sigma = 0.072$ N/m.

The tank is displaced initially to a position $y = y_0$. Then, when the release is activated it is allowed to oscillate freely, measuring the overall force, position, velocity and acceleration. In all cases studied, the initial displacement is always the same, corresponding to $y_0 = H$.

In order to establish a comparison reference, a preliminary test without liquid is carried out. The liquid mass is replaced by structural mass with a

total weight corresponding to a 50% filling condition. This results in the same total nominal mass for all the tests presented in this study.

5.1 Gravity study

The present section is devoted to test how important gravity's action is in this FSI problem. Consequently, three different values of the gravity value $g = 0.1g_0$, g_0 and $5g_0$, with $g_0 = 9.8$ m/s^2 will be used and the results will be compared. For each of the gravity values, three different facilities characterized by their respective damping parameters, see Table 1, will be tested. As the mass and the spring constants are not changed, the characteristic frequency of the problem remains constant for all the combinations of gravity values and damping parameters. These three facilities are: the experimental rig constructed in the UPM facilities, Martinez-Carrascal and Gonzalez-Gutierrez (2021), and an under-damped and over-damped version of the same experimental facilities.

The variation of the structural damping in this gravity study is performed in order to test how dependant gravity's role is on the structural damping of the rig.

Table 1 Structural damping coefficients for the three studied facilities.

	$B_0[N]$	$B_1[kg/s]$
Under-damped	0	1
UPM	0.38	1.73
Over-damped	0.8	2.5

The tank acceleration obtained when the UPM, under-damped and over-damped systems are tested are presented as a function of time in Figures 4, 6 and 9, and as the logarithm of the acceleration envelope in Figures 5, 7 and 10. The first idea that can be extracted is that for the reference value $g = g_0$ and the under-gravity case $g = g_0/10$ the results are very similar for the three different facilities, showing that the absence of gravity and the reference gravity have little influence on the tank acceleration damping. Of course, if the gravity value is increased to $5g_0 = a_0/2$, then its influence is clearly relevant, changing the behavior of the decaying curve considerably. This happens because when the gravity is increased the relative motion of the liquid with respect to the motion of the tank is attenuated sooner, and the liquid recovers a block-like behaviour, acting as an added mass so the trend is similar to the dry experiment, i.e. the liquid behaves as a solid mass. This observation is demonstrated by looking at the flow kinematics displayed in Figure 8. It is seen that for the $g = 0$ case the liquid is allowed to freely slosh with high fragmentation of the free surface and many liquid impacts whereas for the $g = 5g_0$ case, the liquid is not even able to produce the first liquid

impact against the upper wall of the tank and it displays very little relative motion with respect to the tank.

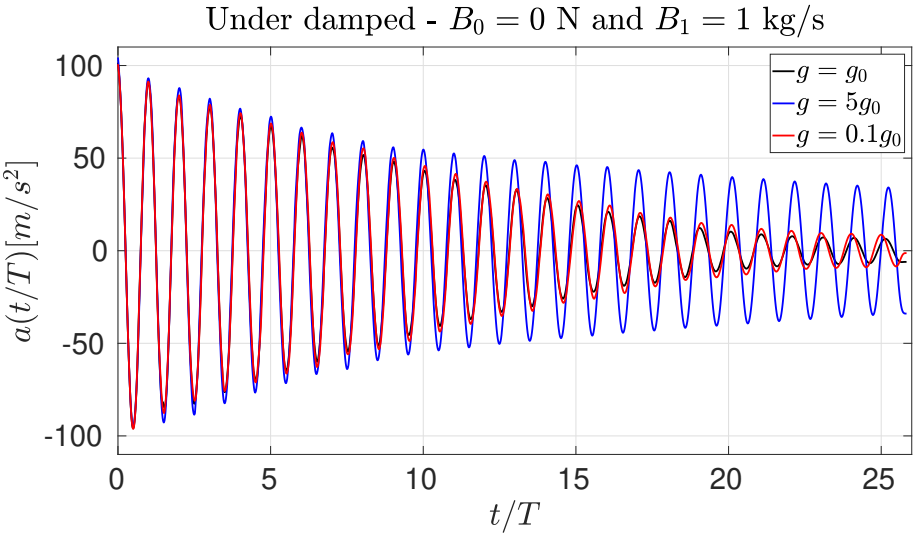


Fig. 4 Evolution of the tank acceleration with different gravity values for the case with damping parameters: $B_0 = 0$ N and $B_1 = 1$ kg/s.

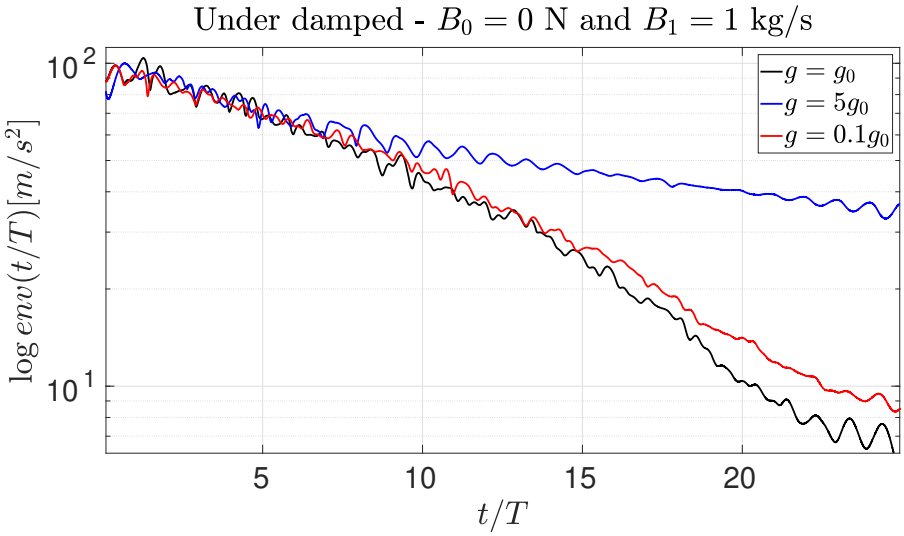


Fig. 5 Logarithm of the acceleration envelope with different gravity values for the case with damping parameters: $B_0 = 0$ N and $B_1 = 1$ kg/s.

Another important idea that can be extracted from these results is that the role of gravity is quite independent of the mechanical damping of the particular rig used. This can be concluded as we have shown that all the structural damping values used have a very similar effect in terms of gravity's influence.

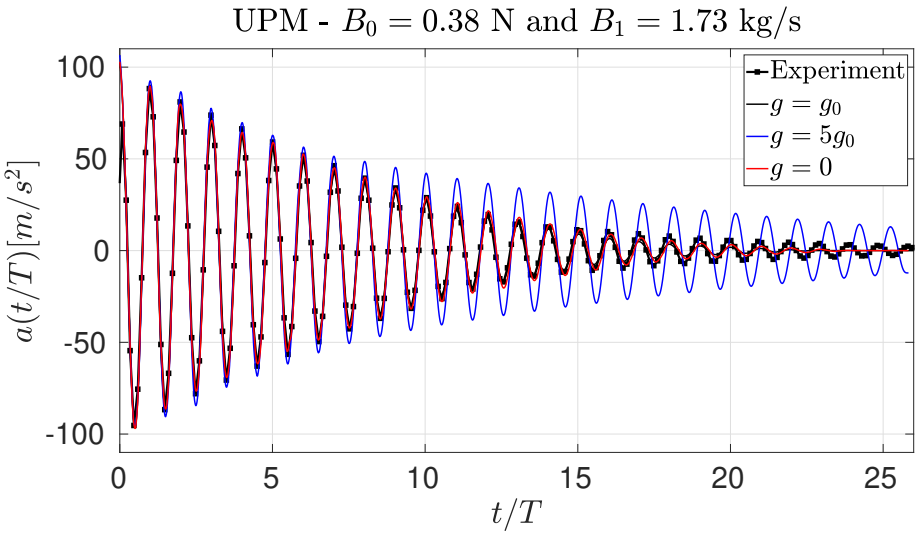


Fig. 6 Evolution of the tank acceleration with different gravity values for the case with damping parameters: $B_0 = 0.38$ N and $B_1 = 1.73$ kg/s. Experimental data obtained in Martinez-Carrascal and Gonzalez-Gutierrez (2021) has been plotted as comparison.

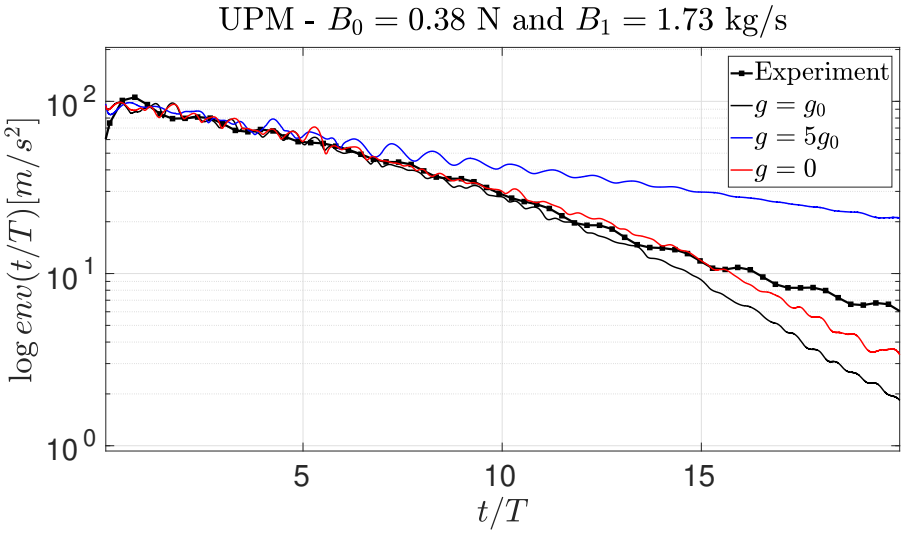


Fig. 7 Logarithm of the acceleration envelope with different gravity values for the case with damping parameters:$B_0 = 0.38$ N and $B_1 = 1.73$ kg/s. Experimental data obtained in Martinez-Carrascal and Gonzalez-Gutierrez (2021) has been plotted as comparison.

5.2 SPH scaling

Initial results from experimental UPM facilities were carried out at scale 1:5. In this work, this scale is reproduced, and two other scales, namely 2:5 and 3:5 are used in order to analyse them numerically. Results are all scaled up to the wing size applying the scaling laws.

In Figure 11 the acceleration curves corresponding to each of the three different scales is presented. As can be observed, the scaling laws work perfectly and the acceleration curves of the three scales are very similar. The equivalent logarithm of the acceleration envelope is also represented for the three scales in Figure 12, showing a similar trend.

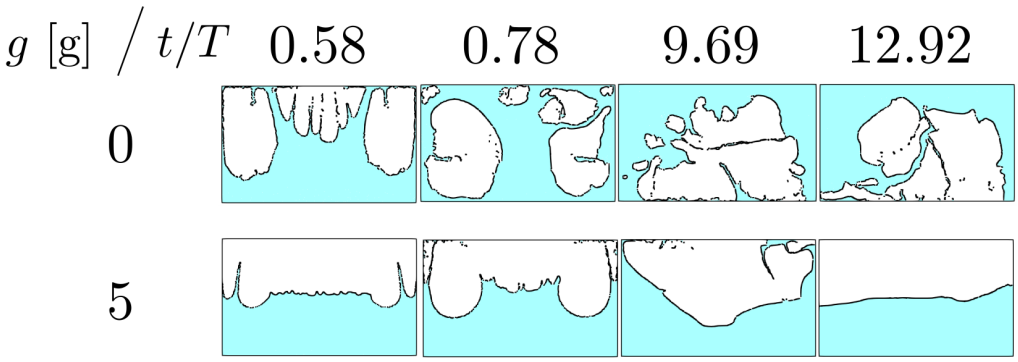


Fig. 8 Comparison of the flow evolution of δ-SPH simulations for cases with $g = 0$ and $g = 5g_0$ in the UPM facility.

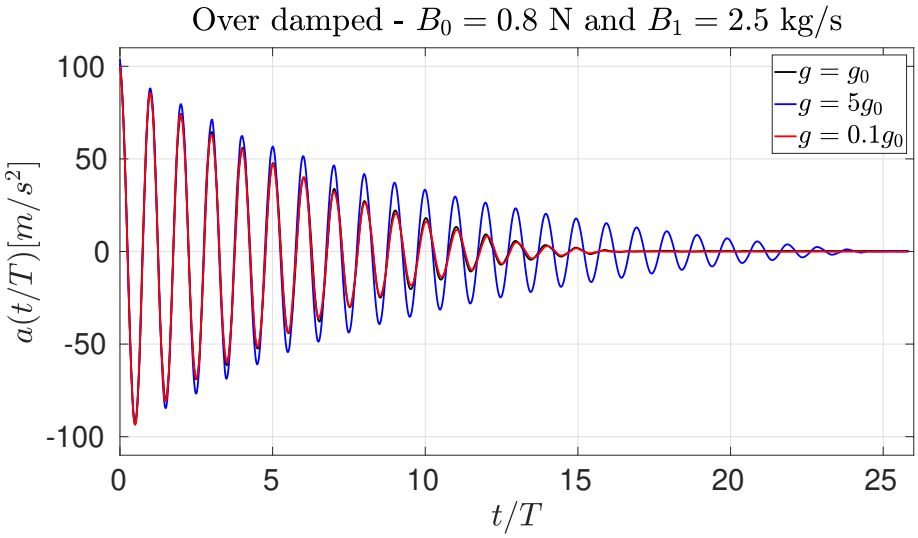


Fig. 9 Evolution of the tank acceleration with different gravity values for the case with damping parameters: $B_0 = 0.8$ N and $B_1 = 2.5$ kg/s.

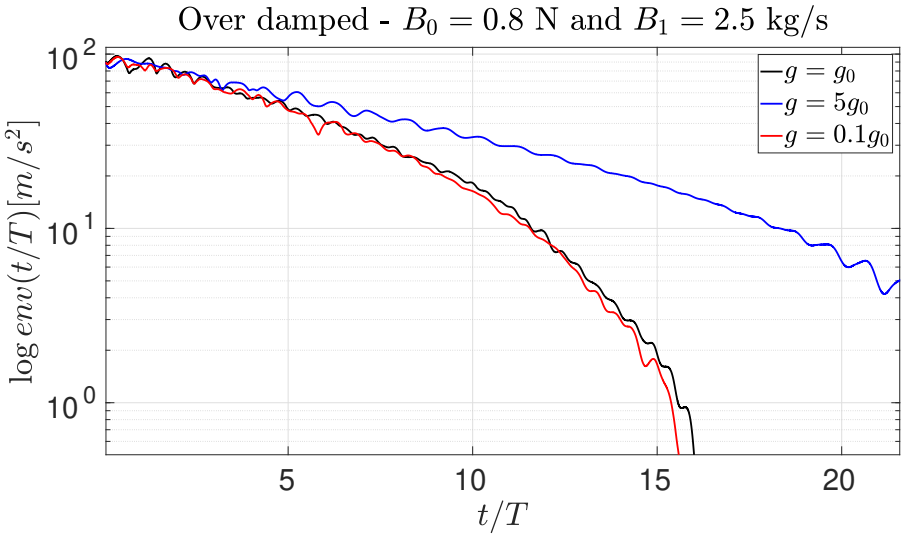


Fig. 10 Logarithm of the acceleration envelope with different gravity values for the case with damping parameters: $B_0 = 0.8$ N and $B_1 = 2.5$ kg/s.

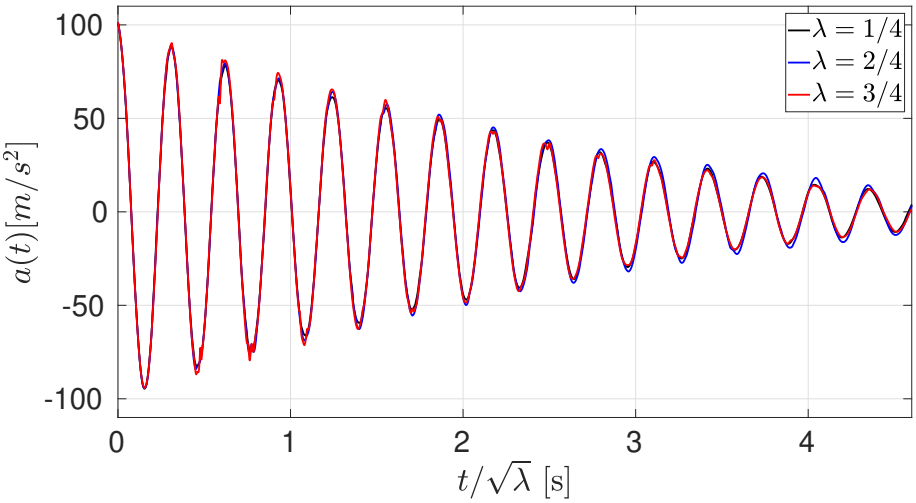


Fig. 11 Evolution of the tank acceleration for the three different scales.

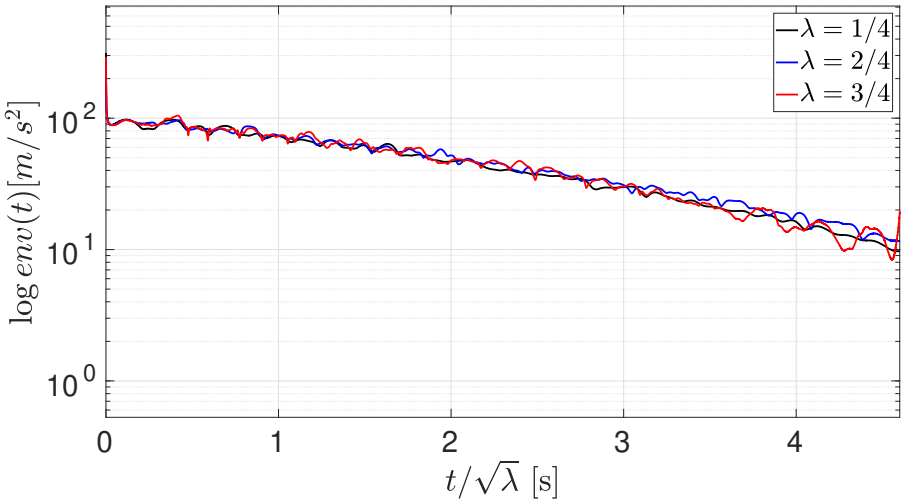


Fig. 12 Logarithm of the acceleration envelope for the three different scales.

Additionally, the forces for the three scales are compared in Figure 13. We can observe that very similar values are obtained for all scales, meaning that the scaling laws reproduce the expected force values. Some discrepancies can be observed at peak values for the three different scales, especially at first stages. This is particularly noticeable for the larger scale. As it is illustrated in Figures 3 and 8, first cycles are characterized by very thin jets that impact the wall. When this happens, excessively high pressures might be obtained at certain locations where the number of neighbors is low, having an impact on the forces that are computed. This trend reduces as the simulation evolves.

In Figure 14, the work performed by the sloshing force is computed according to equation (18), where the force plays a role, at the three different scales. As such, the discrepancies can be traced to the discussion on the sloshing force results presented above. Noting that the work is an integral quantity, the effect is greater at later stages, where curves follow the same trend, but with

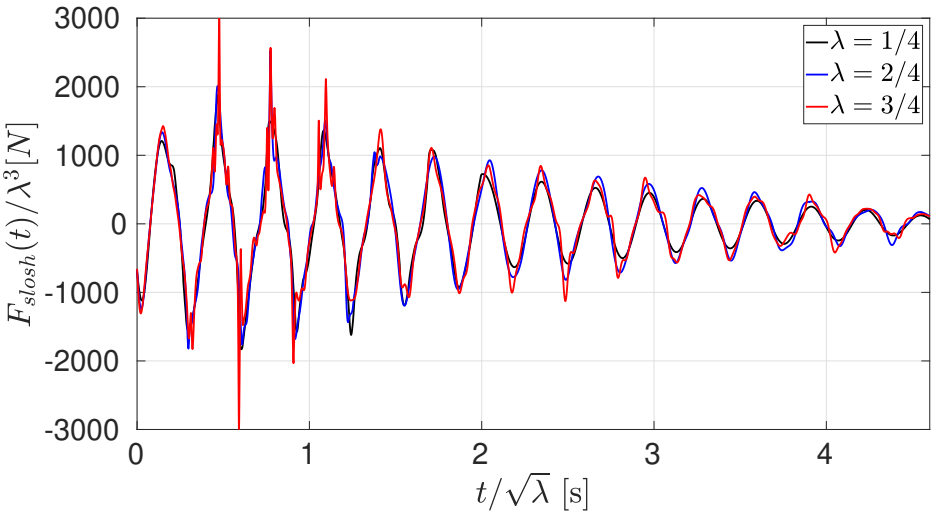


Fig. 13 Full Scaled sloshing force obtained with the extrapolation from the three scales.

an offset. For comparison, the results for each scale are divided by λ^4 as it is indicated by the second equation of (7).

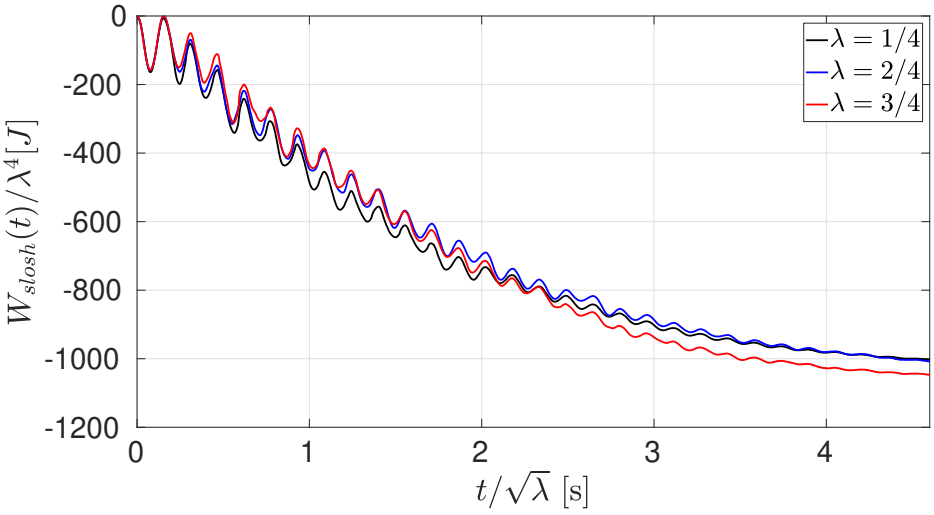


Fig. 14 Full scale Work produced by the sloshing force obtained with the extrapolation from the three scales.

We should remark on the clear advantages of making a scaling study based on computation fluid dynamics (CFD) simulations. In this approach all the fluid parameters can be forced in order to keep all the non-dimensional numbers equal at the different scales. In contrast to the CFD study, in the experimental approach to this coupled fluid-structure problem, the possibility of forcing all the dominant non-dimensional numbers to be equal at different scales is not possible, and consequently larger uncertainties appear when the scales change.

6 Conclusions

In this work, a numerical model of a fully coupled fluid-structure interaction problem is developed. The aim is to analyze the influence of gravity and the scale changes on the damping effects due to liquid sloshing inside the fuel tanks of aircraft wings.

The influence of gravity is very low in this kind of problem with initial acceleration an order of magnitude higher than the typical reference value $g_0 = 9.8m/s^2$. More intense values of gravity are required to have a relevant impact on the acceleration damping. The variation of the damping parameters gives us the confirmation that the gravity's role behaves the same for all cases, allowing this conclusion to be highly generalizable.

Scaling process is necessary to predict wing loading at full scale. Experiments might be limited at some point of the process, as the variation of non-dimensional numbers depend on the existing fluid characteristics. This also implies that normally non-dimensional relations cannot be changed on its own, influencing others. These aspects make numerical analysis an important tool to perform the extrapolation process, as it allows greater flexibility and a larger range of variation for non-dimensional relations.

This paper has investigated the scaling properties of the proposed system by means of the δ-SPH model for the fluid, and a mass-spring-damper system for the tank motion. The results show that the numerical model presented is able to predict the sloshing forces, the tank accelerations and the work produced by the sloshing force in the full scale experiment successfully from the results obtained at different scales. Therefore, from this work it can be concluded that having validated results at one scale is enough to obtain results at any scale, just by applying the corresponding scaling laws. This is a crucial aspect from the perspective of computational time savings.

Acknowledgments

This research is receiving funding from European Union (EU) under H2020 grant 815044 "*Sloshing Wing Dynamics (SLOWD)*" .

The authors also acknowledge the financial support from the Spanish Ministry for Science, Innovation and Universities (MCIU) under grant RTI2018-096791-B-C21 "*Hidrodinámica de elementos de amortiguamiento del movimiento de aerogeneradores flotantes*".

This research has also received funding from Universidad Politécnica de Madrid under a pre-doctoral scholarship.

References

Antuono M, Colagrossi A, Marrone S (2012) Numerical diffusive terms in weakly-compressible SPH schemes. Computer Physics Communications 183(12):2570–2580

Arndt TO, Dreyer ME (2008) Damping behavior of sloshing liquid in laterally excited cylindrical propellant vessels. Journal of Spacecraft and rockets 45(5):1085–1088

Bouscasse B, Colagrossi A, Souto-Iglesias A, et al (2014a) Mechanical energy dissipation induced by sloshing and wave breaking in a fully coupled angular motion system. I. theoretical formulation and numerical investigation. Physics of Fluids 26(3):033,103

Bouscasse B, Colagrossi A, Souto-Iglesias A, et al (2014b) Mechanical energy dissipation induced by sloshing and wave breaking in a fully coupled angular motion system. II. experimental investigation. Physics of Fluids 26(3):033,104

Bulian G, Souto-Iglesias A, Delorme L, et al (2009) Smoothed particle hydrodynamics (SPH) simulation of a tuned liquid damper (TLD) with angular motion. Journal of Hydraulic Research 47(extra issue):28–39

Calderon-Sanchez J, Cercos-Pita J, Duque D (2019) A geometric formulation of the shepard renormalization factor. Computers & Fluids 183:16 – 27. https://doi.org/https://doi.org/10.1016/j.compfluid.2019.02.020

Calderon-Sanchez J, Martinez-Carrascal J, Gonzalez-Gutierrez L, et al (2021) A global analysis of a coupled violent vertical sloshing problem using an SPH methodology. Engineering Applications of Computational Fluid Mechanics 15(1):865–888

Cercos-Pita JL (2015) Aquagpusph, a new free 3D SPH solver accelerated with OpenCL. Computer Physics Communications 192:295–312

Chiron L, De Leffe M, Oger G, et al (2019) Fast and accurate SPH modelling of 3-D complex wall boundaries in viscous and non viscous flows. Computer Physics Communications 234:93–111

Constantin L, Courcy JD, Titurus B, et al (2020) Analysis of damping from vertical sloshing in a SDOF system. Mechanical Systems Signal Processing

Cooper JE, Emmet PR, R. WJ (2017) Envelope function - a tool for analyzing flutter data. International Forum on Aeroelasticity and Structural Dynamics

Di Mascio A, Antuono M, Colagrossi A, et al (2017) Smoothed particle hydrodynamics method from a large eddy simulation perspective. Physics of Fluids 29(3):035,102

Gambioli F (2009) Fuels loads in large civil airplanes. In: 4th ERCOFTAC SPHERIC workshop on SPH applications

Liu W, Sun P, Ming F, et al (2018) Application of particle splitting method for both hydrostatic and hydrodynamic cases in SPH. Acta Mechanica Sinica 34(4):601–613

Marrone S, Colagrossi A, Antuono M, et al (2011) A 2D+t SPH model to study the breaking wave pattern generated by fast ships. Journal of Fluids and Structures 27(8):1199–1215

Marrone S, Colagrossi A, Calderon-Sanchez J, et al (2021a) Numerical study on the dissipation mechanisms in sloshing flows induced by violent and high-frequency accelerations. ii. comparison against experimental data. Physical Review Fluids 6(11):114,802

Marrone S, Colagrossi A, Gambioli F, et al (2021b) Numerical study on the dissipation mechanisms in sloshing flows induced by violent and high-frequency accelerations. i. theoretical formulation and numerical investigation. Physical Review Fluids 6(11):114,801

Martinez-Carrascal J, Gonzalez-Gutierrez L (2021) Experimental study of the liquid damping effects on a SDOF vertical sloshing tank. Journal of Fluids and Structures 100:103,172

Michel J, Vergnaud A, Oger G, et al (2022) On particle shifting techniques (PSTs): Analysis of existing laws and proposition of a convergent and multi-invariant law. Journal of Computational Physics 459:110,999

Morris JP (2000) Simulating surface tension with smoothed particle hydrodynamics. International journal for numerical methods in fluids 33(3):333–353

Randles P, Libersky L (1996) Smoothed Particle Hydrodynamics: some recent improvements and applications. Computer methods in applied mechanics and engineering 39:375–408

Souto-Iglesias A, Rojas LP, Rodríguez RZ (2004) Simulation of anti-roll tanks and sloshing type problems with smoothed particle hydrodynamics. Ocean Engineering 31:1169–1192

Souto-Iglesias A, Delorme L, Pérez-Rojas L, et al (2006) Liquid moment amplitude assessment in sloshing type problems with smooth particle hydrodynamics. Ocean Engineering 33:1462–1484

Sun P, Colagrossi A, Marrone S, et al (2019) A consistent approach to particle shifting in the δ-plus-SPH model. Computer Methods in Applied Mechanics and Engineering 348:912–934

Tait M (2008) Modelling and preliminary design of a structure-TLD system. Engineering Structures 30(10):2644–2655

Tyvand PA, Miloh T (2012) Incompressible impulsive sloshing. Journal of fluid mechanics 708:279–302

Vergnaud A, Oger G, Le Touzé D, et al (2022) C-CSF: Accurate, robust and efficient surface tension and contact angle models for single-phase flows using sph. Computer Methods in Applied Mechanics and Engineering 389:114,292

Wright M, Gambioli F, Malan A (2021) A non-dimensional characterization of structural vibration induced vertical slosh induced damping. The 31st International Ocean and Polar Engineering Conference ISOPE-I-21-3211

Publication 7 (P7)

Jon Martinez-Carrascal, J. Calderon-Sanchez and L. M. González-Gutiérrez (2021). Extended computation of the viscous Rayleigh-Taylor instability in a horizontally confined flow. Physical Review E, 103 053114, 2021. DOI: https://doi.org/10.1103/PhysRevE.103.053114. 1 citation. JCR(2021): 2.707, Physics, Fluids and Plasmas (Q2) and Physics, Mathematical (Q1).

An extended computation of the viscous Rayleigh-Taylor instability in a horizontally confined flow.

Jon Martinez-Carrascal and J. Calderon-Sanchez and
L.M. González-Gutiérrez* and A. de Andrea González†

(Dated: October 21, 2022)

Abstract

In this article, the classical Rayleigh-Taylor instability is extended to situations where the fluid is completely confined, both in the vertical and horizontal directions. This article starts with the 2D viscous periodic case with finite height where the effect of adding surface tension to the interface is analyzed. This problem is simulated from a dual perspective: first, the linear stability analysis obtained when the Navier-Stokes equations are linearized and regularized in terms of density and viscosity; and second, looking at the weakly compressible version of a multiphase smoothed particle hydrodynamics (WCSPH) method. The evolution and growth rates of the different fluid variables during the linear regime of the SPH simulation are compared to the computation of the eigenvalues and eigenfunctions of the viscous version of the Rayleigh-Taylor stability (VRTI) analysis with and without surface tension. The most unstable mode, which has the maximal linear growth rate obtained with both approaches, but also other less unstable modes with more complex structures are reported. The classical horizontally periodic (VRTI) case is now adapted to the case where two additional left and right walls are included in the problem, representing the cases where a two phase flow is confined in a accelerated tank. This 2D case where no periodic assumptions are allowed is also solved using both techniques with tanks of different sizes and a wide range of Atwood numbers. The agreement with the linear stability analysis obtained by a lagrangian method such as multiphase WCSPH is remarkable.

* School of Naval Engineering, Universidad Politécnica de Madrid (UPM), Avda. de la Memoria 4 28040 Madrid Spain

† Departamento de Física, Escuela Politécnica Superior, Universidad Carlos III de Madrid, Av. Universidad 30, 28911 Leganés, Spain

I. INTRODUCTION

In many aircraft models, the fuel is transported inside tanks placed along the wing structures. Due to the great extreme accelerations on the aircraft wings, violent fluid movement and strong impacts with the tank walls are produced. This complex fluid phenomenon is known as sloshing [1]. In the analysis of vertically excited sloshing cases, violent sloshing is of great interest for aeroplane manufacturers, where very interesting hydrodynamic phenomena are found, such as the free surface instabilities that appear at the first stages of the movement. These instabilities are an extended version of Rayleigh-Taylor instabilities, where fluid properties such as viscosity and surface tension play a role.

Normally the Rayleigh-Taylor instability (RTI) appears when a heavy fluid overlies a lighter fluid [2], [3] and gravity is oriented towards the light fluid, in other words, the density gradient and gravity are opposed. This situation is present in a wide variety of applications: ferrofluids [4], tectonics [5], exploding foils [6], aerobreakup [7], and astrophysics [8], [9]. An original extension of the RTI appears in the sloshing phenomena when two different fluids are confined in a accelerated tank. In this case, the light fluid overlies a heavier fluid when gravity is present, but the RTI appears when a larger acceleration than gravity is applied to both fluids in the opposite direction to the force of gravity. As explained before, the density gradient is opposed to the difference between the inertial force and gravity.

Mikaelian [10] analyzed the Rayleigh-Taylor instability in two finite-thickness fluids taking viscosity effects into account. A numerical dispersion relation was obtained for different thicknesses and Atwood numbers. He performed a 1D analysis based on two fluids separated with a sharp interface using homogeneous Dirichlet and Neumann conditions for the velocity at the top and bottom boundaries, and compatibility conditions at the interface. The 2D extension presented in this work allows the analysis of more complex flows and includes the possibility of studying diffuse interfaces, the sharp interface being just a particular case.

Obied Allah[11] investigated the finite-thickness effect of a slab of incompressible fluid with exponentially increasing density supported by a fluid of constant density in the presence of surface tension. He found that the finite-thickness has a stabilizing effect on the RTI.

Morgan et al.[12] studied the behavior of the most unstable VRTI mode initiated with a diffuse interface. The results exhibit good agreement with the dynamic diffusion model of Duff et al. [13] for small wavenumbers, but produces larger growth rates for large

wavenumber perturbations.

Yu et al. [14] investigated the inviscid RTI for a fluid with an hyperbolic tangent density distribution. They obtained the multiple eigenvalues for the growth rates of the RTI and the corresponding eigenfunctions which may have potential applications in comprehending the mixing behavior existing in many areas. Moreover, they obtained a fitting expression for those eigenmodes in the dimensionless form, which agrees well with the numerical results for limited Atwood numbers $A_\rho \leq 0.8$. Dong et al. [15] revisited the physical problem that was studied by[14] by developing a short-wavelength asymptotic solution. Based on the Wentzel-Kramers-Brillouin (WKB) approximation, the growth rates of the RTI were obtained for Atwood numbers close to unity.

However, to the best of our knowledge no numerical study on the eigenvalue problem associated to the VRTI in a confined tank has been performed. Therefore, we need to carry out this research study in the case of two-dimensional (2D) geometries where the no-slip boundary conditions are imposed on the top and bottom walls, but also on the lateral walls. Similarly to [16], a hyperbolic tangent distribution for the density and viscosity profiles are imposed, which allows skipping the compatibility conditions when sharp interfaces are simulated. Starting with the additional step introduced by the presence of the lateral walls, the development of the RTI inside more complex geometries, for example including intermediate vertical baffles, could also be studied using the same methodology.

In order to confirm the findings, the VRTI is also reproduced using the meshless Lagrangian method Smoothed Particle Hydrodynamics (SPH), that is gaining significant attention in the last decades according to its ability to deal with complex physics and complex geometries, such as the field of fluid dynamics involving free-surface flows. SPH exhibits significant advantages when compared to other methods, such as finite elements or finite volumes when dealing with multiphase flow, because density is transported by the particles and there is no need to include an additional scalar transport equation. The transport of scalar functions by advection equations performed in formulations such as Volume of Fluid (VOF) or Level Set is not a numerically trivial problem that normally implies dispersion and diffusion numerical errors and loss of interface sharpness. This particular situation where multiphase formulation is compulsory, seems to be a perfect opportunity to test the modern and robust WCSPH version presented in[17]. Most of the literature addressing the Rayleigh-Taylor problem with SPH, normally focus on the evolution

of the flow and the robustness of the numerical formulation, but very few compare the growth rates with other results from the stability analysis. Some of the first attempts correspond to [18] and [19], using Incompressible (ISPH) and Weakly Compressible (WCSPH) approaches respectively. Works on multiphase SPH developed by [20], [21] or [22] present results for the Rayleigh-Taylor problem to validate their different multiphase SPH or surface tension formulations, but these are only analyzed from a qualitative perspective in terms of free-surface evolution at certain characteristic instants in time.

A further step is performed in the work by [23], where some comparison with approximate solutions of the classical stability analysis is performed. In contrast to the work presented here, the initial free surface is deformed instead of initialized with a velocity field. In that study, a quantitative analysis of the growth rate of the VRTI in a confined geometry is carried out for a single instability mode and a single Atwood number. The analysis focuses on the dependence of the problem with the surface tension.

In this paper the following new ideas are proposed: first, a general 2D formulation is presented to analyze the RTI that considers the possibility of using density-and viscosity-regularized fluids, geometrical flexibility, alternative boundary conditions and surface tension implementation. In particular, the possibility of using no slip lateral boundary conditions allows for the analysis of a completely confined tank, and also the quantification of the differences with the well known periodic VRTI spectrum. Finally, we want to confirm that a meshless lagrangian numerical method such as WCSPH is able to reproduce the dynamics observed in this particular multiphase problem with reasonable accuracy.

The paper is organised as follows: in section II the general description to the RTI is explained and the general equations are presented. In section III both solution methodologies, the linear stability analysis and the SPH formulation, are detailed. In section IV, the results obtained by both methodologies for the VRTI problem with different boundary conditions are monitored and compared. Finally, conclusions are presented in section V.

II. PROBLEM SETUP

The strategies to perform the linear stability analysis are presented in this section. To study the viscous version of the Rayleigh-Taylor instability, we assume a zero velocity base-

flow and regularized density and viscosity distributions that represent two fluids separated by a common interface. We analyze the evolution of the perturbations by the assumed baseflow. In particular, we are interested in the development of two-dimensional flow structures and the growth rates of the different unstable modes. The calculations have been performed in a 2D computational domain. Previous validations of the viscous and inviscid cases without surface tension in 1D and 2D geometries can be found in [16].

Let ρ_1, μ_1, ν_1 and ρ_2, μ_2, ν_2 be the densities, and the kinematic and dynamic viscosities of the top-(heavy) and bottom-(light) fluids respectively. The two phase flow is governed by the incompressible Newtonian Navier-Stokes equations in a domain Ω in the presence of gravity g, which imply mass and momentum conservation, and a density transport equation. As the velocity baseflow is zero, the viscosity transport equation is not necessary in this VRTI formulation, see [24]. The domain will be a rectangle of height $2H$ and width $2L$ contained on the XY plane, mathematically expressed as $\Omega = [-L, L]\text{x}[-H, H]$.

Similarly to [25], the characteristic time, length, velocity, pressure, density and viscosity scales used to transform the problem to its non-dimensional version are defined as:

$$\rho_o = \frac{\rho_1 + \rho_2}{2} \qquad \mu_o = \frac{\mu_1 + \mu_2}{2} \qquad \nu_o = \frac{\nu_1 + \nu_2}{2}, \tag{1}$$

$$t_o = \left(\nu_0/g^2\right)^{1/3} \qquad l_o = \left(\nu_0^2/g\right)^{1/3} \qquad u_o = (g\nu_0)^{1/3}, \tag{2}$$

$$k_o = \left(\nu_0^2/g\right)^{-1/3} \qquad p_o = \rho_0 g\left(\nu_0^2/g\right)^{1/3} \tag{3}$$

The non-dimensional version of this set of equations reads:

$$\rho\frac{\partial \boldsymbol{u}}{\partial t} + \rho\boldsymbol{u}\cdot\nabla\boldsymbol{u} = -\nabla p + \rho\boldsymbol{u}_g + \nabla[\mu(\nabla\boldsymbol{u} + \nabla\boldsymbol{u}^T)], \tag{4}$$

$$\nabla\cdot\boldsymbol{u} = 0, \tag{5}$$

$$\frac{\partial \rho}{\partial t} + \boldsymbol{u}\cdot\nabla\rho = 0. \tag{6}$$

where ρ, $\boldsymbol{u}$, p, t, ∇, μ, τ, $\boldsymbol{u}_g$ are the non-dimensional density, velocity, pressure, time, nabla operator, viscosity, viscous stress tensor and unity vector representing gravity.

A steady nonparallel basic flow $(\overline{u}_i, \overline{\rho}, \overline{p})$ is perturbed by small-amplitude velocity $\widetilde{u}_i$, density $\widetilde{\rho}$ and pressure $\widetilde{p}$ perturbations, as follows:

$$u_i(x,y,z,t) = \overline{u}_i(x,y) + \varepsilon\widetilde{u}_i(x,y,z,t) + c.c. \tag{7}$$

$$p(x,y,z,t) = \overline{p}(x,y) + \varepsilon\widetilde{p}(x,y,z,t) + c.c. \tag{8}$$

$$\rho(x,y,z,t) = \overline{\rho}(x,y) + \varepsilon\widetilde{\rho}(x,y,z,t) + c.c. \tag{9}$$

where $\varepsilon \ll 1$, and $c.c$ denotes the conjugate of the complex quantities $\widetilde{u}_i$, $\widetilde{\rho}$ and $\widetilde{p}$. As baseflow, we consider two superposed fluids at rest $\overline{u}_i = 0$ separated by a regularized interface at $y = 0$ and subjected to a constant gravitational acceleration pointing downwards the vertical direction y.

Therefore, in order to describe the Rayleigh-Taylor (RT) instability of sharp interface, it seems more consistent to attempt to solve the problem for a transition layer of finite thickness, and then take the limit when the thickness tends to zero. Similarly to the sharp jump implementation used in [16], we adopt the density and viscosity profiles

$$\overline{\rho} = 1 + A_\rho \tanh(y/L_s) \qquad \mu = 1 + A_\mu \tanh(y/L_s) \tag{10}$$

where L_s is the gradient scale length of the density and viscosity layers and A_ρ, A_μ the Atwood numbers given by

$$A_\rho = \frac{\rho_1 - \rho_2}{\rho_1 + \rho_2} \qquad A_\mu = \frac{\mu_1 - \mu_2}{\mu_1 + \mu_2} \tag{11}$$

Taking account of equations (10), typical air-water hydrodynamic instabilities in the presence of a sharp interface can be recovered by setting $L_s \to 0$. When equations (7), (8) and (9) are substituted into the Navier-Stokes equations (4), (5) and 6, assuming zero base flow $\overline{u}_i = 0$ and neglecting second order terms, the linearized Navier-Stokes equations for the perturbation quantities are obtained:

$$\overline{\rho}\frac{\partial\widetilde{u}_i}{\partial t} = -\frac{\partial\widetilde{p}}{\partial x_i} + \mu\Delta\hat{u}_i + \left(\frac{\partial\widetilde{u}_j}{\partial x_i} + \frac{\partial\widetilde{u}_i}{\partial x_j}\right)\frac{\partial\mu}{\partial x_j} + \widetilde{\rho}u_{g_i} \tag{12}$$

$$\frac{\partial\widetilde{\rho}}{\partial t} + \widetilde{u}_j\frac{\partial\overline{\rho}}{\partial x_j} = 0 \tag{13}$$

$$\frac{\partial\widetilde{u}_i}{\partial x_i} = 0 \tag{14}$$

Since the coefficients of $\widetilde{u}_i$, $\widetilde{\rho}$ and $\widetilde{p}$ do not depend on z and t the perturbation quantities can be written as normal modes

$$\tilde{u}_i(x,y,z,t) = \hat{u}_i(x,y)\mathrm{e}^{ik_z z}\mathrm{e}^{\gamma t} + \text{c.c.}, \tag{15a}$$

$$\tilde{p}(x,y,z,t) = \hat{p}(x,y)\mathrm{e}^{ik_z z}\mathrm{e}^{\gamma t} + \text{c.c.}, \tag{15b}$$

$$\tilde{\rho}(x,y,z,t) = \hat{\rho}(x,y)\mathrm{e}^{ik_z z}\mathrm{e}^{\gamma t} + \text{c.c.}, \tag{15c}$$

where the complex conjugate (c.c.) is required to render the perturbations real. Additionally, $\gamma = \sigma + \mathrm{i}\omega \in \mathbb{C}$ is the complex growth/decay rate σ and oscillation frequency ω.

Let us add the presence of the surface tension on the free surface that separates both fluid phases to this perturbed system. Following [25], the surface tension presence adds the term $-2(\partial_{xx}\widehat{\xi}_s - k_z^2\widehat{\xi}_s)S\delta_s(y-y_s)$ to the y projection of the equation (12). Where $\widehat{\xi}_s = \widehat{\xi}(x,y_s)\mathrm{e}^{k_z z}\mathrm{e}^{\gamma t}$ is the vertical displacement of the free surface at $y = y_s$, $\delta_s(y-y_s)$ is the Dirac's delta function and S is the non-dimensional surface tension, which can be expressed as:

$$S = \frac{T_s}{(\rho_1+\rho_2)(g\nu^4)^{1/3}} \tag{16}$$

where T_s is the dimensional surface tension. In order to proceed with the numerical integration, the Dirac delta function will be regularized and the term $\widehat{\xi}$ can be related to the vertical velocity perturbation $\widehat{v}$ as

$$\widehat{v} = \frac{\partial\widehat{\xi}}{\partial t} = \gamma\widehat{\xi} \tag{17}$$

In section III, a 2D variational formulation of the equations using a second order finite element discretization is performed. A Taylor-Hood triangular element where the density perturbation was also approximated by second order polynomials is used to solve the linearized Navier-Stokes equations around the base flow, see [26] for details.

III. MATHEMATICAL MODELS

A. Linear stability: 2D eigenvalue-problem formulation and solution methodology

We are particularly interested in the temporal stability analysis on a 2D computational domain ($k_z = 0$). The fluids are confined in the vertical direction, and consequently

homogeneous Dirichlet boundary conditions are used on the top and bottom boundaries $y = \pm H$. On the right and left boundaries $x = \pm L$ either periodic boundary conditions (periodic configuration) or homogeneous Dirichlet boundary conditions (tank configuration) will be used, see both configurations in Figure 1. Consequently, this framework does not contain any explicit z-coordinate. A 3D generalization of this framework, where the perturbations assume a spanwise periodic length (i.e. homogeneous direction) and L_z is defined through the real wave number $k_z = \frac{2\pi}{L_z} \in \mathbb{R}$ is performed in [26].

In the classical 1D instability analysis of the VRTI, a periodic solution with unlimited wavelength in both the horizontal x and spanwise z directions [14] is assumed. In the periodic boundary case, see the top part of Figure 1, the BiGlobal EVP [27] represented by equations (12)-(14) has been solved without the explicit assumption of the periodic structure in the horizontal x direction, but with limited wavelength for the computed eigenvectors in the horizontal direction $k_x > \frac{\pi}{L}$ and infinite spanwise length. The horizontally confined case studied here, see the bottom part of Figure 1, no periodicity assumption is possible, and the 2D formulation is compulsory.

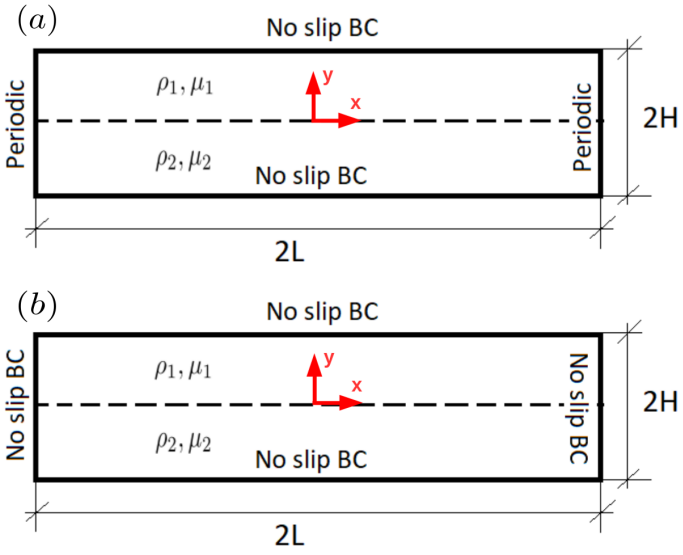


FIG. 1: Schemes of the computational geometry used for the Rayleigh-Taylor simulations. A dashed line at $y = 0$ indicates the interface between fluids. The boundary conditions are also written at each boundary for both cases: periodic (a) and tank (b) configurations.

Substitution of the ansatz (15) into the perturbation equations (12)-(14) yields

$$-\mu\nabla^2\hat{u} + \frac{\partial\hat{p}}{\partial x} - \frac{d\mu}{dy}(\frac{\partial\hat{v}}{\partial x} + \frac{\partial\hat{u}}{\partial y}) = -\gamma\overline{\rho}\hat{u}, \tag{18}$$

$$-\mu\nabla^2\hat{v} + \frac{\partial\hat{p}}{\partial y} - 2\frac{d\mu}{dy}\frac{\partial\hat{v}}{\partial y} + \hat{\rho} - 2(\partial_{xx}\widehat{\xi})S\delta_s(y - y_s) = -\gamma\overline{\rho}\hat{v}, \tag{19}$$

$$-\mu\nabla^2\hat{w} - \frac{d\mu}{dy}(\frac{\partial\hat{w}}{\partial y}) = -\gamma\overline{\rho}\hat{w}, \tag{20}$$

$$\hat{v}\frac{d\overline{\rho}}{dy} = -\gamma\hat{\rho}, \tag{21}$$

$$\frac{\partial\hat{u}}{\partial x} + \frac{\partial\hat{v}}{\partial y} = 0, \tag{22}$$

where ∇^2 is the Laplacian operator limited to our XY 2D domain. As the present study is 2D, $k_z = 0$, the eigenvalue problem given by the equations (18)-(22) is real. As consequence, the projection of the momentum equation (20) on the Z direction is the only one that contains the velocity perturbation component $\hat{w}$ and can be decoupled from the rest. This system can be simplified from six to five differential equations, eliminating the vertical displacement $\widehat{\xi}$. Combining equations (21) and (17) the free surface perturbation can be related to the density perturbation as:

$$\widehat{\xi} = -\frac{1}{\frac{d\overline{\rho}}{dy}}\hat{\rho} \tag{23}$$

We also express the Dirac delta function regularized as:

$$\delta_s(y - y_s) = \frac{1}{2A_\rho}\frac{d\overline{\rho}}{dy} \tag{24}$$

This converts system (18)-(22) into a real generalized eigenvalue problem:

$$A \cdot \boldsymbol{X} = -\gamma B \cdot \boldsymbol{X}, \tag{25}$$

where $\boldsymbol{X} = (\hat{u}, \hat{v}, \hat{w}, \hat{\rho}, \hat{p})^{\mathrm{T}}$ with real linear operators A and B that can be expressed as:

$$A = \begin{pmatrix} \mathfrak{L} & -\frac{d\mu}{dy}\partial_x & 0 & 0 & \partial_x \\ 0 & \mathfrak{L} - \frac{d\mu}{dy}\partial_y & 0 & 1 + \frac{S}{A_\rho}\partial_{xx} & \partial_y \\ 0 & 0 & \mathfrak{L} & 0 & 0 \\ 0 & \frac{d\overline{\rho}}{dy} & 0 & 0 & 0 \\ \partial_x & \partial_y & 0 & 0 & 0 \end{pmatrix} \tag{26}$$

being the operator $\mathfrak{L}$

$$\mathfrak{L} = -\mu\nabla^2 - \frac{d\mu}{dy}\partial_y \tag{27}$$

where the matrix B

$$B = \begin{pmatrix} \overline{\rho} & 0 & 0 & 0 & 0 \\ 0 & \overline{\rho} & 0 & 0 & 0 \\ 0 & 0 & \overline{\rho} & 0 & 0 \\ 0 & 0 & 0 & 1 & 0 \\ 0 & 0 & 0 & 0 & 0 \end{pmatrix}. \tag{28}$$

The boundary conditions for the lateral periodic boundaries are:

$$\hat{u}(-L, y) = \hat{u}(L, y) \tag{29}$$

$$\hat{v}(-L, y) = \hat{v}(L, y) \tag{30}$$

$$\hat{u}(x, \pm H) = 0 \tag{31}$$

$$\hat{v}(x, \pm H) = 0 \tag{32}$$

when no-slip lateral boundaries at $x = \pm L$ are used, conditions (29) and (30) are both equal to zero.

In general, the eigenvalues γ of such a real eigenvalue problem are either real, or they arise as pairs of complex conjugate eigenvalues. Adopting the existing nomenclature from the literature, see e.g. Theofilis et al. [28], the corresponding eigenvectors describe either stationary modes ($\gamma = 0$), or traveling waves ($\gamma = \pm \mathrm{i}\omega \neq 0$).

To discretize the equations, we use a triangular-element-based unstructured mesh. The eigenvalue problem is solved using the Arnoldi method based on a Krylov-subspace iteration, originally proposed by [29] and discussed in detail in [27]. In order to check the accuracy of the results during the stability analysis, the number of mesh nodes was increased until three significant digits of the most unstable eigenvalue converged.

In the case that the horizontal periodicity is assumed in the whole domain, the problem could be reduced to the 1D formulation, see [16] for details. In that case, the problem could be solved by the quadratic eigenvalue problem for the vertical velocity perturbation $\hat{v}$:

$$(A\gamma^2 + B\gamma + C)\hat{v} = 0 \tag{33}$$

where operators A and B are identical to the ones in [16] and operator C changes due to the surface tension term as follows:

$$C = -k^2 \frac{d\overline{\rho}}{dy}(I - k^2 \frac{S}{A_\rho}) \tag{34}$$

where k is the wavenumber associated with the assumed horizontal periodicity.

B. SPH Formulation

One of the objectives of this work is to prove that the SPH formulation is a valid tool to perform a stability analysis of the VRTI. For that purpose, we are going to discretize the set of equations (4) using the multiphase δ-WCSPH formulation detailed in [17]. The software used is AQUAgpusph [30], an open source SPH code based on GPU capabilities. The discretized set of equations reads:

$$\frac{dV_i}{dt} = V_i(\mathbf{u_i} - \mathbf{u_j}) \cdot \nabla W_{ij} V_i + \delta h c_{0_\chi} \sum_{j \epsilon \chi} \mathbf{D^V_{ij}} \cdot \nabla W_{ij} V_j \tag{35}$$

$$\rho_i \frac{d\mathbf{u_i}}{dt} = -\sum_j (p_i + p_j) \nabla W_{ij} V_j + \rho_i \mathbf{g} + \mu_\chi \sum_{j \epsilon \chi} \pi_{\mathbf{ij}} \nabla W_{ij} V_j + \mathbf{\Omega} \tag{36}$$

$$\frac{d\mathbf{r_i}}{dt} = \boldsymbol{u_i} \tag{37}$$

$$\rho_i = \sum_{j \epsilon \chi} m_j W^S_{ij} \tag{38}$$

$$p_i = \frac{\rho_{0_\chi} c^2_{0_\chi}}{\gamma_\chi} \left(\left(\frac{\rho_i}{\rho_{0_\chi}} \right)^{\gamma_\chi} - 1 \right) + p_b \tag{39}$$

This set of equations is composed of a volume conservation equation (35), a momentum conservation equation (36), a time evolution of the trajectory of each particle (37), an evaluation of the density field (38) and an equation of state (39). Where V_j accounts for the volume of the neighbor particles j and $W_{ij} = W(\boldsymbol{r}_j - \boldsymbol{r}_i, h)$ and $\nabla_i W_{ij} = \nabla W(\boldsymbol{r}_j - \boldsymbol{r}_i, h)$ represent the kernel function and its derivative with respect to the $i-th$ particle, at constant h, respectively. In this work, a Wendland C2 kernel with $h/dr = 2$ is used, where h and dr correspond to the smoothing length and the particle distance respectively. The dissipation effects due to viscosity are modeled through the function $\pi_{\mathbf{ij}}$, that is defined as:

$$\pi_{\mathbf{ij}} = \frac{(\boldsymbol{u}_j - \boldsymbol{u}_i) \cdot (\boldsymbol{r}_j - \boldsymbol{r}_i)}{\parallel \boldsymbol{r}_j - \boldsymbol{r}_i \parallel^2} \tag{40}$$

In the volume conservation equation, an additional term is added to avoid spurious high-frequency pressure oscillations, following the work by [31] and extended to the multiphase formulation by [17]. An additional term of this form has actually become a standard in SPH, and this particular model is the so called δ-SPH. The term $\mathbf{D}_{\mathbf{ij}}^{\mathbf{V}}$ is defined as:

$$\mathbf{D}_{\mathbf{ij}}^{\mathbf{V}} = V_i \left[2 \left(1 - \frac{\rho_j}{\rho_i} \right) - \frac{1}{\rho_i} \left(\langle \nabla \rho \rangle_j^L + \langle \nabla \rho \rangle_i^L \right) \cdot (\boldsymbol{r}_j - \boldsymbol{r}_i) \right] \frac{(\boldsymbol{r}_j - \boldsymbol{r}_i)}{\|\boldsymbol{r}_j - \boldsymbol{r}_i\|^2} \tag{41}$$

where $\langle \nabla \rho \rangle_i^L$ represents the renormalized density gradient, as defined by [32]. The value for δ is set always to 0.1, following the value used by [33] based on the study carried out in [31]. Note that the sum of the neighbours is extended to neighbouring particles of the same phase $j \epsilon \chi$.

In the momentum conservation equation, ρ is the fluid density, $\boldsymbol{g}$ represents the gravity, $\boldsymbol{\Omega}$ the surface tension force, p the pressure and μ_χ is the dynamic viscosity of phase χ. The flow velocity, $\boldsymbol{u}$, is defined as the material derivative of a fluid particle position, $\boldsymbol{r}$.

In order to close the system of equations in (35)-(38) a stiff equation of state (39) is needed. In this work a polytropic equation of state is used where γ_χ is the polytropic exponent of phase χ, ρ_{0_χ} represents the reference density of phase χ and p_b represents the background pressure that is set to $p_b = 1$ Pa in all simulations presented in this work. The compressibility of the phase can be adjusted artificially by changing the speed of sound of the phase c_{0_χ} [34].

As the continuity equation is expressed in terms of volume, density is evaluated with a summation formula (38) within phase χ. According to this, the kernel W_{ij}^S is defined for each phase as:

$$W_{ij}^S = \frac{W_{ij}}{\sum_{k \in \chi} W_{ik} V_k} \tag{42}$$

Time integration is performed by means of a predictor-corrector scheme [30]. The Courant-Friedrichs-Lewy (CFL) condition is set to 0.1 to assure time stability.

When surface tension is taken into account an additional term $\boldsymbol{\Omega}$ is added to the momentum equation in Eq. (36) to deal with effects at the interface. This force has been

included in SPH in the same fashion as in [35], and the expression reads:

$$\mathbf{\Omega} = -\frac{T_s}{\rho_i}\sum_j (\boldsymbol{n}_j - \boldsymbol{n}_i)\cdot\nabla W_{ij} V_j\, \boldsymbol{n}_i \tag{43}$$

where T_s is the surface tension coefficient and $\mathbf{n_i}$ represents the local normal vector to the interface of particle i.

Both periodical and wall boundary conditions are set in the corresponding numerical tests carried out in this work.

Periodical boundary conditions are defined such that every generic field f satisfies

$$f(x)|_{\partial\Omega_1} = f(x)|_{\partial\Omega_2} \tag{44}$$

For wall boundary conditions, either slip or no-slip conditions can be imposed.

Boundary integrals methodology is used in this work. The formulation employed here is based on the works by [36] solving these numerically as explained by [30] with the semi-analytical expressions for the kernel obtained by [37] based on [38]

No-slip boundary conditions are imposed at the discrete level in the same fashion as described by [39] for the boundary integrals formulation, such that:

$$\left\langle \frac{\partial \boldsymbol{u}}{\partial \boldsymbol{n}} \right\rangle = \sum_{j\in BE} \left[\frac{(\boldsymbol{I} - \boldsymbol{n}_j \otimes \boldsymbol{n}_j)\ \boldsymbol{u}_{ji}}{|\boldsymbol{r}_{ij}\cdot\boldsymbol{n}_j|} \right] W_{ij}\, V_i\, S_j\,. \tag{45}$$

IV. RESULTS

The generalized eigenvalue problem given by expression (25) is numerically solved using the respective boundary conditions. The solution of this problem gives the dominant eigenvalues and their corresponding eigenfunctions. In parallel, the corresponding SPH simulations are also completed with the same parameters and both results are compared in this section.

First, as the preliminary case, we will solve the viscous 2D Rayleigh-Taylor stability analysis problem with periodic lateral boundary conditions and surface tension. The results will be compared to the well known 1D solution found in the literature.

Hereafter, we will compare the growth rate obtained as being the largest eigenvalue of the linear stability analysis with the growth rate of the velocity interpolation in a fixed point

of the SPH simulation. The comparison will be performed for several Atwood numbers, a wide range of wavenumbers and typical surface tension values.

The completely confined problem, where the lateral boundary conditions will be changed to the no-slip case, is solved by both methodologies. This problem is motivated by the VRTI that appears during the first stage of a vertically accelerated fuel tank typically found in the transport industry. In this particular confined case, the discussion about the meniscus shape and the contact angle will be avoided by assuming no surface tension in the fluid, and consequently the initial SPH and the baseflow interfaces will both be flat everywhere. In this case the dominant part of spectrum and the corresponding eigenvectors obtained after the solution of the eigenvalue problem will be compared for both types of lateral boundary conditions. This change of the spectrum confirms the importance of the 2D formulation, capable of implementing both boundary conditions. This problem will be fully simulated with SPH, and the growth rate of the linear part will be also compared to the results of the eigenvalue problem.

A. VRTI with surface tension and periodic lateral boundary conditions.

1. Linear stability analysis.

In the present section, a linear stability analysis will be performed for the VRTI when the surface tension is added to the problem and quantified by the parameter S. This complete 2D analysis (dominant eigenvalue spectrum and corresponding eigenvectors are computed) includes viscosity, surface tension and finite height and periodic width. Regarding this, we should mention that [10] determined an approximated analytical expression of the dispersion relation for the 1D case that included viscosity, surface tension and finite height, but no eigenvector was represented. The non-dimensional dispersion relation can be expressed as:

$$\sigma = -k^2 + \sqrt{k^4 - k(k^2 S - A_\rho)\tanh(kH)} \tag{46}$$

which gives good results for large wavenumbers. All the computations are performed in a computational domain $H = 1$ and $L = 4$. The number of quadratic mesh nodes and triangular elements is 23145 and 11458 respectively, where the mesh has been refined around the x-axis, see Figure 2.

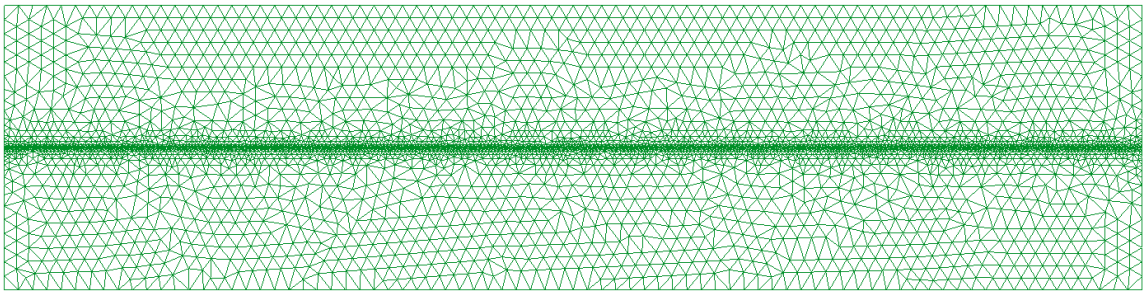


FIG. 2: Mesh used for the 2D viscous simulation.

In Figures 3 and 4 the growth rate has been represented for $L_s = 0.01$ and $H = 1$ as a function of the wavenumber k for two different cases: the first with $A_\rho = A_\mu = 0.2$ and $S = 0.003$, and the second with larger density and viscosity gradients $A_\rho = A_\mu = 0.6$ and more surface tension $S = 0.01$. In both cases, the dispersion relation for the 1D spectral Chebyshev formulation previously presented in [16], but adding the surface tension term as indicated at the end of section III A, was also computed solving the quadratic eigenvalue problem. These results were included as a reference in order to confirm the accuracy of the current 2D formulation and also to evaluate the effect of the surface tension in the problem. Similarly, in the case without surface tension, see [16], all density and viscosity ratios computed present a local maximum that increases with the Atwood number. It can be observed, see Figure 10 in [16] that the higher the Atwood number, the larger the difference between the computed value in 2D and the reference value obtained in the 1D case due to numerical errors caused by the discretization of the density gradient.

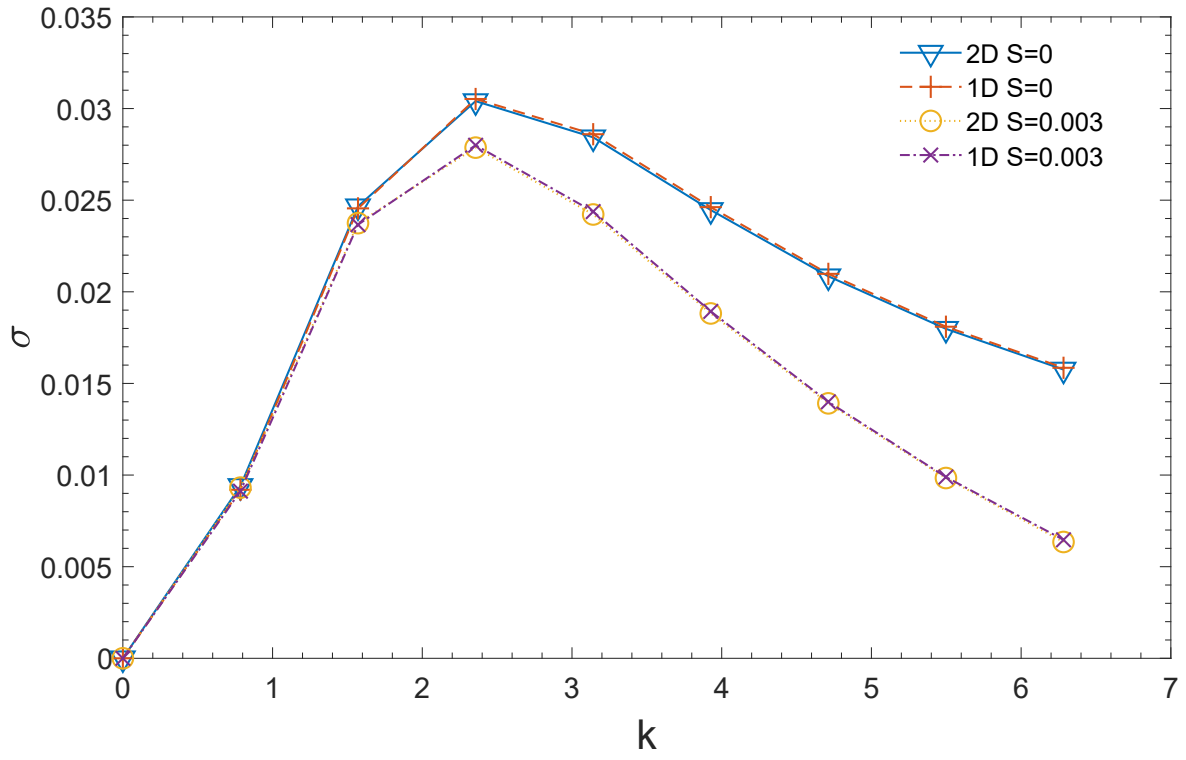


FIG. 3: Growth rate instability as a function of the wave number, for $A_\rho = A_\mu = 0.2$, $L_s = 0.01$, $H = 1$, $S = 0$ and $S = 0.003$.

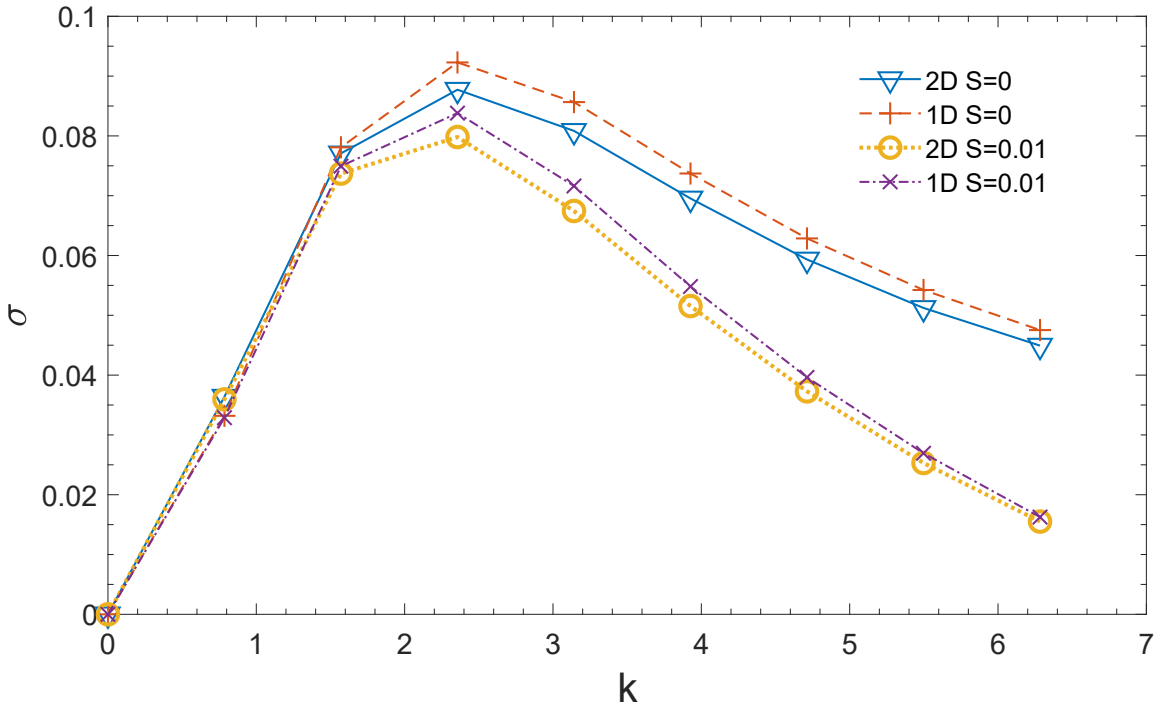


FIG. 4: Growth rate instability as a function of the wave number, for $A_\rho = A_\mu = 0.6$, $L_s = 0.01$, $H = 1$, $S = 0$ and $S = 0.01$.

In Figure 5, the amplitude perturbations corresponding to the eigenvalue are represented for all the fluid variables for an interface scale length $L_s = 0.01$. The horizontal periodicity of the structure is clearly observable. The wavenumber is obtained after measuring the wave length of the structure $\lambda_x = 2$ in the picture, and then computing the wavenumber as $k = 2\pi/\lambda_x = \pi$.

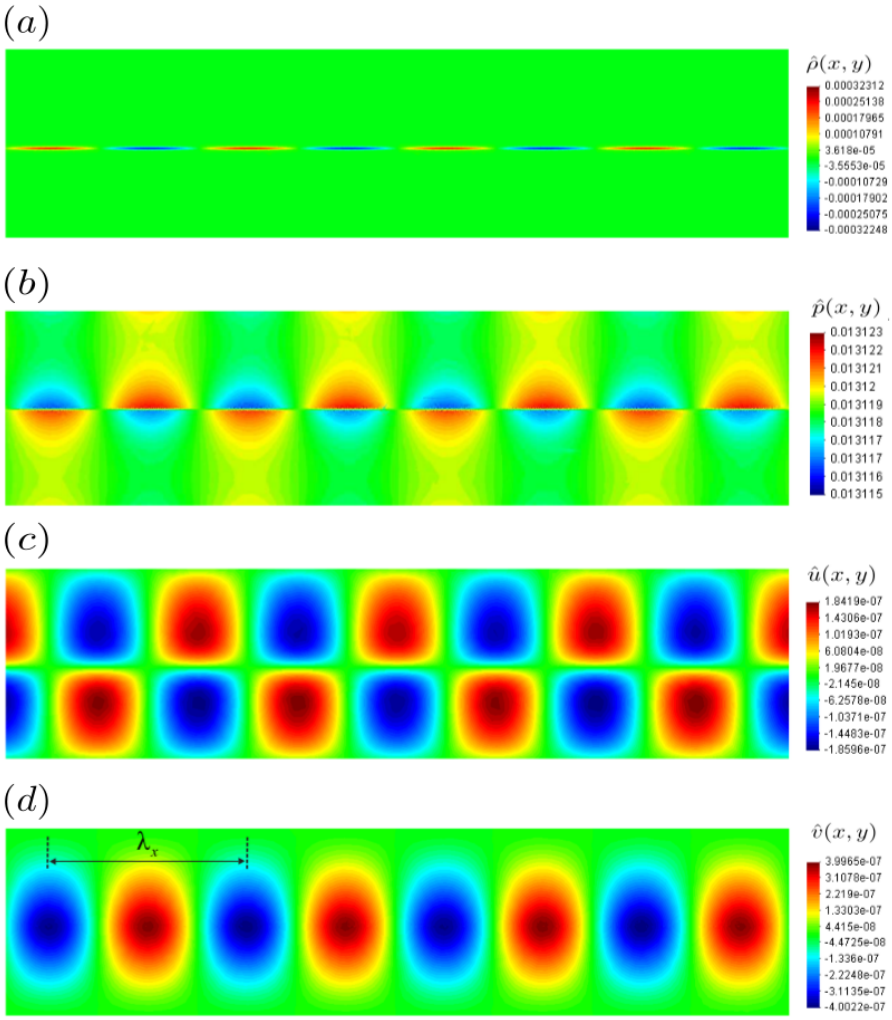


FIG. 5: Perturbation amplitude for the case $k = \pi$, $2H = 2$, $2L = 8$ and $A_\mu = A_\rho = 0.2$ and $S = 0.003$. From top to bottom the amplitude perturbations are represented for the density (a), pressure (b), horizontal velocity (c) and vertical velocity (d). All computations were performed using the interface parameter $L_s = 0.01$.

2. SPH simulation of the VRTI.

In this section the VRTI will be simulated using the non-linear SPH multiphase formulation, see section III B. Most numerical approaches to the simulation of the VRTI are normally limited to visually correct snapshots of the flow evolution and the confirmation of the robustness and speed of the multiphase formulation. Very few SPH approaches

[23, 40] contain a detailed quantitative comparison to other classical numerical formulations where well established results such as the growth rate of the linear part of the VRTI are monitored. Consequently, the objective of this section is not only to present the results of the SPH formulation, but also to compare the initial evolution of the SPH solution with the results presented by the 1D spectral and the 2D finite element validated formulations in terms of growth rate. The comparison will be performed for a wide range of Atwood and wavenumbers, with and without surface tension.

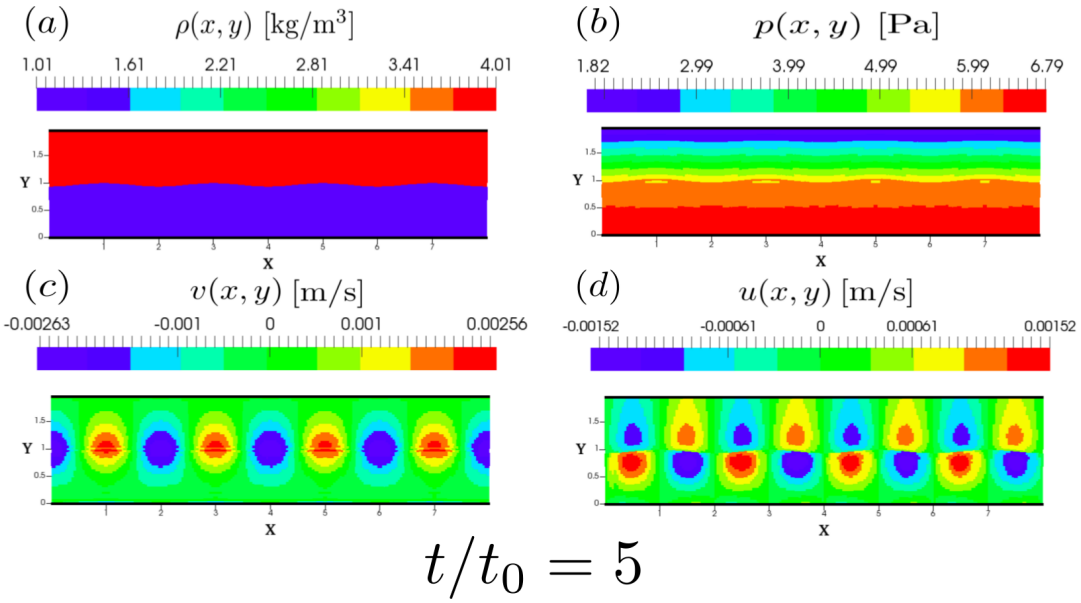


FIG. 6: Snapshots of the SPH simulation at $t/t_0 = 5$ for the case $k = \pi$, $2H = 2$, $2L = 8$ and $A_\mu = A_\rho = 0.6$. The 2D fields are represented for the density (a), pressure (b), vertical velocity (c) and horizontal velocity (d).

To perform this task, a fixed point with coordinates $(x, y) = (0, H/10)$, is selected to monitor the evolution of the interpolated velocity of the surrounding particles. To trigger the VRTI, an initial perturbation $\hat{v}_0(x, y)$ of magnitude $\epsilon \ll \sqrt{gH}$ is added to the initial flow. This perturbation is horizontally periodic with a wavenumber k and exponentially decaying on the vertical axis, and consequently we expect to trigger the instability associated with that particular wavenumber. The expression of the initial vertical velocity perturbation is:

$$\hat{v}_0(x,y) = \epsilon \cos(kx) \exp\left(-\left|\frac{y}{(y+H)(y-H)}\right|\right) \tag{47}$$

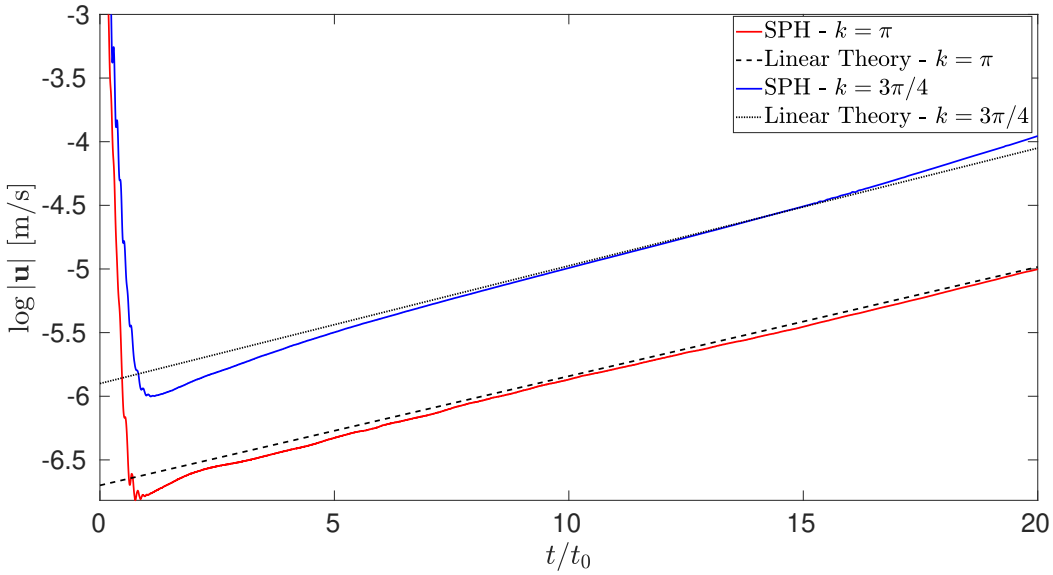


FIG. 7: Comparison of the evolution of the velocity at $(x, y) = (0, H/10)$ when the SPH simulations are compared to the linear stability analysis results represented by the dotted lines for $A_\rho = A_\rho = 0.6$ and $k = \pi$ (red) and $k = 3\pi/4$ (blue).

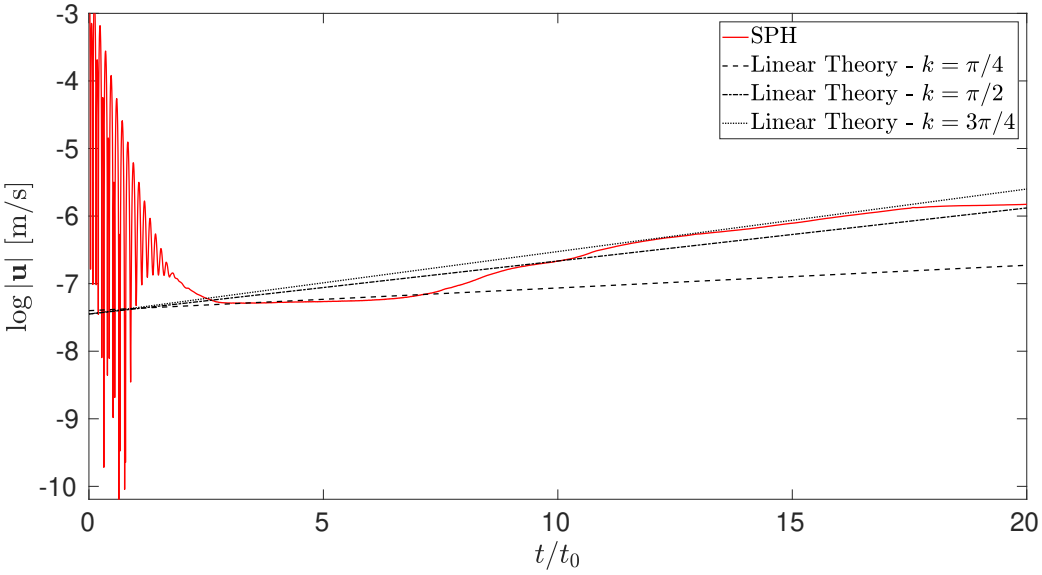


FIG. 8: Comparison of the evolution of the velocity at $(x, y) = (0, H/10)$ when the initial state of the SPH simulation is perturbed with $k = \pi/4$. Results are compared to three reference results of the linear stability analysis represented by the dotted lines for $A_\rho = A_\rho = 0.6$ and $k = \pi/4, \pi/2$ and $3\pi/4$

In Figure 6 a snapshot of the evolution of the pressure, density and velocity fields is shown at time $t/t_0 = 5$, when the initial flow is excited with $k = \pi$ and both Atwood numbers are equal $A_\rho = A_\mu = 0.6$. At this time step, the velocity field is immersed in the linear regime after the initial oscillations caused by the combination of the particle setup and the weakly compressible assumption. It is worth noting that the velocity perturbations corresponding to the most unstable mode obtained after the linear stability analysis, see Figure 5, matching well with the velocity snapshots of the SPH simulation. Pressure and density include the non-zero initial field and consequently are not directly comparable.

An example of the time evolution of the velocity for the case with $A_\rho = A_\mu = 0.6$ and wave numbers $k = 3\pi/4$ and $k = \pi$ is shown in Figure 7. As can be seen, at the beginning the initial perturbation is hidden behind the noise created by the pressure field trying to satisfy the weakly compressible assumption which creates a few oscillations. Once the particles have settled down and the pressure field stabilizes $t/t_0 \sim 1.5$, the perturbation triggers the VRTI and the system evolves in time with a clean, growing linear regime. As can be observed in the figure, the slope of this signal is parallel to the growth rate computed by the linear

stability analysis, which indicates excellent matching with the linear theory.

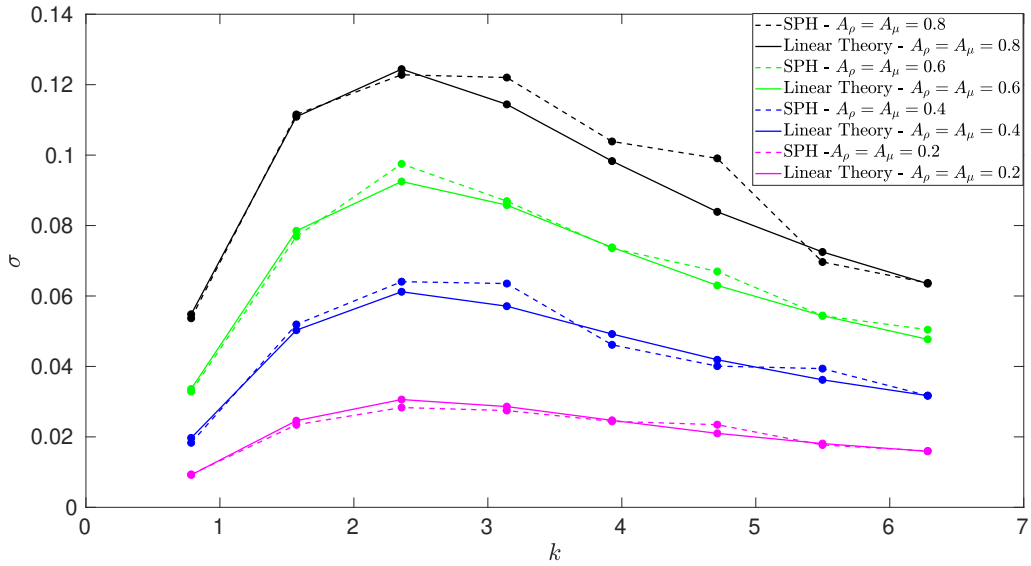


FIG. 9: Growth rate of the vertical velocity at the fixed point $x = 0$, $y = H/10$ versus wavenumber for different values of the density and viscosity Atwood numbers $A_\rho = A_\mu$, $2H = 4$ and $2L = 1$. The growth rate is compared to the values predicted by the linear stability analysis theory[10].

A complete comparison between the growth rates obtained from the transient slopes of the SPH simulations and the corresponding values obtained from the linear stability analysis is shown in Figure 9. The comparison is performed using eight wave numbers in the interval $k \in [0, 2\pi]$ and four density-viscosity Atwood numbers $A_\rho = A_\mu = 0.2, 0.4, 0.6, 0.8$. With the exception of a very few points obtained for the largest Atwood number, the agreement obtained is reasonable and the maximum of each curve is always detected at $k \approx 3\pi/4$. The detection and identification of the slopes of the linear intervals during the SPH simulation is a numerically sensitive task that can also be considered a source of error.

Figure 8 represents what occurs when the wave number of the initial perturbation $k = \pi/4$ is not close to the wave number $k_{max} \approx 3\pi/4$ that gives the maximum growth rate of the instability. After the adaptation interval, three clearly distinguishable slopes are present with a transient between them showing that the dynamical evolution of the linear system jumps from the perturbed mode to the next most unstable mode until it reaches k_{max}. The first slope matches the growth rate of the initial excitation $k = \pi/4$, but around time

$t/t_0 \sim 7.4$, the system evolves to the second mode with $k = \pi/2$ and then at $t/t_0 \sim 12$ it finally jumps to the wave number that gives the maximum growth rate at $k = k_{max} = 3\pi/4$.

In Figure 10 the growth rate of the perturbation is represented against the density Atwood number $A_\rho \in [0.1, 0.9]$ for the case $2H = 2$, $2L = 8$ and $k = 3\pi/4$, being the viscosity equal to 1 in both phases and consequently $A_\mu = 0$. As can be appreciated the agreement with the results presented in [10] is excellent. A similar computation is performed in the same Atwood range but in this case $A_\rho = A_\mu$ and $k = 3\pi/4$, the results predicted by SPH approximate the linear stability calculations well.

When the SPH surface tension model described in section III B is added to the problem, the SPH results still obtain a good prediction and capture the instability reduction due to the surface tension contribution, see Figure 11. Alternatively, a second simplified implementation of the surface tension based on equations (19),(23) and (24) was also performed in SPH. Combining those equations, we can consider that the presence of surface tension is equivalent to a gravity reduction given by the equation:

$$g_S = g(1 - \frac{k^2 S}{A_\rho}) \tag{48}$$

where g_S is the gravity value when the surface tension S is included in the model and the second derivative has been replaced by $-k^2$ assuming during this linear stage a horizontal periodicity of the flow with the same wave number as the initial excitation. This simplification is only valid for comparing the results during the linear regime also computed by the stability analysis, and no realistic results are expected during the nonlinear evolution of the SPH simulation. However, the results obtained by this simplified implementation of the surface tension approximate the ones from the linear theory very well, with little underprediction for the largest growth rate.

In Figure 11 the case without surface tension has been added to the graph to observe the stability decreases for large wave numbers when surface tension is present, showing that the surface tension has a stabilizing effect on the VRTI.

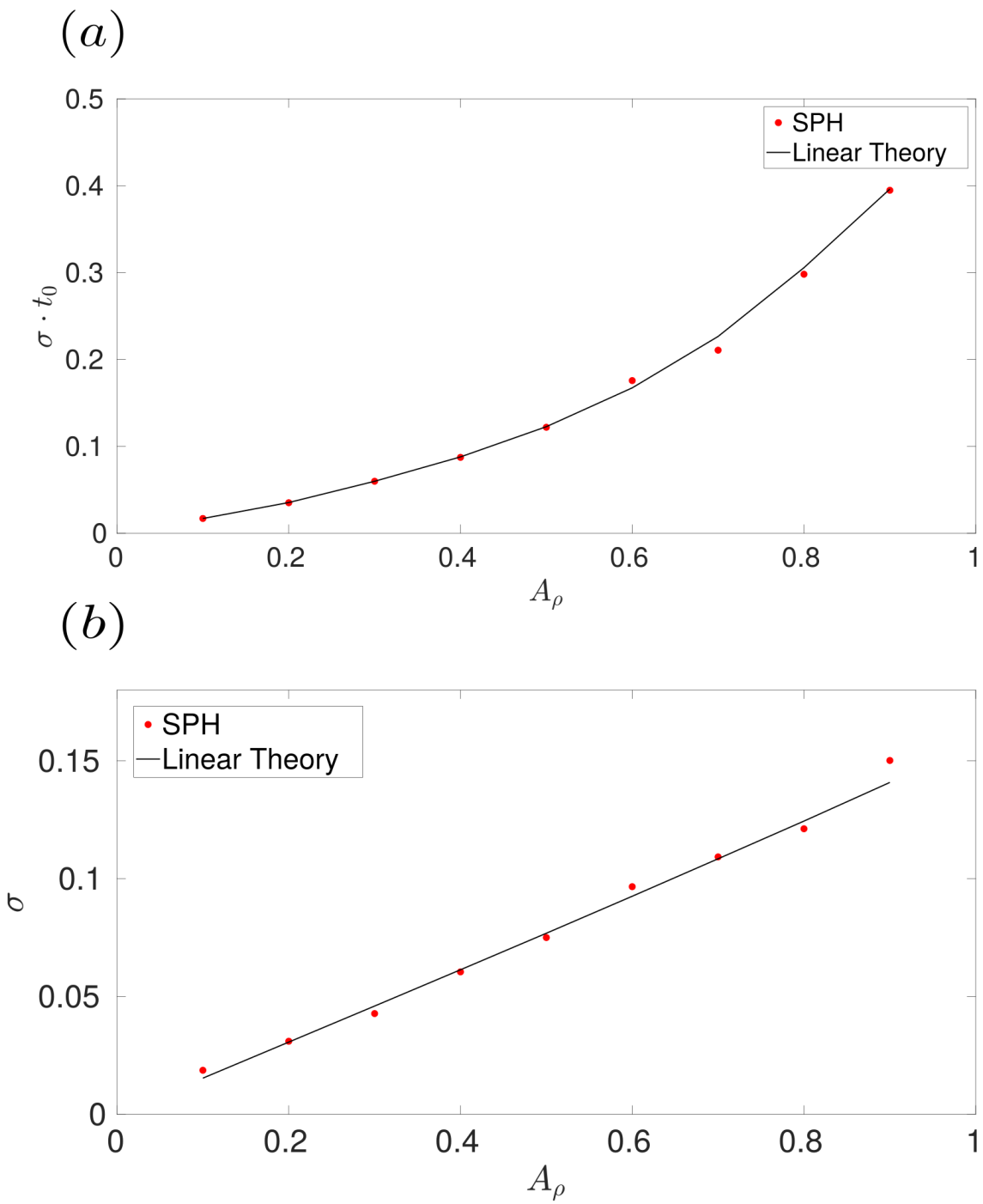


FIG. 10: Growth rate versus density Atwood number obtained in a computational domain $2H = 8$, $2L = 2$. (a): $A_\mu = 0$ and $k = \pi/4$, note that since $A_\mu = 0$ the growth rate σ has to be adimensionalized with t_0. (b): $A_\mu = A_\rho$, and $k = 3\pi/4$. The values predicted by reference [10] are also plotted for comparison.

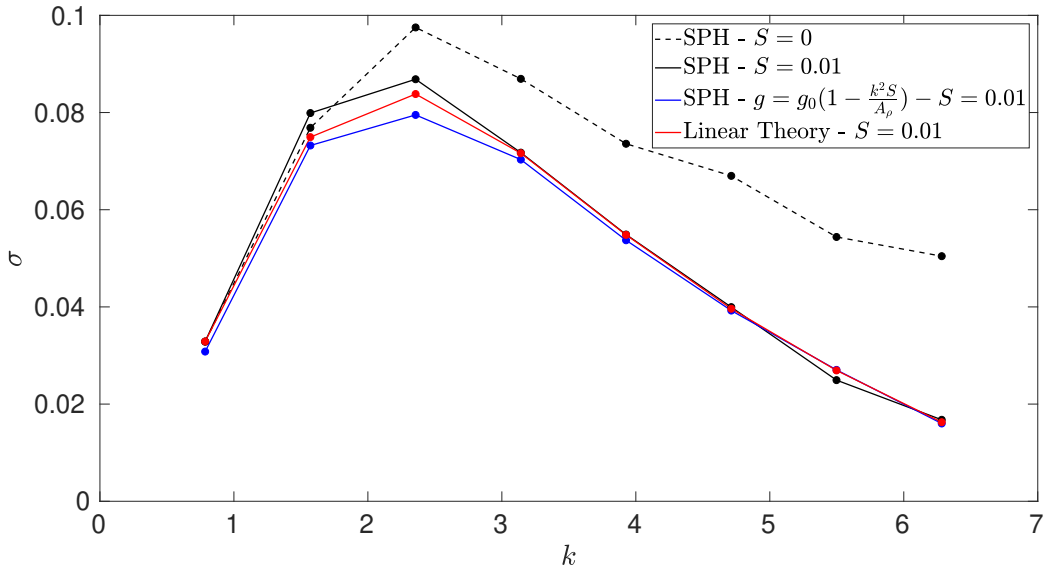


FIG. 11: Growth rate versus wave number for $A_\rho = A_\mu = 0.6$ with and without surface tension. The growth rate is compared to the values predicted by the linear stability analysis theory.

B. VRTI in a confined tank with no-slip lateral boundary conditions.

1. *Linear stability analysis.*

In this section the same linear stability analysis that has been performed in subsection IV A 1 with periodic boundary conditions is now solved with no-slip velocity boundary conditions in the right and left boundaries at $x = \pm L$, see the bottom part of Figure 1. As a non-periodic assumption is allowed in the horizontal direction, the results of this analysis cannot be computed any more using the classical 1D spectral stability analysis, see [16], and can only be performed using a 2D formulation. In Figures 12 and 13 the spectrum obtained in this no-slip case is compared to the previous periodic case for two different geometries, the first one being $(2H, 2L) = (2, 8)$ and the second being $(2H, 2L) = (4, 1)$. As can be observed, the values of the most unstable modes and the vertical velocity perturbation associated with those eigenvalues clearly transformed when the lateral boundary conditions are changed. As expected, the velocity modes associated with the confined case studied in this section satisfy the no-slip boundary conditions imposed, and the modes are attenuated close to the lateral

walls.

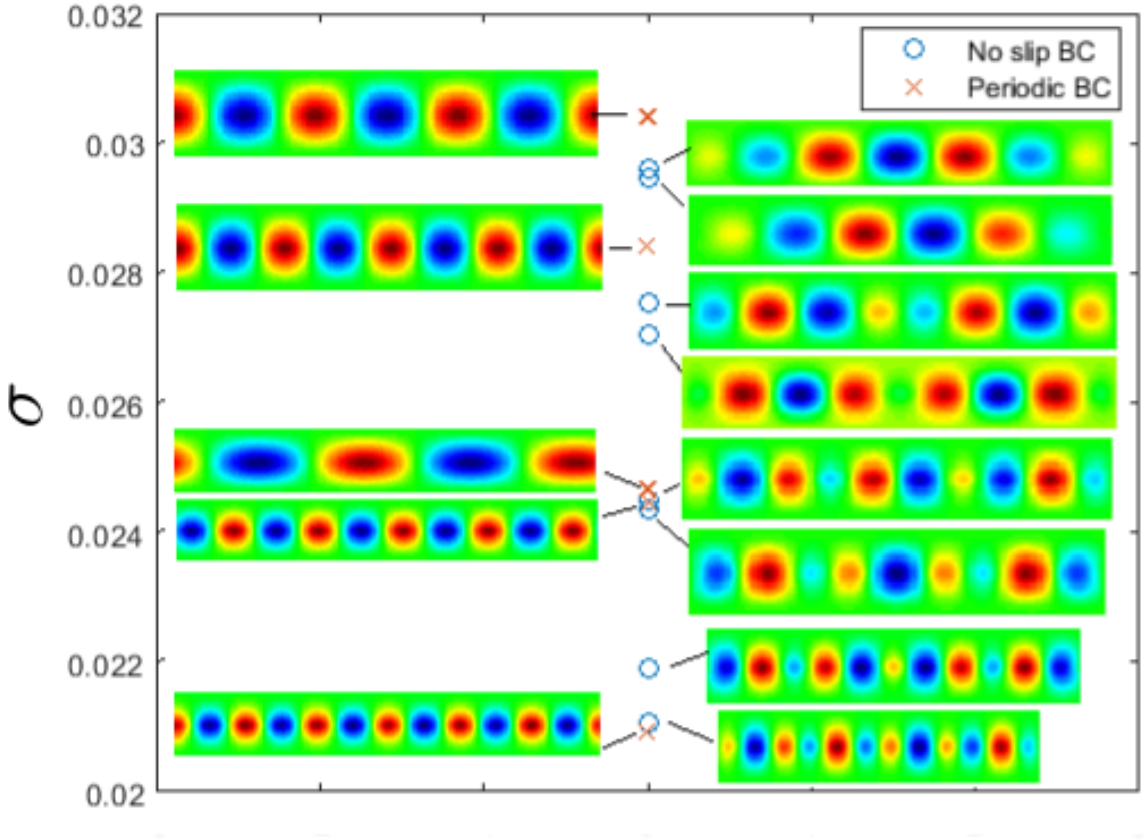


FIG. 12: Comparison of the spectrum and the vertical velocity perturbations associated to the most unstable eigenvalues when periodic and homogeneous no-slip lateral boundary conditions are used for $A_\rho = A_\mu = 0.2$, $2H = 2$ and $2L = 8$.

An important observation when no slip boundary conditions are used in a domain with horizontal fixed length is that we cannot assume a clear spatial periodicity in the horizontal direction, and consequently no wave number can be associated to the different modes. This clearly indicates that changing the lateral boundary conditions implies the absence of horizontal periodicity.

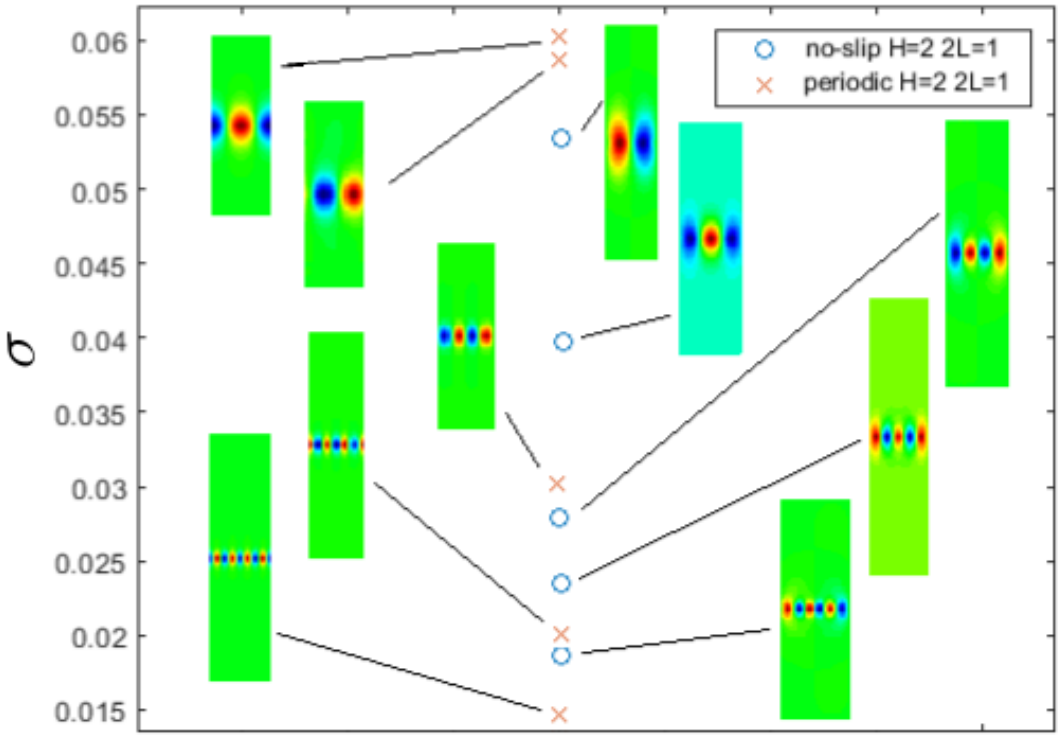


FIG. 13: Comparison of the spectrum and the vertical velocity perturbations associated with the most unstable eigenvalues when periodic and homogeneous no-slip lateral boundary conditions for $A_\rho = 0.7621$, $A_\mu = 0$, $2H = 4$ and $2L = 1$.

2. SPH simulation of the VRTI in a confined tank.

In this section, the SPH formulation will be applied to the tank case. Despite having shown in the previous section that when lateral boundaries are changed to no-slip no clear wavenumber is identified in the eigenvectors of the linear stability analysis, and an approximate wavenumber is necessary to build the initial condition of the SPH problem. In order to compare this with the linear stability analysis, see Figures 12 and 13, the baseflow is excited according to the following expression:

$$\hat{v}_0(x, y) = \epsilon \sin(kx) \exp\left(-\left|\frac{y}{(y+H)(y-H)}\right|\right) \tag{49}$$

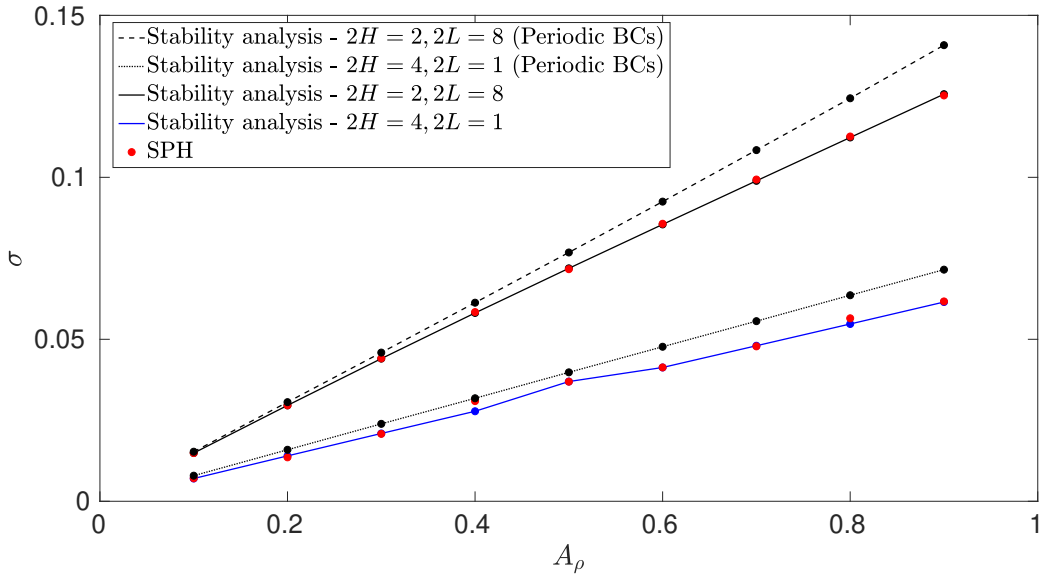


FIG. 14: Growth rate of the vertical velocity at the fixed point $(x, y) = (0, H/10)$ for different values of the density and viscosity Atwood numbers $A_\mu = A_\rho$, $2H = 2$ and 4, $2L = 8$ and 1. The growth rate is compared to the values predicted by the linear stability analysis theory.

where the initial perturbation $\hat{v}_0$ has been selected in order to satisfy the no-slip boundary condition at $x = \pm L$.

In Figure 14, the growth rates obtained measuring the slope of the linear velocity growth at $(x, y) = (0, H/10)$ are compared, for different Atwood numbers, to the most unstable eigenvalue obtained from the linear analysis of both geometries previously analyzed in section IV B 1. For the sake of simplicity, both the viscosity and density Atwood numbers were equal $A_\rho = A_\mu$. As can be observed, excellent agreement is obtained for all Atwood numbers. In order to confirm the reduction in terms of growth rate, the previous results with periodic boundary conditions are also plotted in Figure 14. As expected from the comparison performed using the linear stability analysis in Figures 12 and 13, the linear part presents a lower growth rate (smaller eigenvalue) than the periodic version. We conclude that the presence of the lateral walls decreases the growth rate of the VRTI as they increase the viscous action.

V. CONCLUSIONS

The most important conclusions obtained in this work are the following:

- The RTI instability has been numerically studied in 2D with regularized density and viscosity according to a hyperbolic tangent function. The Navier-Stokes equations are linearized and discretized using the finite element method, and the final generalized eigenvalue problem obtained is solved using the Arnoldi method. The model introduces the possibility of confining the fluid either in the vertical or horizontal directions, adding viscosity to both phases and introducing surface tension to the interface.

- The classical 1D formulation is limited to those cases where the horizontal coordinate is periodic, in contrast with the 2D formulation assumed here, which permits studying more general cases, as for example those cases where the fluids are confined and no-slip boundary conditions are necessary for the lateral walls. This situation appears in engineering applications as a Rayleigh-Taylor instability, which is frequently found in accelerating fuel tanks.

- The VRTI instability has been also been simulated with a lagrangian particle method called the multiphase WCSPH. This method is clearly non-linear but is able to capture the linear regime that is present at the first stage of the simulation. The multiphase SPH formulation presents a robust stability for a wide range of densities and viscosities, gives the possibility of implementing both the no-slip and the periodic boundary conditions, and contains a surface tension model for the interface.

- The matching between both formulations is very good in a relevant range of wavenumbers, indicating that a lagrangian formulation is able to predict not only the growth rate values and the corresponding structures identified with the eigenvalues and the eigenvectors of the generalized LNSE, but also captures the evolution of the internal dynamics of the different growing modes involved in the Rayleigh-Taylor instability.

- Both formulations were also compared with the results provided by [10] obtaining very good agreement for a wide range of density and viscosity ratios.

- The 2D formulation allows for performing the same analysis in geometries more

complex than the simple rectangular tank used here, or even in realistic baffled fuel tanks like the ones used in the aircraft industry.

Acknowledgements

The research leading to these results was undertaken as part of the SLOWD project, which has received funding from the European Union's Horizon 2020 research and innovation programme under grant agreement No. 815044. Leo M. González acknowledges the financial support from the Spanish Ministry for Science, Innovation and Universities (MCIU) under grant RTI2018-096791-B-C21 *Hidrodinámica de elementos de amortiguamiento del movimiento de aerogeneradores flotantes*. All the authors would like to thank Mr. Ciaran Stone for his valuable assistance during the preparation of this manuscript.

---

[1] Odd M. Faltinsen and Alexander N. Timokha, *Sloshing* (Cambridge, 2009).

[2] Lord Rayleigh, "Investigation of the character of the equilibrium of an incompressible heavy fluid of variable density," Proc. London Math Soc **s1-14**, 170–177 (1883).

[3] G. I. Taylor, "Instability of liquid surfaces when accelerated in a direction perpendicular to their planes," Proc. R. Soc. London **192**, 201 (1950).

[4] R. E. Rosensweig, Y. Hirota, S. Tsuda, and K. Raj, "Study of audio speakers containing ferrofluid," J. Phys.: Condens. Matter **20**, 204147 (2008).

[5] C. Harig, P. Molnar, and G. A. Houseman, "Rayleigh-Taylor instability under a shear stress free top boundary condition and its relevance to removal of mantle lithosphere from beneath the sierra nevada," Tectonics **27**, TC6019 (2008).

[6] T. M. Willey, K. Champley, R. Hodgin, L. Lauderbach, M. Bagge-Hansen, C. May, N. Sanchez, B. J. Jensen, A. Iverson, and T. van Buuren, "X-ray imaging and 3D reconstruction of in-flight exploding foil initiation flyers," J. Appl. Phys. **119**, 235901 (2016).

[7] T. G. Theofanous, "Aerobreakup of newtonian and viscoelastic liquids," Annu. Rev. Fluid Mech. **43**, 661 (2011).

[8] A. A. Blinova, M. M. Romanova, and R. V. E. Lovelace, "Boundary between stable and unstable regimes of accretion. ordered and chaotic unstable regimes," Mon. Not. R. Astron. Soc. **459**, 2354 (2016).

[9] A. Tavakoli, L. Hadzievski, and D. D. Tskhakayab, "Rayleigh-Taylor instability of magnetized density transition layer," Phys. Plasmas **7**, 89–93 (1999).

[10] K. O. Mikaelian, "Rayleigh-Taylor instability in finite-thickness fluids with viscosity and surface tension," Phys. Rev. E **54**, 3676 (1996).

[11] M. H. Obied Allah, "Effects of stratification, surface tension and rigid planes on Rayleigh-Taylor instability," Ind. J. Pure Appl. Math. **32**, 303 (2001).

[12] R. V. Morgan, O. A. Likhachev, and J. W. Jacobs, "Rarefaction-driven Rayleigh-Taylor instability I: Diffuse-interface linear stability measurements and theory," J. Fluid Mech. **791**, 34–60 (2016).

[13] R. E. Duff, F. H. Harlow, and C. W. Hirt, "Effects of stratification, surface tension and rigid planes on Rayleigh-Taylor instability," Phys. Fluids **5**, 417–425 (1962).

[14] C. X. Yu, C. Xue, J. Liu, X. Y. Hu, Y. Y. Liu, W. H. Ye, L. F. Wang, J. F. Wu, and Z. F. Fan, "Multiple eigenmodes of the Rayleigh-Taylor instability observed for a fluid interface with smoothly varying density," Phys. Rev. E **97**, 013102 (2018).

[15] M. Dong, Z. Fan, and C. Yu, "Multiple eigenmodes of the Rayleigh-Taylor instability observed for a fluid interface with smoothly varying density. II. Asymptotic solution and its interpretation," Phys. Rev. E **99**, 013109 (2019).

[16] L. M. González-Gutiérrez and A. de Andrea González, "Numerical computation of the Rayleigh-Taylor instability for a viscous fluid with regularized interface properties," Phys. Review E **100**, 013101 (2019).

[17] I. Hammani, S. Marrone, A. Colagrossi, and G. Oger, "Detailed study of the extension of the δ-SPH model to multi-phase flow," Journal of Computational Physics **368**, 113189 (2020).

[18] SJ Cummins and M Rudman, "An SPH projection method," J. Comput. Phys **152**, 584 (1999).

[19] Alexandre M Tartakovsky and Paul Meakin, "A smoothed particle hydrodynamics model for miscible flow in three-dimensional fractures and the two-dimensional Rayleigh–Taylor instability," Journal of Computational Physics **207**, 610–624 (2005).

[20] Nicolas Grenier, Matteo Antuono, Andrea Colagrossi, David Le Touzé, and B Alessandrini, "An Hamiltonian interface SPH formulation for multi-fluid and free surface flows," Journal of Computational Physics **228**, 8380–8393 (2009).

[21] K. Szewc, A. Tanière, and J.P. Minier, "A study on application of smoothed particle

hydrodynamics to multi-phase flows," International Journal of Nonlinear Sciences and Numerical Simulation **13**, 383–395 (2012).

[22] Shadloo MS and Yildiz M., "ISPH modelling of Rayleigh-Taylor instability," in *6th international SPHERIC workshop proceedings* (2011).

[23] MS Shadloo, Amir Zainali, and M Yildiz, "Simulation of single mode Rayleigh–Taylor instability by SPH method," Computational Mechanics **51**, 699–715 (2013).

[24] R. Hide, "The character of the equilibrium of a heavy, viscous, incompressible, rotating fluids of variable density. i. general theory," Quart. J. Mech. Appl. Math. **9**, 22–34 (1955).

[25] S. Chandrasekhar, *Hydrodynamic and Hydromagnetic Stability* (Dover, New-York, 1981).

[26] L. M. González, V. Theofilis V, and R. Gómez-Blanco, "Finite-element numerical methods for viscous incompressible BiGlobal linear instability analysis on unstructured meshes," AIAA Journal **45**, 840–855 (2007).

[27] V. Theofilis, "Advances in global linear instability analysis of nonparallel and three-dimensional flows," Prog. Aero. Sci. **39**, 249–315 (2003).

[28] V. Theofilis, P. W. Duck, and J. Owen, "Viscous linear stability analysis of rectangular duct and cavity flows," J. Fluid. Mech. **505**, 249–286 (2004).

[29] Y. Saad, "Variations of Arnoldi's method for computing eigenelements of large unsymmetric matrices," Lin. Algebra. Appl. **34**, 269–295 (1980).

[30] Jose L Cercos-Pita, "AQUAgpusph, a new free 3D SPH solver accelerated with OpenCL," Computer Physics Communications **192**, 295–312 (2015).

[31] M. Antuono, A. Colagrossi, and S. Marrone, "Numerical diffusive terms in weakly-compressible SPH schemes," Computer Physics Communications (2012).

[32] P. W. Randles and L. D. Libersky, "Smoothed particle hydrodynamics: Some recent improvements and applications," Computer Methods in Applied Mechanics and Engineering (1996).

[33] M. Antuono, S. Marrone, A. Colagrossi, and B. Bouscasse, "Energy balance in the δ-SPH scheme," Computer methods in Applied Mechanics and Engineering (2015).

[34] M. Antuono, A. Colagrossi, S. Marrone, and D. Molteni, "Free-surface flows solved by means of SPH schemes with numerical diffusive terms," Computer Physics Communications (2010).

[35] Joseph P. Morris, "Simulating surface tension with smoothed particle hydrodynamics," Numerical Methods in Fluids (2000).

[36] M. Ferrand, D.R. Laurence, B.D. Rogers, D. Violeau, and C. Kassiotis, "Unified semi-analytical wall boundary conditions for inviscid laminar or turbulent flows in the meshless SPH method," International Journal for Numerical Methods in Fluids (2013).

[37] J. Calderon-Sanchez, J.L. Cercos-Pita, and D. Duque, "A geometric formulation of the shepard renormalization factor," Computers & Fluids **183**, 16 – 27 (2019).

[38] J Feldman and J Bonet, "Dynamic refinement and boundary contact forces in SPH with applications in fluid flow problems," International Journal for Numerical Methods in Engineering **72**, 295–324 (2007).

[39] L Chiron, Matthieu De Leffe, Guillaume Oger, and David Le Touzé, "Fast and accurate SPH modelling of 3d complex wall boundaries in viscous and non viscous flows," Computer Physics Communications **234**, 93–111 (2019).

[40] A. Rahmat, N. Tofighi, M.S. Shadloo, and M. Yildiz, "Numerical simulation of wall bounded and electrically excited Rayleigh–Taylor instability using incompressible smoothed particle hydrodynamics," Colloids and Surfaces A: Physicochem. Eng. Aspects **460**, 60–70 (2014).

Publication 8 (P8)

Marco Pizzoli, Francesco Saltari, Franco Mastroddi, **Jon Martínez-Carrascal** and Leo M. González-Gutiérrez (2022). Nonlinear reduced order model for vertical sloshing by employing neural networks. Nonlinear Dynamics, 107 1469–1478, 2022. DOI: https://doi.org/10.1007/s11071-021-06668-w. 8 citations. JCR(2021): 5.741, Engineering, Mechanical (Q1) and Mechanics (Q1).

Nonlinear reduced-order model for vertical sloshing by employing neural networks

Marco Pizzoli[1], Francesco Saltari[1], Franco Mastroddi[1], Jon Martinez-Carrascal[2] and Leo M. González-Gutiérrez[2]

[1] Sapienza University of Rome, Department of Mechanical and Aerospace Engineering, Rome, Italy
franco.mastroddi@uniroma1.it
[2] Universidad Politécnica de Madrid, Naval Architecture Department, Madrid, Spain

Abstract. The aim of this work is to provide a reduced order model to describe the dissipative behaviour of nonlinear vertical sloshing involving Rayleigh-Taylor instability by means of a feed forward neural network. A 1 degree of freedom system is taken into account as representative of fluid structure interaction problem. Sloshing has been replaced by an equivalent mechanical model, namely a boxed-in bouncing ball with parameters suitably tuned with performed experiments. A large data set, consisting of a long simulation of the bouncing ball model with pseudo-periodic motion of the boundary condition spanning different values of oscillation amplitude and frequency, is used to train the neural network. The obtained neural network model has been included in a Simulink® environment for closed loop fluid structure interaction simulations showing promising performances for perspective integration in complex structural system.

Keywords: Sloshing · Nonlinear Dynamics · Neural Networks.

1 Introduction

Vertical sloshing is a phenomenon that occurs on structures that undergo strong vertical accelerations. Among these we find the aeronautical structures that withstand load occurring from gusts, turbulence and landing impacts. The jolt of fuel generally stowed in the wings caused by vertical accelerations is coupled with the structural dynamics of the aircraft. This type of sloshing is well known to provide a noticeable increase in structural damping but nevertheless remains generally not modeled in the design phase of modern aircraft. This work is therefore part of the research activity within the European project H2020 SLOshing Wing Dynamics (SLOWD) and aims at providing Reduced Order Models (ROMs) for the study of slosh dynamics (Ref. [1]). Vertical slosh dynamics is one of the possible dynamics of the fluid stowed in the tanks which, when it occurs, manifests different characteristics compared to the classic sloshing, generally occurring with rotations and lateral motion of the tank. The latter generates standing waves inside the cavity that provide dynamic coupling with structure and possible

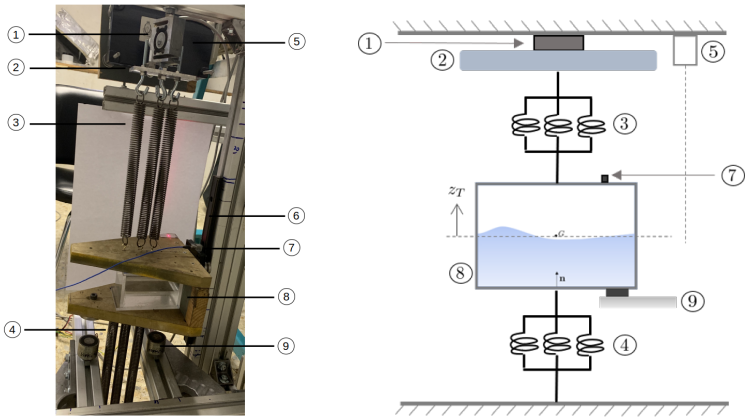
modification of flutter margins. Specifically, the effects of sloshing on aircraft aeroelastic flutter stability was considered in Refs. [2, 3]. On the other hand, the subject of this paper is sloshing induced by high vertical acceleration of the tank, hence perpendicular to the free surface. As long as the acceleration is kept below a certain threshold the free surface does not break. However, the crossing of this acceleration threshold triggers Rayleigh Taylor instabilities (Ref. [4]), determining a chaotic flow regime with air/water mixing. Turbulence, impacts and the continuous generation of the free surface cause additional dissipation of energy (Refs. [5, 6]). The total balancing of elastic potential energy and fluid energy results in a noticeable increase in the effective damping of the structural motion. Moreover, considering vertical harmonic motions, it would be noticeable that the dissipative characteristics depend on the amplitude of the motion and on the frequency.
This work involves the use of acceleration data from sloshing experiments carried out in the laboratories of the *Universidad Politécnica de Madrid* (UPM). The experimental object consists of an elastically scaled single degree of freedom mass-spring system coupled with the slosh dynamics within a hydrodynamically scaled tank. An equivalent mechanical model of a bouncing ball is then used to emulate the fluid behavior inside the tank (specifically the impacts with the tank wall) and provide a numerical model of a tank isolated from the structure on which it is possible to perform simulations with seismic excitation. Indeed, classical sloshing ROMs are intrinsically based on potential fluid theory or small lateral perturbations [7–10] and, the identification of impulsive forces that vertical sloshing dynamics provides is not covered by these models. On the other hand, the main interests of fluid dynamics is addressed on the study of Rayleigh Taylor instabilities and Faraday waves phenomena [8], thus focusing more on getting the stability margins rather than providing ROMs for multi-disciplinary analyses. As far as it concerns the bouncing ball model, in the framework of SLOWD, a one-free-parameter model has been recently proposed in Ref. [11]. However, the model presented in Ref. [11] provides infinitesimal-time impulsive sloshing forces making it not fitting for its use in the neural network framework, thus requiring the introduction of a further model with more extensive features. However, it is worth specifying that the bouncing ball model being introduced in this paper replaces what in the authors' minds will have to be represented either by a long experimental campaign with different arrangements for a complete investigation of the behavior of the fluid or by Computational Fluid Dynamics (CFD) simulations. Finally in the last part of the paper, we will present a reduced order model based on neural networks. Indeed, The use of neural network is getting attention in providing ROM for fluid structure interaction (FSI) as it was already done for external aerodynamics in Ref. [12]. Artificial neural network can be seen as a parallel distributed processors made up of the so called neurons: simple processing units, having the natural capability of storing accumulated knowledge, and then, make it available for subsequent use. In particular, knowledge is acquired by the network from its environment through a *learning process*, and then stored by synaptic weights. Due to their useful

properties and capabilities (Ref. [13]), neural networks are increasingly used in nonlinear system identification. Indeed, they are a powerful tool for approximating nonlinear dynamic systems, even when the system structure is unknown and only input–output data are available, thus allowing a sort of generalized black-box modeling. Specifically, the sloshing forces will be estimated on the basis of the unsteady boundary condition time series. The feed forward natural network (Ref. [14]) is trained with an appropriate data series (consisting of motion of the tank and forces provided by bouncing ball model) spanning different values of frequencies and amplitude in order to provide a complete characterization of the fluid dissipative behaviour. Once the neural network is identified and integrated in the simulation framework, the results provide a good agreement with simulations with the bouncing ball model and experiments as well.

2 Experimental set-up and related experiments

In order to scale down the actual wing to the SDOF tests it is important to consider the dimensional analysis of the problem. Applying the Π theorem to a reference variable [15], for example the dissipated power by the fluid, one can find a dimensional relation between this variable and several non-dimensional numbers, such as, the Reynolds number, Froude number, filling level, etc. It is common practice in sloshing problems to perform a Froude scaling [15] where $Fr = \sqrt{w_0^2 h/Ng}$ is defined based on the maximum acceleration of the problem which is N times the gravity. In the Froude number definition, w_0 is the characteristic angular frequency of the problem, h represents the height of the tank, Ng is the maximum acceleration of the problem, being $N \approx 10$ in our case. Then, a perfect geometrical scaling parameter is considered $\lambda = h_{SDOF}/h_W$ defined as the ratio between the heights of the SDOF tank and the wing tank. For the SDOF sloshing tests, a 1:5 scale was selected ($\lambda = 0.2$) which results in a tank geometry of 10x6x6 cm. The scaled tank is filled up to 50 % of its volume with a water mass of $m_l = 0.18$ kg and it oscillates at a characteristic frequency of $f_0 = 6.56$ Hz.

A picture of the experimental setup at the Model Basin Research group sloshing laboratory of the UPM and a simplified outline are both shown in figure 1. The sloshing rig is a SDOF system composed of a mechanical guide that allows the 1 degree of freedom constraint. This guide is attached to a C-shaped wooden structure that holds the tank with a structural mass of $m = 2.06$ kg. Similarly, the C-shaped wooden structure is attached to a set of 6 springs, 3 on the upper side and 3 on the lower side. The lower springs are mechanically embedded into the floor, and on the opposite side the upper set of springs is attached to a metallic plate that acts as a joint between them and the the embedded load cell. This setup also includes an accelerometer glued to the C-shaped wooden structure, a laser sensor pointing at the wooden block and two solenoids acting as a release mechanism. The structure is deflected an initial amplitude until it is fixed by the action of the solenoids. When the electrical current is turned on, they release the structure triggering the beginning of the experiment where acceleration and



(a) Experimental setup (b) Outline of the setup

Fig. 1. (1) Load cell, (2) Metallic plate (3) Upper springs $k_1 = 1904.4$ N/m, (4) Lower springs $k_2 = 1904.4$ N/m, (5) Laser sensor, (6) Mechanical guide, (7) Accelerometer, (8) Methacrylate tank and C-shaped wooden structure (9) Solenoids for release mechanism.

position of the tank as well as load cell measurements are recorded allowing the calculation of the sloshing force acting on the system. A more detailed description of the sloshing rig and the sloshing force can be found in Ref. [16].

3 Bouncing ball model replacing slosh dynamics

In the present model the sloshing forces are replaced by the forces exchanged between the tank wall (floor and ceiling) and a ball bouncing inside the rigid tank. The energy balance after each impact is negative due to the presence of viscoelastic element inside the ball that characterizes energy dissipation. Indeed, the behaviour of the fluid inside the tank is such that it is possible to appreciate impacts of the fluid mass on the tank walls (see Figs. 2(b) and 2(c)) as well as instants when the most of water mass is floating inside the cavity (see Fig. 2(a)). As illustrated in Fig. 3, the bouncing ball model aims at reproducing this behaviour. Specifically three different conditions are illustrated representing the ball floating in the tank, and, respectively, the impacts with the ceiling and floor. The system is ideally represented as a rigid bubble without mass properties that has a concentrated mass inside hanged to its wall by means of a spring-damper system. Part of the fluid total mass is considered associated to the ball m_b, whereas another portion is considered frozen m_f, namely attached to the wall. When the rigid bubble touches the ceiling or the floor of the tank, the impact condition is verified so causing viscoelastic forces exchanged between the case and the bouncing ball. The equation of motion of the bouncing ball can be thus

summarized as follows

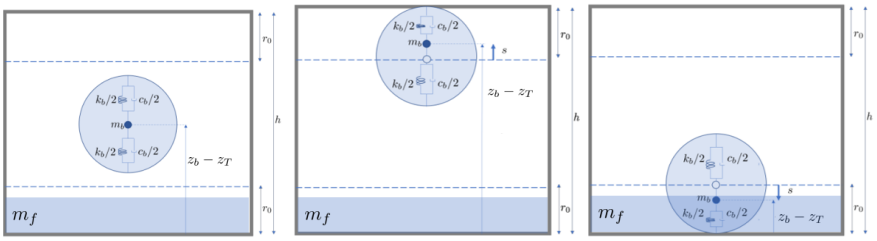
$$m_b \ddot{z}_b = -m_b g + F_b(z_b(t), z_T(t)) \tag{1}$$

where F_b is the force exchanged at the wall, $z_T(t)$ represents the motion of the tank whereas z_b is the absolute vertical motion of the bouncing ball. The latter will be expressed as $(1-\beta)\, m_l$ being m_l the total fluid mass of the ball and β a parameter that can take values between zero and 1. In this framework, it is



(a) Floating (b) Ceiling Impact (c) Floor Impact

Fig. 2. Snapshots of the sloshing experiment.



(a) Floating (b) Ceiling Impact (c) Floor Impact

Fig. 3. Bouncing ball motion phases.

convenient to introduce a new variable s such that $s = z_b - z_T - r_0$ (where r_0 is the radius of the bubble and h is the height of the tank) if the ball is impacting in the floor region, $s = z_b - z_T - h + r_0$ if the ball is impacting in the ceiling region and zero elsewhere. Moreover it is introduced also the variable $\nu = \dot{z}_b - \dot{z}_T$. It follows that we can define the viscoelastic forces as

$$F_b(s(t), \nu(t)) = k_b s + c_b \nu \tag{2}$$

where k_b and c_b are, respectively the stiffness and damping associated to the bouncing ball. It is worth to notice that $k_b = \hat{k}_b f_{nl}(s)$ may eventually be, in turn, nonlinear function of $s(t)$ by introducing a penalty function $f_{nl}(s) = 1 +$

$\alpha s^2/(r_0 - |s|)$ that avoid the ball to go out by the limits of the tank. The overall sloshing force exchanged between the tank and fluid mass inside consists of two terms yielded by bouncing ball impacts and frozen mass inertia:

$$F_s(s(t), \nu(t)) = F_b(s(t), \nu(t)) - m_f(\ddot{z}_T + g) \tag{3}$$

3.1 The simulation environment

The experimental reality was modeled within a Simulink® simulation environment by replacing the sloshing dynamics with the bouncing ball model. The structural system consists of mass-spring-damper identified during the conducted experimental campaign. It is worth noting that the structural damping model includes viscous and Coulomb damping to represent the identified frictious. The flowchart of the overall system (structure and sloshing) is shown in Fig. 4 where the input of the structural subsystem is represented by the sloshing forces, while the input of the sloshing subsystem is represented by the vertical rigid displacement and the velocity of the tank. In particular, the latter can be studied separately from the structure by assigning a suitable seismic excitation, or connected in a closed loop with the structure.

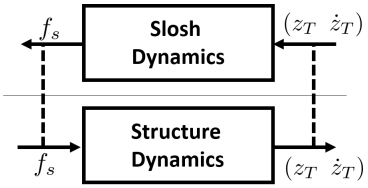


Fig. 4. Flowchart of the fluid structure interaction problem.

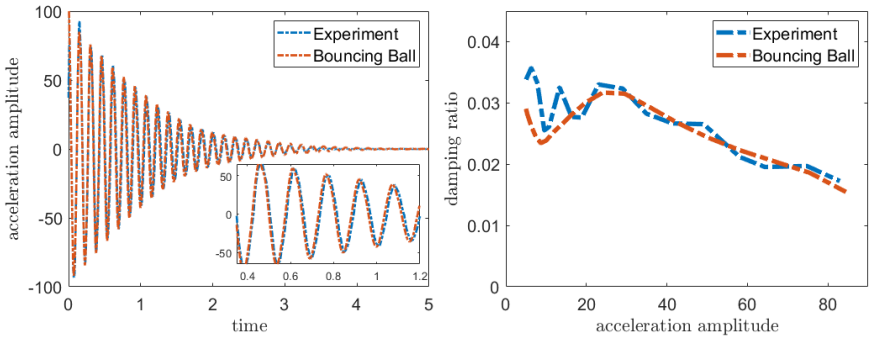
3.2 Bouncing ball tuning via experimental test

The main parameters of the bouncing ball are then estimated from the experimental data by means of an optimization process, in order to obtain a virtual equivalent configuration such as to present the model of the ball in place of the sloshing liquid. This optimization process takes into account the vertical acceleration of the tank. The reference experimental analysis was characterized by a free response with initial displacement equal to $z_T = 0.064$ m. From this vertical acceleration (blue curve in Fig.5(a)) the first step was to get the envelope in order to estimate the instantaneous damping ratio via logarithmic decay, subsequently expressed as a function of the acceleration amplitude (see blue curve in Fig.5(b)). This function, that is influenced also by the structural damping (viscous and Coulomb), represent the target function to fit. By exploiting the model presented in Sec.3.1 it is possible to get the acceleration signal related to the free response analysis (red curve in Fig.5(a)). By repeating the procedure above we are able to obtain the virtual instantaneous damping as a function of the acceleration amplitude as the red curve in Fig.5(b). This curve comes from an already

optimized problem with the objective function $J = \sum_{i=1}^{N} \left(\zeta_i^{exp} - \zeta_i^{sim}\right)^2$. The design variables are reported in Tab.1 (where the liquid mass m_l and the tank height h are kept fixed and equal respectively to 0.18 Kg and 0.06 cm).

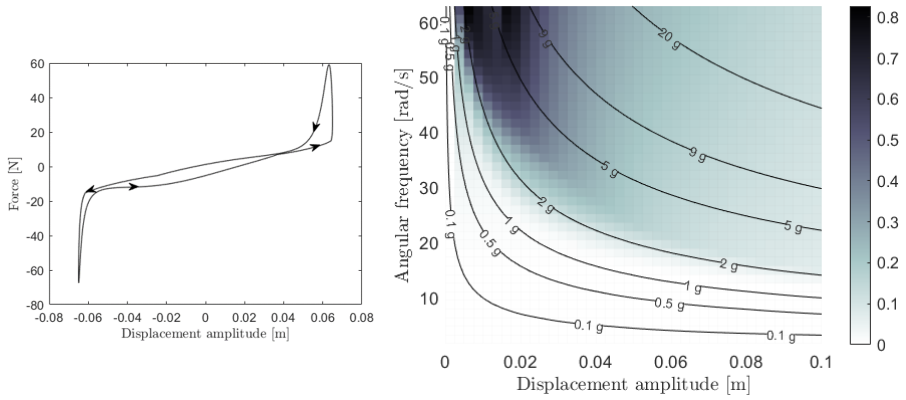
r_0 [m]	$\hat{k}_b$ [Nm^{-1}]	$\hat{c}_b$ [Nsm^{-1}]	α [m^{-1}]	β
0.0244	1103.00	13.04	74.04	0.0017

Table 1. Optimal parameters of the bouncing ball



(a) Time decaying acceleration (b) Instantaneous damping ratio

Fig. 5. Identification of the optimal bouncing ball parameters.



(a) Hysteresis cycle (b) Loss Factor map

Fig. 6. Hysteresis cycle and loss fact map of the optimal bouncing ball ROM.

3.3 Nonlinear dissipative behavior

In order to show the dissipative capabilities of the reduced order model of the identified bouncing ball, an open-loop simulation campaign of the sloshing subsystem (*i.e.* bouncing ball) is carried out. Since the dissipative content is dependent on the amplitude and frequency of the imposed motion, several analyzes have been performed with permanent harmonic motion considering different amplitude-frequency pairs covering a range of acceleration that is even beyond the range of interest of the performed experiment. For each of these simulations, the sloshing forces produced by the equivalent mechanical model were obtained as output. The hysteresis cycles were plotted (see Fig. 6(a)) from which the work dissipated by the sloshing forces was computed, once a stationary regime is reached, by evaluating the area subtended by the cycle. This last quantity allows to define the loss factor as the ratio between the dissipated work and the kinetic energy of the overall system (sloshing and structure) in the case of frozen fluid ($\eta := W_D/(\pi\,(m+m_l)\,\Omega^2 A^2)$). Finally, Fig. 6(b) shows the dependency of the loss factor from both amplitude and frequency by means of pseudo-color plot. It looks evident how there exists a specific value of amplitude A (that appears to be between 1 cm and 3 cm) that maximizes the loss factor (darker region). A contour line plot of maximum values of g-force are also superimposed on the loss factor map. Moreover, the occurrence of something similar to Rayleigh-Taylor instabilities, that is the detachment of the ball from the bottom of the tank, is verified when the maximum value of acceleration reaches approximately 2g. Before the 2g frontier, since there is no impact, the dissipation is negligible. On the contrary, for acceleration values greater than this threshold value, the ball detaches and impacts cause dissipation.

4 Neural-Network-based Reduced Order Models

Identification techniques based on the use of Neural Networks (NN) can therefore be exploited to obtain a new class of ROMs for vertical sloshing. In order to identify the NN based ROM, input/output data related to the vertical sloshing system are needed. In this paper, in order to cover the lack of experimental and CFD data, the NN is trained by exploiting data that are output by low-fidelity bouncing ball model. This model is now considered as a black-box to be identified that provides sloshing forces as a function of the history of the assigned vertical displacement. Before the integration of the NN based ROM into a simulation framework in Sec. 4.2, a *training* campaign for the identification of the network is provided in Sec. 4.1.

4.1 Training phase

The training phase consists in the definition of a neural network able to emulate vertical slosh dynamics. In this framework, the use of a proper data set is critical, thus requiring an investigation among different types of inputs, after which,

the choice fell on a pseudo-harmonic signal with amplitude and frequency slowly varying over time ($z_T = A(t)\sin(\int_0^t \Omega(\tau)\,\mathrm{d}\tau)$). This time law is such as to suitably cover the amplitude-frequency domain of interest as in Fig. 6(b), that, in turn, covers the range of accelerations provided by the performed experiments. The time derivative of z_T is used as input for the training. On the other hand, the output consists of the sloshing force that the ball returns when the tank is set on motion. The need to cover the more frequency-amplitude pairs leads to a *data set* represented by time series (velocity as input and sloshing force as output) obtained by only one 200 s long simulation with a sample frequency of 1 kHz. Among the wide variety of NN architectures *Feed Forward Neural Network* (FF NN) has been considered, in which the information simply propagates from left to right in the network through a manifold of hidden layers. The proposed scheme of the identified neural network shown in Fig. 7 consists of 7 hidden layers with 35 nodes/neurons each. Moreover, 50 tapped delay lines are considered for the input. This kind of NN is proved to work efficiently by using non-polynomial activation functions like radial basis functions (Refs. [17, 18]). As a consequence, these latter are employed as activation functions in all nodes of the considered hidden layers, whereas the output layer is made up with a simple linear function. The choice of the number of hidden nodes and layers is based on a qualitative sensitivity analysis that did not require the use of specific techniques. Specifically, given the same number of epochs considered in the network training, the selected NN is the one that proved to provide more fitting results when the ROM is introduced in the FSI environment that follows in Sec. 4.2. The algorithm used for the training consists of *Bayesian Regularization*, implemented in Matlab® through the *trainbr* function (Ref. [14]), with a fixed number of epochs equal to 1000, in which the mean-squared error performance is observed to converge to a constant value, thus guaranteeing the convergence of the network. The total time spent for the NN training is 44 hours without employing any kind of parallel computing.

4.2 Integration of Neural Network into closed loop simulation

Subsequently, the equivalent mechanical model of bouncing ball was replaced by the identified neural-network-based ROM in the simulation framework depicted in Fig. 5. The same free response analysis as in the experiments and simulation in Sec. 3.2 has been performed. It is worth to highlight that this kind of response has nothing to do with the data used to train the network. Since the sloshing tank system is of the type *single input/single output*, the simulation takes only a few seconds to perform the fluid structure interaction analysis where the sloshing block is replaced with a neural network. Figs. 8(a), 8(b) and 8(c) provide, respectively, the acceleration response, the instantaneous damping ratio as a function of the acceleration envelope, and the sloshing force comparing the experiments, the simulation with the bouncing ball and the one with the neural-network-based ROM. Specifically, Fig. 8(a) shows that response in terms of acceleration obtained with the NN-based ROM for sloshing is close to the the response obtained with the bouncing ball model (used to train the

network) and the experimental response as well. Fig 8(b) demonstrates the capability of the NN-based ROM to provide a value of the instantaneous damping ratio matching the one of the bouncing ball model at each value of response amplitude even though better performances are noticeable at higher acceleration values. The results show that although the methodology is at its preliminary stage, the NN-based ROM is able to reproduce the behaviour of the model with the bouncing ball and, in turn, also of the experiments. Moreover, as shown in Fig. 8(c), the neural network is also capable to reproduce the nonlinear behavior of the bouncing ball impact force.

5 Conclusions

The goal of this paper was to study and provide a reduced order model to describe the dissipative behaviour of nonlinear vertical sloshing (involving Rayleigh-Taylor instability) of fuel-inside-wing tanks by means of a feed forward neural network. The data used to build an equivalent mechanical model (EMM) was provided by an experimental study about the coupling between fluid sloshing and a 1 DoF system performed at UPM. The EMM consists of a boxed-in bouncing ball model, able to emulate the fluid sloshing into the tank and to replace the fluid behaviour in FSI simulations for different scenarios than the one of the experiments. Next, the network was trained using a large data set, consisting of a long simulation of the bouncing ball model with pseudo-periodic motion assigned as unsteady boundary condition spanning different values of oscillation amplitude and frequency. Indeed, the vertical sloshing forces were proved to be highly nonlinear and dependent on the amplitude of oscillation and its frequency content. Despite the training phase of the Neural Network has revealed time consuming, it has provided a sufficiently fast reduced order model able to reproduce the behaviour of sloshing forces. The obtained Neural Network Input-Output model was included in a Simulink® environment for closed loop fluid structure interaction simulations showing good matching with the experiments.

In the framework of SLOWD project, this research will go towards several directions, such as the use of higher fidelity data provided by CFD simulations specific for vertical sloshing or by proper experiments even though large tank sizes requires for important facilities to assign motion to trigger such a dissipative behaviour. On the other hand, neural networks may allow for generalization of tank motion including all 6 DoFs of the tank instead of the only vertical motion at the cost of increasing the computational cost in the identification since more inputs and more outputs increase the complexity of the network. Moreover, a specific issue to be faced in the next future concerns the integration of the network into a multiple degrees of freedom system, in which the behaviour of the ROM will need to be assessed for multi-harmonic motion. Although the neural network is computationally more expensive in both training and simulation phases, these points mark the difference with the bouncing ball model. NN-based ROM, following an adequate learning phase employing the right data set (also taking into consideration different types of inputs with respect to the pseudo-

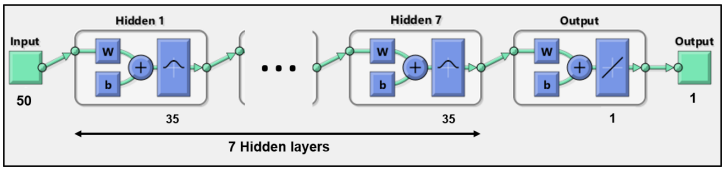
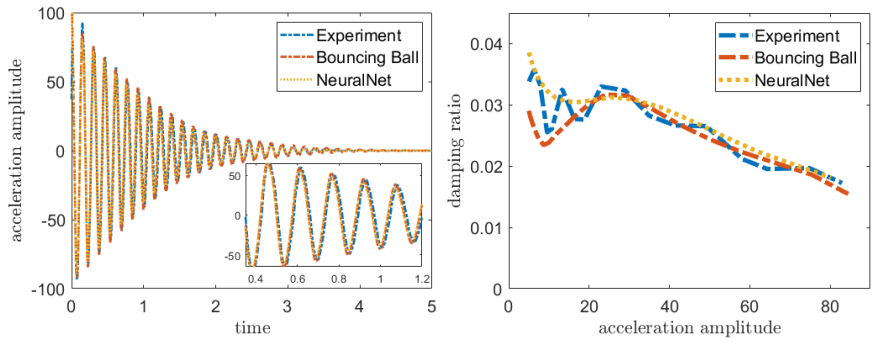
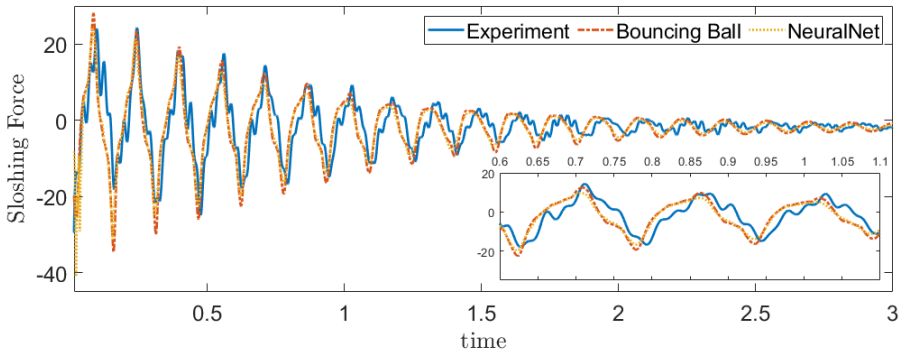


Fig. 7. Feed forward neural network flowchart.



(a) Free Response (b) Instantaneous damping ratio



(c) Sloshing Forces

Fig. 8. Comparison between FFNN, Bouncing Ball and experiment.

harmonic), has the potential to accurately replace the behavior of the sloshing forces even by increasing the degree of complexity of the FSI environment.

Acknowledgements

This paper has been supported by SLOWD project. The SLOWD project has received funding from the European Union's Horizon 2020 research and innovation programme under grant agreement No 815044.

Compliance with ethical standards

Conflict of interest: The authors declare that they have no conflict of interest.

References

1. F. Gambioli, A. Chamos, S. Jones, P. Guthrie, J. Webb, J. Levenhagen, P. Behruzi, F. Mastroddi, A. Malan, S. Longshaw, J. Cooper, L. Gonzalez, and S. Marrone, "Sloshing Wing Dynamics -Project Overview Sloshing Wing Dynamics – Project Overview," in *Proceedings of 8th Transport Research Arena TRA 2020*, 2020.
2. R. D. Firouz-Abadi, P. Zarifian, and H. Haddadpour, "Effect of fuel sloshing in the external tank on the flutter of subsonic wings," *Journal of Aerospace Engineering*, vol. 27, no. 5, p. 04014021, 2014.
3. C. Farhat, E. K.-y. Chiu, D. Amsallem, J.-S. Schotté, and R. Ohayon, "Modeling of fuel sloshing and its physical effects on flutter," *AIAA Journal*, vol. 51, no. 9, pp. 2252–2265, 2013.
4. D. J. Lewis and P. R. S. L. A, "The instability of liquid surfaces when accelerated in a direction perpendicular to their planes. II," *Proc. R. Soc. London. Ser. A. Math. Phys. Sci.*, vol. 202, no. 1068, pp. 81–96, 1950.
5. F. Gambioli, R. A. Usach, T. Wilson, and P. Behruzi, "Experimental Evaluation of Fuel Sloshing Effects on wing dynamics," in *18th Int. Forum Aeroelasticity Struct. Dyn. IFASD 2019*, 2019.
6. B. Titurus, J. E. Cooper, F. Saltari, F. Mastroddi, and F. Gambioli, "Analysis of a sloshing beam experiment," in *International Forum on Aeroelasticity and Structural Dynamics. Savannah, Georgia, USA*, vol. 139, 2019.
7. E. Graham and A. M. Rodriquez, "The characteristics of fuel motion which affect airplane dynamics," tech. rep., Douglas Aircraft Co. inc., Defense Technical Information Center, 1951.
8. H. N. Abramson, "The dynamic behaviour of liquids in moving containers with applications to space vehicle technology," *Natl. Aeronaut. Sp. Adm.*, p. 464, 1966.
9. J.-S. Schotté and R. Ohayon, "Various modelling levels to represent internal liquid behaviour in the vibration analysis of complex structures," *Computer Methods in Applied Mechanics and Engineering*, vol. 198, no. 21, pp. 1913–1925, 2009. Advances in Simulation-Based Engineering Sciences – Honoring J. Tinsley Oden.
10. F. Saltari, A. Traini, F. Gambioli, and F. Mastroddi, "A linearized reduced-order model approach for sloshing to be used for aerospace design," *Aerospace Science and Technology*, vol. 108, p. 106369, 2021.
11. L. Constantin, J. De Courcy, B. Titurus, T. Rendall, and J. Cooper, "Analysis of damping from vertical sloshing in a sdof system," *Mechanical Systems and Signal Processing*, vol. 152, p. 107452, 2021.
12. A. Mannarino and P. Mantegazza, "Nonlinear aeroelastic reduced order modeling by recurrent neural networks," *Journal of Fluids and Structures*, vol. 48, pp. 103 – 121, 2014.
13. S. O. Haykin, *Neural Networks and Learning Machines*. Pearson, 3 ed., 2009.
14. M. H. Beale, M. T. Hagan, and H. B. Demuth, *Deep Learning Toolbox*. Mathworks, r2020a ed.
15. R. L. Bass, "Modeling criteria for scaled lng sloshing experiments," *Transactions of the ASME Journal of Fluids Engineering*, vol. 107, June 1985.

16. J. Martínez-Carrascal and L. González-Gutiérrez, "Experimental study of the liquid damping effects on a sdof vertical sloshing tank," *Journal of Fluids and Structures - Submitted*, 2020.
17. M. Leshno, V. Pinkus, and A. Schocken, "Multilayer feedforward networks with a polynomial activation function can approximate any function," *Neural Networks*, vol. 6, pp. 861–867, 1993.
18. D. Broomhead and D. Lowe, "Radial basis functions, multi-variable functional interpolation and adaptive networks," *Complex Systems*, vol. 2, pp. 321–355, 1988.

Appendix A

Unpublished results

Summary: this chapter provides an analysis of the unpublished results from the work related to **P.9** - **P.11** and their relation to the research objectives of the thesis.

A.1 P.9: SPH and Bouncing Ball model

In this work the possibility of providing the bouncing ball model with a predictive capability is explored. This activity is related to research objectives **O.8** and **O.14**. The bouncing ball model is able to capture the dissipative behaviour of the vertical sloshing problem by minimizing the objective function $J = \sqrt{\sum_{i=1}^{N} \left(\zeta_i^{obj} - \zeta_i^{bb}\right)^2}$. As it has been shown in **P.8** the match between the ball model and experimental data is good but this model does not provide a prediction of the liquid dissipation given a set of physical parameters of the problem. In order to give the ball model a predictive capability, a database of 2D single phase δ-SPH has been generated where the filling level, liquid dynamic viscosity and surface tension are varied. A total of 54 free response simulations are performed at the same initial amplitude $y_0/H = 1$, natural frequency, tank geometry corresponding to scale $\lambda = 1/5$ and liquid density $\rho = 998$ kg/m^3. For each one of these simulations, the optimization procedure is performed and a set of artificial parameters are identified $(\hat{k_b}, c_b, \alpha, \beta, r_0)$. Then, an interpolation hypersurface is generated which allows to correlate the physical parameters $(fill, Re, We)$ with the artificial ones, as shown in figure A.1.

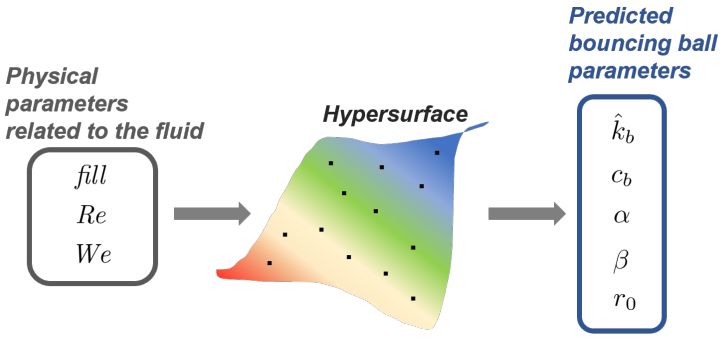


Figure A.1: Mapping procedure between fluid parameters and bouncing ball parameters.

The physical parameters that were varied are the following ones:

- Filling level $fill$: [10 - 90] %
- Reynolds number Re: [62 - 1257480] (corresponding to μ: [10^{-4} - 2] Pa s)
- Weber number We: [2640 - 26400] (corresponding to σ: [10 - 90] mN/m)

All these simulations started at the same initial condition, equal to $y_0 = 0.0584$ m, and among them there is also the reference one, for which we have $fill = 50\%$, $Re = 140000$ and $We = 3668$. The Re and We values given for the reference case correspond to a test with water. Once the hypersurfaces were identified, to validate the process of identifying the interpolating surface, an additional blind test with physical parameters different from those used for the other simulations is considered. However, these always fall within the ranges defined above, and correspond specifically to $fill = 90\%$, $Re = 251496$ and $We = 4400$. Figure A.2 shows the comparison between SPH data and bouncing ball model (with the interpolated and optimized parameters) for the tank acceleration, instantaneous damping ratio and sloshing force for the blind case. The overall match between the three curves is good. In particular, the distance

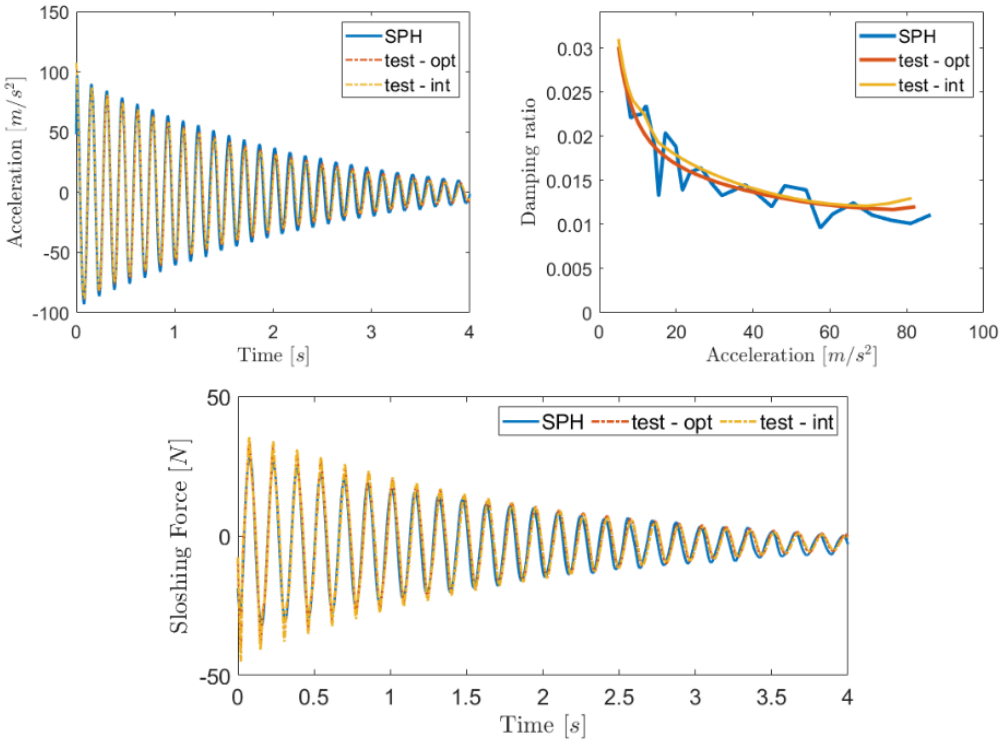


Figure A.2: Comparisons between SPH data and bouncing ball predictions (with interpolated and optimized parameters) in the validation test case ($Re = 2514960$, $We = 4400$ and $fill = 0.9$)

between the damping curves obtained by direct optimization and by interpolation is quantified by the J function, which in this case is equal to 0.022. This value is comparably lower to the values obtained for other simulations of points of the parameters space.

Another interesting aspect of this work is to compare the bouncing ball model with SPH in

regard with some other magnitudes of the sloshing problem. In the left part of figure A.3 we see a comparison of three snapshots of an SPH simulation using water at $fill = 0.5$ and the bouncing ball model counterparts. The three snapshots correspond to instants when the ball is impacting the upper wall tank ($t = 0.4$ s), floating ($t = 0.44$ s) or impacting the lower wall ($t = 0.47$ s). In the δ-SPH simulation counterparts we see that the bulk liquid is located at the ceiling or floor of the tank when the ball is impacting these walls and we find that the fluid is scattered across the tank space when the ball is floating. Similar observations where made in **P.8** or Pizzoli et al. [2022b] when the bouncing ball model was compared with experimental snapshots. This observation suggests that the bouncing ball follows the trayectory of the COG of the liquid phase. In the right part of figure A.3 the velocity of the COG of the liquid is compared to the ball velocity displaying a good match between both curves. This result agrees with what it is shown in figure 3.22 and therefore confirms that matching the liquid dissipation of the vertical sloshing problem implies matching the relative motion of the liquid with respect to the tank.

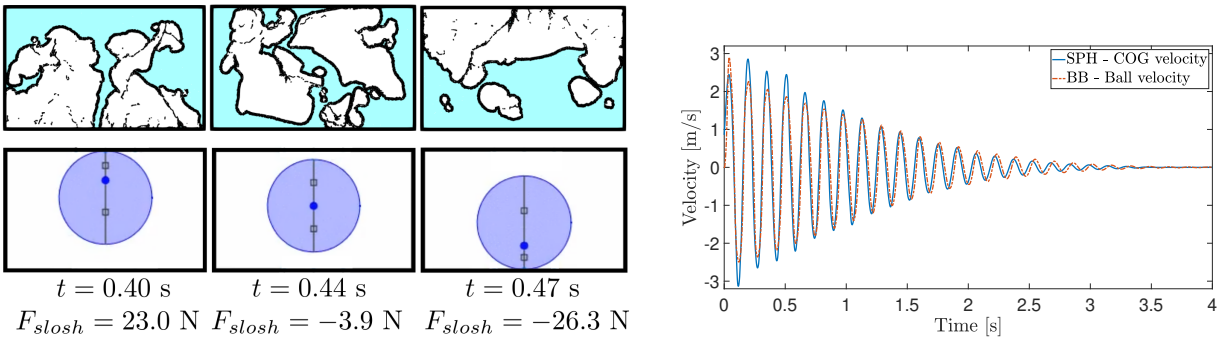


Figure A.3: Left: comparison of snapshots coming from a δ-SPH simulation (top) and a bouncing ball model simulation (bottom) for instants $t = 0.4$ (floating) , 0.44 (ceilling impact) and 0.47 (floor impact) seconds. Right: velocity of the COG over time. Comparison between the SPH simulation and the BB model for water tests at $Re = 140000$, $We = 3668$ and $fill = 0.5$.

A.2 P.10: Forced harmonic experiments and neural-networks

Thanks to the research stay done at USRS, vertical sloshing experiments were carried out using the forced harmonic facility described in subsection 2.2.2. Two experimental campagins were performed: a Froude scaling study (related to objectives **O.5** and **O.14**) and a filling level variation study (related to objectives **O.6** and **O.15**).

A.2.1 Froude scaling study

In this experimental campaign, the Froude scaled tanks presented in table 2.1 that were previously tested in the decay experiments performed in **P.1** and **P.2**, are tested in the forced harmonic facility of USRS for an amplitude and frequency range of $[0, 1.2]$ cm and $[5, 20]$ Hz and a constant filling level of $f = 0.8$. The vertical sloshing force is computed following the methodology described in 2.2.2. In figure A.4 the frequency-amplitude maps of the vertical sloshing force are displayed for the three tested scales. In these plots, all magnitudes have been scaled up to the plane size using the Froude scaling laws presented in expression (2.16).

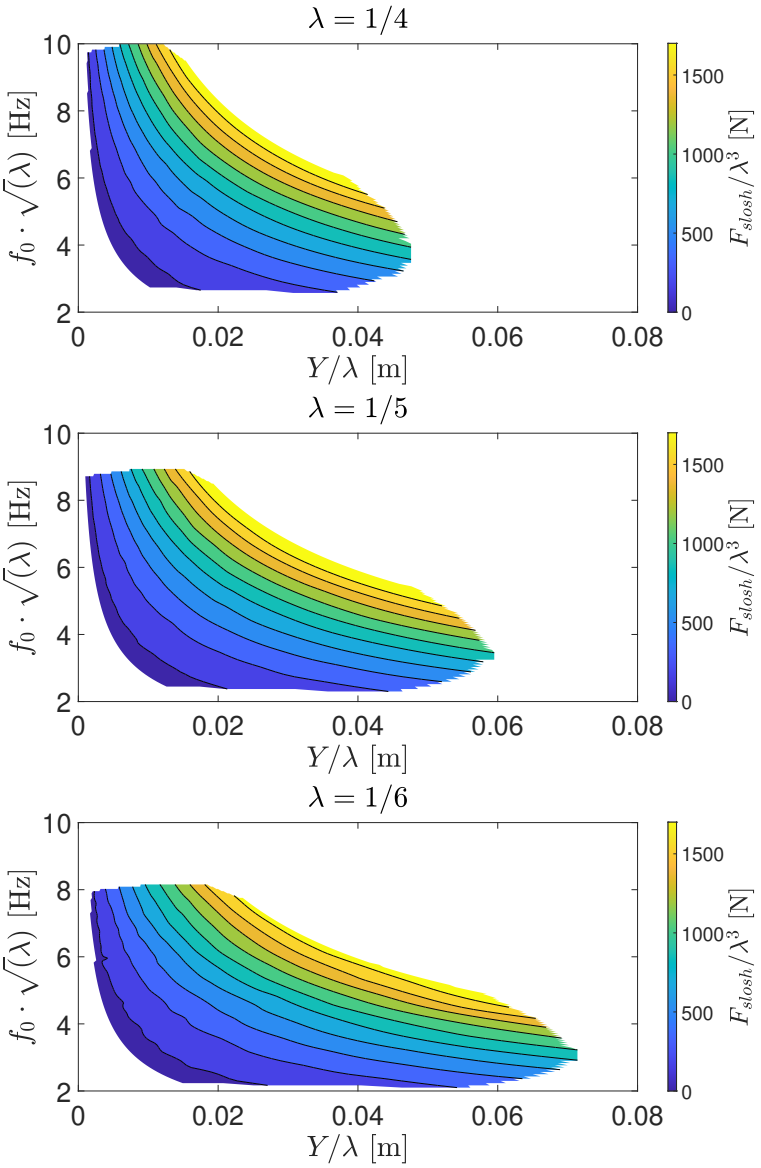


Figure A.4: Frequency and amplitude maps of the vertical sloshing force for force harmonic tests using scaled tanks of scales $\lambda = 1/4$, $1/5$ and $1/6$ at $f = 0.8$.

In the forced harmonic tests all the dimensional groups are conserved (see expression (2.23)) and therefore the three maps present a similar vertical sloshing force for the tested amplitude and frequency range. It is worth noting that due to limitations of the experimental setup the same amplitude and frequency range was tested for the three scales resulting in different amplitude-frenquency bounds in the scaled magnitudes.

The experimental data generated in this campaign was used for neural-network training. For each scaled tank two tests were carried out at different octave rates as specified in table 2.3 in order to generate the validation and training data sets. The identified neural-network (labeled as "NN - UPM tank") was then compared with experimental decay data for $\lambda = 1/6$ and $f = 0.8$ as shown in figure A.5. Additionally, another neural-network was identified based on data generated from a previous experimental campaign with another tank with dimensions $2.72 \times 11.72 \times 7.8$ cm (labeled as "USRS tank"). Since the USRS tank presents different aspect ratio and scale, two froude scale gains were applied before and after the neural-network in the close loop simulation environment. The re-scaled neural network model must therefore work in similarity of non-dimensional velocity and non-dimensional frequency, as well as non-dimensional dissipated energy, in order to reproduce the actual dissipative behavior of sloshing. More in details, from the non-dimensional frequency similarity between the identification experiment $\bar{\Omega}^{(USRS)}$ and the scaled tank $\bar{\Omega}^{(\lambda=1/6)}$, we obtain:

$$\frac{\Omega^{(USRS)}}{\sqrt{g/H^{(USRS)}}} = \frac{\Omega^{(\lambda=1/6)}}{\sqrt{g/H^{(\lambda=1/6)}}} \Longrightarrow dt^{(\lambda=1/6)} = dt^{(USRS)} \sqrt{\frac{H^{(\lambda=1/6)}}{H^{(USRS)}}} \tag{A.1}$$

Thus, a proper time rate translator is used within the simulation to make the neural network working with a time rate compliant with the one used for its identification. Furthermore, the similarity of the non-dimensional velocity of the vertical tank motion yields:

$$\frac{v_t^{(USRS)}}{\sqrt{gH^{(USRS)}}} = \frac{v_t^{(\lambda=1/6)}}{\sqrt{gH^{(\lambda=1/6)}}} \Longrightarrow v_t^{(\lambda=1/6)} = v_t^{(USRS)} \sqrt{\frac{H^{(\lambda=1/6)}}{H^{(USRS)}}} \tag{A.2}$$

that provides a gain to the vertical tank velocities before the call to the neural network.Assuming the similarity of the non-dimensional dissipative function $\frac{W^{slosh}}{m_l Y^2 \Omega^2}$ (see expression (2.23)), we obtain:

$$\Delta F_{slosh}^{(\lambda=1/6)} = \Delta F_{slosh}^{(USRS)} \frac{m_l^{(\lambda=1/6)}}{m_l^{(USRS)}} \tag{A.3}$$

Equation A.3 provides the gain for the dynamic sloshing forces to be applied after the call to the neural network within the simulation framework. In this scaling procedure, velocity and displacements of the tank are adjusted according to tank size, but the maximum accelerations achievable when the tank works in similarity with the tank used for the network identification are retained. The identified neural-network with the USRS tank (labeled as "NN - Sapienza tank") is integrated in the simulation environment with the Froude scaling gains explained before and it is compared to experimental decay data in figure A.5. The match between the two neural-networks and the decay data is good which validates the usage of Froude scaling gains and indicates that there is no need to train a different neural-network when changing the scale of the tank since the Froude scaling gains are sufficient to capture the scaling effects of the problem.

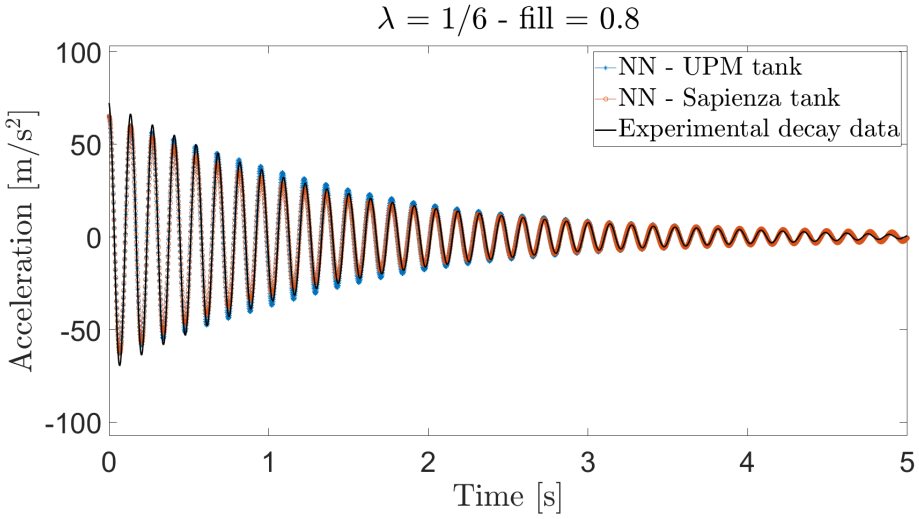


Figure A.5: Tank acceleration over time. Comparison between experimental decay data, neural-network trained with $\lambda = 1/6$ tank and neural-network trained with USRS tank. Water test at $f = 0.8$ and $y_0/H = 0.56$.

A.2.2 Filling level variation study and multi-input neural-network

The second experimental campaign carried out consisted in performing a filling level variation study covering the range $f \in [0.1, 0.9]$ with the USRS tank and a frequency and amplitude range of $[0, 1.2]$ cm and $[5, 20]$ Hz. Figure A.6 shows the energy dissipated by the vertical sloshing force calculated as specified in equation (2.52) for the tested filling levels. A maximum of energy dissipation is observed for filling levels $f \in [0.4, 0.6]$ and dissipation decreases for

higher and lower filling levels.

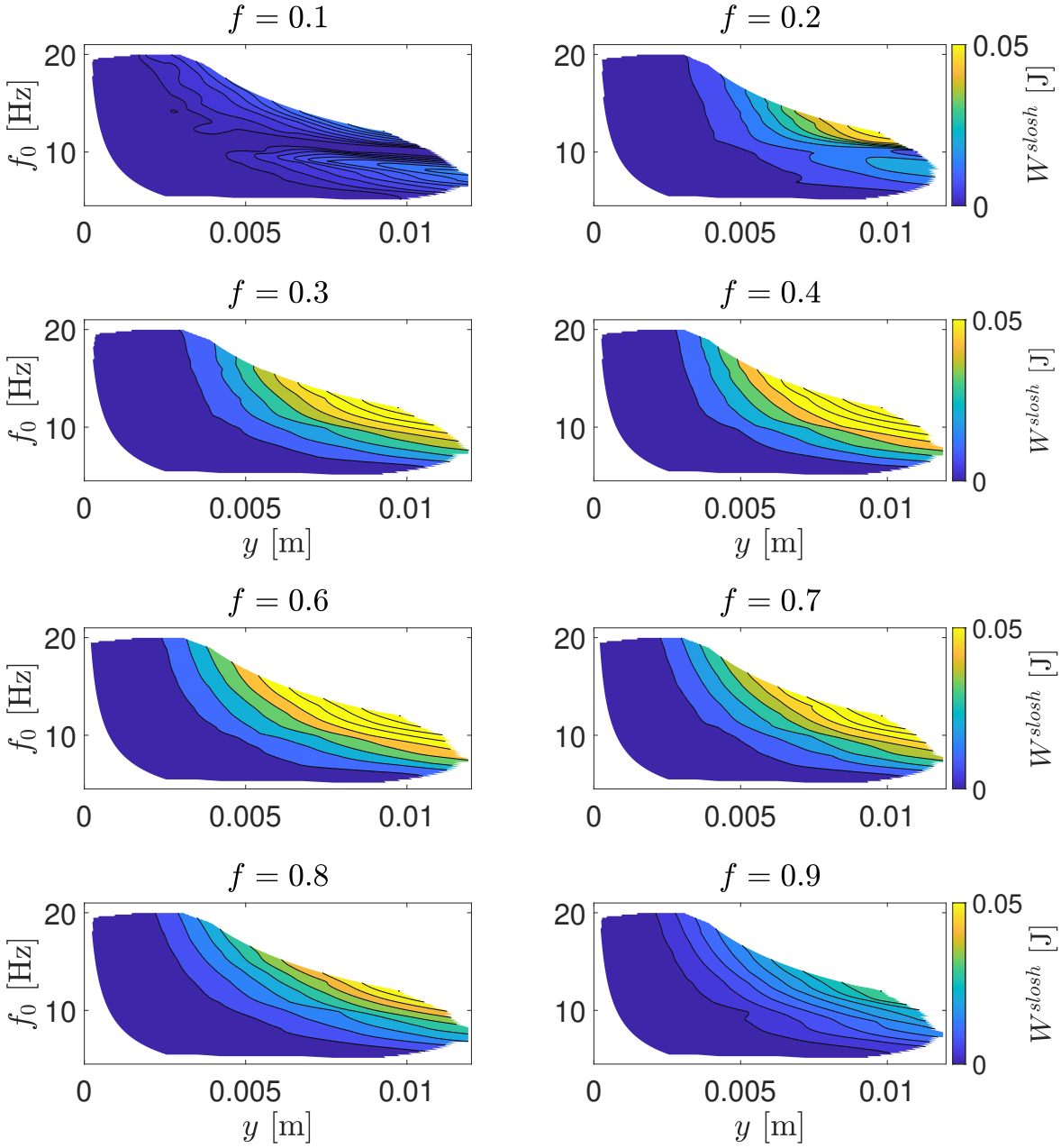


Figure A.6: Dissipated energy by the sloshing force for filling levels $f = 0.1$, 0.2, 0.3, 0.4, 0.6, 0.7, 0.8 and 0.9 as a function of the excitation amplitude and frequency. Tests performed with the USRS tank.

The experimental results seen in the filling level variation study agree well with previous experimental studies performed at the same facility Saltari et al. [2021a] and with the filling level variation studies done with decay facilities at UPM or UB Martinez-Carrascal and Gonzalez-Gutierrez [2022], Constantin et al. [2021a].

In this experimental campaign, the same procedure was followed as for the Froude scaling tests.

Two experimental runs were performed for each filling level in order to generate the validation and trainng data sets for the neural-networks identification. The final goal of this ongoning activity is to develop a multi-input neural-network that takes into account different excitation amplitudes, excitation frequencies and filling levels. Different scales could be also considered by applying the beforementioned Froude scaling gains. Figure A.7 shows the evolution of the tank acceleration over time for a $\lambda = 1/6$ and $f = 0.2$. The decay experiment performed at UPM is compared with the identified multi-input neural-network. This neural-network constitutes a first attempt to the problem and it is currently under development.

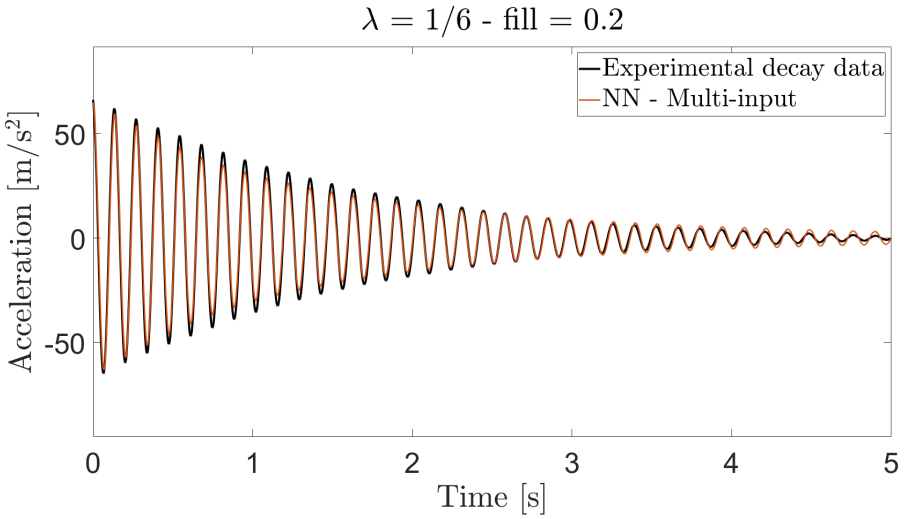


Figure A.7: Tank acceleration evolution over time for a $\lambda = 1/6$ and $f = 0.2$ water test at $y_0/H = 0.56$. Comparison between experimental data and the multi-input neural-network.

A.3 P.11: Multiphase δ-SPH applied to vertical sloshing

The δ-SPH multiphase formulation presented in Hammani et al. [2020] has been implemented in AQUAgpusph and then validated in Martinez-Carrascal et al. [2021] or **P.7** with the vertical RTI problem. The next step is to apply this multiphase formulation to the vertical sloshing problem and compare the results obtained with monophase simulations. The multiphase formulation also allows us to study the dimensional groups related to the gas phase: ρ/ρ_a and μ/μ_a by varying the gas density and dynamic viscosity. This ongoing work is related to research objective **O.11** and contribution **C.4**.

In terms of flow kinematics, figure A.8 shows the evolution of the flow for the experiment,

monophase SPH simulation and multiphase SPH simulation. In the multiphase simulation at time instant $t = 0.075$ s, many Rayleigh-Taylor instabilities develop that are not present in the monophase counterpart or in the experiment. This could be related to the surface tension model that has been adapted to the multiphase formulation and should be revisited. These instabilities grow forming many jets that impact the upper wall at $t = 0.1$ s. Then, the chaotic regime develops with a lot of bubble entraptment.

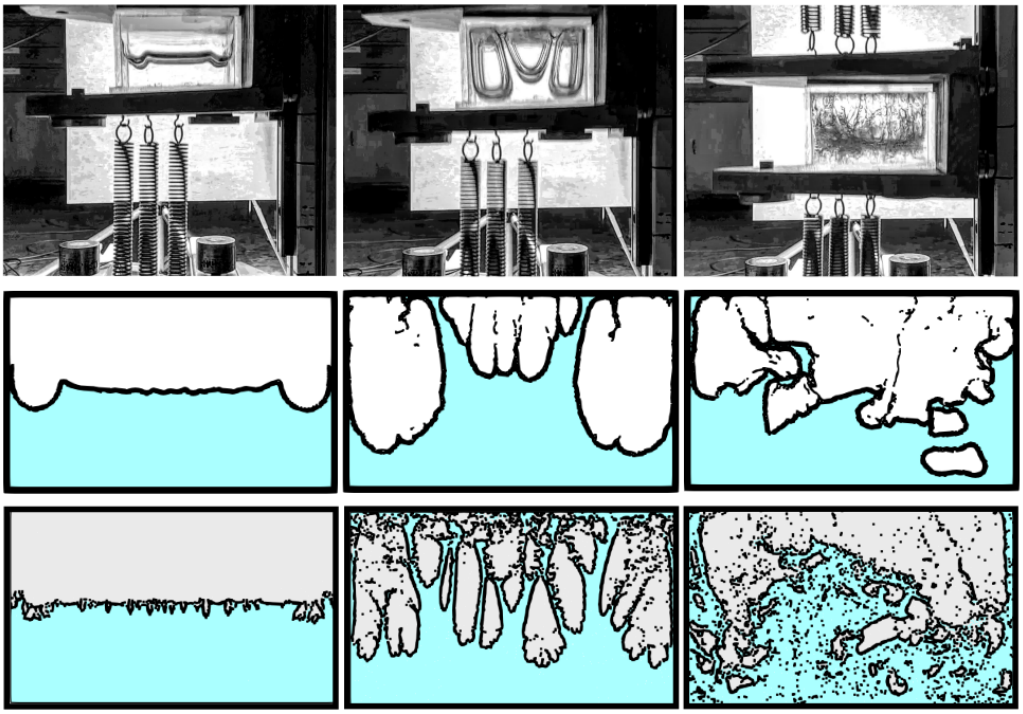


Figure A.8: Snapshots of a vertical sloshing water test at $f = 0.5$ and $y_0/H = 1$ at time instants 0.075 s, 0.1 s and 1.43 s. Comparison between experiment (top), monophase SPH simulation (middle) and multiphase SPH simulation (bottom).

Even though some differences are found in the free surface evolution, these differences do not seem to affect the overall liquid dissipation and tank motion as shown in figure A.9. An excellent match is found between both monophase and multiphase simulations and the experimental data. This match should be further checked for other test cases in order to confirm the validity of the multiphase formulation for the vertical sloshing problem.

An additional thing we can study thanks to the multiphase formulation is the influence of the non-dimensional groups ρ/ρ_a and μ/μ_a (see expression (2.5)) in the liquid induced damping.

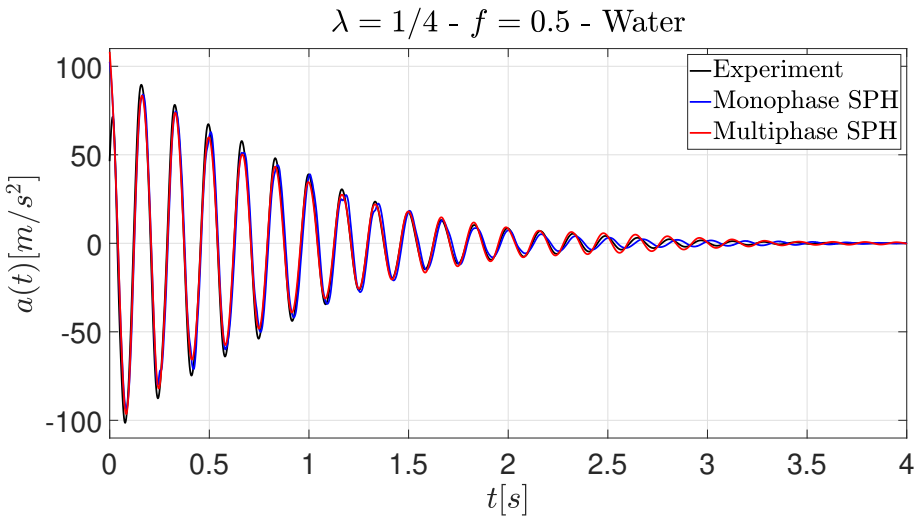


Figure A.9: Tank acceleration over time for a $\lambda = 1/4$ and $f = 0.5$ water test at $y_0/H = 1$. Comparison between experimental data, SPH monophase simulation and SPH multiphase simulation.

Figure A.10 shows the evolution of the logarithm of the acceleration envelope for four different gas densities $\rho_a/\rho_{a0}) = 1$, 4, 25 and 50 where ρ_{a0} corresponds to the density of air at a temperature of 20° C. It is observed that the sloshing induced damping ratio decreases as the gas density increases. As the gas becomes more dense, it hinders the development of strong liquid jets that impact the upper wall of the tank which results in a loss of liquid induced damping.

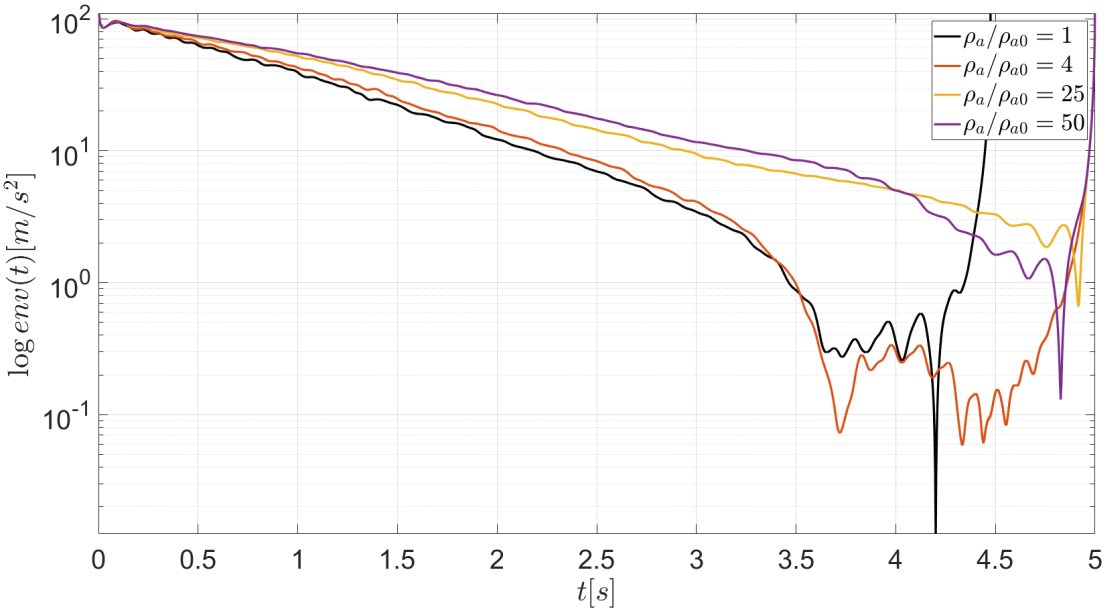


Figure A.10: Logarithm of the acceleration envelope over time for $\rho_a/\rho = 1$, 4, 25 and 50 in water tests at $\lambda = 1/4$, $f = 0.5$ and $y_0/H = 1$.

Lastly, figure A.11 shows the evolution of the logarithm of the acceleration envelope for $\mu_a/\mu_{a0} =$ 0.01, 0.1, 1, 10, 100 and 1000 where μ_{a0} is the dynamic viscosity of air at a temperature of 20° C. In this study, it seems that the sloshing induced dissipation remains unaffected by changes of the gas viscosity, concluding that it does not constitute a relevant parameter of the vertical sloshing problem.

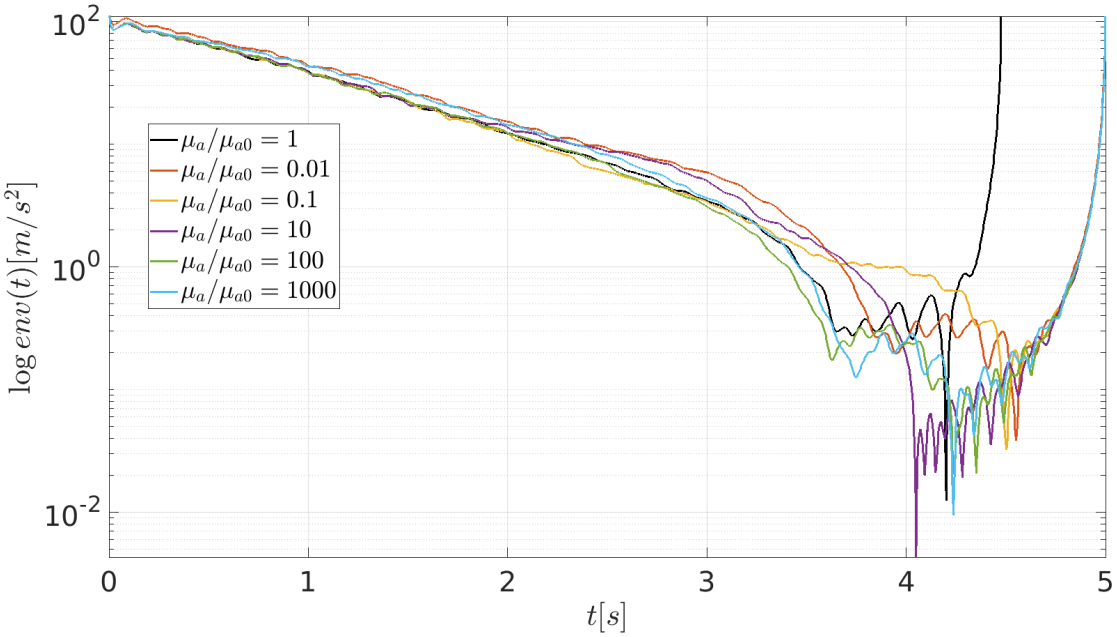


Figure A.11: Logarithm of the acceleration envelope over time for $\mu/\mu_a = 0.01$, 0.1, 1, 10, 100 and 1000 in water tests at $\lambda = 1/4$, $f = 0.5$ and $y_0/H = 1$.

Bibliography

Norman Abramson, Helmut F Bauer, George W Brooks, Wen-Hwa Chu, John F Dalzell, Franklin T Dodge, Daniel D Kana, William C Reynolds, Hugh M Satterlee, and Sandor Silverman. *The dynamic behaviour of liquids in moving containers*. Government Press, Washington D. C., 1966.

AIAA. Assessment of the wind tunnel data uncertainty. *Technical Report*, pages S–071–1995,AIAA, 1995.

M. Antuono and A. Colagrossi. The damping of viscous gravity waves. *Wave Motion*, 50(2): 197–209, 2013.

M Antuono, PN Sun, S Marrone, and A Colagrossi. The δ-ALE-SPH model: An arbitrary Lagrangian-Eulerian framework for the δ-SPH model with particle shifting technique. *Computers & Fluids*, 216:104806, 2021.

Matteo Antuono, Andrea Colagrossi, Salvatore Marrone, and Diego Molteni. Free-surface flows solved by means of SPH schemes with numerical diffusive terms. *Computer Physics Communications*, 181(3):532–549, 2010.

Matteo Antuono, Andrea Colagrossi, and Salvatore Marrone. Numerical diffusive terms in weakly-compressible SPH schemes. *Computer Physics Communications*, 183(12):2570–2580, 2012.

Ehsan Askari, Farhang Daneshmand, and Marco Amabili. Coupled vibrations of a partially fluid-filled cylindrical container with an internal body including the effect of free surfaces waves. *Journal of Fluids and Structures*, October 2013.

Robert Banim, Rob Lamb, and Melissa Bergeon. Smoothed particle hydrodynamics simulation of fuel tank sloshing. In *25th International Congress of Aeronautical Sciences, Hamburg*, 2006.

D. Bass. Roll stabilization for small fishing vessels using paravanes and anti-roll tanks. *Mar. Technol.*, 35:74–84, 1998.

Mark Hudson Beale, Martin T. Hagan, and Howard B. Demuth. *Deep Learning Toolbox*. Mathworks, r2020a edition.

J. S. Bendat and A. G. Piersol. Random Data. Analysis and Measurements Procedures. *WILEY*, Fourth Edition, 2010.

Emili Bhattacharjee and Lipika Halder. An experimental study on tuned liquid damper for mitigation of structural response. *International Journal of Advanced Structural Engineering*, 5, 2013.

Benjamin Bouscasse, Matteo Antuono, Andrea Colagrossi, and Claudio Lugni. Numerical and experimental investigation of nonlinear shallow water sloshing. *International Journal of Nonlinear Sciences and Numerical Simulation*, 14(2):123–138, 2013.

Benjamin Bouscasse, Andrea Colagrossi, Antonio Souto-Iglesias, and JL Cercos-Pita. Mechanical energy dissipation induced by sloshing and wave breaking in a fully coupled angular motion system. I. Theoretical formulation and numerical investigation. *Physics of Fluids*, 26 (3):033103, 2014a.

Benjamin Bouscasse, Andrea Colagrossi, Antonio Souto-Iglesias, and JL Cercos-Pita. Mechanical energy dissipation induced by sloshing and wave breaking in a fully coupled angular motion system. II. Experimental investigation. *Physics of Fluids*, 26(3):033104, 2014b.

Gabriele Bulian, E Botia-Vera, and A Souto-Iglesias. Experimental sloshing pressure impacts in ensemble domain: transient and stationary statistical characteristics. *Physics of Fluids*, 26(3):032102, 2014.

J. Calderon-Sanchez, J.L. Cercos-Pita, and D. Duque. A geometric formulation of the shepard renormalization factor. *Computers & Fluids*, 183:16 – 27, 2019. doi: https://doi.org/10.1016/j.compfluid.2019.02.020.

J. Calderon-Sanchez, L. M. Maritnez-Carrascal J., Gonzalez-Gutierrez, and Colagrossi A. A global analysis of a coupled violent vertical sloshing problem using an sph methodology. *Engineering Applications of Computational Fluid Mechanics*, 2021.

Jose L Cercos-Pita. Aquagpusph, a new free 3D SPH solver accelerated with OpenCL. *Computer Physics Communications*, 192:295–312, 2015.

S. Chandrasekhar. *Hydrodynamic and Hydromagnetic Stability*. Dover, New-York, 1981.

L Chiron, Matthieu De Leffe, Guillaume Oger, and David Le Touzé. Fast and accurate SPH modelling of 3-D complex wall boundaries in viscous and non viscous flows. *Computer Physics Communications*, 234:93–111, 2019.

A. Colagrossi, A. Souto-Iglesias, M. Antuono, and S. Marrone. Smoothed-particle-hydrodynamics modeling of dissipation mechanisms in gravity waves. *Phys. Rev. E*, 87, 2013.

Andrea Colagrossi, Matteo Antuono, and David Le Touzé. Theoretical considerations on the free-surface role in the smoothed-particle-hydrodynamics model. *Physical Review E*, 79/5: 1–13, 2009.

L. Constantin, J. De Courcy, B. Titurus, T. Rendall, and J.E.Cooper. Analysis of damping from vertical sloshing in a SDOF system. *Mechanical Systems and Signal Processing*, 2021a.

L. Constantin, J. J. De Courcy, B. Titurus, T. C. S. Rendall, and J. E. Cooper. Statistical analysis of sloshing-induced dissipative energy across a range of froude numbers. *IOP Conference Series: Materials Science and Engineering*, 1226, 2022.

Lucian Constantin, JJ De Courcy, Branislav Titurus, Thomas CS Rendall, and Jonathan E Cooper. Sloshing induced damping across froude numbers in a harmonically vertically excited system. *Journal of Sound and Vibration*, 510:116302, 2021b.

M. Cooker. Water waves in a suspended container. *Wave Motion*, 20:385–395, 1994.

M. Cooker. Wave energy losses from a suspended container. *Physics of Fluids*, 8:283, 1996.

J. E. Cooper, P. R. Emmet, and Wright J. R. Envelope function - a tool for analyzing flutter data. *International Forum on Aeroelasticity and Structural Dynamics*, 2017.

L. Delorme, A. Colagrossi, A. Souto-Iglesias, R. Zamora-Rodríguez, and E. Botía-Vera. A set of canonical problems in sloshing, Part I: Pressure field in forced roll-comparison between experimental results and SPH. *Ocean Engineering*, 36:168–178, 2009.

Z. Demirbilek. Energy dissipation in sloshing waves in a rolling rectangular tank — i. mathematical theory. *Ocean Engineering*, 10(5):347 – 358, 1983a. ISSN 0029-8018. doi: https://doi.org/10.1016/0029-8018(83)90006-9. URL http://www.sciencedirect.com/science/article/pii/0029801883900069.

Z. Demirbilek. Energy dissipation in sloshing waves in a rolling rectangular tank — ii. solution method and analysis of numerical technique. *Ocean Engineering*, 10(5):359 – 374, 1983b. ISSN 0029-8018. doi: https://doi.org/10.1016/0029-8018(83)90006-9. URL http://www.sciencedirect.com/science/article/pii/0029801883900069.

Z. Demirbilek. Energy dissipation in sloshing waves in a rolling rectangular tank — iii. results and applications. *Ocean Engineering*, 10(5):375 – 382, 1983c. ISSN 0029-8018. doi: https://doi.org/10.1016/0029-8018(83)90006-9. URL http://www.sciencedirect.com/science/article/pii/0029801883900069.

A Di Mascio, M Antuono, A Colagrossi, and S Marrone. Smoothed particle hydrodynamics method from a large eddy simulation perspective. *Physics of Fluids*, 29(3):035102, 2017.

L. Diebold et al. Experimental and numerical investigations of internal global forces for violent irregular excitations in lngc prismatic tanks. *The Twenty-first International Offshore and Polar Engineering Conference*, 2011.

Franklin T. Dodge. The new dynamic behavior of liquids in moving containers. Technical report, Southwest Research Institute, 2000.

O.M. Faltinsen and A.N. Timokha. *Sloshing*. Cambridge University Press, 2009. ISBN 9780521881111.

A. Farhadi, H. Emdad, and E. G. Rad. Incompressible sph simulation of landslide impulse-generated water waves. *Natural Hazards*, 82(3):1779–1802, 2016.

C. Farhat, E. K. Chiu, D. Amsallem, J. Schotte, and R. Ohayon. Modelling of fuel sloshing and its physical effects on flutter. *AIAA Journal*, 51(9):2252–2265, 1998.

J Feldman and J Bonet. Dynamic refinement and boundary contact forces in SPH with applications in fluid flow problems. *International Journal for Numerical Methods in Engineering*, 72(3):295–324, 2007.

M. Ferrand, D.R. Laurence, B.D. Rogers, D. Violeau, and C. Kassiotis. Unified semi-analytical wall boundary conditions for inviscid laminar or turbulent flows in the meshless SPH method. *International Journal for Numerical Methods in Fluids*, 2013.

F.Gambioli and A. Malan. Fuel loads in large civil airplanes. pages 161–174, 2017.

F Gambioli, R Alegre Usach, J Kirby, T Wilson, and P Behruzi. Experimental evaluation of fuel sloshing effects on wing dynamics. In *International Forum on Aeroeslasticity and Structural Dynamics IFASD*, 2019.

T Gavory and PE De Seze. Sloshing in membrane LNG carriers and its consequences from a designer's perspective. In *Proceedings of the Nineteenth International Offshore and Polar Engineering Conference*, 2009.

Robert A Gingold and Joseph J Monaghan. Smoothed particle hydrodynamics: theory and application to non-spherical stars. *Monthly notices of the royal astronomical society*, 181(3): 375–389, 1977.

L. M. González-Gutiérrez and A. de Andrea González. Numerical computation of the Rayleigh-Taylor instability for a viscous fluid with regularized interface properties. *Phys. Review E*, 100:013101, 2019.

Mateusz Graczyk. *Experimental Investigation of Sloshing Loading and Load Effects in Membrane LNG Tanks Subjected to Random Excitation.* PhD thesis, 2008.

Mateusz Graczyk, Torgeir Moan, and Olav Rognebakke. Probabilistic analysis of characteristic pressure for LNG tanks. *Journal of Offshore Mechanics and Arctic Engineering*, 128:133, 2006.

Mateusz Graczyk, Torgeir Moan, and M Wu. Extreme sloshing and whipping-induced pressures and structural response in membrane LNG tanks. *Ships and Offshore Structures*, 2(3):201–216, 2007.

E. Graham and A. M. Rodriquez. The characteristics of fuel motion which affect airplane dynamics. Technical report, Douglas Aircraft Co. inc., Defense Technical Information Center, 1951.

N. Grenier, M. Antuono, A. Colagrossi, D. Le Touzé, and B. Alessandrini. An hamiltonian interface sph formulation for multi-fluid and free surface flows. *Journal of Computational Physics*, 228(22):8380–8393, 2009.

I. Hammani, S. Marrone, A. Colagrossi, G. Oger, and D. Le Touzé. Detailed study on the extension of the delta-sph model to multi-phase flow. *Computer Methods in Applied Mechanics and Engineering*, 368, 2020.

Simon O. Haykin. *Neural Networks and Learning Machines.* Pearson, 3 edition, 2009.

A. Herczyński and P.D. Weidman. Experiments on the periodic oscillation of the free containers driven by liquid sloshing. *Journal of Fluid Mechanics*, 1:1–27, 2012.

Raouf A Ibrahim. *Liquid sloshing dynamics: theory and applications.* Cambridge University Press, 2005.

International-Towing-Tank-Conference. Recommended procedures and guidelines. testing and extrapolation methods. uncertainty analysis in efd. uncertainty assessment methodology. *Technical Report*, 1999.

Qiao Jin, Xin Li, Ning Sun, Jing Zhou, and Jiong Guan. Experimental and numerical study on tuned liquid dampers for controlling earthquake response of jacket offshore platform. *Marine Structures*, 20:238–254, 2007. ISSN 4.

SJ Lind, Rui Xu, PK Stansby, and Benedict D Rogers. Incompressible smoothed particle hydrodynamics for free-surface flows: A generalised diffusion-based algorithm for stability and validations for impulsive flows and propagating waves. *Journal of Computational Physics*, 231(4):1499–1523, 2012.

WT Liu, PN Sun, FR Ming, and AM Zhang. Application of particle splitting method for both hydrostatic and hydrodynamic cases in SPH. *Acta Mechanica Sinica*, 34(4):601–613, 2018.

Leon B Lucy. A numerical approach to the testing of the fission hypothesis. *The astronomical journal*, 82:1013–1024, 1977.

Andrea Mannarino and Paolo Mantegazza. Nonlinear aeroelastic reduced order modeling by recurrent neural networks. *Journal of Fluids and Structures*, 48:103 – 121, 2014. ISSN 0889-9746. doi: https://doi.org/10.1016/j.jfluidstructs.2014.02.016. URL http://www.sciencedirect.com/science/article/pii/S0889974614000383.

S Marrone, A Colagrossi, M Antuono, C Lugni, and MP Tulin. A 2d+t SPH model to study the breaking wave pattern generated by fast ships. *Journal of Fluids and Structures*, 27(8): 1199–1215, 2011.

S. Marrone, A. Colagrossi, A. Di Mascio, and D. Le Touzé. Prediction of energy losses in water impacts using incompressible and weakly compressible models. *J. Fluids Struct.*, 54:802–822, 2015.

S. Marrone et al. A numerical study on the dissipation mechanisms in sloshing flows induced by violent and high-frequency accelerations. i. theoretical formulation and numerical investigation. *Physical Review Fluids*, 11, 2021.

Salvatore Marrone, Andrea Colagrossi, David Le Touzé, and Giorgio Graziani. Fast free-surface detection and level-set function definition in SPH solvers. *Journal of Computational Physics*, 229(10):3652–3663, 2010.

A. Marsh, M. Prakash, S. E. Semercigil, and O. Turan. An investigation and modeling of energy dissipation through sloshing in an egg-shaped shell. *Journal of Sound and Vibration*, 330: 6287–6295, 2011.

J. Martinez-Carrascal and L. M. Gonzalez-Gutierrez. Experimental study of the liquid damping effects on a sdof vertical sloshing tank. *Journal of Fluids and Structures*, 100:103172, 2021.

J. Martinez-Carrascal and L. M. Gonzalez-Gutierrez. On the experimental scaling and power dissipation of violent sloshing flows. *Journal of Fluids and Structures*, 2022.

Jon Martinez-Carrascal, J. Calderon-Sanchez, L. M. González-Gutiérrez, and A. de Andrea González. Extended computation of the viscous rayleigh-taylor instability in a horizontally confined flow. *Phys. Rev. E*, 103:053114, May 2021.

Domenico D Meringolo, Salvatore Marrone, Andrea Colagrossi, and Yong Liu. A dynamic δ-SPH model: How to get rid of diffusive parameter tuning. *Computers & Fluids*, 179:334–355, 2019.

K. O. Mikaelian. Rayleigh-Taylor instability in finite-thickness fluids with viscosity and surface tension. *Phys. Rev. E*, 54(4):3676, 1996.

JJ Monaghan and H Pongracic. Artificial viscosity for particle methods. *Applied Numerical Mathematics*, 1(3):187–194, 1985.

Joe J Monaghan. Simulating free surface flows with SPH. *Journal of computational physics*, 110(2):399–406, 1994.

Joseph J Monaghan. SPH without a tensile instability. *Journal of Computational Physics*, 159 (2):290–311, 2000.

Joseph P Morris. Simulating surface tension with smoothed particle hydrodynamics. *International journal for numerical methods in fluids*, 33(3):333–353, 2000.

B.W. Nam and Y. Kim. Effects of sloshing on the motion response of LNG-FPSO in waves. In *International Workshop on Water Waves and Floating Bodies*, 2007.

R. Ohayon and H. J-P. Morand. *Fluid-Structure Interaction*. Wiley, 1995.

R. Ohayon and J.-S. Schotté. Fluid-Structure Interaction Problems. *Encyclopedia of Computational Mechanics, 2nd Edition, Vol. 2*, March 2018.

O.F. Oxtoby, A. G. Malan, and J. A. Heyns. A computationally efficient 3d finite-volume scheme for violent liquid–gas sloshing. *International Journal for Numerical Methods in Fluids*, 79: 306–321, 2015.

M. Perlin, W. Choi, and Z. Tian. Breaking waves in deep and intermediate waters. *Annu. Rev. Fluid Mech.*, 45:115–145, 2013.

Marco Pizzoli, Francesco Saltari, Giuliano Coppotelli, and Franco Mastroddi. Experimental validation of neural-network-based nonlinear reduced-order model for vertical sloshing. In *AIAA Scitech 2022 Forum*, 2022a.

Marco Pizzoli, Francesco Saltari, Franco Mastroddi, Jon Martinez-Carrascal, and Leo González-Gutiérrez. Nonlinear reduced-order model for vertical sloshing by employing neural networks. *Nonlinear Dynamics*, 107, 2022b.

P.W. Randles and L.D. Libersky. Smoothed Particle Hydrodynamics: some recent improvements and applications. *Computer methods in applied mechanics and engineering*, 39:375–408, 1996.

D. Reed et al. Investigation on tuned liquid dampers under large amplitude excitation. *J. Eng. Mech.*, 124:405–413, 1998.

J. Rogers and W. Szymczak. Computations of violent surface motions: comparisons with theory and experiments. *Philos. Trans. R. Soc. A*, 355:649–663, 1997.

Y. Saad. Variations of Arnoldi's method for computing eigenelements of large unsymmetric matrices. *Lin. Algebra. Appl.*, 34:269–295, 1980.

Francesco Saltari, Marco Pizzoli, Giuliano Coppotelli, Francesco Gambioli, Jonathan E. Cooper, and Franco Mastroddi. Experimental characterisation of sloshing tank dissipative behaviour

in vertical harmonic excitation. accepted for publication on to *Journal of fluids and structures*, 2021a.

Francesco Saltari, Alessandro Traini, Francesco Gambioli, and Franco Mastroddi. A linearized reduced-order model approach for sloshing to be used for aerospace design. *Aerospace Science and Technology*, 108:106369, 2021b. ISSN 1270-9638. doi: https://doi.org/10.1016/j.ast.2020.106369. URL https://www.sciencedirect.com/science/article/pii/S1270963820310518.

Francesco Saltari, Marco Pizzoli, Francesco Gambioli, Christina Jetzschmann, and Franco Mastroddi. Sloshing reduced-order model based on neural networks for aeroelastic analyses. *Aerospace Science and Technology*, page 107708, 2022. doi: https://doi.org/10.1016/j.ast.2022.107708.

J.-S. Schotté, T. Miras, and R. Ohayon. Effect of internal liquids on the vibrations of aerospace structures. *AIAA 53rd conference*, April 2012.

Jean-Sébastien Schotté and Roger Ohayon. Various modelling levels to represent internal liquid behaviour in the vibration analysis of complex structures. *Computer Methods in Applied Mechanics and Engineering*, 198(21):1913–1925, 2009. ISSN 0045-7825. doi: https://doi.org/10.1016/j.cma.2008.12.016. URL https://www.sciencedirect.com/science/article/pii/S0045782509000061. Advances in Simulation-Based Engineering Sciences – Honoring J. Tinsley Oden.

M. S. Shadloo and M. Yildiz. ISPH modelling of Rayleigh-Taylor instability. In *6th international SPHERIC workshop proceedings*, 2011.

M. S. Shadloo, A. Zainali, and M. Yildiz. Simulation of single mode rayleigh–taylor instability by sph method. *Computational Mechanics*, 51:699–715, 2013.

A. Souto-Iglesias, L. Delorme, L. Pérez-Rojas, and S. Abril-Pérez. Liquid moment amplitude assessment in sloshing type problems with smooth particle hydrodynamics. *Ocean Engineering*, 33:1462–1484, 2006.

A. Souto-Iglesias, E. Botia-Vera, A. Martín, and F. Pérez-Arribas. A set of canonical problems in sloshing, part 0: Experimental setup and data processing. *Ocean Engineering*, 38:1823–1830, 2011.

Jessica Stasch, Bircan Avci, and Peter Wriggers. Numerical simulation of fluid-structure interaction problems by a coupled sph-fem approach. *Proc. Appl. Math. Mech.*, 16(1):491–492, 2016.

L. Sun and Y. Fujino. A semi-analytical model for tuned liquid damper (tld) with wave breaking. *Journal of Fluids and Structures*, 8:471–488, 1994.

PN Sun, Andrea Colagrossi, Salvatore Marrone, Matteo Antuono, and AM Zhang. Multi-resolution delta-plus-SPH with tensile instability control: Towards high reynolds number flows. *Computer Physics Communications*, 224:63–80, 2018.

PN Sun, A Colagrossi, S Marrone, M Antuono, and A-M Zhang. A consistent approach to particle shifting in the δ-plus-SPH model. *Computer Methods in Applied Mechanics and Engineering*, 348:912–934, 2019.

K. Szewc, A. Tanière, J. Pozorksi, and J.-P. Minier. A study on application of smoothed particle hydrodynamics to multi-phase flows. *International Journal of Nonlinear Sciences and Numerical Simulation*, 2012.

V. Theofilis. Advances in global linear instability analysis of nonparallel and three-dimensional flows. *Prog. Aero. Sci.*, 39:249–315, 2003.

V. Theofilis, P. W. Duck, and J. Owen. Viscous linear stability analysis of rectangular duct and cavity flows. *J. Fluid. Mech.*, 505:249–286, 2004.

Branislav Titurus, J Cooper, Francesco Saltari, Franco Mastroddi, and Francesco Gambioli. Analysis of a sloshing beam experiment. In *International Forum Aeroelasticity and Structural Dynamics, Savanah, Georgia, USA*, 2019.

Michael Dennis Wright, Francesco Gambioli, and Arnaud George Malan. Cfd based non-dimensional characterization of energy dissipation due to verticle slosh. *Applied Sciences*, 11: 10401, 2021.